



University of
Southern
Queensland

**DESIGN AND FABRICATION OF MICRONEEDLE
PATCHES, MICROBLADES AND FEATURED
INSERTION APPLICATOR FOR OPTIMISING
TRANSDERMAL DRUG DELIVERY**

A Thesis submitted by

Vahid Ebrahimejad

MEngSc (Mechanical), BSc (Mechanical)

For the award of

Doctor of Philosophy

2023

ABSTRACT

Microneedles are promising devices for transdermal drug delivery and biofluid sampling. Microneedle devices provide a non-invasive and painless insertion, which has the potential for self-administration. Despite recent advances, microneedle technology suffers from time-consuming manufacturing processes, inefficient penetration, and unreliable drug delivery. Hence, therapeutic activities are often associated with uncertainties in the reliability and repeatability of the results. To address these research gaps, the initial approach of this thesis is to reduce the fabrication time without compromising accuracy by optimising the fabrication techniques, such as stereolithography, micro moulding, and soft embossing. Moreover, to improve the skin penetration efficiency and drug diffusion of microneedles, the study investigates the effects of microneedle geometrical parameters and external stimulants, such as skin strains and vibrations. This is coupled with applications of artificial skin models, simulation of microneedle and microblade insertion, plus drug diffusion modelling as a validation tool to usher fidelity and reliability to the experimental outcome.

Throughout the thesis, microneedle arrays and microblade masters were made with a photoresist using the two-photon polymerisation, followed by fabrication of polydimethylsiloxane moulds for soft embossing thermoplastic samples. Two approaches were used to reduce the fabrication and replication times of microneedle masters and replicas. Firstly, through modifications to stereolithography codes, multiple master microblades were printed on a single substrate. Hence, the approach for printing six microblades on a single substrate reduced the two-photon polymerisation fabrication time by ~ 63.3 % compared to the fabrication of a 9×9 microneedle array on the identical substrate. Secondly, the thermoplastic replicas were further considered secondary masters for simultaneous centrifugation of multiple polyvinyl alcohol/polyvinylpyrrolidone dissolving microneedle patches. This later approach to employing primary (IP-photoresist) and secondary (Zeonor 1060R) masters reduced the overall fabrication time by ~ 86.9 %.

In the next stage, mechanical and insertion tests are conducted to determine the safety margin of the replicated microblades and microneedles. A series of mechanical compression and transverse tests are conducted on thermoplastic microneedles, dissolving patches, and microblades. For the case of microblade devices, the compression test results indicated that the microblade tip angle and test speed were directly related to the initial stiffness and failure point. In addition, increasing the microblade blade eccentricity resulted in the reduction of initial stiffness and failure point. The margin of safety for both microblades and microneedles is then

determined based on the peak insertion forces using experiments and computer simulations. Insertion tests were conducted experimentally by inserting single microneedles on the polydimethylsiloxane model (strain: 0 - 20 %, vibration: 0 - 250 Hz). These tests are coupled with a novel finite element analysis paradigm, which integrates a series of analyses to model the microneedle insertion on a multi-layered hyperelastic skin model incorporating skin surface strains and vibrations. The results showed an inverse relationship between increasing skin strains (0 - 10 %) and vibrations (0 - 250 Hz) with the peak insertion force. Thus, applying skin strains and vibrations improved the insertion safety of microblades and microneedles.

According to the outcome of the skin strains and vibrations, a novel multifeatured impact applicator is designed, manufactured, and provisionally patented. The prototype impact applicator can be adjusted using the pre-set or manual regulation of impact velocities from 1.5 to 5.5 m/s. The applicator can also enable a range of skin surface stretching utilising a pair of side arms controlled with compression springs for height adjustment and torsion springs for the actual strains of up to 22 N. The applicator can stimulate a range of rotational and linear vibrations with frequency ranges of 0 to 250 Hz and 0 to 200 Hz, respectively.

During the experiments, skin insertion tests were conducted on the porcine back and abdominal skins using fluorescein sodium salt as the model drug coated on solid thermoplastic microneedle arrays and microblades and encapsulated in dissolving patches. Increasing the frequency for two modes of vibrations (0 - 250 Hz) on dissolving patches resulted in higher drug concentrations. The model drug diffusion flux and concentrations were also simulated for different microblades. The results indicated a direct relationship between increased blade angle and higher diffusion flux and concentration. However, finite element analysis results showed that a higher blade angle was associated with reducing microblade penetration depth.

The current thesis introduced new techniques for time and cost-effective fabrication of solid and dissolving microneedles. The study also gave insight into the new methods of application systems for improving insertion safety, penetration efficiency, and drug diffusion. The reliability of the results was validated by coupling the *in vitro* experiments on porcine skin with artificial models and computer simulations. This research also investigated the potential application of microblades for biomedical applications, focusing on geometrical parameters, such as blade angle and eccentricity level. Furthermore, the effects of skin stimulants, such as strain and vibration, were evaluated by studying the mechanics of microneedle insertion/extraction phases. These techniques were introduced into a novel provisionally patented impact applicator capable of regulatable impact speeds, skin strains, and two modes of induced vibrations.

CERTIFICATION OF THESIS

I, Vahid Ebrahimejad, declare that the PhD Thesis entitled *Design and Fabrication of Microneedle Patches, Microblades and Featured Insertion Applicator for Optimising Transdermal Drug Delivery* is not more than 100,000 words in length including quotes and exclusive of tables, figures, appendices, bibliography, references, and footnotes.

This Thesis is the work of Vahid Ebrahimejad except where otherwise acknowledged, with the majority of the contribution to the papers presented as a Thesis by Publication undertaken by the student. The work is original and has not previously been submitted for any other award, except where acknowledged.

Date: 23/05/2023

Endorsed by:

Dr. Zahra Faraji Rad
Principal Supervisor

Professor Peter Schubel
Associate Supervisor

Student and supervisors' signatures of endorsement are held at the University.

STATEMENT OF CONTRIBUTION

The articles published as an outcome of current research are the joint contributions of the authors. The scientific contribution of each author is described below:

Paper 1 (Status: Published):

Ebrahimejad, V., Prewett, P. D., Davies, G. J., Faraji Rad, Z. (2022). Microneedle Arrays for Drug Delivery and Diagnostics: Toward an Optimized Design, Reliable Insertion, and Penetration, *Advanced Materials Interfaces*, 9, 2101856. (Impact Factor: 6.147, Top 10 %). [hTTPs://doi.org/10.1002/admi.202101856](https://doi.org/10.1002/admi.202101856)

The overall contribution of Vahid Ebrahimejad was 60 % for the literature review publication. This includes analysis of skin mechanics and influential factors, MN robustness and mechanical tests, artificial skin models, and FEA methods, followed by methods of reducing skin insertion force and improving penetration efficiency. Zahra Faraji Rad contributed 25 % in concept development, editing, revising, writing, supervision, and providing technical advice. Philip Prewett and Graham James Davies contributed 10 % and 5 %, respectively; they assisted in writing, editing, and providing technical feedback.

Paper 2 (Status: Published):

Ebrahimejad, V., Faraji Rad, Z., Prewett, P. D., Davies, G. J., (2022). Fabrication and Testing of Thermoplastic Microneedles for Transdermal Drug Delivery, *Beilstein Journal of Nanotechnology*, 13, 629-640 (Impact Factor: 3.649, Top 25 %). [hTTPs://doi.org/10.3762/bjnano.13.55](https://doi.org/10.3762/bjnano.13.55)

The overall contribution of Vahid Ebrahimejad was 60 % for the current research publication. This includes research literature review, MN array design, fabrication of the masters using the TPP technique, PDMS micro moulding, and replication of MN arrays. This was followed by MN mechanical compression tests and scanning electron microscopy (SEM) imaging. The insertion tests were then conducted on the porcine skin with subsequent skin cryostat sectioning for imaging using stereo and confocal microscopy. For validation purposes, a 2D axisymmetric simulation was used to model the insertion of MN on the multi-layered hyperelastic skin model. Zahra Faraji Rad contributed 20 % in defining scopes, writing, editing, revising, supervision, and providing technical advice. Philip Prewett contributed 15 % in the form of analytical models for MN robustness and skin penetration, writing and revising drafts and providing technical feedback. Graham James Davies had 5 % participation, providing comments and technical feedback.

Paper 3 (Status: Published):

Ebrahiminejad, V., Faraji Rad, Z. (2022). Design, Development, and Testing of Polymeric Microblades: A Novel Design of MNs for Biomedical Applications, *Advanced Materials Interfaces*, 9, 2201115. (Impact Factor: 6.389, Top 10 %).
[hTTPs://doi.org/10.1002/admi.202201115](https://doi.org/10.1002/admi.202201115)

The overall contribution of Vahid Ebrahiminejad was 65 % for the current research publication. This includes research literature review, design of various MB geometries, fabrication of master MBs using TPP technique, PDMS micro moulding, and thermoplastic replication of MBs. The study continued with mechanical compression tests on various MBs followed by SEM imaging. *In vitro* insertion tests were conducted on porcine abdominal skin with subsequent skin cryostat sectioning for imaging using stereo and confocal microscopy. Two methods of 3D computer simulation were used to evaluate the insertion mechanics of individual MBs on the multi-layered hyperelastic skin model, followed by drug diffusion modelling to determine the drug diffusion flux and concentrations. Zahra Faraji Rad contributed 35 % in defining scopes, editing, experiment supervision, revising and writing, and providing technical advice.

Paper 4 (Status: Ready for Submission – *Provisional Patent (In Progress)*):

Ebrahiminejad, V. Malek-Khatibi, A., Faraji Rad, Z. (2023). Effects of Low-Frequency Vibration and Skin Strains on Insertion Mechanics and Drug Diffusion of PVA/PVP Dissolving Microneedles.
To be submitted after the outcome from Patent Australia.

The overall contribution of Vahid Ebrahiminejad was 60 % for the current research publication. This includes research literature review, design and fabrication of master MN arrays using the TPP technique, PDMS micro moulding of primary and secondary masters, and replication of PVA/PVP DMNPs. This is followed by compression and transverse mechanical tests on the DMNPs and SEM imaging. Furthermore, experimental tests were conducted to evaluate the effects of skin strains and vibrations on the mechanics of insertion and extraction, which was further validated using a novel FEA paradigm to evaluate the insertion of MN into the 3D multi-layered hyperelastic skin model. A novel impact applicator capable of regulatable impact speeds, skin stretching, and inducing ERM/LRA vibrations was introduced to conduct the insertion tests with different vibration frequencies on the porcine skin. This was followed by confocal imaging and liquid chromatography-mass spectrometry (LCMS) analysis to determine the concentration of the model drug. Zahra Faraji Rad contributed 30 % in defining scopes, editing, supervision, writing and revising, and providing technical advice. During this study, Atefeh Malek-Khatibi contributed 10 % to making PVA/PVP solutions and processing DMNP replications by providing advice and feedback.

Patent (Status: Provisional Patent)

Ebrahimejad, V., Faraji Rad, Z. (2022). *An applicator and method of use thereof*, Australian Patent Office, Application Number: 2022903335.

- International-type search outcomes indicated the application is *novel and inventive*.

The invention is created by Vahid Ebrahimejad and Zahra Faraji Rad, and the intellectual property (IP) rights are reserved for the University of Southern Queensland.

ACKNOWLEDGEMENTS

I would like to take the opportunity to thank organisations and individuals who assisted during the studies. My sincere gratitude and appreciation go to:

- Dr **Zahra Faraji Rad**, *my principal supervisor*, for continuous support during the experimental research and article publications. The study could not be presented in this form without inspiration from her past experiences in biomedical engineering.
- Professor **Peter Schubel**, *my associate supervisor*, for valuable support during the research.
- Professors **Philip D. Prewett** (University of Birmingham), and **Graham J. Davies** (University of New South Wales), for their scientific feedback and proof-reading contributions for publication of review paper and research article in the journals of *Advanced Materials Interface* and *Beilstein Journal of Nanotechnology*.
- Dr **Fabian Zander** for his dedicated time and support for high-speed camera experiments.
- **Centre for Future Materials (CFM)** (UniSQ) for support for accessing different research labs.
- **Centre for Microscopy and Microanalysis (CMM)**, **Institute for Molecular Bioscience (IMB)**, and **Australian Institute for Bioengineering and Nanotechnology (AIBN)** (UQ) for providing access to the research labs, with special thanks to Plant Pathology Laboratory at UQ Pandanus building.
- **Oxacus Ltd.** scientific consultant (UK) for financial support for the Micro & Nano Engineering (MNE) Conference 2021, Turin, Italy.

And those who helped during this research journey which are not listed above.

This research has been supported by the Australian Government Research Training Program Scholarship.

TABLE OF CONTENTS

ABSTRACT	i
CERTIFICATION OF THESIS	iii
STATEMENT OF CONTRIBUTION	iv
ACKNOWLEDGEMENTS	vii
LIST OF FIGURES	x
LIST OF ABBREVIATIONS	xi
CHAPTER 1: INTRODUCTION	1
1.1 Background	1
1.1.1 Importance of microneedle devices for drug delivery and sampling	1
1.1.2 Types of microneedles	2
1.1.3 Microneedle materials.....	3
1.1.4 Microneedle manufacturing techniques	4
1.1.5 Microneedle medical applications	6
1.1.6 Challenges associated with microneedle technology.....	7
1.2 Aims and Objectives	10
1.2.1 Design, manufacturing, and replication for mass scale producibility	11
1.2.2 Improving MN and MB safety margin.....	11
1.2.3 Simulation of MN insertion and drug diffusion into multilayered skin models	11
1.2.4 Improving model drug diffusion and penetration using different modes of vibration ..	11
1.3 Scope and limitations	11
1.4 Thesis structure	13
CHAPTER 2: LITERATURE REVIEW– PAPER 1: Microneedle Arrays for Drug Delivery and Diagnostics: Toward an Optimized Design, Reliable Insertion, and Penetration	18
2.1 Introduction.....	18
2.2 Developments of Applicators for MN Insertion.....	46
2.3 Microblade Technology	51
2.4 Chapter Summary.....	52
CHAPTER 3: PAPER 2 - Fabrication and Testing of Polymer Microneedles for Transdermal Drug Delivery	54
3.1 Introduction.....	54
CHAPTER 4: PAPER 3 - Design, Development, and Testing of Polymeric Microblades: A Novel Design of MNs for Biomedical Applications	68
4.1 Introduction.....	68

4.2	Chapter Summary.....	86
CHAPTER 5: PAPER 4 - Effects of Low-Frequency Vibration and Skin Strains on Insertion Mechanics and Drug Diffusion of PVA/PVP Dissolving MNs.....		
5.1	Introduction.....	88
5.2	Chapter Summary.....	135
CHAPTER 6: DISCUSSION AND CONCLUSION.....		
6.1	General.....	136
6.2	Effects of skin strain, modes of low-frequency vibration, and impact speed on MN penetration and model drug diffusion mechanism.....	137
6.3	Design, fabrication, and assembly of multifeatured impact applicator prototypes for drug delivery and diagnostics applications.....	139
6.4	Evaluating the potential application of MB devices for biomedical applications.....	140
6.5	Investigations on simulation of drug diffusion and novel FEA paradigm for MN and MB skin insertions incorporating skin strains and vibration.....	142
6.6	Outcome and significance of the Study.....	143
6.7	Recommendations for future research.....	144
6.7.1	General.....	144
6.7.2	Material composition optimisation for PVA/PVP MN patches for Sampling.....	144
6.7.3	MNs for monitoring and diagnostics.....	145
6.7.4	Advancement for impact applicator.....	147
REFERENCES.....		
APPENDIX A: High-Performance Computing.....		
A.1	High-performance computing paradigm.....	159
A.2	PBS Code and ANSYS journal file.....	160
APPENDIX B: Impact applicator test results.....		
B.1	Impact speed and locking mechanism.....	162
B.2	Stretching arm mechanism.....	165
B.3	ERM/LRA vibration excitation system.....	167
APPENDIX C: Development of GWL codes for printing multiple samples on a single substrate...170		
APPENDIX D: Micro & Nano Engineering Conference (Turin, Italy 2021).....172		
APPENDIX E: COPYRIGHT PERMISSIONS.....173		

LIST OF FIGURES

(This excludes the figures presented in the publications within chapters 2-5)

Figure 1: Schematic representation of MN microdevices used for different therapeutic applications (Madden et al. 2020).....	2
Figure 2: Organisation chart representing different MN designs, manufacturing techniques and materials.....	6
Figure 3: Representation of design features for applicators capable of MN drug delivery....	47
Figure 4: Side-by-side comparison of a sample thermoplastic MB with corresponding MN array, with respective diffusion depths at 4.5 m/s impact insertion.....	142
Figure 5: The PVA/PVP MN patch replication for the sampling process.....	146
Figure 6: Proposed impact applicator advancements and possible integration with existing technology.....	148
Figure A.1: The schematic paradigm representation of the HPC process indicates the link between the user's database, HPC directory, and ANSYS workbench.....	160
Figure B.1: Impact applicator assembly featuring regulatable impact speed, skin strain, and vibration.....	162
Figure B.2: High-speed camera setup for measurements of the prototype impact velocity at different positions.....	163
Figure B.3: Graph representation of high-speed camera experimental results for applicator impact velocity compared with energy method.....	164
Figure B.4: Test setup for estimating actual tension at different arm orientations, with overall tension plotted in Box and Whisker format for different arm orientations (15° - 40°).....	166
Figure B.5: Graph representation of potentially applicable tension of applicator prototype at different arm orientations.....	166
Figure B.6: Schematic representation of impact applicator vibration system and circuit board.	167
Figure B.7: Graph representation of average voltage and current records for ERM and LRA micro-vibration devices for 5 k Ω potentiometer at different orientations.....	168
Figure B.8: Potentiometer knob position versus frequency for LRA and ERM micro-vibration devices.....	169
Figure C.1: TPP prints of different MB samples on a single ITO substrate.....	171

LIST OF ABBREVIATIONS

AM	Additive Manufacturing
AMSM	Artificial Mechanical Skin Model
APE	Array Penetration Efficiency
CFL	Courant–Friedrichs–Lewy
COP	Cycloolefin Polymers
DDS	Drug Delivery System
DLW	Direct Laser Writing
DMNP	Dissolving Microneedle Patch
ERM	Eccentric Rotating Mass
FEA	Finite Element Analysis
FPL	Fractional Penetration Length
F_{ins}	Peak Insertion Force
FSS	Fluorescein Sodium Salt
GWL	General Writing Language
HPC	High-Performance Computing
IPA	Isopropyl alcohol
ISF	Interstitial Fluid
ITO	Indium Tin Oxide
LCMS	Liquid Chromatography–Mass Spectrometry
LRA	Linear Resonant Actuator
MB	Microblade
MEMS	Micro-electromechanical Systems

MN	Microneedle
MW	Molecular Weight
OCT	Optimal Cutting Temperature
PDMS	Polydimethylsiloxane
PGMEA	Propylene Glycol Methyl Ether Acetate
PLA	Polylactic Acid
POC	Point-of-Care
PVA	Polyvinyl Alcohol
PVP	Polyvinylpyrrolidone
SC	Stratum Corneum
SEM	Scanning Electron Microscopy
SM	Safety Margin
STL	Stereolithography
TDD	Transdermal Drug Delivery
TPP	Two-Photon Polymerisation
UV	Ultraviolet

CHAPTER 1: INTRODUCTION

1.1 Background

1.1.1 Importance of microneedle devices for drug delivery and sampling

MNs are promising micro-meter scale projections in the forms of single or MN arrays, which can be used for transdermal drug delivery (TDD), interstitial fluid (ISF) and capillary blood sampling (Figure 1). Hypodermic needles are semi-invasive, uncomfortable, produce waste, and need to be handled by qualified staff. In comparison, MN devices are painless, non-invasive, and can be self-administrative (Cheung, Han & Das 2014; Ranamukhaarachchi & Stoeber 2019). MN applications range from delivering large molecular weight (MW), ionic or hydrophilic drugs to collecting ISF and capillary blood for diagnostics. MNs are geometrically designed based on height, width, tip area, array size, and density. These microdevices can form a cylindrical, conical, prismatic, pyramidal, or blade shape (Faraji Rad et al. 2017; Faraji Rad et al. 2020). By possessing 50 - 900 μm projection lengths and widths of up to a few hundred microns, MNs are designed to bypass the *stratum corneum* (SC) layer of skin while avoiding stimulation of the nerve system (Donnelly, Ryan F. et al. 2010; Bhatnagar, Dave & Venuganti 2017).

For instance, due to MN's attributes, such as their micron size, biocompatibility, biodegradability, and water solubility, it is predicted that the majority of these miniature devices possess minimal hazards and require moderate regulations for sharp handling and disposal procedures. Kim et al. stated that while coated MNs may be considered biohazardous sharps waste, dissolving MNs, which are generally made from inert water-soluble polymers or sugars, should be discarded as non-sharps waste (Kim, Park & Prausnitz 2012). The painless and minimal hazardous nature of MN devices facilitates the patient self-administrating practices. This particularly benefits the point-of-care (POC) diagnostic and monitoring system.

POC reduces the time-consuming and costly procedures associated with laboratory tests for the detection of disease-specific biomarkers (Dixon et al. 2021). Tehrani et al. (2022) integrated the POC diagnostics and monitoring system into a wearable MN device featuring wireless and continuous sensing technology to detect the ISF biomarkers, enabling the real-time monitoring of patient condition on smart phones (Tehrani et al. 2022). The remote monitoring of patient health conditions removes the cost associated with regular consultation while enabling the emergency notification of healthcare services.

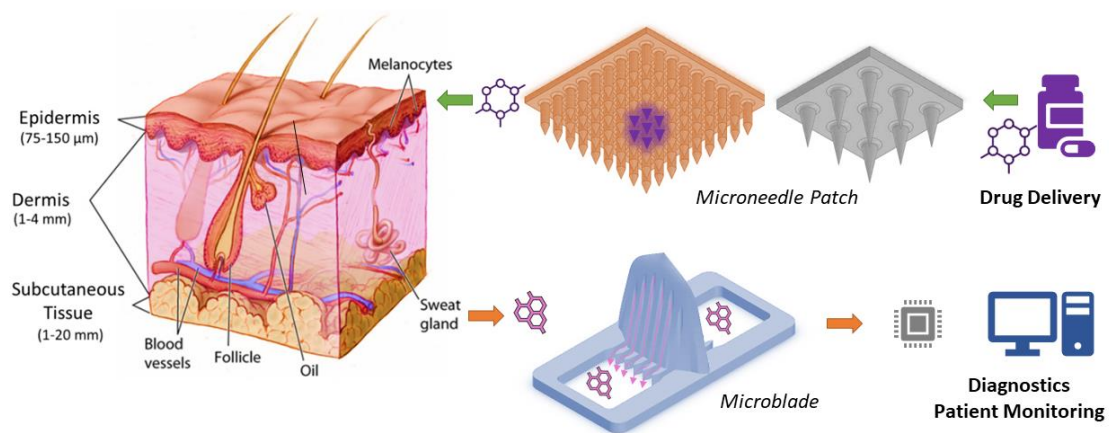


Figure 1: Schematic representation of MN microdevices used for different therapeutic applications (Madden et al. 2020).

1.1.2 Types of microneedles

Depending on the therapeutic applications, MNs can be solid, coated, hollow, dissolving, or open channel types capable of vaccination, drug delivery, and diagnostics (Faraji Rad et al. 2017; Yang et al. 2019). Solid MNs possess good mechanical strength and sharpness compared to hollow MNs. They can enhance the bioavailability and kinetic transport through skin layers, with the potential for delivery of vaccines with higher antibody response (Jacoby et al. 2015; Aldawood, Andar & Desai 2021). Solid MNs coated with drugs may transfer a limited number of compounds, such as proteins and DNAs, through a rapid release. Hollow MNs with inner cores can deliver drugs with higher MW in a controlled and rapid release compared to the solid/dissolving MNs (Ita 2015; Cheung & Das 2016). Dissolving MNs follows a “poke-and-

release” approach, enabling the rapid and waste-free transfer of macromolecules. However, dissolving MNs suffer from delays in dissolution and effective skin penetration (Waghule et al. 2019).

1.1.3 Microneedle materials

MNs are manufactured using materials such as metals, silicon, ceramics, silica glass, or polymers. The selection of these materials depends on their mechanical properties, biocompatibility, biodegradability, and potential for large-scale production. Metals such as stainless steel are the traditional materials widely used in biomedical applications, ranging from hypodermal needles to medical device applications and implant tools. Palladium, titanium, and nickel are also used for MN fabrication (Donnelly, Raj Singh & Woolfson 2010). Compared to other materials, metals and related alloys are biocompatible, with high elastic moduli reaching 180 GPa in SUS-316L stainless steel (Niinomi & Nakai 2011). Silicon materials are also widely used for MN manufacturing, which possess anisotropic behaviour in crystal lattice orientations in each direction. This mechanical behaviour leads to a range of elasticity modulus from 50 to 180 GPa (Hopcroft, Nix & Kenny 2010; Indermun et al. 2014). Although silicon is deemed biocompatible, it can possess granulomas in the skin subcutaneous layer or result in the emergence of nodules in the tooth periodontal ligament (Donnelly et al. 2018). MNs can also be fabricated using carbohydrates, silica glass, and ceramics. This includes simple sugar carbohydrates (e.g. maltose, galactose, sucrose, trehalose, xylitol, etc.) or complex compounds (e.g. polysaccharides), which are considerably cheap and safe for MN drug delivery (Miyano et al. 2005). Silica glass (e.g. borosilicate) are inert material, enabling fluid flow visualisations and quick production for small-scale and non-commercial research purposes (Larrañeta et al. 2016). Ceramics are frequently used for musculoskeletal bones, dental or orthopaedic implants, and bone substitutes. The main ceramic material for MN fabrication is alumina (Al_2O_3), which

is highly resistant, noncorrosive, highly biocompatible, and porous and has been applied in coated drug delivery (Donnelly et al. 2018, p. 27).

Polymers are considerably used both for the delivery of target drugs and ISF sampling in the forms of solid, dissolving, or hydrogel-forming MNs (Park, Allen & Prausnitz 2005; Faraji Rad et al. 2017; Cordeiro et al. 2020). Polymers applied in medical science can be classified into natural, synthetic, and thermoplastics. Polysaccharides and synthetic polymers such as polyvinylpyrrolidone (PVP), poly D L-lactic-co-glycolic acid (PLGA), polylactic acid (PLA), poly (glycolic acid) (PGA), and chitosan are mainly used for dissolving MNs which act as drug cargo for drug delivery. These polymers are biocompatible and similar to the extracellular matrix components. These polymers can be easily removed in the kidney based on their size and MW (Markovsky et al. 2012; Shelke et al. 2014). Cyclic olefin polymers (COP) were used by Sammoura et al. (2006) to fabricate in-plane MNs with open channels from these biocompatible and mechanically robust materials (Sammoura et al. 2006). In recent publications, COPs such as Zeonor 1060R are also used to manufacture open-channel MN arrays (Faraji Rad et al. 2017). Due to the polymer's relatively low melting temperature, it has the potential for a cost-effective and mass-scalable manufacturing process (Lee, Han & Park 2013). Although polymers possess less mechanical strength than other materials, their toughness is higher than ceramics and glass (Hong et al. 2013; Larrañeta et al. 2016).

1.1.4 Microneedle manufacturing techniques

MN devices are manufactured using techniques such as laser cutting/ablation, additive manufacturing (AM), or photolithography coupled with dry/wet etching (Jung & Jin 2021). Photolithography has a multistep procedure, initiating with ultraviolet (UV) exposure of photoresists spin-coated on silicon substrates. To create the desired patterns, photomasks are placed in the direction of the UV source. The samples are then post-processed through etching techniques to form the overall MN shapes. Dry etching, such as reactive ion etching (RIE),

incorporates an exposure process using masks with dots to form the desired MN diameter. These samples are etched inside reactive ion etching chambers. High aspect ratio spikes are formed through trenches created by plasma-based oxygen/fluorine chemistries. This may be followed by wet etching for metallic and silicon MNs to sharpen the tip by submerging the substrate in chemical etchant via dynamics/static etching approaches (Dharadhar et al. 2019). In general, photolithography is a time-consuming technique involving a multistage manufacturing process. Another manufacturing technique is laser ablation, which focuses the optical light beam to form the MNs on the substrate by material elimination. Although this method is fast and effective, this costly technique is associated with initiating cracks or fatigue in the substrate, mainly due to the thermal effects (Desai, Craps & Esho 2013).

AM enables the 3D printing of microstructures with high throughput and lower cost using techniques such as stereolithography (STL), continuous liquid interface production (CLIP), and direct writing lithography (DWL) such as the TPP technique (Jung & Jin 2021). The AM methods are cost-effective, making them a promising means for scalable MN fabrications. TPP technique is another highly precise AM approach that involves exposing photosensitive materials to laser photons. It is also known as direct laser writing (DLW), including a nonlinear process based on the two-photon absorption (TPA) theory. During the process, polymerisation occurs upon focusing two photons carrying half of the excitation energy (Faraji Rad et al. 2017). TPP at its current pace is still a time-consuming approach despite having high precision and accuracy (Ebrahiminejad, Vahid et al. 2022).

Upon the initial fabrication of MN masters, they can be replicated using cost-effective methods such as micro moulding or injection moulding, which has a high potential for mass production (Griffiths 2008). Micro moulding involves casting a polymeric solution containing the active pharmaceutical agents into the mould. Injection moulding and soft embossing are based on filling the mould cavities with molten polymers using injection or applied pressure (Aldawood,

Andar & Desai 2021). The moulds used for the MN replications are mainly fabricated using PDMS. The low-cost PDMS moulds possess high thermal stability, biocompatibility, and ease of use (Park, Allen & Prausnitz 2005; Aldawood, Andar & Desai 2021). Figure 2 summarises the current designs, manufacturing processes, and materials used for the MN technology.

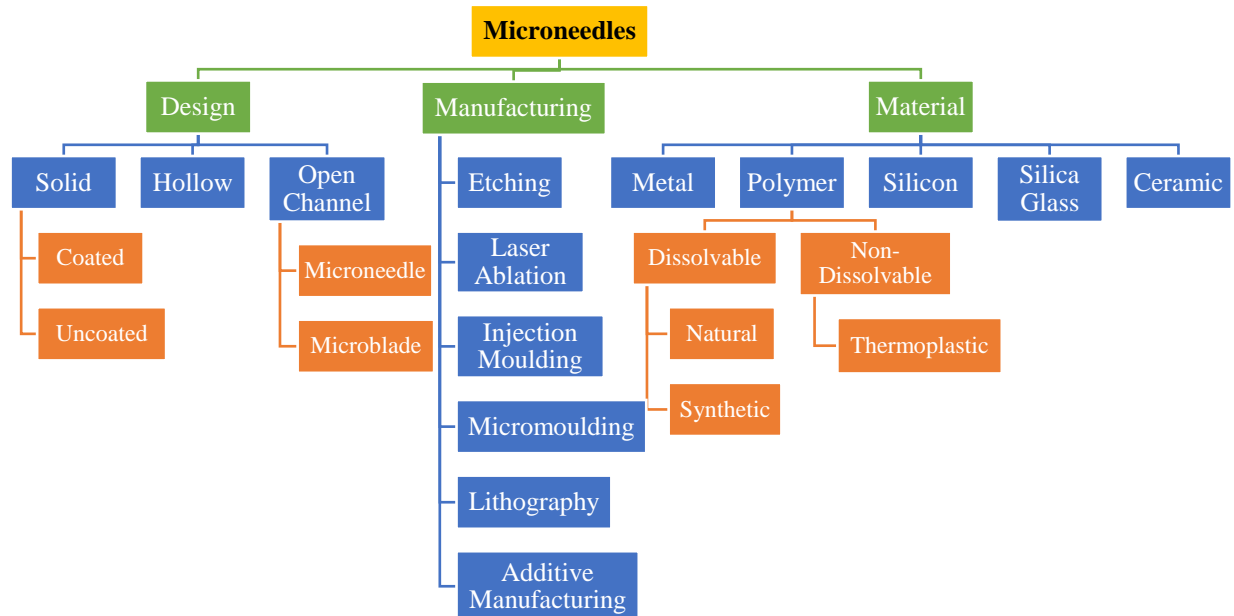


Figure 2: Organisation chart representing different MN designs, manufacturing techniques and materials.

1.1.5 Microneedle medical applications

Medical practices that offer drug delivery, sampling, and diagnostics must use high-efficacy therapeutic methods. Drug formulations are delivered using various drug delivery systems (DDS). Oral administration is a common DDS method associated with the possibility of poor absorption, enzymatic degradation, and rare cases of long-term side effects on liver and kidney organs (Lin et al. 2017). DDS can also take the form of parenteral intravenous, intramuscular, or subcutaneous delivery accompanied by pain and discomfort to the patients (Date & Nagarsenker 2008; Aldawood, Andar & Desai 2021). A painless drug delivery method is

inhalation, mainly used to treat respiratory diseases. Upon self-administration, this DDS technique often poses the risk of overdosing (Rau 2005). Alternatively, TDD can be used for delivering target drug compounds via creams, hypodermic needles, ultrasound, electroporation, iontophoresis, or recently publicised MNs technology (Rau 2005; Lee, G. et al. 2018; Khan et al. 2021).

Therapeutic monitoring and diagnostics require samples mainly extracted from venous blood, breath, stool, and sputum. Despite the variety of sampling procedures, most drug molecules and endogenous substances are identified in samples from whole blood. Yet, blood sample handling is costly and time-consuming, requiring high-performance equipment and trained staff for detection and analysis (Donnelly et al. 2018). Moreover, reports point out that sampling from underlying skin tissues can give a suitable and more predictive clinical response compared to the concentrations within the plasma (Leboulanger, Guy & Delgado-Charro 2004; Donnelly et al. 2018). Therefore, interstitial fluid (ISF) extracted from skin tissues has biomarkers applicable for diagnostics. ISF contains 83 % serum proteins, and only 50 % of these proteins are found in serums (Romanyuk et al. 2014; Samant & Prausnitz 2018). Recently, MN-assisted point-of-care (POC) diagnosis has shown potential for extraction of ISF, which can enable real-time monitoring and detection of diseases such as cancer diagnostics, prognosis, and skeletal or cardiac injury (Keum et al. 2015; Miller et al. 2016; Lee, D.-S. et al. 2018).

1.1.6 Challenges associated with microneedle technology.

Despite the promising potential of MN applications for TDD and biofluid sampling, hurdles during the concept design, manufacturing, and skin insertion remain a challenge. Literature reports on the plethora of manufacturing methods using costly multistage processes, with some requiring cleanroom conditions, which can delay the MN scale-up production. Moreover, during the drug encapsulation into the dissolving MNs or coating on the solid MNs, the active

pharmaceutical ingredient or vaccine's antigenicity may be destroyed (Donnelly et al. 2018). Regulatory bodies such as the FDA (US) and the Medicine and Healthcare Products Regulatory Agency (MHRA) in the UK further state the need for an approved method of MN insertion and provision of end-user training to ensure a successful MN penetration (Vicente-Perez et al. 2016). Therefore, effective MN-based TDD requires the development of rapid and cost-effective production, along with an in-depth study of the MN insertion mechanism, effective penetration, and diffusion of the target drug.

For a successful insertion, MNs should be mechanically stable to avoid possible failure scenarios due to excessive axial and lateral loads. The buckling failure occurs due to the skin *SC* barrier, while the skin's natural elasticity and irregular topologies are responsible for transverse bending failure (Larrañeta et al. 2016). During the actual MN insertion on the skin, the load is linearly increased, then peaks at insertion force (F_{ins}). This is followed by a sudden drop due to the rupture initiated on the skin *SC* layer (Khanna et al. 2010). Integration of MN mechanical strength and insertion force is defined in the concept of safety margin (SM: MN failure force/MN insertion force), which must be greater than unity ($SM > 1$). Thus, higher SM values can be achieved by enhancing the MN mechanical strength or reducing the F_{ins} value (Park, Allen & Prausnitz 2005).

Several studies are performed to evaluate the effects of MN geometrical factors such as increasing MN interspacing, reduction of tip size, and base diameter on the reduction of F_{ins} . External factors, including application velocity and skin conditions such as relative humidity and storage conditions, are also assessed (Ebrahimejad, Vahid et al. 2022). For instance, Yang & Zahn showed a ~ 70 % reduction in F_{ins} when using a vibratory actuator with an undefined kHz frequency range (Yang & Zahn 2004). The study does not specify the frequency and modes of vibration; hence, the relationship between frequency and peak insertion and extraction forces cannot be determined. Recently, the effects of skin strains on the mechanics

of MN insertion were investigated by Shu et al. through FEA of multi-layered skin with hyperelastic materials. Application of various strains from 0 % to 10 % indicated a 13 % and 15 % reduction in F_{ins} and penetration efficiency, respectively (Shu et al. 2021). However, experimental evaluation of these effects may not yield reliable and repeatable outcomes. This is due to the inability to mimic skin *in vivo* state and precise controls on the amount of skin stretching.

MN should reach the desired penetration depth for effective transfer of drugs or biofluids. In general, improper MN geometrical design, insufficient methods of skin application, and natural skin folding around MN projections result in partial penetration (Verbaan et al. 2008). Some parameters such as MN height, interspacing, and base diameter are associated with MN geometry; however, factors such as application force and impact velocity depend on the skin application method (Ebrahimejad, Vahid et al. 2022). While MN pressing force and impact velocity indicated remarkable improvements in the penetration, factors such as MN height and SC layer removals showed no effects on the penetration efficiency (Donnelly, Ryan F. et al. 2010). For instance, one of the common issues associated with MN parametric design includes improper MN interspacing, which can result in the “bed of nails” effect. This phenomenon which commonly occurs at interspacing of lower than 150 μm , initiates when skin is locally stretched by the outermost needles. Thus, the inner MNs apply the insertion forces on an already stretched skin. Therefore, partial penetration occurs due to insufficient MN pressure on the skin (Gülçür et al. 2021). Although single MN protrusion may avoid the “bed of nails” effects, it cannot transfer sufficient drug or biofluid samples. Thus, the patented MB devices with a singular microstructure may be a potential alternative to MN arrays.

Despite the advancements in MEMS technology, cost-effective and timely mass production, replication reliability, reliable penetration, and enhanced drug delivery of MNs remain a challenge. Some potential research avenues are investigating the novel designs of microdevices

and applicators, optimisation of MN fabrication processes, and inclusion of external stimulants, such as skin strains and vibrations. The research gap can then be narrowed to design, manufacturing, and insertion processes. By now, no research has focused on the potential application of novel MB designs as an alternative means of drug delivery and sampling for MN arrays. Moreover, research has not addressed the time-consuming nature of MN master fabrications using TPP and its associated micro moulding processes for MN replications. Ultimately, during the actual skin insertion process, there is an absence of a versatile impact applicator capable of adjustable impact speed and skin external stimulants to improve the efficacy of drug delivery and sampling. Despite studies on the effects of vibrations on the model drug dissolution rate, no study has compared the impact of the linear resonant actuator (LRA) and eccentric rotating mass (ERM) vibration modes on the diffusion kinetics of drugs with larger MW (> 350 Da). LRA generates single vertical motions using magnetic mass attached to a spring and driven by a voice coil, while ERM enables the motions in two axes with unbalanced forces created by the rotation of an eccentric mass. According to the limitations mentioned above, [section 1.2](#) discusses the aims and objectives of the thesis.

1.2 Aims and Objectives

To enhance therapeutic drug delivery and skin penetration, current research intends to design and fabricate MN arrays and MB devices to perform skin insertions using an innovative impact applicator. Current research signifies the need to replicate mechanically stable MNs for safe skin insertions. This can also be achieved by investigating the effects of external stimulants, such as skin vibrations and strains, on facilitating the insertion and extraction phases. Upon MN insertions, penetration efficiency should be maximised for effective drug delivery or sampling diagnostics by improving the geometrical parameters and skin application method. The subheadings below summarise the main objectives of this research, which are further broken down by a series of experiments and simulations to achieve these aims:

1.2.1 Design, manufacturing, and replication for mass scale producibility

- Design and fabrication of different MB and MN patches using COPs, Zeneor 1060R, and dissolvable polymers with the composition of PVA and PVP.
- Development of cost and time-beneficial processes for manufacturing MN/MB masters and replicas

1.2.2 Improving MN and MB safety margin.

- Mechanical testing of MB and MN patches to evaluate their points of failure.
- Study the effects of controlled skin strains and vibration excitations on MN insertion and extraction force reduction.
- Design, manufacture, and develop an integrated impact applicator capable of regulating impact speeds, skin strains, and LRA/ERM vibrations modes.

1.2.3 Simulation of MN insertion and drug diffusion into multilayered skin models

- FEA of MN insertion into the multi-layered hyperelastic skin model considering the effects of strains and vibrations.
- Drug diffusion modelling of MBs with different geometrical parameters into the multi-layered skin model.

1.2.4 Improving model drug diffusion and penetration using different modes of vibration

- Experiments on the penetration of the model drug into the porcine skin using MBs with different geometrical parameters.
- In vitro experiments on porcine skin to define the effects of ERM and LRA vibrations on the kinetics of model drug diffusion and concentrations.

1.3 Scope and limitations

To accomplish the aims and objectives, the project is subdivided into a sequential series of literature reviews, experiments, and simulations as stated below:

- a) The initial section of the thesis studies the current literature on skin mechanics, MN mechanical strength, artificial skin models (AMSM), MN insertion/diffusion simulations, and improving MN penetration efficiency. The literature section also covers the recent applicator patents and their functions.
- b) The next part of the research investigates the fabrication of high-density MN masters, PDMS micro moulding, and replication of thermoplastic MN arrays. The study also aims to characterize the replication process and improve the reliability and repeatability of the skin insertion tests by improving the experiment setups and methods of MN application.
- c) In this part of the study, a series of tests are conducted to optimise the TPP parameters and create/modify the writing codes within the STL files to enable the fabrication of multiple microdevices on a single Indium Tin Oxide (ITO) substrate. This section aims to print a wide range of MBs with different geometrical parameters on a single substrate. The study also investigates the mechanical strength, skin insertion mechanics and drug diffusion of MBs as a potential alternative for MN arrays.
- d) This part of the study is conducted through *in vitro* experiments on porcine skin and FEA explicit dynamic simulation of MN insertions into the multi-layered hyperelastic skin model to estimate the effects of external stimulants on improving MN safety and penetration. The outcomes are integrated into a prototype impact applicator capable of regulatable skin straining, LRA/ERM vibration modes, impact speed, and pressing force. The novel featured impact applicator is then provisionally patented.
- e) In the final part of the study, larger-scale replication of DMNPs is further investigated. The research uses the novel applicator to evaluate the effects of

two modes of induced vibrations at different low frequencies on the dissolution of DMNPs. This study also aims to incorporate a novel FEA paradigm for the simulation of MN insertion on skin with vibrations and strains.

1.4 Thesis structure

The thesis starts with an abstract to give a concise summary of the entire research. This is followed by the introduction chapter explaining the research theme and background. The gaps that require further investigation are identified based on the current literature. Therefore, the aims and objectives are combined into four major studies; the first study focuses on a comprehensive literature review (section 1.3a)), while the other three studies cover the remaining objectives explained in sections 1.3b-e. The thesis ends with conclusions and recommendations for potential areas of research. The appendix presents the ANSYS HPC codes and procedures, details for the impact applicator fabrication and performance assessments, codes for the TPP technique stage movements, and suggested MN patch for sampling diagnostics. During current research, four quality journal articles were produced with high-impact factors, three of which are published, and one is submitted at the time of thesis submission. In addition to the introduction (chapter 1) and conclusion (chapter 6), these publications will cover different chapters as detailed below:

Chapter 2: Article I from Study 1

This section presents a comprehensive literature review and gaps in skin mechanics, MN technology, and skin insertion related to MN devices. The study begins by explaining the skin structure and its mechanical behaviours. Factors influencing mechanical behaviours, such as age, location, humidity, orientation, and strain rates, are explained inclusively. Moreover, MN strength, mechanical tests, and corresponding mathematical models were reviewed. This is followed by an extensive report on experimental skin artificial models and computer

simulations to evaluate failure behaviours, insertion mechanics, and drug diffusion modelling. The last sections of the literature review give an insight into the effects of different parameters on reducing MN insertion force and penetration efficiency (section 1.3 a)).

Published journal article:

Ebrahiminejad, V., Prewett, P. D., Davies, G. J., Faraji Rad, Z. 2022, ‘Microneedle Arrays for Drug Delivery and Diagnostics: Toward an Optimized Design, Reliable Insertion, and Penetration’, *Advanced Materials Interfaces*, vol. 9, 2101856. (Top 10 % journal; Impact Factor: 6.147)

DOI: <https://doi.org/10.1002/admi.202101856>

Chapter 3: Article II and conference participation from Study 2 (section 1.3 b)):

This study focuses on the design and fabrication of MN array masters using the TPP technique, followed by the replication of low-cost thermoplastic MN arrays with high precision and fidelity. Highly dense MN patches are replicated through the simple process of soft embossing cyclo-olefin polymer (COP) polymers (Zeonor 1060R) on PDMS moulds. Experiments and mathematical models determined the shrinkage and mechanical robustness of these replicas. The actual insertion tests were conducted on *in vitro* porcine skin fixed by a premade stretching mechanism using the prototype impact/pressing force applicator. In addition, FEA analysis and experiments determined the insertion forces of single MNs. The safety of the replicated thermoplastic MNs was assessed by determining the SM values from the MN compression failure and skin insertion tests. During this research, a comparison was made between our primary prototype impact applicator and a commercial counterpart by estimating the penetration efficiencies using cryostat sectioning, stereomicroscope, and multiphoton confocal imaging.

Published journal article:

Ebrahiminejad, V., Faraji Rad, Z., Prewett, P. D., Davies, G. J. 2022, 'Fabrication and Testing of Thermoplastic Microneedles for Transdermal Drug Delivery', *Beilstein Journal of Nanotechnology*, vol. 13, pp. 629-640. (Top 25 % journal; Impact Factor: 3.649)

DOI: [hTTPs://doi.org/10.3762/bjnano.13.55](https://doi.org/10.3762/bjnano.13.55)

Conference presentation:

Ebrahiminejad, V., Faraji Rad, Z., Prewett, P. D., Davies, G. J. 2021, 'Polymer Microneedles for Transdermal Theranostics and Vaccination', *Micro and Nano Engineering Conference*, Turin, Italy.

[hTTPs://www.mne2021.org/wp-content/uploads/2021/09/GuidaMNE2021_final2_v3_compressed.pdf](https://www.mne2021.org/wp-content/uploads/2021/09/GuidaMNE2021_final2_v3_compressed.pdf)

Chapter 4: Article III from Study 3 (section 1.3 c):

A recent patent of novel microfluidic devices and fabrications introduced MB designs with a singular microstructure with side microchannels and reservoirs (Faraji Rad et al. 2020). Current innovation has initiated the need for investigations on the potential application of these microdevices as an alternative mean for MN drug delivery and diagnostics. The current study replicated MB devices with various geometrical parameters, including the blade angle and eccentricity, using the soft embossing process for skin insertion experiments. Theoretical and experimental investigations are used to evaluate the mechanical strength and stiffness of each MBs. Subsequently, skin insertion of MBs coated with the FSS model drug was conducted on porcine skin using the adjustable impact/pressing force applicator. Permeability analysis was conducted via confocal microscopy to detect FSS penetration within skin samples. Here, explicit dynamics simulation was used to calculate the insertion forces of individual MBs onto the multi-layered hyperelastic skin models. Similarly, diffusion of the FSS-coated MBs was simulated to calculate the model drug concentrations and their gradients at specific skin layers.

Published journal article:

Ebrahiminejad, V., Faraji Rad, Z. 2022 'Design, Development, and Testing of Polymeric Microblades: A Novel Design of MNs for Biomedical Applications', *Advanced Materials Interfaces*, vol. 9, 202201115.

(Top 10 % journal; Impact Factor: 6.389)

DOI: <https://doi.org/10.1002/admi.202201115>

Chapter 5: Article IV from Study 4 (section 1.3 d):

This study aimed to introduce a high-precision and fidelity replication of DMNPs using a time and cost-effective fabrication process. This research is formed based on the previous study to use replicated thermoplastic MN arrays as a secondary master for making multiple PDMS moulds used for larger-scale replication of DMNPs. The study also quantified the effects of external skin strains and vibration excitations on MN insertion and extraction mechanics. An FEA simulation paradigm was also designed to model the MN insertion into the skin hyperelastic model considering different skin strains and vibration effects. A novel multifeatured impact applicator (Australian Provisional Patent Application No. 2022903335) capable of regulatable impact velocity, skin stretching, and LRA/ERM low-frequency vibrations was manufactured for the skin insertion tests. The prototype applicator was used on the porcine abdominal skin to determine the effects of LRA and ERM vibrations on the diffusion profile and concentration level of the encapsulated FSS model drug inside the DMNPs. For the skin insertion analysis, the FSS penetration depth and concentrations, confocal imaging and LCMS techniques were used, respectively.

Submitted journal article:

Ebrahiminejad, V., Prewett, P. D., Davies, G. J., Faraji Rad, Z. (2023). Effects of Low-Frequency Vibration and Skin Strains on Insertion Mechanics and Drug Diffusion of PVA/PVP Dissolving MNs, **Ready for Submission** – Provisional Patent (In Progress).

Chapter 6: Discussion and Conclusion

This chapter discusses the main results and presents a conclusion for the research. In addition, limitations and recommendations for future research are discussed in this chapter.

CHAPTER 2: LITERATURE REVIEW– PAPER 1: Microneedle Arrays for Drug Delivery and Diagnostics: Toward an Optimized Design, Reliable Insertion, and Penetration

2.1 Introduction

A thorough overview of the literature is presented in this chapter published in the Journal of Advanced Materials Interfaces (2022). Sections 2.2 and 2.3 further provide a comprehensive review of recent MN patent applicators, MB technologies and their advancement. The main areas of coverage include (1) skin anatomy and mechanics, (2) MN materials, manufacturing, and associated mechanical tests, and (3) an in-depth analysis of parameters influencing the MN insertion mechanics and penetration efficiency. The first section introduces the skin layers and their material compositions. This is followed by introductions to the skin's mechanical behaviours, characterisations of stiffness, and failure criteria. The effects of external factors such as viscoelasticity, anisotropic behaviour, skin site, age, humidity, species variation, post-processing, ethnicity, gender, test type, and strain rate on the overall skin mechanical properties are discussed. The effects of geometrical features, materials, and manufacturing techniques on MN mechanical robustness are elaborated. In addition, this section elaborates on MN failure scenarios during skin insertions and main MN mechanical tests, including axial, transverse, and shear loading. The review paper also provides insight into the commonly used AMSM, finite element simulation, and drug diffusion modelling techniques. The final sections of the review paper focus on two main challenges for improving MN safety and effectiveness through reducing the force of insertion and enhancing penetration depth. This section compares the literature outcomes related to MN geometrical characteristics, insertion tools, test conditions, and time to enhance the MN insertion force and penetration efficiency.

Section 2.2 provides literature on different applicator patents for facilitating the MN insertion and delivery of target drugs. An in-depth analysis of their insertion methods, drug reservoir setups, release mechanisms, and skin stimulants are described. This section aims to provide background information for the novel multifeatured impact applicator patented as an outcome of the current thesis.

This article cannot be displayed due to copyright restrictions. See the article link in the Related Outputs field on the item record for possible access.

2.2 Developments of Applicators for MN Insertion

2.2.1 General

Reliable skin application methods provide effective MN drug delivery and sampling, which are essential to any therapeutic practice. Due to skin's inherent elasticity and irregular surfaces (Donnelly, R. F. et al. 2010), achieving insertion reproducibility, accuracy, and precision remains challenging (Donnelly et al. 2012). The MN skin insertion method can be of thumb pressing force or using applicators to generate a controlled pressing force or predetermined impact energy (Leone et al. 2018). Applicators are reliable tool for MN skin insertion in order to improve penetration, drug delivery, or biofluid sampling. Several companies have investigated the design and manufacture of these devices. The most notable companies in the field of applicator design are 3M, Norwood Abbey, Vaxxas, Therajet, Nanopass Technology, Integrated sensing system (ISSYS), Apogee Technology, Animas Corporation-Debiotech, Intek, Kumetrix, Micronit, Microfluidics B.V., Silex Microsystems, Nano Device, Zeopane, SpectRx, Valeritas, and Elegaphy (Donnelly et al. 2012). For instance, in Australia, Vaxxas Ltd. has developed a spring-loaded applicator for MN patches, which is capable of delivering vaccines to targeted skin layers while enhancing patient's bodily immune responses (Vaxxas 2023).

Depending on the therapeutic practices, MN applicators can be comprised of different features to facilitate drug delivery or biofluid sampling. Despite the prevalence of coated and encapsulated MNs for drug delivery purposes, some applicators use internal reservoirs to preload or mix the drug solutions. The MN patches are applied to the target site using pressing force, spring load or electrically driven insertion methods. MN applicators generally incorporate a lock and release mechanism to activate the insertion process. Upon the skin insertion, external skin stimulants, such as skin tautness, vacuum, and vibration, may also be

applied to improve the overall therapeutic result. Figure 3 shows the common components used in MN applicators and the associated patents.

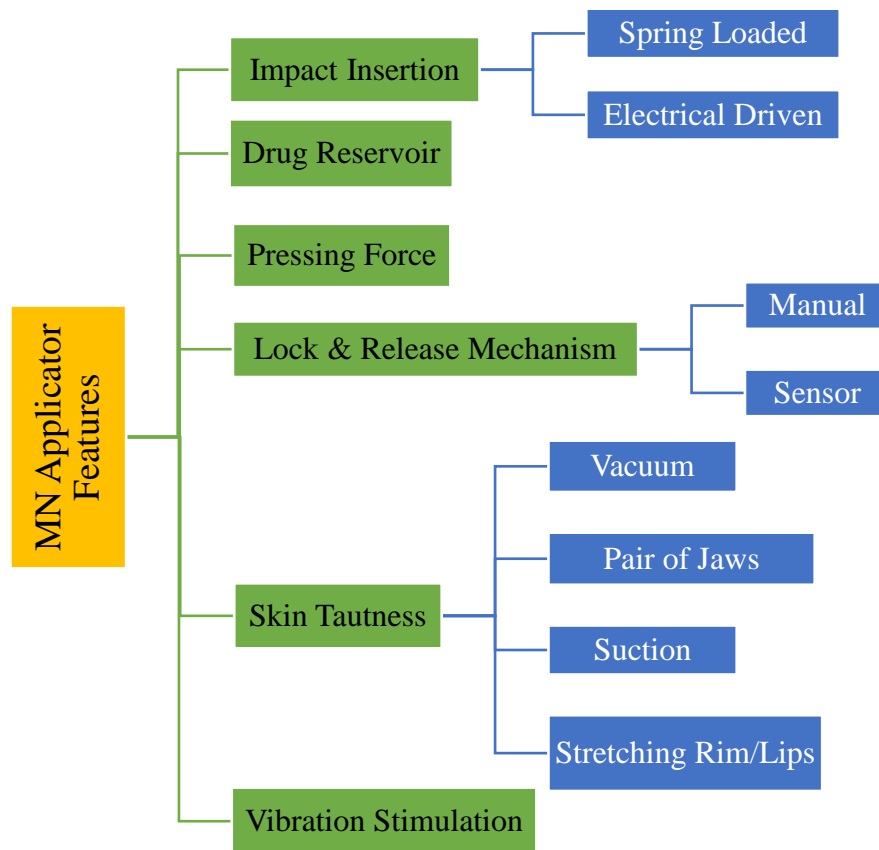


Figure 3: Representation of design features for applicators capable of MN drug delivery.

2.2.2 Methods of MN Insertion

The mechanics of MN insertion into the skin directly affect the drug delivery performance. In general, MN devices can be applied on the skin using manual pressing or mechanical impact on the skin. Comparing the impact insertion versus the manual force insertion methods, Van der Maaden et al. (2014) found 40 % lower MN penetration efficiency and reproducibility of manual insertions (van der Maaden et al. 2014). To apply impact insertion, researchers have implemented methods, such as electronically controlled or stepped plunger mechanisms (Verbaan et al. 2008; Leone et al. 2018).

Several patented applicators use manual skin insertion, which generally requires patient's manual hand effort. For instance, the Microneedle Therapy System roller (MTS-roller™) has been developed by Lee and Hong to treat skin ageing signs by stimulating collagen production through a series of MN projections. In this method, MNs are mounted on a plurality of disks joined together, forming a cylinder supported by ending covers. A shaft is passed through the cylinder and supported by the handle, enabling manual rolling action on the skin (Lee & Hong 2006). Similarly, MicroCor™ is a relatively simple and single-use applicator with a surrounding annulus and solid disc. The applicator is designed by Corium International Ltd. (Menlo Park, CA, USA), claiming to deliver peptides, proteins, and vaccines. For application purposes, MN patch is placed on the inner part of the applicator to be finger-pressed onto the skin surface from a push-button placed on the outer part (Trautman & Olson 2006). Similar to the previous design, Cantor et al. (2008) introduce another relatively simple applicator with a flexible central raised sheet for holding the MN patch, with a supporting membrane near the sheet. This applicator has stepped movement perpendicular to the sheet. Once a specific thumb force is reached, a sudden motion can create skin microporous, accompanied by a clicking noise (Cantor et al. 2008).

Alternatively, impact applicators are designed based on the potential energy stored in spring or equivalent electrical energy. Zosano pharma™ has invented a Microflux applicator (Cormier et al. 2003), which consists of a body and an internal movable piston with an impact spring, enabling the impact insertion of a protrusion membrane. The protrusion membrane is held onto a breakable retainer section and can be loaded on the applicator from the skin's distal end. A patent by Ringsred and Frederickson (2015) from 3M Company used different types of elastic bands which can be wrapped around patients' arms. The elastic bands containing the MN patch is then pulled back using a gripping membrane (handle). Upon breakage from the connecting membrane, the MN patch is released from a suitable distance, snapping against the skin surface,

creating micropores (Ringsred & Frederickson 2015). An applicator using a similar concept has been invented by placing an innerspring between the cap and piston inside upper and lower housings, accompanied by a locking system that releases a locking lever from the upper housing shoulders. In this design, a leaf spring is deflected with the help of a rotor maintained on an axis through a pin connected to the outer knob. An actuator push button then releases the piston (Clarke et al. 2003).

2.2.3 Applicators with Drug Reservoir

Target drugs can be coated or encapsulated into MN devices to perform TDD. Alternatively, applicators with internal reservoirs are designed and patented to transfer the drug through hollow MN devices into the skin subject. In 1999, Valeritas first introduced an applicator for drug delivery which connected the MN patch substrate to a reservoir (Prausnitz, Allen & Gujral 1999). In a similar approach, Tokumoto et al. (2007), through Hisamitsu pharmaceutical invention, incorporate a drug absorber medium and a vehicle container inside the patent applicator. Upon applying the pressure, the solution is released, mixed with the coated drug, and further absorbed by the skin (Tokumoto, Matsudo & Kuwahara 2007). Similarly, Wilkinson and Newby (2003) from Becton Dickinson have invented a device in which the drug can be visually seen when delivered through a reservoir with an elastic wall (Wilkinson & Newby 2003). The reservoir has an inlet for substances to flow into the container. A Pen type applicator commercially called BD SoluviaTM was also first invented by Pettis et al. (2009) through BD & Company (Sparks, MD, USA), enabling drug transfer through a MN-based pen device. The applicator consists of a cartridge (drug reservoir), a plunger, and a driving mechanism. A hub which holds the MN firmly at the centre can be attached to the Pen device (Pettis, Martin & Kaestner 2009). Sausse et al. (2012) have patented a reusable applicator with a reservoir to contain liquid drug solutions, which couples with MN arrays capable of interrupting the reservoir membrane using their back needles (Sausse et al. 2012).

2.2.4 Locking and Release Mechanism

Applicators with impact insertion are usually triggered by a lock-and-release mechanism. For instance, the Microflux applicator uses a piston which can be locked in the cocked position before releasing into the skin. This mechanism uses a pin that disengages a latch from a catch using a flexible finger (Donnelly et al. 2012). Similarly, Trautman et al. patent indicates a self-actuating spring applicator mounted between piston and cap, enabling patients with lower dexterity and strength to move the piston and cap to a pre-set position. By pressing down the cap, the piston is triggered to puncture through the retainer with the micro protrusion membrane, resulting in skin impact insertion (Trautman & Olson 2006). Another innovative patent from 3M by Cantor (2005) includes sensors such as photo-reflective, laser triangulation, or ultrasonic sensors that can measure the distance from the sensor to the skin surface. The sensor is attached to the housing's outer section, which causes the release of the trigger, striking the MN patch on the skin once a certain distance is reached (Cantor 2005).

2.2.5 Skin Stimulants

External stimulants, such as skin tautness and vibration, are effective on reduction of MN peak insertion force and improving penetration efficiency during drug delivery and sampling practices (Yang & Zahn 2004; Samant & Prausnitz 2018). For instance, Lastovich et al. (2002) from BD Company has filed several applicators, including one for sampling and drug delivery, using methods such as vacuum, in which the applicator can be inserted into a syringe as the reservoir to contain the substance (Lastovich, Evans & Pettis 2002). A similar concept by Palmer (2001) introduces skin tightening using side lips. These lips can stretch the skin surface once the applicator is pressed against the skin (Palmer 2001). Furthermore, Inou et al. (2010) has filed a patent describing a device capable of removing the SC layer, enabling drug delivery of shorter MN arrays (with the possibility of convex shapes). This device also introduces side

lips to enhance skin tightness during insertions (Inou et al. 2010). Prausnitz et al. (2004) designed a MN applicator featuring a key and shoulder to overcome skin elasticity by enabling skin stretching at the insertion site. The shoulder limits the stretched area while the skin surface is stretched inside the key. However, they propose methods such as vacuum, cold treatment, suction, use of curved MN arrays, and application of a pair of jaws to pinch or stretch the skin to overcome the skin elasticity. They introduce a flexible stretching cone with a circular outer rim capable of stretching the skin by manually pressing the inner MN patch on the skin surface. The adjustable stretching cone stretches the skin upon engaging with skin surface friction (Prausnitz et al. 2004).

Effects of MN vibratory actuation on needle force reduction were first proposed for the hypodermic needles, indicating around ~ 70 % reduction in the peak insertion force (Yang & Zahn 2004). Methods of skin vibration have since been introduced for applications such as skin treatments and drug delivery. This includes a skin ultrasonic injector, which has been invented by Mi-young and Tae-gyu (2018) that oscillates ultrasonic waves protruding through a fastening hole. The ultrasonic skin stimulator can enhance drug absorption through skin layers (Mi-young & Tae-gyu 2018). Park (2008) also introduces a vibration skin stimulator consisting of a vibration generator, amplifier and a head portion that holds the MN patch. The device can induce ultrasonic vibration to stimulate the skin, which enhances drug absorption through pathways generated by MN arrays (Park 2008). Similarly, Seung-goo and Geun-sik (2015) patent incorporates ultrasonic vibration to massage the skin, which is coated with the drug to enhance drug delivery into the skin (Seung-goo & Geun-sik 2015).

2.3 Microblade Technology

Despite advancements in MN array, there are significant challenges which are solely associated with this technology. One of these drawbacks is the “bed of nails” effect associated with partial penetration of inner MN projections due to insufficient interspacing (Olatunji et al. 2013).

Advanced fabrication techniques such as TPP enable highly precise 3D printing of highly complex micron-scale structures (Faraji Rad, Prewett & Davies 2022). However, large MN arrays can take significantly more fabrication time than single microstructures. Thus, Faraji Rad et al. (2020) patented a complex singular microblade device with multiple side channels for the transfer of drugs or biofluids. This patent, which is part of the research focus in this thesis, constitutes a sharp upright blade with side channels extending downward to the front and rear reservoirs. The reservoirs can act as biofluid sample containers, or drug container for drug delivery, and sampling purposes, respectively.

2.4 Chapter Summary

The current literature review covered the growing interest in MN technology as an alternative to hypodermal needles which are associated with pain, waste residues, and expert administration. Ebrahiminejad, Vahid et al. (2022) published a comprehensive literature review on the advancements of MN technology in pursuit of safer, time and cost-effective MNs with the potential for self-administration. An insight was given into MN design and fabrication through applications on the skin subjects. The first section reviewed the role of skin material composition on the elastic, anisotropic, and hyperelastic mechanical behaviour of skin. Moreover, the effects of factors such as skin orientation, location, gender, skin ageing, relative humidity, and temperature on mechanical characterisations were discussed.

The next section focused on the effects of geometrical, material selection, and manufacturing processes on MN mechanical robustness. Parameters including MN length, width, and base geometry were the key factors in the MN's mechanical strength. The failure scenarios, such as buckling, bending, and shear failures, are evaluated using axial, bending, and shear tests. The following sections elaborated on the significant literature gap in the reliability and

reproducibility of *in vivo* and *ex vivo* experimental tests. Alternative approaches discussed were different AMSMs, computational simulation of the MN insertion, and drug diffusion.

During the insertion of MNs on the skin subjects, the margin of safety is not limited to MN mechanical strength. Improving insertion safety also depends on reducing the peak MN insertion force. Thus, one section detailed the effects of various parameters on reducing the insertion force. Drawing comparisons indicated that tip diameter, MN array density, and MN application velocity were critical in decreasing MN insertion force. Following MN insertion, MN penetration depth and array efficiency directly influence the delivery of the target drug or sampling ISF. Thus, MN fractional penetration length (FPL) and MN array penetration efficiency (APE) concepts were introduced, and measurements from different studies were presented. Impact velocity, pressing force, and array density had the utmost significant effects on improving FPL and APE.

The review article systematically introduced MN design, fabrication, and skin insertion for biomedical applications. The review concluded by pointing out the challenges for MN mass production, such as reproducibility, fabrication preciseness, in-line monitoring, and production time. Recent investigations into scale-up manufacturing of MN technology included advancement in leading techniques such as TPP micro moulding and injection moulding. Optimisations and improvements of the most promising fabrication techniques can pave the way for the mass production of MNs for biomedical applications.

CHAPTER 3: PAPER 2 - Fabrication and Testing of Polymer Microneedles for Transdermal Drug Delivery

3.1 Introduction

This chapter provides an extract copy of the published article in the Beilstein Journal of Nanotechnology. This research addresses two of the main thesis objectives: determination of safety margins for thermoplastic MNs ([section 1.2.2](#)) and axisymmetric simulation of MN insertion into the multilayered hyperelastic skin model ([section 1.2.3](#)). The study incorporated biocompatible thermoplastic polymers (Zeonor 1060R) to fabricate highly dense 9×9 MN arrays, compared to previous 5×5 thermoplastic MN arrays manufactured using similar techniques. Master MN arrays were fabricated using TPP with high accuracy and precision. PDMS moulds from the masters are then used to replicate thermoplastic MN arrays using the soft embossing process. The transdermal delivery used the concept of solid MN arrays coated with an FSS model drug. Porcine skin insertion of MN arrays was conducted using a predesigned skin stretching device and prototype impact applicators capable of adjusting impact speed and pressing force. FSS model drug penetration and diffusion were then determined using a stereomicroscope, cryostat sectioning, and multiphoton confocal imaging techniques.

Moreover, the study investigated the application of a prototype skin stretching mechanism for mimicking the skin *in vivo* conditions and provided a comparison between commercial and prototype applicators. The computer simulation of MN insertion into the multi-layered hyperelastic skin was also used to gain further insight into MN insertion mechanics. The ratio of compression failure result to MN peak insertion force was then used to evaluate the SM value.



Fabrication and testing of polymer microneedles for transdermal drug delivery

Vahid Ebrahimejad¹, Zahra Faraji Rad^{*1}, Philip D. Prewett^{2,3} and Graham J. Davies^{4,5}

Full Research Paper

Open Access

Address:

¹School of Engineering, University of Southern Queensland, Springfield Central, QLD 4300, Australia, ²Department of Mechanical Engineering, University of Birmingham, Birmingham B15 2TT, United Kingdom, ³Oxacus Ltd., Dorchester-on-Thames, OX10 7HN, United Kingdom, ⁴Faculty of Engineering, University of New South Wales, Sydney, NSW 2052, Australia and ⁵College of Engineering & Physical Sciences, School of Engineering, University of Birmingham, Birmingham, B15 2TT, United Kingdom

Email:

Zahra Faraji Rad* - zahra.farajirad@usq.edu.au

* Corresponding author

Keywords:

hot embossing; microneedles; penetration efficiency; thermoplastic polymers; two-photon polymerization

Beilstein J. Nanotechnol. **2022**, *13*, 629–640.

<https://doi.org/10.3762/bjnano.13.55>

Received: 16 March 2022

Accepted: 30 June 2022

Published: 08 July 2022

This article is part of the thematic issue "Microneedles for vaccination and drug delivery".

Associate Editor: S. Giordani

© 2022 Ebrahimejad et al.; licensee Beilstein-Institut.

License and terms: see end of document.

Abstract

Microneedle (MN) patches have considerable potential for medical applications such as transdermal drug delivery, point-of-care diagnostics, and vaccination. These miniature microdevices should successfully pierce the skin tissues while having enough stiffness to withstand the forces imposed by penetration. Developing low-cost and simple manufacturing processes for MNs is of considerable interest. This study reports a simple fabrication process for thermoplastic MNs from cycloolefin polymers (COP) using hot embossing on polydimethylsiloxane (PDMS) soft molds. COP has gained interest due to its high molding performance and low cost. The resin master MN arrays (9 × 9) were fabricated using two-photon polymerization (TPP). A previous gap in the detailed characterization of the embossing process was investigated, showing an average of $4.99 \pm 0.35\%$ longitudinal shrinkage and $2.15 \pm 0.96\%$ lateral enlargement in the molded MN replicas. The effects of bending, buckling, and tip blunting were then examined using compression tests and also theoretically. MN array insertion performance was studied in vitro on porcine back skin using both a prototype custom-made applicator and a commercial device. An adjustable skin stretcher mechanism was designed and manufactured to address current limitations for mimicking skin in vivo conditions. Finite element analysis (FEA) was developed to simulate single MN insertion into a multilayered skin model and validated experimentally using a commercial Pen Needle as a model for the thermoplastic MNs. Margins of safety for the current MN design demonstrated its potential for transdermal drug delivery and fluid sampling. Experimental results indicated significant penetration improvements using the prototype applicator, which produced array penetration efficiencies as high as >92%, depending on the impact velocity setting.

Introduction

During the past two decades, MN devices have become a promising tool for transdermal drug delivery, vaccination, and point-of-care diagnostics [1,2]. MNs are a painless and non-invasive method of drug delivery or sampling which can bypass the skin's outermost layer, the stratum corneum (SC), without stimulating nerves, causing irritation, or initiating infections [2,3]. These miniature devices enable disease diagnosis and control testing beyond viruses to bacterial infections and medical emergencies, with point-of-care patch diagnostics replacing ponderous and expensive laboratory testing. Therefore, there is a growing interest in small patches incorporating mass manufacturable polymer MNs [4,5], with the point-of-care rapid diagnosis market alone predicted to grow to \$50.6 billion by 2025 [6].

To enable mass manufacturing of MNs, factors such as reproducibility, fabrication precision, lower production cost, and time should be addressed. For instance, manufacturing techniques such as reactive ion etching and deep reactive ion etching incorporate multistage fabrication processes with high production costs [7]. Similarly, laser ablation and lithography techniques are costly, requiring extended production time [8]. To overcome the current manufacturing limitations, MNs might be fabricated cost-effectively, with high precision and accuracy, using 3D printing and TPP techniques [9-11]. Although additive manufacturing (AM) techniques are usually viewed as time-consuming processes, modifications and optimizations of printing parameters within the codes and algorithms of AMs can lead to significant reductions in production time [11].

MN arrays are classified into solid, hollow, coated, hydrogel-forming, and dissolvable types, which depending on the specific medical applications [12,13], are fabricated using silicon, metal, ceramic, silica glass, carbohydrate, and polymers [7,14]. In recent years, polymeric MNs have gained a lot of interest due to their biocompatibility, biodegradability, and potential for mass production [12]. Polymers such as polylactic acid (PLA), poly(methyl methacrylate) (PMMA), poly(carbonate), cyclic olefin copolymer (COC) and cycloolefin polymers (COP), polystyrene, and SU-8 photoresists, have all been used for fabrication of MNs. The low manufacturing cost and desirable mechanical properties of medical-grade thermoplastics such as COPs make them a particularly attractive choice of materials [15,16]. MN thermoplastic replicas are readily fabricated using injection molding or hot embossing [17]. However, process characteristics such as operating temperature, axial force range, and embossing time depend on material properties, geometrical size, and complexity, requiring multiple optimization studies.

MN arrays must be capable of being handled without risk of damage and must penetrate the skin with low force to the required depth [18]. There should be no MN-induced skin contamination, for example, due to breakage of the tips, and zero toxicity demands medical-grade materials. Evaluation of MN mechanical strength requires an investigation of MN insertion characteristics and possible failure scenarios. During the normal insertion of MNs, the applied force is linearly increased to the moment of rupture, which breaks the skin's SC layer, followed by a sudden drop in the force-displacement graph [19,20]. However, the MN can be subjected to sudden excessive axial or lateral loads, which may induce early failure of the MN before skin rupture. Several methods are used to estimate these critical loads and their associated stresses, including theoretical analysis, experimental investigations, and FEA simulations [21]. For example, due to the skin's SC barrier, the normal (vertical) insertion of MN patches on the skin may result in MN failure due to buckling. The skin's irregular topology and inherent elasticity can also impose undesired lateral loads, resulting in transverse bending failure [14]. Prevention of possible failure scenarios can avoid MN breakage and reduce the risk of leaving residues in the skin, hence improving overall insertion safety. For the MN insertion to be mechanically safe, the safety margin (SM), which is the ratio of failure force to insertion force, should be maximized and greater than unity ($SM > 1$) [22].

MNs must penetrate deep enough into the skin layers to enable an effective therapeutic drug or vaccine delivery and extraction of capillary blood or interstitial fluid while avoiding stimulation of the underlying nerve system, which can cause pain to the patient [21,23]. To facilitate the penetration of the MNs, the axial force applied to the MN must be greater than the resistive force of the skin. Successful insertion is achieved upon reaching sufficient penetration depth and creating microchannels within the skin. However, the skin's inherent elasticity and its irregular surface, with the tendency to fold around MN projections, result in unpredictable array penetration efficiency (APE), defined as the fraction of the MNs in the array passing through the stratum corneum layer without damage [24,25]. Further quantification of MN penetration is the fractional penetration length (FPL), defined as the proportion of a MN's length penetrating the skin relative to its overall length. Meanwhile, several commercial insertion devices are patented and marketed to provide a platform for quick and pain-free insertion of MN patches, mainly for drug delivery; however, they may only be suitable for specific MN designs [26].

During MN insertion tests, the experimental setups for the measurement of FPL and APE affect the fidelity and repeatability of results [21]. To mimic the in vivo conditions of the skin, some

researchers pre-stretch the sample [27,28]. But the uncontrolled initial skin strain may yield different results for otherwise similar experiments. Shu et al. recently indicated the significance of controlled skin strains on both force of insertion and MN penetration [29].

This paper investigates the reliability and fidelity of dense thermoplastic MN arrays (9×9) fabricated using TPP and hot embossing techniques. It considers the mechanical integrity and insertion characteristics of the arrays using theoretical, experimental, and simulation approaches. The arrays are coated with fluorescein to simulate transdermal low molecular weight drug delivery. To study MN penetration, the replicated polymer MN arrays were applied on the skin with various application methods, including dynamic impact insertion using a commercial applicator and insertion using an in-house designed and manufactured spring-loaded prototype applicator. A custom skin stretching mechanism was built to mimic skin in vivo conditions in a controlled manner. MN arrays were applied on the full-thickness porcine back skin. Pig skin possesses similarities to human skin [30]; excised dorsal (back) skin has greater stiffness compared to other skin locations [31]. The experimental results include the MN mechanical strength, mechanisms of MN damage, skin insertion force, and margin of safety prediction, along with an estimation of FPL and APE applied using different methods. The study shows the importance of custom-made impact applicators tailored for specific MN arrays to improve the APE and FPL and maintain a higher margin of safety during insertions.

Materials and Methods

Design and fabrication of master MN array

The MN array fabrication process uses the commercial Nanoscribe Photonic Professional GT 3D printer (Nanoscribe GmbH, Karlsruhe, Germany), providing a TPP process to make a master MN array by additive manufacturing. The 9×9 MN array with an overall height of 1100 μm , 250 μm base diameter, 500 μm interspacing, and 75 μm base fillet were initially designed in SolidWorks (Dassault Systems SolidWorks Corporation, Concord, NH, USA), then exported to stereolithography (STL) code.

The generated STL code is then imported into the DeScribe (Nanoscribe GmbH, Karlsruhe, Germany) software to adjust settings such as slicing, shell and scaffolding, laser power, and scanning speeds before converting to General Writing Language (GWL) codes. Parameters such as slicing distance of 2 μm , multiple base slide counts of 4 layers, shell and scaffolding filling method, null shear angle (0°), and laser power of 100 mW were selected after process optimization to reduce MN fabrication time and delamination from the substrate. GWL files

are then imported to NanoWrite software (Nanoscribe GmbH, Karlsruhe, Germany), which is synced with NanoScribe to initiate the polymerization. The IP-S negative-tone photoresist was drop cast onto an indium tin oxide (ITO) glass substrate prior to starting the printing process. A dip-in laser lithography (DiLL) objective ($25\times$ magnification, $\text{NA} = 0.8$) was used for printing, after which the MN array was washed in propylene glycol methyl ether acetate (PGMEA) for 10 minutes, then rinsed in isopropanol (IPA) solution for 3 minutes. The final master MN array was carefully rinsed with deionized water and air-dried (Figure 1a).

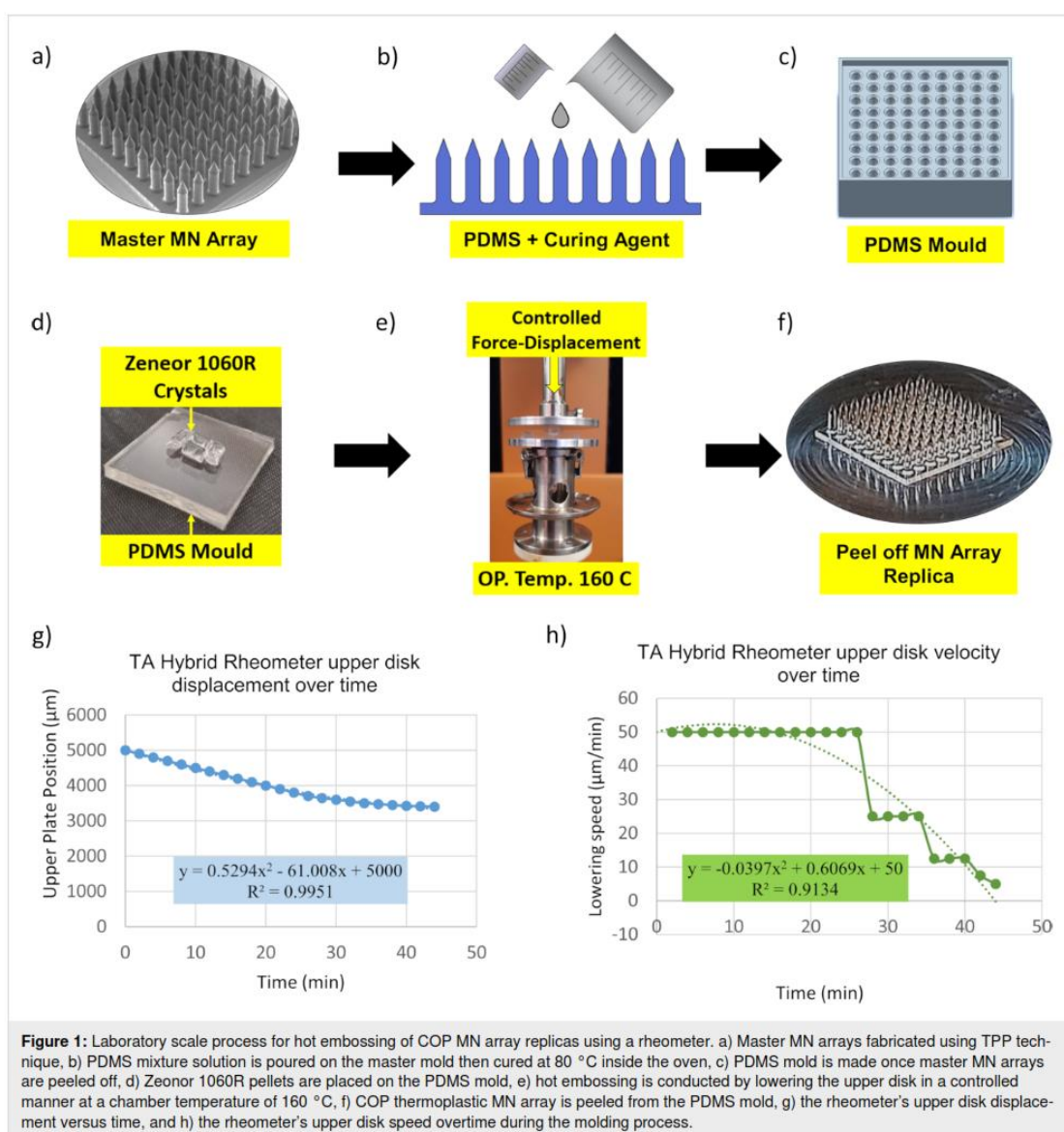
Manufacturing PDMS molds and MN replication

The master MNs were subsequently used to make soft polydimethylsiloxane (PDMS) molds for hot embossing the MN arrays in Zeonor 1060R COP. The PDMS solution was made by degassing the mixture of 1:10 curing agent/base ratio, which was then poured onto the master MN array and heated at 80 $^\circ\text{C}$ for 1 hour (Figure 1b). Samples were kept overnight to cure the PDMS mixture (Figure 1c).

To perform the hot embossing process, a rheometer (TA Instruments, New Castle, USA) was used to melt the Zeonor 1060R COP crystals, and placed in the cavities of the PDMS mold, while press forcing the sample against the mold. During this process, Zeonor 1060R crystals are placed on the PDMS mold cavities (Figure 1d), with the chamber temperature raised to 160 $^\circ\text{C}$, which is 60 $^\circ\text{C}$ above the Zeonor 1060R's glass transition temperature (100 $^\circ\text{C}$). The rheometer is equipped with an enclosable chamber to maintain a constant temperature during the process. To perform the embossing process, the upper plate displacement and the lowering speed were set to decrease overtime to overcome the effects of viscosity that can impose abrupt pressure on the mold cavities (Figure 1e). The upper disk was lowered by ≈ 1.5 mm (Figure 1g) at a speed which was non-linearly reduced from ≈ 50 to 5 $\mu\text{m}/\text{min}$ ensuring that the maximum axial force did not exceed 30 ± 2 N (Figure 1h). After embossing, the chamber temperature was set to 10 $^\circ\text{C}$ for 15 minutes to cool down the PDMS and thermoplastic sample and solidify the replicated microstructure. The polymeric replica of the MN array was then carefully peeled off from the PDMS mold (Figure 1f). The entire replication process for each MN array took 45 minutes.

MN mechanical compression test

To study the failure modes of the MN arrays, a quasi-static compression test was conducted using the rheometer. A single MN with similar geometry to the 9×9 MN array was separately manufactured using the same process. It was assumed that the single MN projection linearly represents the 9×9 MN



array by the factor of the number of MN projections. The single MN was attached to the lower disk of the rheometer using a double-sided tape. The upper disk was lowered with a constant velocity of 1 $\mu\text{m}/\text{s}$ and traveled for 400 μm , measured from the MN tip. During the compression test, the force-displacement data were collected and plotted with MATLAB (Natick, Massachusetts, USA).

Skin preparation and MN array insertion tests

Porcine back skin was used to test the penetration efficiency and insertion depth of the 9 × 9 MN arrays, using experimental

procedures approved by the University of Southern Queensland (USQ) and the University of Queensland (UQ) animal ethics and biosafety committees. The skins were shaved to remove the excess hairs and kept frozen at −20 °C on a flat aluminum surface, then sectioned using a surgical knife to remove the fat layer to the thickness of 3 ± 0.1 mm [31], and thawed before insertion testing on a 3D printed stretching mechanism to mimic skin in vivo conditions (Figure 2a). The MN arrays were initially oxygen plasma cleaned for 1 minute before dip coating with a concentrated aqueous solution of fluorescein (Sigma-Aldrich Corp., St. Louis, MO, USA). Subsequently, the MN

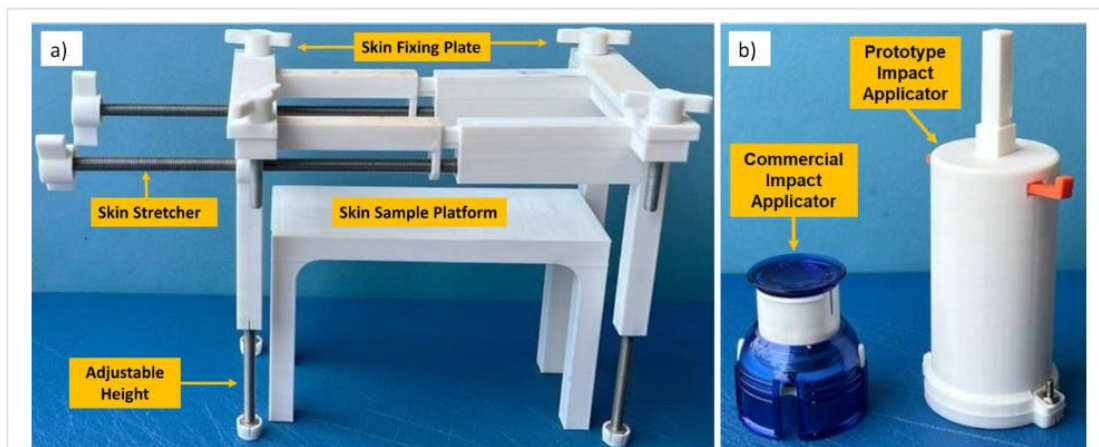


Figure 2: a) Skin stretching mechanism used to mimic skin condition in vivo. The skin sample is placed on the skin sample platform. Then, the stretching mechanism's height is adjusted. Skin is then secured at both ends by fixing plates before stretching by the stretcher screws. b) A commercial applicator with a single impact speed and a prototype custom-made impact applicator capable of insertion with different impact speeds was used to apply MN arrays dynamically onto the porcine skin subjects.

arrays were fixed onto a commercial spring-loaded applicator (Medtronic MiniMed Quick-Serter), providing an insertion velocity of 0.5 m/s. The tests were repeated using a custom-made prototype applicator, providing an insertion velocity of 1.5–4.5 m/s (Figure 2b). MN arrays were attached to the applicators' plungers with double-sided tape and applied to the skin. The skin samples were then tape-stripped to remove the SC layer of skin before imaging.

Stereomicroscopy was then performed using a Nikon SMZ-18 microscope to determine the APE on skin subjects. The skin samples were fixed in optimal cutting temperature (OCT) compound, then sectioned to 50 μm thick slices using Leica CM3050 cryostat (Wetzlar, Germany) and placed on Superfrost glass slides. The sectioned samples were then imaged by a Zeiss LSM 710 Meta NLO confocal laser scanning microscope (Carl Zeiss, Jena, Germany) to visualize the penetration depth and estimate the FPL for individual MN projections. The images were further analyzed using ImageJ software (U. S. National Institutes of Health, Bethesda, Maryland, USA).

Measuring the force of insertion

Skin insertion tests were designed to measure the insertion force during the experiments. To facilitate the force recordings during MN insertions on porcine skin, BD Ultra-Fine™ 4 mm Pen Needles were used (Franklin Lakes, New Jersey, USA), having similar geometry to the fabricated MN array projections described above. The main reason for using PEN needles was their greater length (4 mm) which prevents early attachment of skin to the base plate, which is a common phenomenon when

testing the MNs. The force of insertion is directly proportional to the square of the MN base diameter (Equation 1). Compared to other MN geometrical parameters, the dependence on the interfacial area was previously reported by Park et al. for an insertion test of polymeric MNs on human cadaver skin [22]. The representative PEN needle had a diameter of 230 μm and tip size of 2.5 μm (Figure 3a). This is similar to polymeric MNs made from Zeonor 1060R with a base diameter of 245 μm and tip size of 1.6 μm (Figure 3b). The Ultra-Fine PENs were attached to the upper disk of the rheometer using double-sided tape. The porcine back skin is fixed on the custom-made 3D printed skin stretching mechanism described above (Figure 2a) and subsequently pre-stretched to mimic the skin in vivo conditions [27]. The upper plate was lowered at 0.1 mm/s speed towards the skin while recording the force versus displacement data.

FEA of MN insertion into the skin

To determine the MN and skin interactions during the penetration, a 2D axisymmetric simulation model was performed using ANSYS (2020 R1, ANSYS, Canonsburg, Pennsylvania, USA) Explicit Dynamics. The skin was assumed to be comprised of three layers (1) stratum corneum, (2) dermis, and (3) hypodermis with 26 μm , 2 mm, and 1.1 mm thicknesses, respectively. An Ogden (first-order) model [32] was introduced for the dermis layer, while SC and hypodermis layers were considered to possess a linear elastic mechanical response. Quadrilateral meshing with a bias factor of 5 was used to increase the number of elements in the vicinity of the skin piercing zone. Moreover, the sphere of influence meshing algorithm was used to create fine elements at the tip of the MNs.

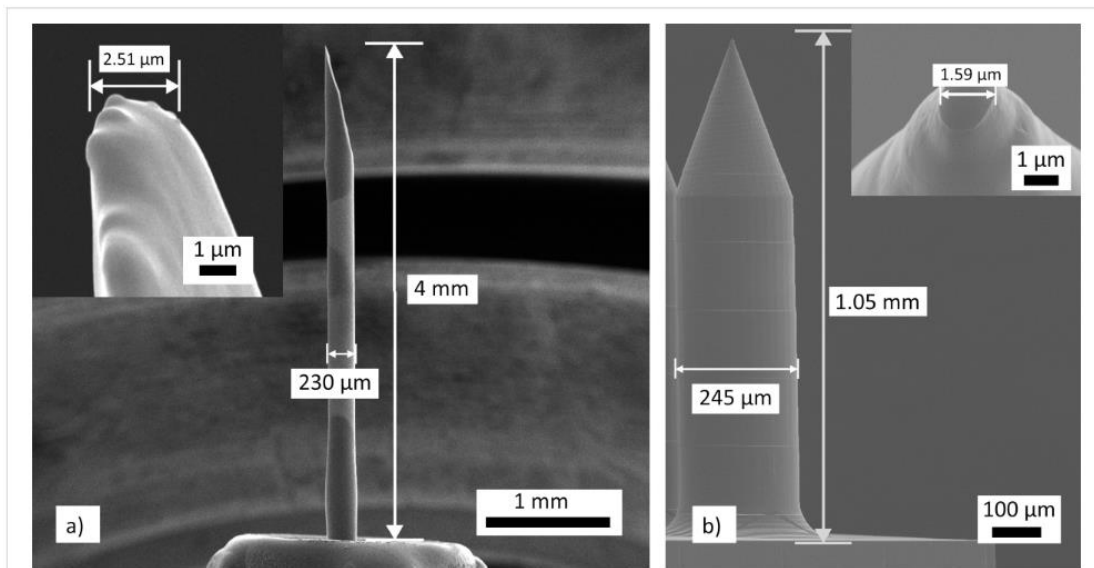


Figure 3: SEM images of length, tip size, and diameter of the a) BD Ultra-Fine™ 4 mm Pen Needle and b) thermoplastic Zeonor 1060R replicas.

The coefficient of friction between the contact surfaces was set to 0.42 [29]. Upon MN penetration, with a constant impact speed of 4.5 m/s, the force-displacement data were recorded to estimate the insertion force. To enable the skin piercing model, an erosion algorithm was used to eliminate the elements that reached their failure stress. To optimize the run time, the automatic mass scaling method was activated with a minimum Courant–Friedrichs–Lewy (CFL) time step of 1 picosecond [33]. The mass scale algorithm artificially increases the elemental density, which in turn reduces the overall time step by increasing the time required for a sound wave to traverse the smallest elements. Table 1 summarizes the material properties used for the individual components in the insertion simulation.

Results and Discussions

Design and fabrication of MN array master and replica

The 9×9 MN arrays were successfully fabricated by TPP, and Zeonor 1060R replicas were made (>20 cycles) using hot embossing on PDMS mold. During the cycles, no damage was observed to the PMDS mold or its microcavities. Three 9×9 MN patch replicas were selected from different replication cycles of equal intervals (cycles: 1, 15, and 30). Nine projections per MN patch ($n = 27$) were selected and measured against MN master length and base diameter. The overall average length and base diameter were $1045.04 \pm 3.83 \mu\text{m}$ and

Table 1: Mechanical properties of different skin layers used in ANSYS Explicit Dynamics simulation.

Parameter	Microneedle	SC	Dermis	Hypodermis
mathematical model	linear elastic	linear elastic	hyperelastic: Ogden 1st order with uniaxial test data	linear elastic
thickness (mm)	n.a.	0.026	2	1.1
Young Modulus (MPa)	2100	67	n.a.	0.1
Poisson ratio	0.48	0.49	0.49	0.48
density (kg/m^3)	$1.01 \text{ E}-6$	$1.3 \text{ E}-6$	$1.2 \text{ E}-6$	$9.71 \text{ E}-7$
hyperelastic coefficients MU1, A1 (MPa)	n.a.	n.a.	0.0568, 13.3	n.a.
incompressibility factor (1/MPa)	n.a.	n.a.	0.0745	n.a.
failure criteria (MPa)	n.a.	20	7	n.a.
Ref.	[9]	[29,30,34]	[29,35]	[29,34]

255.37 ± 2.39 μm (mean ± standard deviation), respectively. The results recorded for the cycles 1, 15, and 30 indicated the respective average projection's axial shrinkages of 4.72 ± 0.15%, 5.37 ± 0.27%, 4.9 ± 0.21% (mean ± standard deviation) (ANOVA, $p < 0.001$). Measurement for base diameters indicated enlargements of 3.22 ± 0.21%, 2.02 ± 0.33%, 1.07 ± 0.2% (mean ± standard deviation) (ANOVA, $p < 0.001$), respectively. The base diameter enlargements indicated excessive lateral forces on the cavity walls compared to longitudinal force along the axis. Figure 4a shows the SEM images of the MN array resin master, and Figure 4b,c shows the Zeonor 1060R replicas after the hot embossing, indicating slight shrinkages in both height and diameter after replication; the occurrence of small shrinkage has been reported for these thermoplastic COP materials before [9]. Thus, the effect of shrinkage needs to be considered within the initial design to ensure the dimensional accuracy of final MN replicas.

Analytical and experimental characteristics of MN failures by mechanical compression test

Bending, buckling, and fracture are the main possible failure risks of polymer MN arrays upon insertion into the skin. Thus, investigations on the MN failure scenarios are essential and can be performed using experimental and analytical approaches. For a MN array of N projections to puncture the skin with the application of a vertical force F , the tip radius of the MNs must be small enough to exceed the puncture stress σ_p . Assuming an approximately hemispherical tip, the condition on the tip radius for an array of N MNs applied with a force F is:

$$r_t \leq \sqrt{\frac{F}{2\pi\sigma_p N}} \quad (1)$$

For a particular application force (F), the maximum tip radius r_t can be approximated based on the skin's ultimate stress before puncture (σ_p).

During actual insertions, MNs are not always inserted in an exactly vertical fashion which results in lateral shear loads. This horizontal shear force component (f_h) that is perpendicular to the axis of each MN may cause fracture at an approximate distance x from the base where the yield stress σ_y of the material is exceeded. Therefore, for MNs having a cylindrical shaft of radius a , with yield stress σ_y the fracture location from the base can be estimated as [36]:

$$x = \frac{\pi a^3 \sigma_y}{4 f_h} \quad (2)$$

If bending is avoided and true vertical insertion is achieved, failure may be due to buckling when the vertical force on each MN reaches the critical value (f_B) [37]:

$$f_B = \frac{\pi^3 a^4 E}{16 L^2} \quad (3)$$

where L is the MN length, a is the MN radius, and E is the elastic modulus. Buckling failure load f_B is the most important figure of merit used to determine the margin of safety of MNs.

Figure 5a shows the results of mechanical quasi-static compression tests for the single replicated MN. The results revealed both near-tip yield stress failure, presumed due to the horizontal shear stress forces, and buckling failure, which occurred

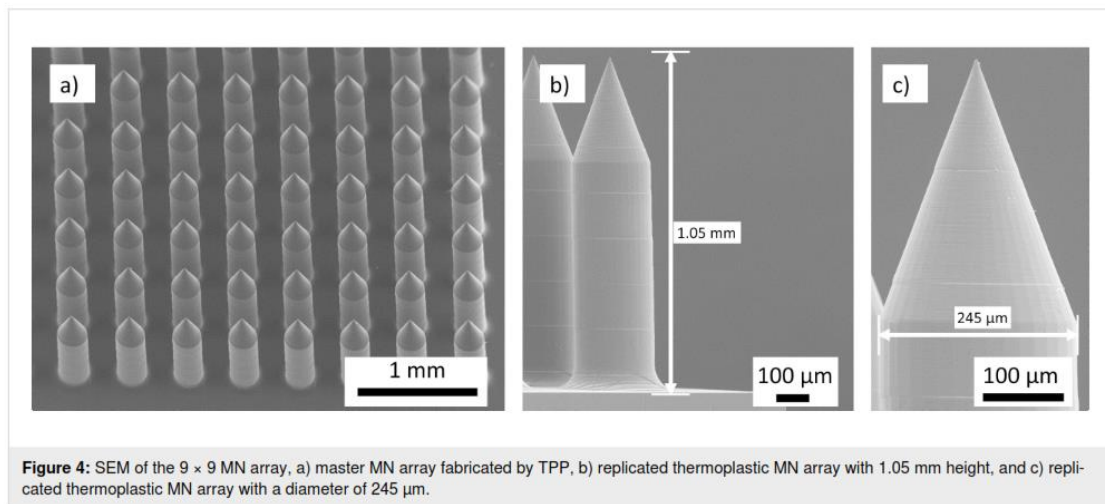


Figure 4: SEM of the 9 × 9 MN array, a) master MN array fabricated by TPP, b) replicated thermoplastic MN array with 1.05 mm height, and c) replicated thermoplastic MN array with a diameter of 245 μm.

at the axial applied force of 1.29 N. Figure 5b illustrates the experimental force-displacement diagram for the theoretical prediction of the moment of critical buckling load. The peak on the graph indicated the MN failure. However, due to the viscoelastic nature of Zeonor 1060R, the initial near-tip failure was indistinct on the force-displacement diagram. These mechanical responses have been previously observed during compression tests on polymeric MN materials, including carboxymethyl cellulose (CMC) and polylactic acid (PLA) [1,38]. This unique viscoelastic behavior prevents the MN tip fracture, which can leave residuals in the skin. As indicated in Figure 5a, the bending location (x) and magnitude of buckling load are in alignment with Equation 2 and Equation 3. The exact location is dependent on the base diameter ($125\ \mu\text{m}$), Zeonor 1060R yield stress ($53\ \text{MPa}$), and lateral shear force component estimated during insertion. According to SEM images from samples ($n = 3$), the location of bending from the base (x) is at $244.4 \pm 2.03\ \mu\text{m}$ corresponding to a lateral shear load of 0.33 to $0.34\ \text{N}$. Buckling modeling was based on elastic modulus ($2100\ \text{MPa}$) and effective penetrative length ($1.025\ \text{mm}$) using Equation 3 and compared with experimental data. This critical buckling load was predicted to occur at $0.95\ \text{N}$, based on theory, whereas the experimental value was $1.29\ \text{N}$ during compression tests. The higher value found in experimental results compared to buckling theory (Equation 3) is due to the reinforcing effects of the fillets at the MN base that improved MN stability toward sudden bending [9]. The thermoplastic Zeonor 1060R MNs had a higher failure force when compared to failure forces (0.1 – $0.22\ \text{N}$) of polylactic-*co*-glycolic acid (PLGA) MNs with a similar base diameter ($200\ \mu\text{m}$) and lengths (700 – $1500\ \mu\text{m}$) [22].

Simulation and experimental investigation on MN insertion force

To investigate the insertion force and failure modes of MN arrays into the skin, the insertion of a single MN was simulated using FEA software. Figure 6a illustrates the axisymmetric model incorporating a three-layer skin model with the relevant boundary conditions. For mesh generation, the inclusion of quadrilateral elements for skin layers with a bias factor of 5 and the sphere of influence technique for MN tip yielded more accurate results due to finer meshing at the regions of MN–skin interactions. The results from the simulation showed that maximum von-Mises stress in the skin layers reached $18.9\ \text{MPa}$ on the SC layer near the MN insertion, which is in line with the predefined failure criteria for SC and dermis layers (Figure 6b). Force displacement data were recorded and plotted during the MN insertion. The graph represented a linear increase that peaked at $0.18\ \text{N}$ before a sudden drop due to skin fracture at the SC layer (Figure 6c).

The results were coupled with a representative in vitro experimental model using BD Ultra-Fine™ 4 mm Pen Needles. In this test, the force was linearly increased to a peak value of $0.26\ \text{N}$ before penetrating the skin, followed by an abrupt drop in the recorded force. The ratio of buckling failure force to the insertion force was calculated using the simulation method, showing a SM of 7.16. For in vitro insertion by BD Ultra-Fine™ 4 mm Pen Needles, the SM was calculated as 4.95 (Figure 6d). The SM for both methods was above 1, indicating a sufficient safety level for skin insertions. However, SM directly depends on the MN material, its base diameter and the fillet, overall length, and the mechanics of skin subjects.

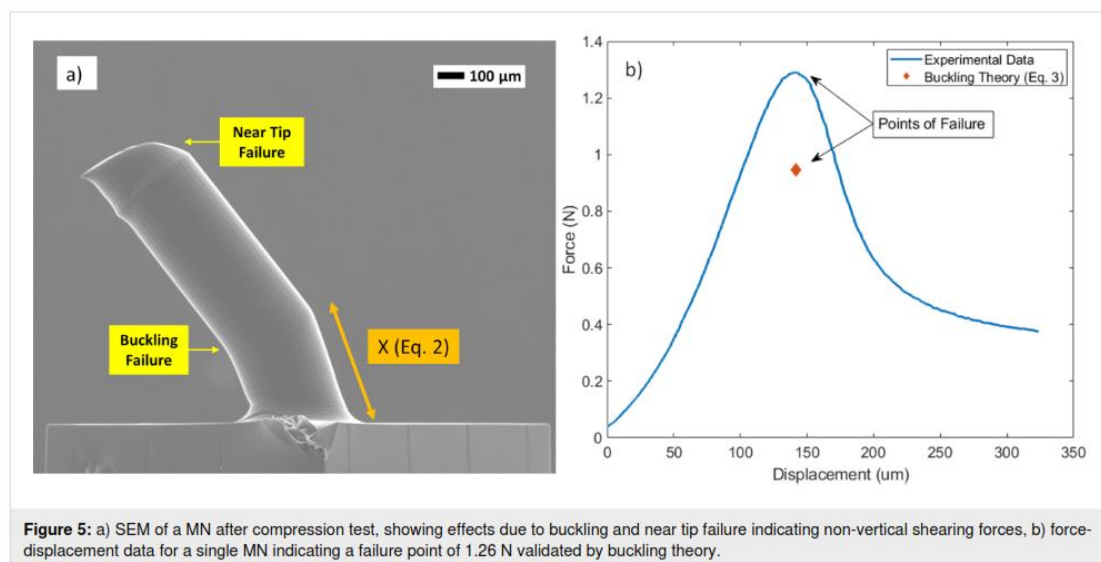
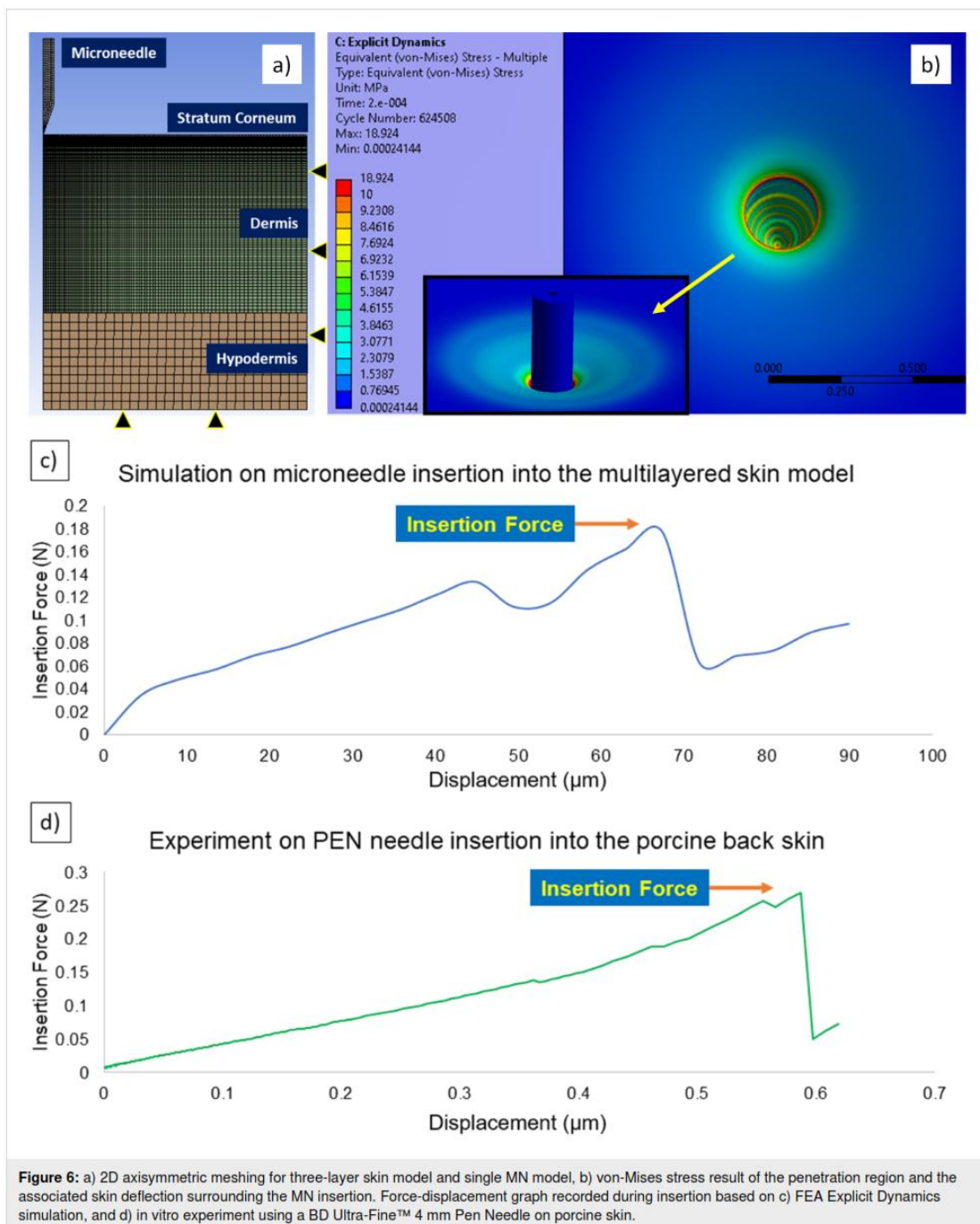


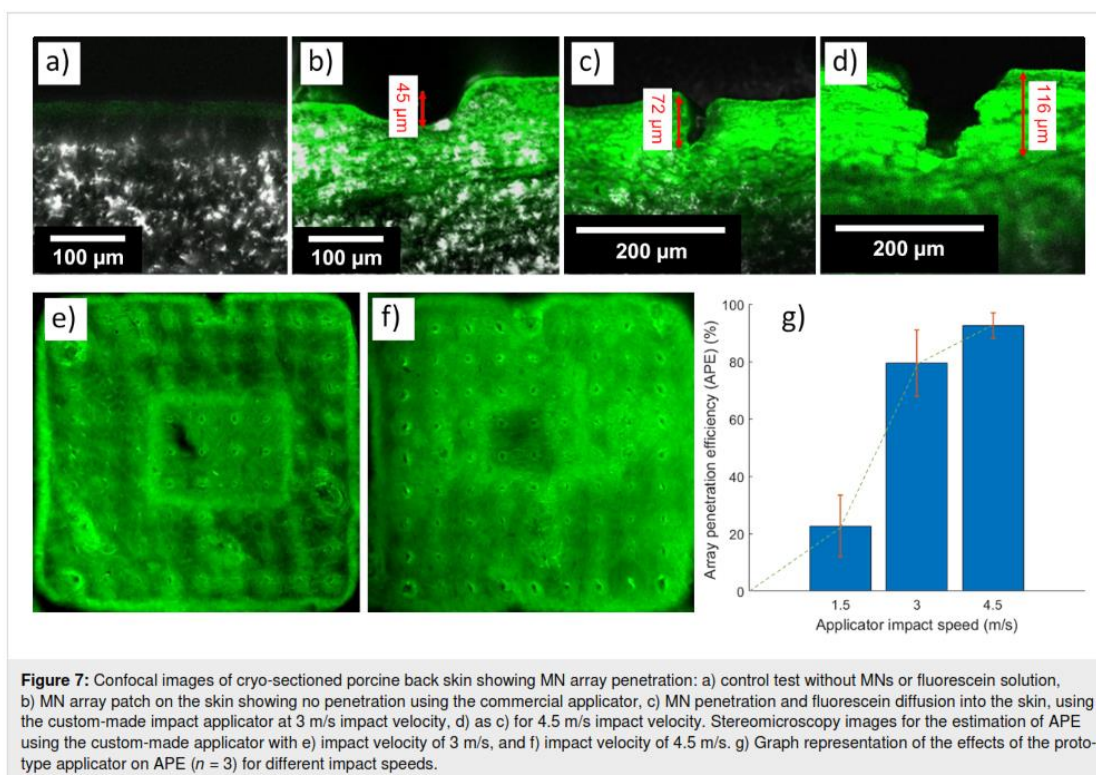
Figure 5: a) SEM of a MN after compression test, showing effects due to buckling and near tip failure indicating non-vertical shearing forces, b) force-displacement data for a single MN indicating a failure point of 1.26 N validated by buckling theory.



Penetration and delivery of fluorescein into skin

For MN array insertion tests on porcine skin, confocal and stereo microscopes were used to estimate the FPL and APE

penetration metrics. Figure 7a–d shows confocal microscopy results of skin insertion tests for various insertion methods: (a) control, (b) using a commercial applicator, (c) using the prototype applicator at impact velocity of 3 m/s, and d) again at



4.5 m/s impact velocity. Figure 7a shows the control results where no MN array was inserted into the skin. Figure 7b indicates a skin deflection of 45 μm using the commercial applicator with 0.5 m/s impact speed revealing no penetration through the SC. In contrast, the custom applicator produced penetration of 72 μm and 116 μm (FPL of 7% and 11%) for impact velocities of 3 m/s and 4.5 m/s (Figure 7c,d). For comparison, the insertion tests of Meliga et al. on mouse ear skin produced penetration of ≈ 20 μm to 60 μm when their application speed increased from ≈ 0.25 m/s to 2 m/s [33]. In our experiments, for both applicators, insertion performance depends not only on impact velocity, but also on the number of MNs, MN interspacing, MN base diameter, and skin type, though, in this work, only impact velocity was varied. Our previous results showed that the same commercial applicator with an insertion velocity of 0.5 m/s successfully inserted a 4×4 thermoplastic MN patch (height: 700 μm , base diameter: 150 μm) into rabbit ear skin without deformation of the MN patch [9].

After initial penetration, APE was measured from stereomicroscopy of the diffused fluorescein patterns. There was a total failure to deliver fluorescein into the skin using the commercial applicator. In contrast, fluorescein delivery to the skin using the prototype applicator revealed APE from $22.63 \pm 10.78\%$

through $79.42 \pm 11.47\%$ to $92.52 \pm 4.45\%$ (mean \pm standard deviation, $n = 3$ for each test) when the impact velocity was increased from 1.5, through 3, to 4.5 m/s (Figure 7e,f). Figure 7g shows the APE effects in bar chart form. The results show an increase of 56.79% in APE on increasing impact velocity from 1.5 to 3 m/s and an increase of 13.17% for an impact velocity increase from 3 to 4.5 m/s.

It is worth noting that Crichton et al. [39] studied the effect of varying skin strain rates on MN insertion into a rabbit's ear. At low strain rates (≈ 0 , 0.56, and 1.22 m/s), the APE for their NanopatchTM was as low as 25%; however, by increasing the strain rate to $5,300 \text{ s}^{-1}$, at an insertion velocity of 1.96 m/s, an APE value of $\approx 95\%$ was achieved.

The work summarized here demonstrates the potential of high-fidelity and low-cost thermoplastic MN arrays for coated drug delivery. In addition, thermoplastic MN arrays have the potential for collecting interstitial fluid more safely than using glass [40] or silicon MNs.

Conclusion

MN arrays have considerable potential for cost-effective, rapid, and non-invasive therapeutic drug delivery, vaccination, and

point-of-care diagnostics, with potential for self-administration. While large-scale manufacturing of MN arrays with high accuracy remains a challenge, the emerging technique of TPP coupled with hot embossing provides a promising, cost-effective, and highly precise method to produce batches of polymer MNs with the potential for mass production. This study fabricated Zeonor 1060R polymer MN arrays from PDMS secondary molds using a controlled hot embossing process with only minor shrinkage of the thermoplastic protrusions. The hot embossing process, tailored for current MN geometrical complexity and size, was described, including embossing time and compression speed. Key parameters were optimized to minimize the polymerization time and enhance the structural integrity during the TPP process.

A series of experiments was performed to characterize the mechanical failure and insertion characteristics of MNs: (1) axial compression test, (2) controlled insertion of BD Ultra-Fine™ 4 mm Pen Needle on porcine back skin, along with (3) Explicit Dynamics simulation of single MN insertion on a three-layered skin model. The comparisons between the results found for insertion force and quasi-static buckling test showed sufficient margins of safety ($SM \gg 1$), indicating the potential of Zeonor 1060R MNs for applications in drug delivery and vaccination, with minimal associated risks. The insertion test setups for current research introduced a mechanism to enable controlled skin stretching to mimic in vivo conditions. Experiments also showed that the commercial applicator was less effective than our customized impact insertion applicator, demonstrating the need to design and manufacture customized applicators tailored for specific MN array designs.

Acknowledgements

This work was performed in part at the Queensland node of the Australian National Fabrication Facility, a company established under the National Collaborative Research Infrastructure Strategy to provide nano and microfabrication facilities for Australia's researchers. This research was undertaken with the assistance of resources provided at the University of Southern Queensland.

ORCID® iDs

Zahra Faraji Rad - <https://orcid.org/0000-0001-6528-5965>

References

- Lee, J. W.; Park, J.-H.; Prausnitz, M. R. *Biomaterials* **2008**, *29*, 2113–2124. doi:10.1016/j.biomaterials.2007.12.048
- Uddin, M. J.; Scoutaris, N.; Economidou, S. N.; Giraud, C.; Chowdhry, B. Z.; Donnelly, R. F.; Douroumis, D. *Mater. Sci. Eng., C* **2020**, *107*, 110248. doi:10.1016/j.msec.2019.110248
- Bariya, S. H.; Gohel, M. C.; Mehta, T. A.; Sharma, O. P. *J. Pharm. Pharmacol. (Chichester, U. K.)* **2011**, *64*, 11–29. doi:10.1111/j.2042-7158.2011.01369.x
- Faraji Rad, Z. *Microneedles Fabrication for Subcutaneous Fluid Sampling and Drug Delivery*. Ph.D. Thesis, University of Birmingham, Birmingham, UK, 2016. <http://etheses.bham.ac.uk/id/eprint/6734/>
- Ventrelli, L.; Marsilio Strambini, L.; Barillaro, G. *Adv. Healthcare Mater.* **2015**, *4*, 2606–2640. doi:10.1002/adhm.201500450
- Vashist, S. K. *Biosensors* **2017**, *7*, 62. doi:10.3390/bios7040062
- Jung, J. H.; Jin, S. G. *J. Pharm. Invest.* **2021**, *51*, 503–517. doi:10.1007/s40005-021-00512-4
- Aldawood, F. K.; Andar, A.; Desai, S. *Polymers (Basel, Switz.)* **2021**, *13*, 2815. doi:10.3390/polym13162815
- Faraji Rad, Z.; Nordon, R. E.; Anthony, C. J.; Bilston, L.; Prewett, P. D.; Arns, J.-Y.; Arns, C. H.; Zhang, L.; Davies, G. J. *Microsyst. Nanoeng.* **2017**, *3*, 17034. doi:10.1038/micronano.2017.34
- Faraji Rad, Z.; Prewett, P. D.; Davies, G. J. *Microsyst. Nanoeng.* **2021**, *7*, 71. doi:10.1038/s41378-021-00298-3
- Johnson, A. R.; Procopio, A. T. *3D Print. Med.* **2019**, *5*, 2. doi:10.1186/s41205-019-0039-x
- Faraji Rad, Z.; Prewett, P. D.; Davies, G. J. *Beilstein J. Nanotechnol.* **2021**, *12*, 1034–1046. doi:10.3762/bjnano.12.77
- Waghule, T.; Singhvi, G.; Dubey, S. K.; Pandey, M. M.; Gupta, G.; Singh, M.; Dua, K. *Biomed. Pharmacother.* **2019**, *109*, 1249–1258. doi:10.1016/j.biopha.2018.10.078
- Larrañeta, E.; Lutton, R. E. M.; Woolfson, A. D.; Donnelly, R. F. *Mater. Sci. Eng., R* **2016**, *104*, 1–32. doi:10.1016/j.mser.2016.03.001
- Faraji Rad, Z.; Nordon, R. E.; Davies, G. J.; Anthony, C. J.; Prewett, P. D. *Microfluidic devices and fabrication*. U.S. Patent US10850082B2, Dec 1, 2020.
- Faraji Rad, Z.; Prewett, P. D.; Davies, G. J. *Manuf. Lett.* **2021**, *30*, 39–43. doi:10.1016/j.mfglet.2021.10.007
- Juster, H.; van der Aar, B.; de Brouwer, H. *Polym. Eng. Sci.* **2019**, *59*, 877–890. doi:10.1002/pen.25078
- Davis, S. P.; Landis, B. J.; Adams, Z. H.; Allen, M. G.; Prausnitz, M. R. *J. Biomech.* **2004**, *37*, 1155–1163. doi:10.1016/j.jbiomech.2003.12.010
- Khanna, P.; Luongo, K.; Strom, J. A.; Bhansali, S. *J. Micromech. Microeng.* **2010**, *20*, 045011. doi:10.1088/0960-1317/20/4/045011
- Ranamukhaarachchi, S. A.; Stoeber, B. *Biomed. Microdevices* **2019**, *21*, 100. doi:10.1007/s10544-019-0449-y
- Ebrahiminejad, V.; Prewett, P. D.; Davies, G. J.; Faraji Rad, Z. *Adv. Mater. Interfaces* **2022**, *9*, 2101856. doi:10.1002/admi.202101856
- Park, J.-H.; Allen, M. G.; Prausnitz, M. R. *J. Controlled Release* **2005**, *104*, 51–66. doi:10.1016/j.jconrel.2005.02.002
- Ma, G.; Wu, C. J. *J. Controlled Release* **2017**, *251*, 11–23. doi:10.1016/j.jconrel.2017.02.011
- Badran, M. M.; Kuntsche, J.; Fahr, A. *Eur. J. Pharm. Sci.* **2009**, *36*, 511–523. doi:10.1016/j.ejps.2008.12.008
- Donnelly, R. F.; Garland, M. J.; Morrow, D. I. J.; Migalska, K.; Singh, T. R. R.; Majithiya, R.; Woolfson, A. D. *J. Controlled Release* **2010**, *147*, 333–341. doi:10.1016/j.jconrel.2010.08.008
- Singh, T. R. R.; Dunne, N. J.; Cunningham, E.; Donnelly, R. F. *Recent Pat. Drug Delivery Formulation* **2011**, *5*, 11–23. doi:10.2174/187221111794109484
- Olatunji, O.; Das, D. B.; Garland, M. J.; Belaid, L.; Donnelly, R. F. *J. Pharm. Sci.* **2013**, *102*, 1209–1221. doi:10.1002/jps.23439

28. Xenikakis, I.; Tzimitzimis, M.; Tsongas, K.; Andreadis, D.; Demiri, E.; Tzelzsis, D.; Fatouros, D. G. *Eur. J. Pharm. Sci.* **2019**, *137*, 104976. doi:10.1016/j.ejps.2019.104976
29. Shu, W.; Heimark, H.; Bertollo, N.; Tobin, D. J.; O’Cearbhaill, E. D.; Annaidh, A. N. *Acta Biomater.* **2021**, *135*, 403–413. doi:10.1016/j.actbio.2021.08.045
30. Ranamukhaarachchi, S. A.; Lehnert, S.; Ranamukhaarachchi, S. L.; Sprenger, L.; Schneider, T.; Mansoor, I.; Rai, K.; Häfeli, U. O.; Stoeber, B. *Sci. Rep.* **2016**, *6*, 32074. doi:10.1038/srep32074
31. Pramudita, J. A.; Shimizu, Y.; Tanabe, Y.; Ito, M.; Watanabe, R. *J. Jpn. Soc. Exp. Mech.* **2014**, *14*, s245–s250. doi:10.11395/jjsem.14.s245
32. Shergold, O. A.; Fleck, N. A.; Radford, D. *Int. J. Impact Eng.* **2006**, *32*, 1384–1402. doi:10.1016/j.ijimpeng.2004.11.010
33. Meliga, S. C.; Coffey, J. W.; Crichton, M. L.; Flaim, C.; Veidt, M.; Kendall, M. A. F. *Acta Biomater.* **2017**, *48*, 341–356. doi:10.1016/j.actbio.2016.10.021
34. Levi, K.; Weber, R. J.; Do, J. Q.; Dauskardt, R. H. *Int. J. Cosmet. Sci.* **2010**, *32*, 276–293. doi:10.1111/j.1468-2494.2009.00557.x
35. Silver, F. H.; Seehra, G. P.; Freeman, J. W.; DeVore, D. *J. Appl. Polym. Sci.* **2002**, *86*, 1978–1985. doi:10.1002/app.11119
36. Beer, F. P.; Johnston, E. R., Jr.; DeWolf, J. T.; Mazurek, D. F. *Mechanics of Materials*; McGraw Hill: New York, NY, USA, 2015.
37. Gittard, S. D.; Chen, B.; Xu, H.; Ovsianikov, A.; Chichkov, B. N.; Monteiro-Riviere, N. A.; Narayan, R. J. *J. Adhes. Sci. Technol.* **2013**, *27*, 227–243. doi:10.1080/01694243.2012.705101
38. Kim, S.; Yang, H.; Eum, J.; Ma, Y.; Fakhræi Lahiji, S.; Jung, H. *Biomaterials* **2020**, *232*, 119733. doi:10.1016/j.biomaterials.2019.119733
39. Crichton, M. L.; Ansaldo, A.; Chen, X.; Prow, T. W.; Fernando, G. J. P.; Kendall, M. A. F. *Biomaterials* **2010**, *31*, 4562–4572. doi:10.1016/j.biomaterials.2010.02.022
40. Wang, P. M.; Cornwell, M.; Prausnitz, M. R. *Diabetes Technol. Ther.* **2005**, *7*, 131–141. doi:10.1089/dia.2005.7.131

License and Terms

This is an open access article licensed under the terms of the Beilstein-Institut Open Access License Agreement (<https://www.beilstein-journals.org/bjnano/terms>), which is identical to the Creative Commons Attribution 4.0 International License (<https://creativecommons.org/licenses/by/4.0>). The reuse of material under this license requires that the author(s), source and license are credited. Third-party material in this article could be subject to other licenses (typically indicated in the credit line), and in this case, users are required to obtain permission from the license holder to reuse the material.

The definitive version of this article is the electronic one which can be found at:
<https://doi.org/10.3762/bjnano.13.55>

3.2 Chapter Summary

In this work, Ebrahimejad, V. et al. (2022) replicated thermoplastic MN arrays through a combination of TPP, PDMS micro moulding, and soft embossing of Zeonor 1060R polymers. SEM imaging of the replicated samples showed high accuracy with 4.99 ± 0.35 % longitudinal shrinkage and 2.15 ± 0.96 % lateral enlargement. MN Mechanical failures such as bending, buckling, and tip blunting were experimentally and theoretically discussed. Based on Equations 1 and 3 from the publication, considering five cases of lateral and longitudinal shrinkage, the average reduction in safety margin is 2.35 %. However, the worst-case scenario yields an 18.67 % reduction in SM value, which occurs for the lowest lateral shrinkage for F_{ins} and the highest lateral and lowest longitudinal shrinkages for the case of failure force. The stretching mechanism enabled a controlled mimicking of *in vivo* skin conditions, which can improve the reliability and repeatability of test results. Experimental results showed a significant improvement in MN array penetration using the prototype impact applicator. Increasing the impact velocity from 1.5, 3, to 4.5 m/s increased the APE from 22.63 ± 10.78 %, 79.42 ± 11.47 %, to 92.52 ± 4.45 % (mean \pm standard deviation, $n = 3$ for each test) which produced array penetration efficiencies as high as > 92 % on the 4.5 m/s impact velocity settings. APE of > 92 % indicating that about 75 out of 81 projections have passed the SC layer of the skin and are hence suitable for drug delivery, relatively low FPL values (7 - 11 %) can still delay the diffusion time. The research results also concluded the importance of the need for specific applicator settings tailored for individual MN designs. Hence, this research provided the basis for developing a more advanced impact applicator (see [Chapter 5](#)), which can integrate features such as regulatable skin strains, low-frequency vibrations, and impact speed.

CHAPTER 4: PAPER 3 - Design, Development, and Testing of Polymeric Microblades: A Novel Design of MNs for Biomedical Applications

4.1 Introduction

Although MN arrays are a promising transdermal method for painless drug delivery or sampling of biofluids, the technology suffers from a costly and time-consuming process. Moreover, highly dense MN arrays may result in partial penetration caused by “bed of nails” effects. The current chapter aims to address three of the main thesis objectives, including improvements to mass scale producibility ([section 1.2.1](#)), safety margin ([section 1.2.2](#)), and mechanical insertion and drug diffusion simulation for MBs with various geometrical parameters ([section 1.2.3](#)). To address current issues associated with MN arrays, this research article introduced a possible alternative design for MNs called MB, possessing a singular microstructure rather than an array of projections. These MBs microdevices incorporate concentric or eccentric blade shapes and multiple side channels with reservoirs for drug or sample containment. TPP technique with modified program codes (see [Appendix C](#)) was used to fabricate five types of MB designs on a single substrate. Microfabricated PDMS moulds were then made to replicate five MB devices through a soft embossing process. The replicated MBs underwent axial compression tests at different speeds and were compared with mathematical models. MBs were further plasma treated using oxygen plasma to improve hydrophilicity, then coated with FSS solution as the model drug. A version of the impact applicator used in Chapter 3 was designed and manufactured, then theoretically and experimentally tested using a high-speed camera to quantify the skin impact velocities. Subsequently, skin insertions were conducted on the porcine abdominal skin using the prototype applicator at three different impact speeds of 1.5, 3, and 4.5 m/s. The penetration

depths of the MBs were evaluated using the Z-Stack technique of confocal microscopy. Current research also simulated MB penetration and force of insertion on multi-layered hyperelastic skin models. Furthermore, diffusion mechanisms for various MBs were also simulated to estimate the concentrations and gradients of the model drug at different skin layers based on time.

Design, Development, and Testing of Polymeric Microblades: A Novel Design of Microneedles for Biomedical Applications

Vahid Ebrahimejad and Zahra Faraji Rad*

Conventional microneedles (MNs) are designed as an array of micrometer-sized projections that can painlessly penetrate the skin. Fabrication of MN arrays can be costly and time-consuming; additionally, full penetration of an array of MNs with ten to thousands of projections into the skin may not be achievable. This paper reports a new design of MNs known as microblades (MBs) which consist of a singular microstructure. The single integrated design of the MBs reduces the fabrication cost and time, facilitates more effective penetration, and may pave the way for the scale-up manufacturing of MN devices. Different designs of MBs are fabricated by two-photon polymerization technique, followed by polydimethylsiloxane micromolding and soft embossing to create replicas. The mechanical integrity of the designs is determined by a series of compression tests. Skin insertion and drug diffusion studies are conducted using a custom-made applicator to insert the MBs into the porcine abdominal skin to demonstrate delivery of fluorescein tracer. MBs insertion and penetration capabilities and the diffusion of a model drug into a multi-layered human skin are demonstrated using finite element analysis and 3D diffusion models. The results demonstrate the functional capabilities of the MBs as an alternative to MN arrays.

sampling biomarkers such as interstitial fluid for point-of-care (POC) diagnostics by bypassing the stratum corneum (SC) barrier of the skin.^[2,3] The COVID-19 pandemic, more than any other time, highlights the necessity for new methods to overcome the issues associated with mass vaccination, distribution, logistics, drug delivery, and inexpensive and rapid POC testing.

MNs are generally made from silicon, metals, ceramics, silica glass, carbohydrates, and polymers and are studied for vaccination, drug delivery, and diagnostics purposes.^[4] Based on the application, MNs are classified into solid, coated, dissolving, hollow or open-channel, and hydrogel-forming structures.^[5] MNs are manufactured using methods such as wet etching, reactive ion etching (RIE), deep reactive ion etching (DRIE), lithography, micromolding, injection molding, laser drilling, 3D printing, and two-photon polymerization (2PP).^[4-9] The geometries consist of cylindrical, conical, pyramidal, or prismatic shapes of miniaturized needles arranged in an array.

Even though significant research has been done on MN technologies, not all geometries and materials can be fully inserted into the skin, which limits the MN arrays' functionality.


Although traditional MN designs are promising tools for transdermal drug delivery and diagnostics, some issues remain during fabrication, insertion, and testing. For instance, scale-up fabrication of these designs is still challenging due to the need to manufacture high-density arrays. Current conventional manufacturing techniques such as RIE, DRIE, lithography, and laser ablation are expensive multistage methods that are limited to select materials and geometrical designs.^[10,11] Additive manufacturing methods such as stereolithography, 2PP, and micromolding are more flexible, cost-effective, and involve simpler processes; however, they are deemed as more time-consuming methods.^[12,13] Process modification and optimization may improve the fabrication time and the accuracy of these techniques.^[14,15]

MN devices require adequate strength to penetrate the skin while maintaining mechanical integrity. Mechanical failures are usually due to buckling failure during normal insertion or transverse bending failure due to the excessive lateral loads caused by skin natural elasticity and irregular topology.^[4] MN mechanical integrity primarily depends on the geometrical shape, material selection,^[16-18] and manufacturing process.^[19,20] The MN geometrical aspects affecting mechanical strength

1. Introduction

Recent developments in micro-electromechanical systems (MEMS) have paved the way for the advancement of microscale devices, especially in biomedical research. One of these remarkable research developments is the application of microneedles (MNs) as an alternative to conventional hypodermic needles.^[1] Traditional hypodermic needles are invasive, stimulate pain, produce hazardous wastes, and need trained medical staff for administration. MNs are minimally invasive devices which enable painless administration of therapeutic molecules and

V. Ebrahimejad, Z. Faraji Rad
 School of Engineering
 University of Southern Queensland
 Springfield Central, QLD 4300, Australia
 E-mail: zahra.farajirad@usq.edu.au

 The ORCID identification number(s) for the author(s) of this article can be found under <https://doi.org/10.1002/admi.202201115>.

© 2022 The Authors. Advanced Materials Interfaces published by Wiley-VCH GmbH. This is an open access article under the terms of the Creative Commons Attribution License, which permits use, distribution and reproduction in any medium, provided the original work is properly cited.

DOI: 10.1002/admi.202201115

Adv. Mater. Interfaces 2022, 2201115

2201115 (1 of 16)

© 2022 The Authors. Advanced Materials Interfaces published by Wiley-VCH GmbH

are correlated with MN length,^[16] aspect ratio (the ratio of the length to width),^[21,22] base diameter,^[16,21] base vertices,^[23] wall thickness, and tip area.^[24] Thereby, geometrical optimization plays a remarkable role in improving the device's stability, performance, and insertion safety. Nondissolving solid MNs possess higher mechanical strength; however, only a limited amount of drugs can be loaded on them.^[25,26] For POC diagnostics, solid MNs should also be accompanied by a secondary device to enable sample extraction and storage.^[27] Hollow MNs with microscale inner channels allow for increased drug delivery and sampling; though, channel clogging and early fracture due to thinner walls still pose a risk during insertion.^[26] Furthermore, once MN arrays are applied to the skin, partial penetration causes the "bed of nails" effect where outer-most MNs locally stretch the skin, causing the inner MNs to only partially or not at all penetrate an already stretched skin^[28] which is one of the most limiting phenomena in effective MN array penetration.

In addition, the mechanics of MN penetration into the skin is equally important to the MN's mechanical strength to enable a safe and effective insertion. Insertion characteristics assist in determining the safety margin (SM), known as the ratio of MN's fracture force to the skin's insertion force.^[24] The SM should be maximized and be greater than unity for an MN to be mechanically safe.^[16] During the MN insertion, the applied force linearly increases before reaching a peak force, the so-called insertion force, prior to breaking the skin's top layer (SC).^[2,29] Reduction in the insertion force can directly influence safety by improving the SM. In addition, reducing the force required to insert into the skin reduces the overall compression of the skin, which minimizes tissue damage and the amount of pain experienced by patients.^[26] The application method is another approach to improve insertion safety and effectiveness. In general, insertions can be made via a pressing force through manual thumb force or using an applicator. Applicators can be used to generate a controlled pressing force or impact force by predetermining the impact velocity or energy.^[30] The conventional method of MN thumb pressing is known to have less force uniformity and reproducibility,^[31] which can lead to early breakage or bending of MNs during insertion. Studies by Ranamukhaarachchi and Stoeber and Olatunji et al. showed the effect of increasing impact velocity, which reduced the insertion force and improved the SM ratio.^[2,32] These studies indicated that an increase of impact velocity from 0 to 4.3 m s⁻¹ for metallic hollow MNs reduced the insertion force from 0.88 to 0.37 N.

The aforementioned issues can be minimized by introducing new designs and mechanically stable microdevices capable of transferring different molecular size drugs and sampling biofluids with a single mechanically sturdy structure. In this study, we report a new design of MN called a microblade (MB) with the futuristic potential for drug delivery. Our recently patented MB structure incorporates a solid design with multiple side channels and reservoirs to enable effective penetration into the skin for different applications as required.^[33] Similar to MNs, MBs require sufficient mechanical strength to endure the potential failure risks during insertion into the skin. This work aims to design, fabricate, and test the mechanical strength of MBs with different geometrical features. This is followed by in vitro insertion tests of the MBs using a custom-made prototype applicator with adjustable impact velocity and pressing force. The MB insertion mechanics, such as insertion force and penetration depth on the skin subjects, were modeled and simulated with the explicit dynamics method of finite element analysis (FEA). Additionally, the diffusion and concentration of the model drug were investigated and compared for each individual MB using experimental and simulation approaches.

2. Experimental Section

2.1. Design of Open-Channel MBs

The geometrical design of the five MBs presented in this study was generated using SolidWorks (Dassault Systems SolidWorks Corporation, Concord, NH, USA). The MB height was 900 μm , with six 50 μm diameter microfluidic channels on each side to enable the transfer of large cells and drug contents. The channels were connected to two microfluidic reservoirs at the sides. The five MBs presented geometrical differences based on the blade angle and the eccentricity level with respect to the center. While the first three models incorporated 90°, 120°, and 180° (square shape) blade angles, in the other two models, the MB tips were located half- and full-eccentric with respect to the centers (Figure 1). Table 1 shows the schematic design of each MB (Types 1–5) and summarizes their geometrical features.

2.2. Fabrication of Master Microblades using 2PP

Five individual open-channel master MBs were printed by 2PP using the commercial Nanoscribe Photonic Professional GT

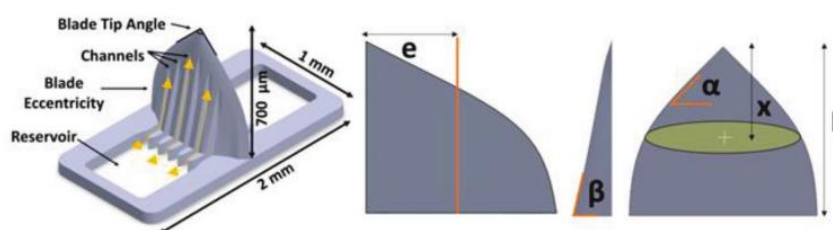





Figure 1. An overall view of the features and dimensions associated with the MB designs. Each MB has a $1 \times 2 \text{ mm}^2$ base plate, including two side reservoirs connected to multiple channels. MBs have a 0.9 mm length with various tip angles and eccentricity. Parameters including eccentricity (e), side angles (α , β), distance to the MB tip (x), and overall length (L) are defined for mathematical models.

Table 1. Geometrical features and dimensions of five different types of MBs.

Type	Blade angle [°]	Height [μm]	Eccentricity	Schematic
1	90	900	Concentric	
2	120	900	Concentric	
3	180	900	Concentric	
4	60	900	Full-eccentric	
5	90	900	Half-eccentric	

system (Nanoscribe GmbH, Karlsruhe, Germany). The system was provided with a pulsed erbium-doped femtosecond fiber laser source with a center wavelength of 780 nm for exposing the photosensitive materials. The 3D CAD models were imported to Nanoscribe's Describe software for adjusting different parameters and generating general writing language (GWL) codes required for printing. The GWL codes arranged all the parameters to be applied during the printing and specified the paths followed by the laser focus inside the photoresist.

The model structures were printed with laser power of 100 mW, scanning speed of 100 mm s⁻¹, and 1 μm fixed slicing distance. Triangular scaffolds with a wall spacing of 20 μm were selected for scaffolding. Before printing, each MB was split into blocks of 285 μm × 285 μm × 285 μm (XYZ) with a shear angle of 0°. The GWL codes were adjusted to print multiple MB structures on the same substrate to reduce fabrication time. This code adjustment enabled the fabrication of MB structures by controlling the stage movements through X and Y directions, followed by the movement in the Z-direction to return the laser to the interface position. Additionally, the code redefined the interface between the laser and the substrate. This enabled printing of all MBs simultaneously without delamination from the substrate (Figure S1, Supporting Information).

The negative-tone IP-S photoresist (Nanoscribe GmbH, Karlsruhe, Germany) was used for printing the MBs. A drop of the photoresist was drop cast on the conductive side of the indium tin oxide (ITO) coated glass slide and placed inside the system. To initiate the print process, the final GWL file containing all the specifications of the print was loaded to the NanoWrite software (NanoScribe GmbH, Karlsruhe, Germany) connected to the NanoScribe system. The laser beam focused into the photoresist using a × 25 magnification objective and NA of 0.8. To ensure the final polymerized MBs were fully fixed to the supporting substrate, the MBs were printed with 0.6 μm overlap into the substrate. The MBs were written in the galvo scan mode in XY directions, while the piezo offsetting mode was used for offsetting in the Z-direction. After polymerization,

the printed samples were developed in a propylene glycol monomethyl ether acetate (PGMEA) bath for 10 min, rinsed for 2 min in isopropyl alcohol (IPA), and finally air-dried (Figure S2, Supporting Information).

2.3. Casting of Negative PDMS Mold

Negative molds of master MBs were made using polydimethylsiloxane (PDMS) (SYLGARD 184 Silicone Elastomer Kit, Dow Corning, Midland, MI, USA). PDMS solution with a 1:10 curing agent/base ratio was mixed and degassed in a planetary mixer to remove air bubbles. The solution was poured on the MB masters in a petri dish and cured inside a laboratory oven at 80 °C for 2 h. The soft negative PDMS mold was then peeled off from the masters for replication (Figure 2a).

2.4. Fabrication of Polymeric MBs using PDMS Mold and Soft Embossing

MB replicas were produced using the soft embossing process. A rheometer (TA Instruments, New Castle, USA) was used to replicate thermoplastic MBs using the negative PDMS mold. A total of ten pellets (two pellets per MB replica) of thermoplastic material (cyclo-olefin polymer, Zeonor 1060R) were mounted onto the PDMS cavities and placed in-between two 40 mm diameter stainless steel plates inside the rheometer's chamber. The temperature inside the chamber was set to 163 °C, which is 63 °C above the glass transition temperature of the thermoplastic ($T_g = 100$ °C), to facilitate the flow of low viscous thermoplastic polymer into the mold cavities. While the thermoplastic material was melting, the lower plate was kept fixed, and the upper plate lowered as a function of time and limited to the maximum of 30 ± 5 N axial force. During the embossing process, the upper plate's downward displacement reduced nonlinearly from 100 to 25 μm per interval over the course of 1 h until the upper plate reached 700 μm above the surface of the PDMS mold. The chamber temperature was then reduced to 10 °C for 15 min to allow solidification of the replicas before demolding. Once solidified, the replicas were peeled off from the negative PDMS mold (Figure 2b). The PDMS mold was used several times (>20 cycles) with no defects such as cracks or deformation forming on the mold.

2.5. Mechanical Strength Test of MB Replicas

A series of compression tests were conducted at two different speeds to study the mechanical strength and integrity of the MBs. Five MB replicas were tested using the axial compression test module of the TRIOS package linked to the rheometer used for the soft embossing process. Each MB replica was placed on the lower disk of the rheometer using double-sided tape while the upper plate was lowered at speeds of 1 and 25 μm s⁻¹. The software was programmed to initiate from a predefined distance from the MB tip and lowered by 400 μm. During the test, force and displacement data were recorded to plot the mechanical behavior of individual MBs. The data were

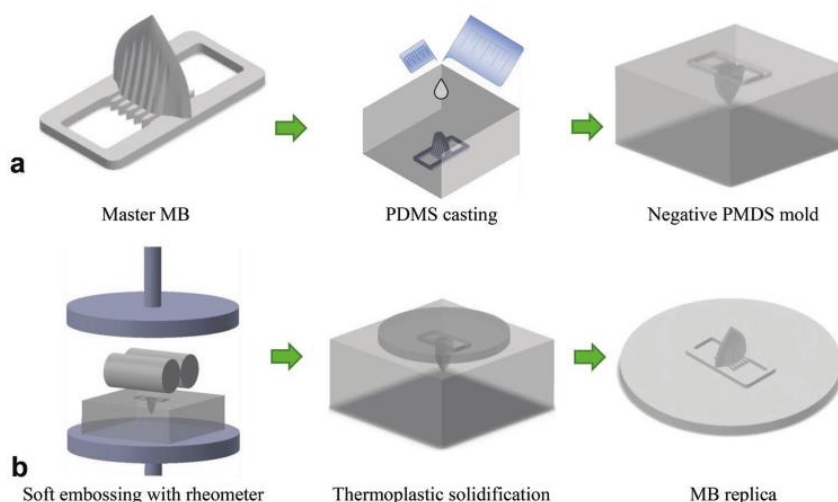


Figure 2. Schematic representation of the polymer MB replication process, a) casting of negative PDMS mold from the master MB, b) soft embossing of the polymeric MB.

then processed using MATLAB (Natick, MA, USA) software to compare MBs' mechanical responses, including initial stiffness and failure points.

2.6. Scanning Electron Microscopy

The MB morphology and dimensions before and after compression testing were observed using a scanning electron microscope (SEM, JOEL JSM-7001F). Samples were attached to a metal stub using double-sided carbon tape. The stubs containing the MB samples were then coated with a 10 nm layer of platinum using JOEL Desktop Sputterer to avoid sample charges during SEM imaging. To study the MB tip size and angle, metal stubs with 90° angled holders capable of vertically mounting samples were used. The secondary electron detector with an accelerating voltage of 15 kV in high vacuum mode was used for SEM.

2.7. Manufacturing an Impact Applicator

A spring-loaded applicator prototype was designed in SolidWorks and printed using a Teirtime X5 3D printer (Teirtime Corporation, Milpitas, CA, USA) from PLA filaments to test the effect of application conditions. This applicator could adjust impact velocity and included a locking mechanism for activation. The design was consisted of three slots in the plunger and a top screw to regulate the impact velocity (Figure 3a). A high-speed camera (Photron Fastcam SA3), equipped with Nikon Nikkor 50 mm f 1.4 lens was used to measure the applicator impact velocities. During the test, the plunger was fixed by the locking mechanism, then released by pressing the push button from all three positions while motion images were captured at 4000 fps. The images were further analyzed using ImageJ (U. S. National Institutes of

Health, Bethesda, MD, USA) to determine the applicator's impact velocities. Figure 3b shows the stacked images at equally spaced time intervals to estimate the impact velocity of three different positions.

2.8. Skin Insertion and Diffusion Tests

The penetration efficiency and drug delivery of the MBs were tested using abdominal porcine cadaver skins.^[34] Studies were performed using experimental procedures approved by the University of Southern Queensland (USQ) and the University of Queensland (UQ) animal ethics (Ethics Number: 20EXE005) and biosafety committees (Biosafety Number: 21BIOS003). Porcine cadaver skins were carefully shaved and cut into 3 ± 0.1 mm thick samples using a scalpel blade, and the fat layer underneath the hypodermis layer was removed. The tissue samples were then kept frozen at -20 °C and naturally thawed before the tests. The skin tissue was fixed by a custom-made skin stretching mechanism to control the skin strains (Figure S3, Supporting Information). The skin was gently stretched $\approx 5\%$ from the original undeformed state to mimic the skin in vivo condition.^[35]

Oxygen plasma treatment (Harrick Plasma Cleaner PDC-001, Harrick Plasma, Ithaca, NY, USA) was conducted for a minute with 30 W RF power on the MBs before the tests to increase the hydrophilicity of the MBs surface. Fluorescein was used as a model drug with 376.27 g mol⁻¹ molecular weight (sodium salt, F6377, Sigma-Aldrich Corp., St. Louis, MO, USA). The concentrated aqueous solution was prepared from the mixture of fluorescein and deionized water (0.1% w/v). The tips of the MBs were dipped into a 0.1 μ L droplet of the solution, enabling the flow through the channels into the reservoir by capillary flow. Fluorescence-coated MBs were then attached to the plunger of the prototype applicator with double-sided tape and applied to the abdominal porcine skin.

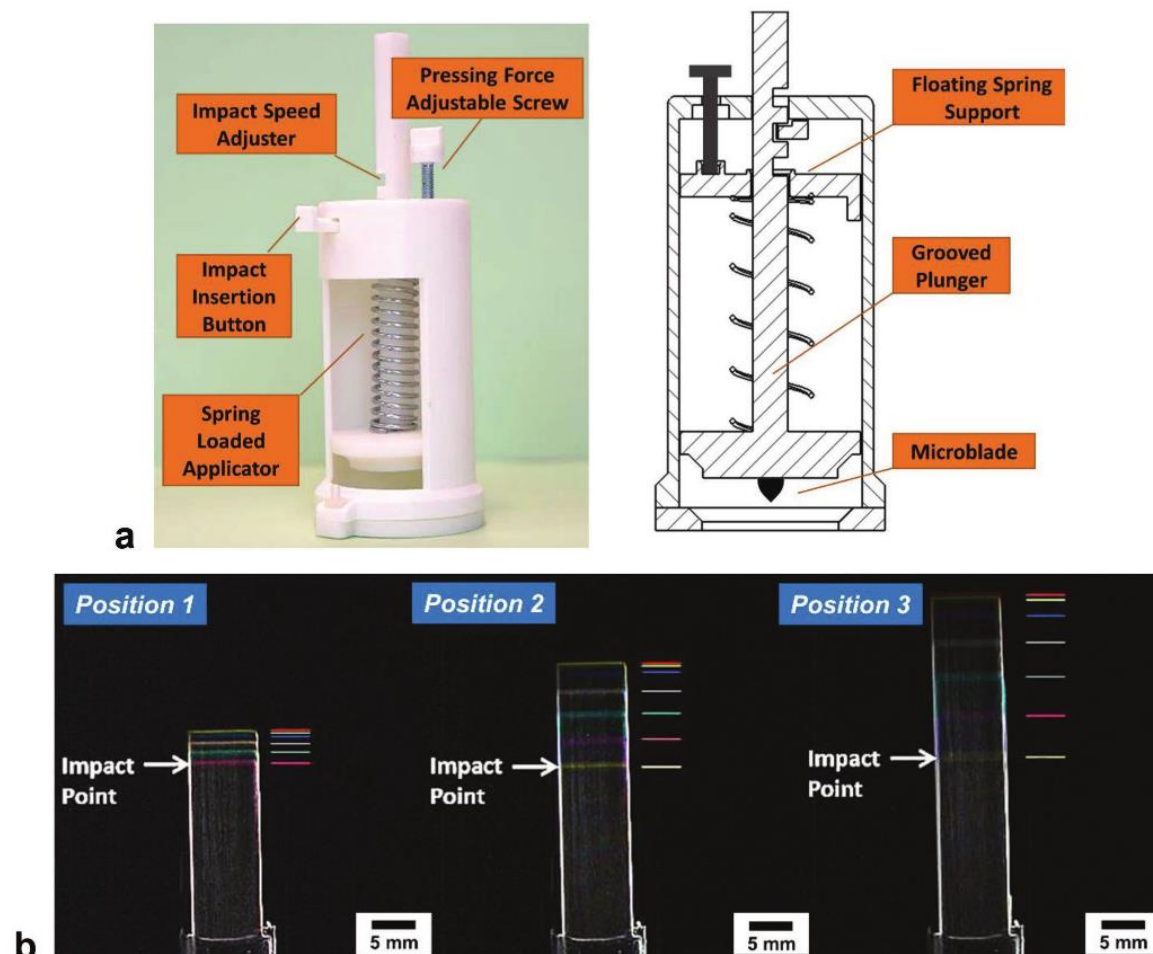


Figure 3. a) 3D-printed prototype applicator capable of adjusting impact velocity. b) High-speed camera images track the location of the plunger.

The first set of experiments was conducted with the insertion of all MB designs on the abdominal porcine skin with an impact velocity of 4.5 m s^{-1} . The second set of experiments was performed by inserting only the MB Type 1 on the skin tissue with impact velocities of 1.5, 3, and 4.5 m s^{-1} . After insertion, MBs were held on the skin surface for 5 min; upon removing the MBs from the skin tissues, the surface of the skin was tape stripped (20 ± 3 cycles) using 3 M Scotch Magic tape (3 M, USA) from different directions to remove the SC layer of the skin.^[36,37] The penetration of fluorescein below the surface of the skin was visualized 20 min after each test by a confocal laser scanning microscope (CLSM, Zeiss LSM710, Germany) using Z-stack imaging with run times of 15 min.

2.9. Histology of MBs Penetration

Histology was used to confirm MBs penetration into the porcine skin. Sections were obtained using the cryosectioning

technique. MB insertion sites were excised using scalpels, then placed upright into the cryostat mold, partially covered by optimal cutting temperature (OCT) compound (Tissue-Tek, Sakura Finetek, Torrance, USA). Once the skin sample was positioned inside the cryostat mold, the remaining mold cavities were filled by OCT and then frozen inside dry ice containers. Subsequently, the frozen specimens were sectioned into $50 \mu\text{m}$ thick slices using a Leica CM3050 cryostat (Leica Microsystems, Wetzlar, Germany) and placed on the Superfrost glass slides. The tissue sections were imaged by CLSM to visualize the MB penetration and diffusion of the model drug inside the skin.

2.10. FEA of MBs Insertion

A 3D planar symmetric finite element model was generated using the ANSYS (Canonsburg, PA, USA) explicit dynamics module to evaluate the MBs insertion mechanics into the skin.

Table 2. Material parameters of the MB and the multilayered human skin model used in ANSYS explicit dynamics.

Parameter	Microblade	Stratum corneum	Dermis	Hypodermis
Mathematical model	Linear elastic	Linear elastic	Hyperelastic: Ogden 1st order	Linear elastic
Thickness [mm]	–	0.026	2	1.1
Young Modulus [MPa]	2100	28.4	–	0.1
Poisson ratio	0.48	0.49	0.49	0.48
Density [kg mm ⁻³]	1.01 E-6	1.3 E-6	1.2 E-6	9.71 E-7
Hyperelastic coefficients MU1, A1 [MPa]	–	–	0.0568, 13.3	–
Incompressibility factor [MPa ⁻¹]	–	–	0.0745	–
Failure criteria [MPa]	–	20	7	–
Refs.	[38]	[39,40]	[40,41]	[40]

Skin models comprised three layers, SC, dermis, and hypodermis, with 26 μm, 2 mm, and 1.1 mm thicknesses, respectively. An Ogden (first-order) model with uniaxial test data was applied for the dermis layer, while SC and hypodermis were assumed to respond following a linear elastic model. Quadrilateral meshing with specific bias types, with factors of 3 to 4, was used to increase the number of elements near the MB–skin interfaces. FEA models calculated the insertion forces required to penetrate all MB types into the skin with a constant velocity of 4.5 m s⁻¹ during insertion. Additionally, the FEA model calculated the penetration depth of all MBs with an initial velocity of 4.5 m s⁻¹, which was reduced upon insertion into the multilayered skin model. The material erosion method was used to enable MBs penetration into the skin model. The erosion algorithm eliminated the elements that reached the material failure point while retaining their inertia effect. **Table 2** summarizes the parameters used for the MBs and the multilayered skin models.

2.11. 3D Modeling of Drug Diffusion into Skin

A 3D simulation using COMSOL Multiphysics (COMSOL Multiphysics, COMSOL AB, Sweden) was used to model the diffusion of the fluorescein model drug into the skin. A two-layered skin model (SC and dermis) with negative cavity volumes representing fully penetrated individual MBs were initially created in SolidWorks. The 3D model was then imported to COMSOL Multiphysics to perform a series of time-dependent numerical simulations. The diffusion model incorporated nonconvection mass transport based on the time-dependent concentration of the model drug. The concentration decay function for the model drug was derived according to the Fick's second law of nonsteady-state diffusion (Equation (1))

$$\frac{\partial C}{\partial t} = D \left(\frac{\partial^2 C}{\partial x^2} \right) \quad (1)$$

where $\frac{\partial C}{\partial t}$ is the concentration rate and $\frac{\partial C}{\partial x}$ is the concentration gradient. Thus, the concentration $C_{(t)}$ on the MB surface was described by the decay function in Equation (2)^[42]

$$C_{(t)} = C_0 + (C_s - C_0) \left(1 + \operatorname{erf} \left(\frac{x}{2\sqrt{Dt}} \right) \right) \quad (2)$$

where C_0 (mol m⁻³) is the initial concentration of the model drug within the skin, C_s (mol m⁻³) is the MB initial surface concentration, D (m² s⁻¹) is the diffusion coefficient, t is the time (s), and x is the skin thickness at the location of penetration (m). Based on the simulation setup, no initial drug concentration pre-existed in the skin ($C_0 = 0$), and a no flux condition was assumed for the skin boundaries. The dermal-subcutaneous junction (the boundary between the dermis layer and the subcutaneous fat layer beneath) was set to act as the sink condition of the model. A fluorescein model drug with an initial concentration of 2.66 (mol m⁻³), along with diffusion coefficients of 3.97E-16 and 5.8E-10 m² s⁻¹, was used for the SC and dermis layers.^[43,44] The simulation calculated the average concentrations (mol m⁻³) of the model drug near the tip of the MB and at the bottom of the dermis layer (subcutaneous layer junction) within 20 min. Additionally, the concentration gradient of the model drug was calculated through the skin from the near tip to the end of the dermis layer.

2.12. Statistical Analysis

Experimental and simulation results were presented as the mean ± standard deviation ($n = 3$). Error bars were expressed as the standard deviations from the mean. For statistical comparisons, one-way analysis of variance (ANOVA) was used for insertion and penetration characteristics of all MBs (Types 1–5), and the p -value was set at < 0.05 for statistical significance. The statistical calculations were conducted using Office 365 Microsoft Excel (Microsoft Corporation, Redmond, WA, USA).

3. Results

3.1. Fabrication of MBs

Five types of complex master MBs were printed directly from CAD models using 2PP with submicron resolution. **Figure 4a** shows an MB replicated from its master fabricated using 2PP technique. Thermoplastic replicas of the masters were fabricated from the negative PDMS molds using soft embossing process with high spatial resolution. The negative PDMS molds of the masters were used for >20 cycles without any defect or impacting the overall quality and fidelity of the replicas. Replicated MBs had 849.29 ± 3.1 μm (mean ± SD; $n = 5$) overall height with ≈5.63% overall shrinkage from the masters. **Figure 4b–f** shows the SEM images of the MB replicas, and **Figure 4g** shows a typical tip of the MB Type 2 with a tip size of less than 5 μm.

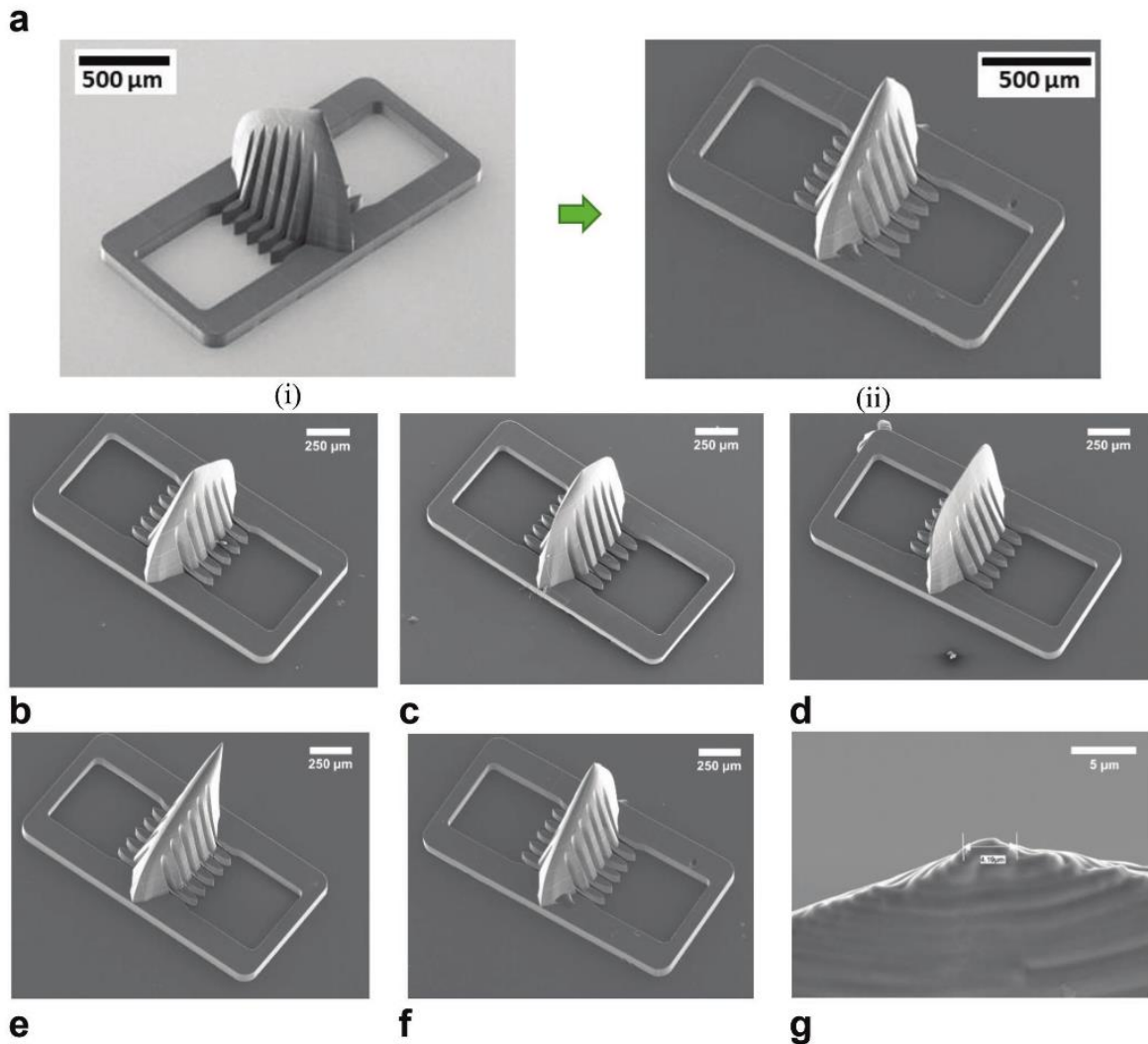


Figure 4. a) Comparison of the i) master MB fabricated by 2PP versus ii) MB replica fabricated by soft embossing. SEM images of the MB replicas b) Type 1, c) Type 2, d) Type 3, e) Type 4, f) Type 5, and g) tip sharpness of the MB Type 2.

3.2. Mechanical Compression Testing of MBs

Compression tests were conducted at compression speeds of 1 and 25 $\mu\text{m s}^{-1}$ to evaluate the insertion damage, initial stiffness, and failure points of each MB when a compressive force was applied along the vertical axis of the MB. **Figure 5a–e** shows the SEM images of the MBs after compression tests, where failure is defined by the deformation occurring close to the MB's tip by bending. Initial stiffness in the compression test can be defined as the slope in the linear region of the force–displacement graph, and failure points are the first occurrence of a sudden drop in the force–displacement graph, which leads to permanent deformation of the MB. **Figure 5f,g** shows the force–displacement graphs of the MBs

compression tests for 1 and 25 $\mu\text{m s}^{-1}$ compression speeds. At the compression speed of 1 $\mu\text{m s}^{-1}$, the initial stiffness varied across MB Types 1–5 with values of 11.12, 13.22, 17.03, 8.78, and 2.71 N mm^{-1} , respectively. The trend remained the same for the 25 $\mu\text{m s}^{-1}$ compression speed; however, due to the effects of strain rate on viscoelastic material response, the stiffness values increased to 22.10, 24.30, 29.98, 19.56, and 9.06 N mm^{-1} for Types 1–5, respectively. In both experiments, MB Type 3 showed the highest stiffness, whereas MBs Types 4 and 5 had the lowest stiffness. Effects of strain rate were also observed on failure points when the compression test speed increased from 1 to 25 $\mu\text{m s}^{-1}$. For instance, the failure point increased from 1.71 N at 1 $\mu\text{m s}^{-1}$ to 5.43 N at 25 $\mu\text{m s}^{-1}$ test speed for MB Type 3.

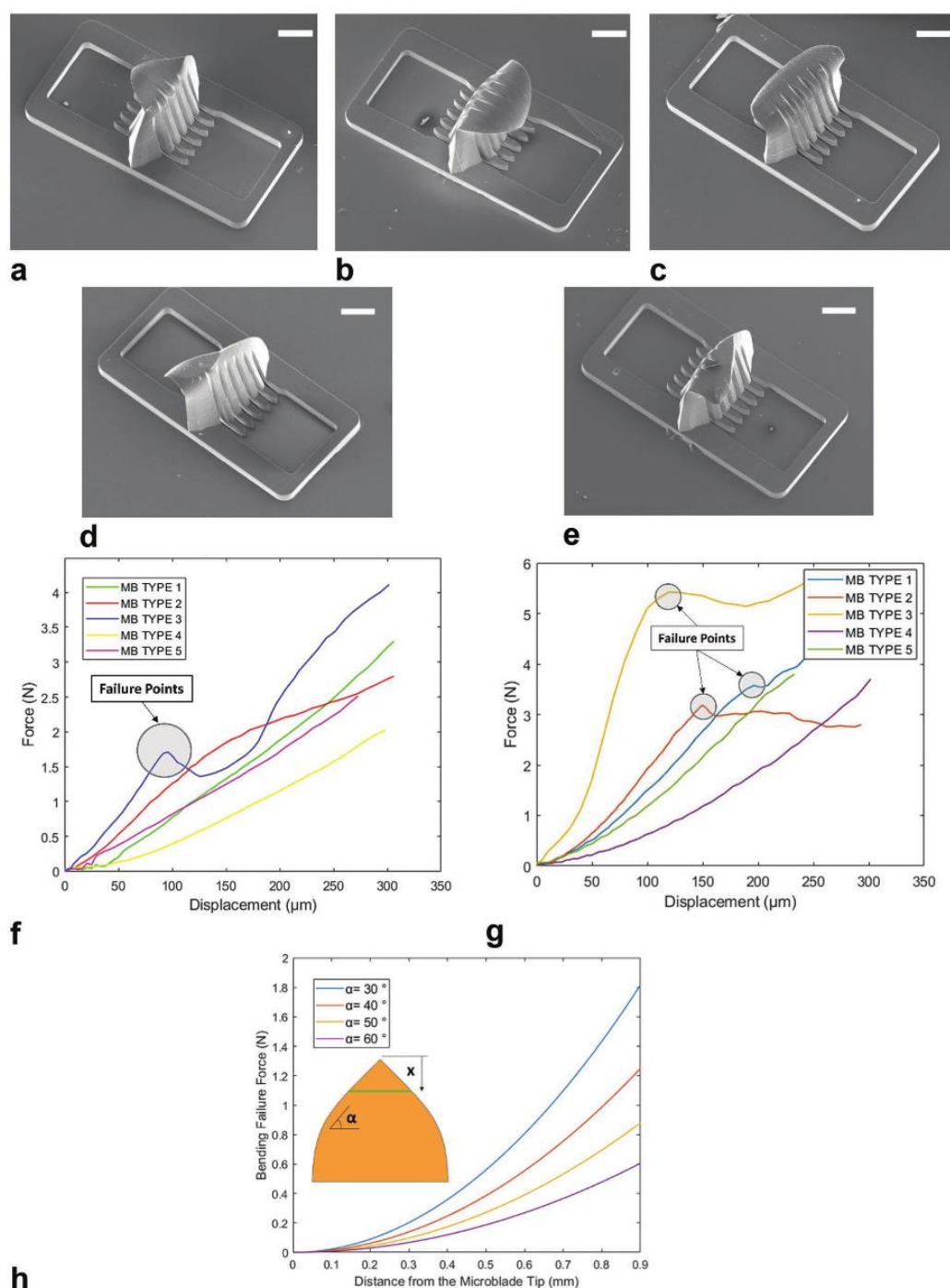


Figure 5. SEM images of MBs after mechanical compression tests for a) MB Type 1, b) MB Type 2, c) MB Type 3, d) MB Type 4, and e) MB Type 5 (scale bar = 200 μm). Force–displacement graphs of compression tests at f) $1 \mu\text{m s}^{-1}$ speed and g) at $25 \mu\text{m s}^{-1}$ speed for Types 1–5 of MBs. h) Theoretical representation of the critical failure bending load at different locations (x) from the MB tip based on varying MB tip angles ($30^\circ < \alpha < 60^\circ$) with a constant side angle ($\beta = 80^\circ$).

As evident from Figure 5a–e, bending is the primary mode of failure for MBs. In addition to experimental data, theoretical analysis can give an in-depth understanding of the effects of various factors on the overall MB mechanical integrity. During MB insertion, the skin elastic behavior and irregular topology impose axial and lateral loads on the microstructure that may result in different failure scenarios. The mathematical models assist in predicting the influence of geometrical parameters on MB bending, which is one of the most probable causes of MB failure. Assuming an MB acts as a cantilever beam with a point load perpendicular to the neutral axis, the varying second moment of inertia $I_{(x)}$ is determined in terms of the distance from the MB tip (x). The Euler–Bernoulli beam theory predicts a decrease in bending stress when moving toward the MB base. The critical bending load (F_{bending}) can be calculated using Equation (3)

$$F_{\text{bending}} = \frac{\pi\sigma_y L^2}{4 \tan(\alpha) \tan^2(\beta)} \quad (3)$$

where σ_y is the yield stress, L is the MB length, α and β represent the MB angles from either side (see Figure 1). The model predicts that the critical F_{bending} is directly proportional to L and σ_y , while inversely proportional to α and β . According to this model, L and β parameters have the most influential effect on determining the critical F_{bending} . For a constant value of $\beta = 80^\circ$, Figure 5h shows the critical F_{bending} at different locations from the MB tip for side angles ranging from $30^\circ < \alpha < 60^\circ$.

3.3. Penetration and Delivery of Fluorescein into Skin

The penetration and drug delivery capabilities of the MBs were determined by measuring the penetration depth of fluorescein solution within the skin layers. A series of insertion tests ($n = 15$) were conducted on the porcine cadaver skin using the custom-made applicator with an impact velocity of 4.5 m s^{-1} for all MB designs. To determine the depth of dye penetration, the Z-stacks imaging was conducted from the top surface of the MB-treated porcine skin with $10 \text{ }\mu\text{m}$ intervals over 15 min for each test. Figure 6a shows the penetration and diffusion images of the fluorescein solution after insertion of an MB Type 1 to the tissue sample, taken from the top of the skin surface to $\approx 230 \text{ }\mu\text{m}$ underneath the skin. The depth of penetration of each MB was determined based on the mean \pm standard deviation (Figure 6b). In addition, fractional penetration length (FPL: percentage of MB penetrated length/overall MB length) was determined using the data from the Z-stack images. The results indicated that all Types 1–5 of MBs successfully penetrated the skin's SC layer having FPLs of $24.5 \pm 5.32\%$, $23.78 \pm 3.46\%$, $16.25 \pm 4.3\%$, $26.59 \pm 3.11\%$, $28.58 \pm 7.28\%$ (mean \pm SD; $n = 3$), respectively (Figure 6c). According to the data (shown in Figures 6b,c), the Type 3 MB had the least penetration at $138 \pm 36.51 \text{ }\mu\text{m}$ with FPL of $16.25 \pm 4.3\%$, and MB Types 4 and 5 had the furthest penetration achieving depths of $224.73 \pm 26.42 \text{ }\mu\text{m}$ (FPL: $26.59 \pm 3.11\%$) and $242.63 \pm 61.76 \text{ }\mu\text{m}$ (FPL: $28.58 \pm 7.28\%$).

In another experiment, the Type 1 MB was inserted in the abdominal porcine tissues using the applicator with impact

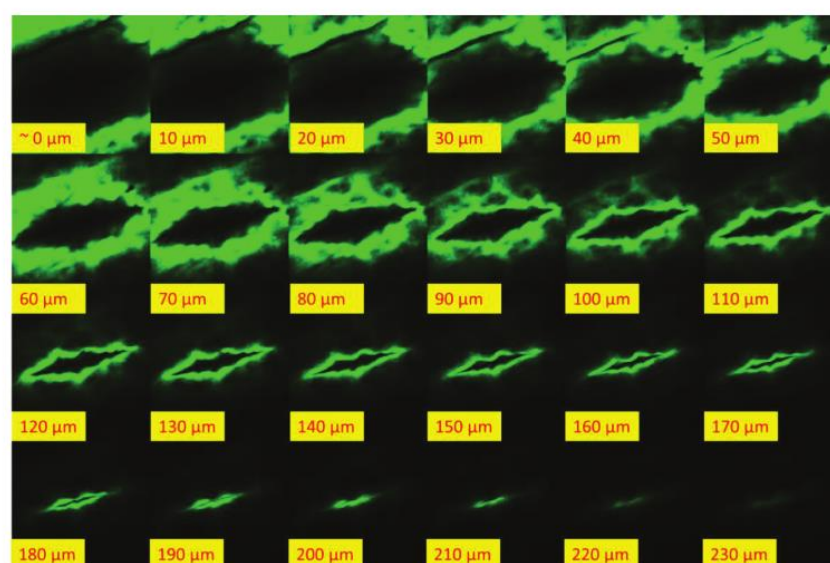
velocities of 1.5, 3, and 4.5 m s^{-1} to investigate the effect of impact velocity on penetration. The results show that increasing the impact velocity significantly increased the depth of penetration of this MB from $172 \text{ }\mu\text{m}$ for 1.5 m s^{-1} impact velocity to 196 and $254 \text{ }\mu\text{m}$ for 3 and 4.5 m s^{-1} impact velocities. This is equivalent to $\approx 45\%$ increase in the overall penetration depth from 1.5 to 4.5 m s^{-1} impact velocities (Figure 7a). Figure 7b shows the diffusion pattern of the fluorescein solution in the skin after applying an MB Type 1 at 4.5 m s^{-1} impact velocity. As can be seen from Figure 7b, the 3D image resembled the MB's overall shape within the tissue. Histology studies for MB Type 2 also showed the skin penetration and diffusion pattern of the model drug deep into the skin epidermal layer (Figure 7c).

3.4. FEA of MB Insertion into Skin

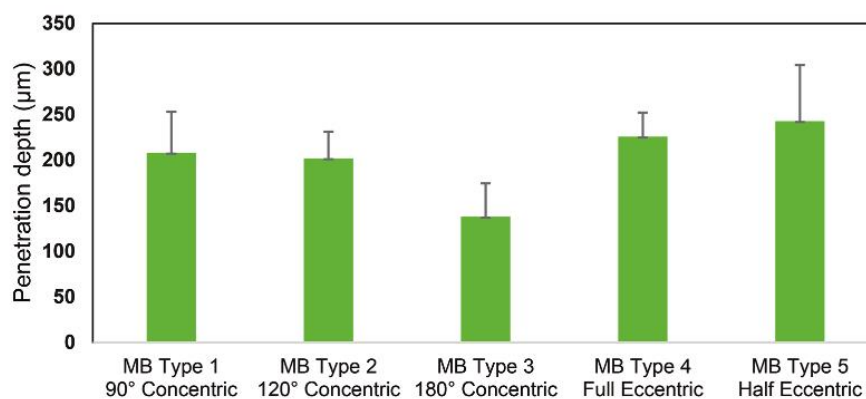
The explicit dynamic module of ANSYS was used for FEA simulations (Video S1, Supporting Information). The skin was modeled as a multilayered model with a planner symmetry region combined with hyperelastic and linear elastic material properties. The boundary conditions of the model are indicated according to Figure 8a. The force of insertion and the penetration depth of MBs were calculated and plotted against their displacement into the skin model. The results indicated an increase in the force peaking at insertion before a drop as the skin was punctured. Figure 8b shows that the forces of insertion for Types 1–5 MBs were 0.1, 0.17, 0.52, 0.085, and 0.092 N. The Type 3 MB had the highest insertion force among all MBs, indicating that approximately five times more force is required to insert this design of the MB into the skin in comparison to the other designs. Figure 8c shows the insertion force of each MB design. In addition, penetration depth was determined during the FEA simulations of the MBs. Although the FEA results indicated a similar pattern to experiments, the results for penetration depth were smaller in FEA models. For Types 1–5 MBs, these penetration depths were 167.36, 155.70, 65.61, 198.74, and $169.18 \text{ }\mu\text{m}$, respectively. Results for MB penetration indicated that the Type 4 MB had the maximum penetration depth of $198.74 \text{ }\mu\text{m}$ with FPL of 22.08%. Similar to the experiments, the Type 3 MB had a minimum penetration of $65.61 \text{ }\mu\text{m}$ with FPL of 7.3%. Figure 8d shows the values of penetration depth obtained for five MB designs after insertion into the multilayered skin model.

3.5. Drug Diffusion Modeling

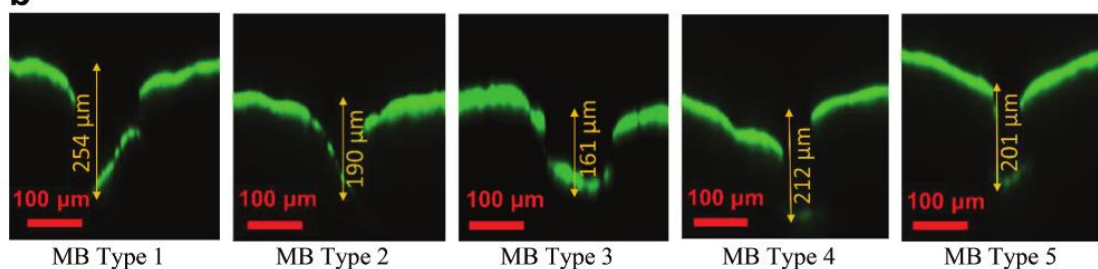
COMSOL Multiphysics was used to simulate the diffusion of fluorescein as a drug through the multilayered skin model. Figure 9a shows the overall setup of the 3D model used for diffusion simulation of the model drug. This setup consisted of a two-layered skin model with no flux condition around the skin, a time-dependent MB concentration as described by Equation (2), and the data collection paths (1–3) (Figure 9a). The initial concentration of the drug in the skin model was assumed to be zero. Based on the simulation results, the concentration of the model drug significantly increased around the penetration



a



b



c

Figure 6. a) Fluorescein solution diffusion underneath the porcine skin surface after application of a Type 1 MB with an impact velocity of 4.5 m s^{-1} illustrated from the skin surface to the deepest detectable fluorescein dye using confocal Z-stacks technique, b) penetration depth of five MB designs after insertion into the porcine abdominal skin with 4.5 m s^{-1} impact velocity, the data are expressed as mean \pm SD ($n = 3$, $p < 0.1$; one-way ANOVA). c) Cross-sectional view of the tissues showing the maximum detectable penetration of Types 1–5 MBs, applied at a constant impact velocity of 4.5 m s^{-1} , having FPLs of $24.5 \pm 5.32\%$, $23.78 \pm 3.46\%$, $16.25 \pm 4.3\%$, $26.59 \pm 3.11\%$, $28.58 \pm 7.28\%$ (mean \pm SD; $n = 3$), respectively.

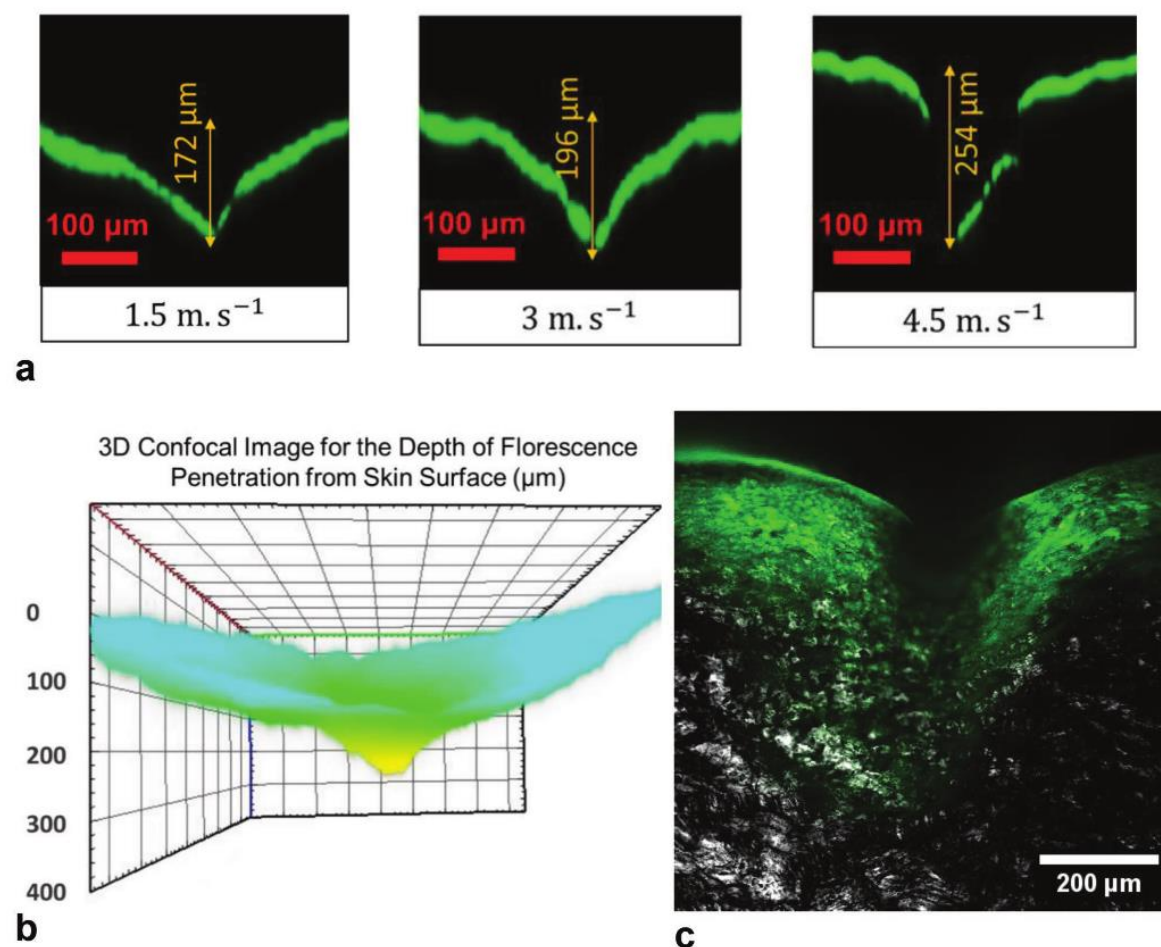


Figure 7. a) Cross-sectional view of the tissues showing the maximum detectable penetration of Type 1 MB, applied at impact velocities of 1.5, 3, and 4.5 m s⁻¹. b) 3D confocal image showing the penetration and diffusion of fluorescein dye underneath the skin's epidermal layer. c) The histology section for Type 2 MB illustrates skin penetration and the diffusion of fluorescein as a model drug deep into the skin's epidermal layer.

region in the first 5 min; however, the diffusion rate started to slow significantly after the first 12 min (Figure 9b) (Video S2, Supporting Information). The results from the simulation are presented as concentration profiles and streamlines (Figures 9c,d), demonstrating that the diffusion flux depends on the MB geometry. By increasing the tip angle from 90° to 180° (MB Types 1–3) the concentration gradient shifted toward the dermal-subcutaneous junction. Concentration gradients for eccentric MB Types 4 and 5 appeared to generate a nonuniform drug distribution (Figure 9d). After 20 min, for MB Types 1–5, a concentration of 1.07, 1.15, 1.37, 1.05, and 1.06 mol m⁻³ was achieved near the tip of each MB. Thus, the maximum concentration of 1.37 mol m⁻³ was noted for MB Type 3, while MB Types 1, 4, and 5 had the least concentration of ≈1.05 mol m⁻³. At the near subcutaneous layer, concentrations of 0.49, 0.51, 0.57, 0.5, 0.5 mol m⁻³ were observed for MB Types 1–5. Again, for MB Types 1, 4, and 5, which have a similar tip shape and angle, a lower drug concentration was observed near the

subcutaneous layer. Figure 9e shows the average fluorescein concentration at the two locations (near MB tip and subcutaneous layer) for each MB, and Figure 9f shows the fluorescein concentration gradient across the skin thickness.

4. Discussion

In this study, complex microstructures were created directly from CAD drawing using the 2PP technique and replicated using PDMS micromolding and soft embossing methods. These fabrication methods allow the production of complex MBs with good repeatability and high mechanical strength, which are not achievable by other micro-manufacturing processes. 2PP is the most versatile method for manufacturing microstructures, especially MNs and MBs.^[8] Our previous studies demonstrated the fabrication of complex MN arrays using 2PP techniques.^[9,38] Similar to MNs, MBs need

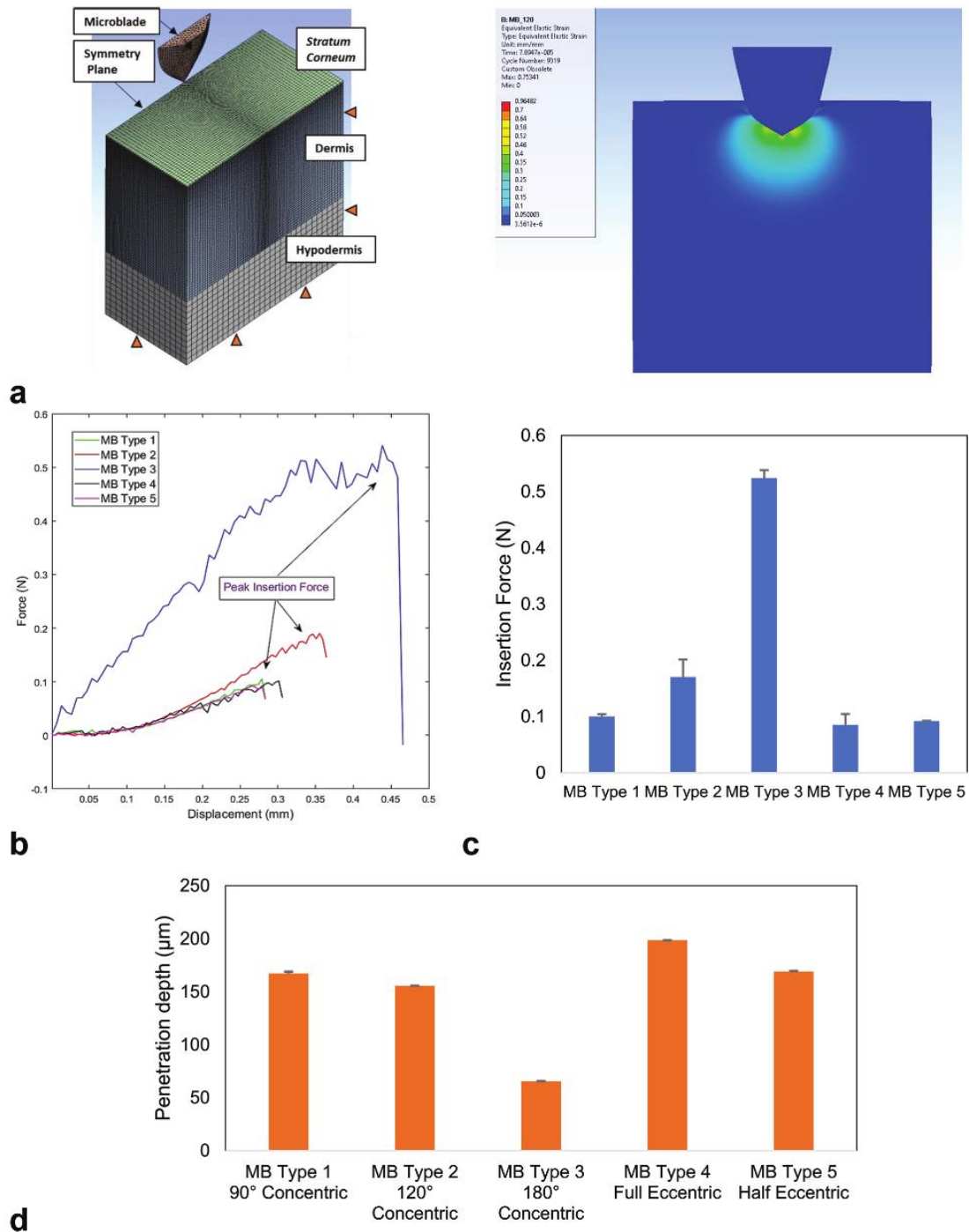


Figure 8. a) Boundary conditions and quadrilateral bias meshing used for FEA of the MBs, showing SC, dermis, and hypodermis layers. b) Calculation of peak insertion force before MBs pierce the SC layer of the skin model. c) Bar chart showing the insertion force achieved from the simulation of the MBs during insertion into the skin model with a velocity of 4.5 m s^{-1} . The data are expressed as mean \pm SD ($n = 3$, $p < 0.001$; one-way ANOVA). d) Penetration depth was achieved from the simulation of the MBs during insertion into the skin model with a velocity of 4.5 m s^{-1} . The data are presented as mean \pm SD ($n = 3$, $p < 0.001$; one-way ANOVA).

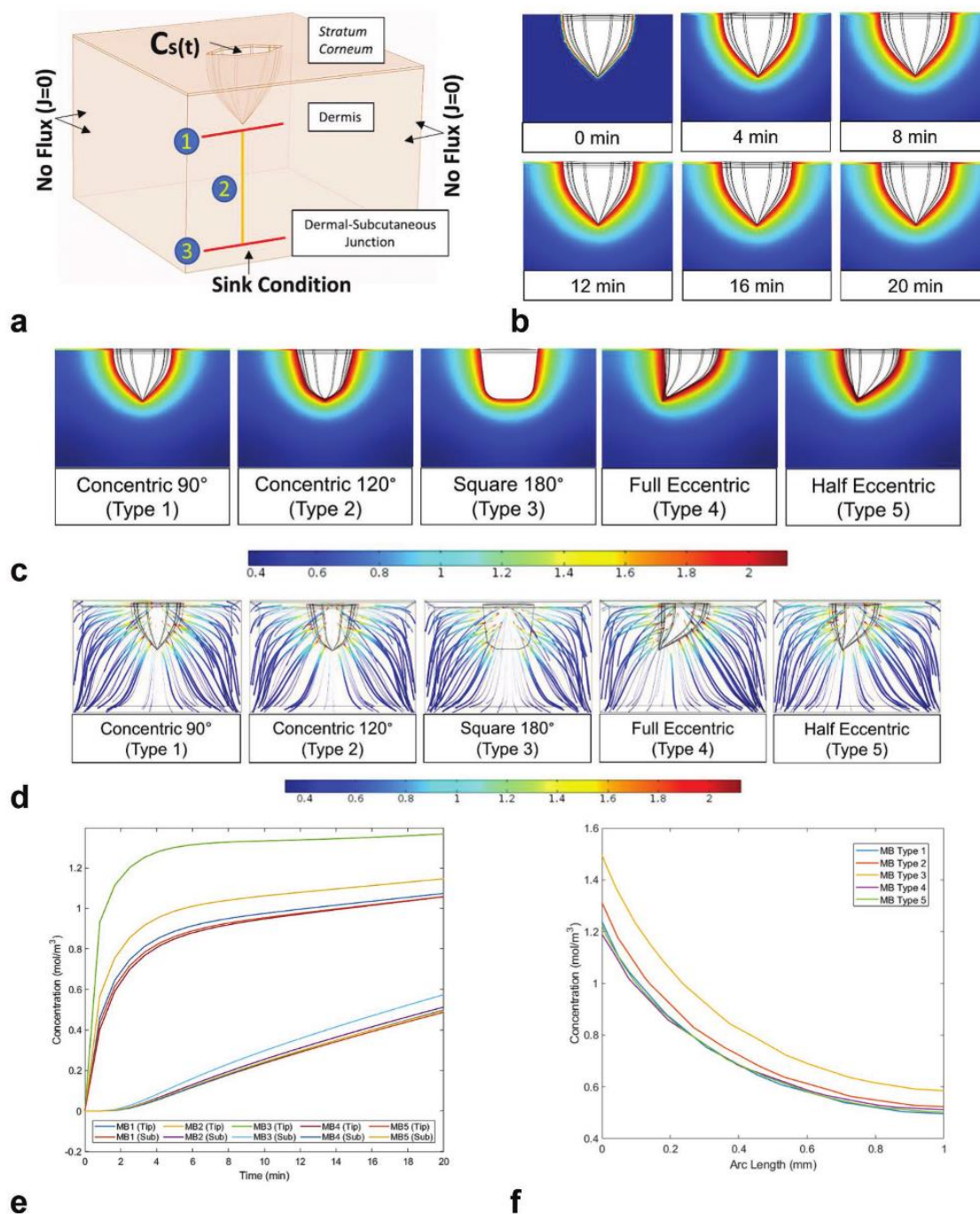


Figure 9. a) The simulation setup for the diffusion model consists of time-dependent concentration, no flux boundary condition, and measurement lines for data collection. Model drug concentrations on lines 1 and 3 are averaged at different time intervals, while line 2 represents the concentration gradient through the skin underneath the penetration region. b) Concentration profile for MB Type 1 at different time intervals 0, 4, 8, 12, 16, and 20 min. c) Fluorescein concentration profile of all five MBs at 20 min. d) Color-coded concentration gradient streamlines showing the diffusion of the model drug after 20 min across the skin thickness for five MBs. e) Average fluorescein concentration (mol m^{-3}) versus time (min) at two locations (near MB tip and at subcutaneous layer). f) Concentration (mol m^{-3}) versus arc length (mm) extended from MB tip to subcutaneous layer.

sufficient strength to safely and reliably insert into the skin.^[45] To improve the MB integrity and reduce the 2PP fabrication time, a series of process optimizations were conducted on the main printing parameters such as laser power, scanning speed, slicing distance, scaffolding method, and block size to select the most optimum set of parameters,^[38,46] and print rigid microstructures with high durability. PDMS micromolding is a well-known technique to replicate microstructure. In this study, we used PDMS mold for soft embossing of a complete microfluidic device, including MB structure with open fluidic channels and reservoirs in a single embossing step. The reservoirs and fluidic channels are integrated into the design of the MBs to store and enable the transfer of fluids in and out of the skin. PDMS molds produced from master MBs were reused for several cycles without damage (>20). The axial force applied during the soft embossing process was carefully controlled to enable fabrication of high-precision replicas while avoiding microcracks to the PDMS mold. The maximum allowable pressure on the mold was adjusted based on the microstructures' geometrical complexity and the volume of thermoplastic materials required per replication cycle. Our previous study used lower pressure to replicate MN arrays,^[38] which indicates the dependence of the applied force on the design geometries and the mold structure.

Axial compression tests were conducted at 1 and 25 $\mu\text{m s}^{-1}$ compression speeds to evaluate the mechanical strength of the MBs. The data indicate an increase in mechanical strength upon the increase in the compression speed, i.e., faster insertion of MBs into the skin decreases the chances of early failure of MBs. During the tests, bending failures were observed (Figure 5), deemed the critical limitation to successful MB insertion.^[47]

In this study, we demonstrated the successful insertion of MBs into the dermal layer with our customized applicator equipped with variable impact velocities. All the MB replicas ($n = 22$) successfully penetrated the skin with no breakage or separation, leaving no residue on the skin (Figure S4, Supporting Information). Enhancing the MB penetration can improve the drug delivery and sampling for diagnostics,^[48,49] while reducing the fabrication costs associated with partial penetrations. As opposed to manual applications, using an applicator will assure the patient or carer that enough force has been applied to insert the MBs into the skin. In addition, increasing the impact velocity (and hence the strain rate) has remarkably improved the penetration.^[48,50] Our results showed that increasing impact velocity from 1.5 to 4.5 m s^{-1} resulted in up to 45% increase in the overall FPL. According to the data, reducing the MB angle and introducing eccentricity in the design also improved the MBs' FPL. For a constant MB height and base size, the effects of eccentricity can be interpreted as a reduction in the MB angle as eccentricity increases from the center toward the sides. The effect of impact application on MN penetration has also been demonstrated in the literature.^[48,51,52] Maaden et al. showed 40% lower MN array penetration efficiency and reproducibility when manual insertion was used over an impact insertion.^[53] In another study, Meliga et al. showed that by increasing the impact velocity from ≈ 0.25 to 2 m s^{-1} a profound penetration depth enhancement from $\approx 20\%$ to 60% was achieved.^[50] In addition, through a series of simulations in ANSYS explicit dynamics, the insertion force required

to penetrate the skin for various MB designs was calculated. Insertion forces varied between 0.085 and 0.52 N depending on the MB overall geometrical shapes. These insertion force data were in accordance with the experimental results.

The diffusion pattern from the simulation of the drug model was comparable with the permeability studies using confocal imaging, with a steep decline in the concentration and diffusion flux over time. This diffusion pattern can be described based on the Fick's first law of diffusion (Equation (4))

$$J = -D \frac{\partial C}{\partial x} \quad (4)$$

where J is the diffusion flux ($\text{mol m}^{-2} \text{s}^{-1}$), D is the drug diffusivity ($\text{m}^2 \text{s}^{-1}$) in skin, and $\frac{\partial C}{\partial x}$ (mol m^{-4}) is the concentration gradient. The rate of decrease in the concentration over time $\frac{\partial C}{\partial t} < 0$ (Equation 2), reduced both $\frac{\partial C}{\partial x}$ and the diffusion flux (J). At equal penetration depths, MB Types 2 and 3 showed the highest diffusion compared to other counterparts. The simulation data showed a 27.3% higher drug concentration near the MB Type 3 tip which was the highest concentration among concentric MBs. At the subcutaneous junction, this increase in concentration was less noticeable (17.7%). Uniformity and homogeneity of concentration are important factors in therapeutic drug delivery,^[54] whereas in the current study introducing eccentricity to MBs Types 4 and 5 led to an uneven distribution of the model drug. Al-Qallaf et al. also previously reported the effects of MN nonsymmetrical features on drug distribution behavior.^[54] Moreover, using fluorescein as a drug model with a molecular weight (MW) of 376.27 gr mol^{-1} can possess similar diffusivity compared to other FDA-approved drugs for transdermal delivery, such as Fentanyl (MW: 336.47 gr mol^{-1}), Oxybutynin (MW: 357.49 gr mol^{-1}), Donepezil (MW: 379.49 gr mol^{-1}) with comparable molecular weights.^[55]

5. Conclusion

Microdevices such as MN and MB arrays are becoming promising means of drug delivery and sampling. In this research, a scalable manufacturing process^[56] was used to fabricate MBs offering single integrated designs, which may reduce the fabrication cost and time while promoting safe and effective insertion into the skin subjects. MBs are a new design of MNs for transdermal drug delivery. Different geometries of MB were designed and fabricated using 2PP. Master MBs were then reproduced using micromolding and embossing processes.

Experiments were conducted to test the penetration capabilities by mounting MBs on prototype impact applicators and placing porcine abdomen cadaver skin on an adjustable stretching mechanism.^[57] MB insertion simulations were carried out on a combination of hyperelastic and linear elastic multilayered skin models for individual MB designs to determine the insertion force and penetration capabilities. All MBs successfully penetrated through the skin SC layer, and a reduction in blade angle for concentric models and introduction of eccentricity to the MB overall shape was found to

increase the penetration. The simulation of model drug diffusion conducted across all MBs indicated a steep decline in the diffusion flux over time for solid MBs. While increasing the tip angle improved the concentration, eccentricity resulted in nonuniform concentration distribution. In terms of penetration, approximately a 45% increase was observed in penetration depth upon increasing the impact velocity by a factor of three. The results demonstrate the functional capabilities and potential for future applications of MBs for transdermal drug delivery.

Supporting Information

Supporting Information is available from the Wiley Online Library or from the author.

Acknowledgements

This work was performed in part at the Queensland node of the Australian National Fabrication Facility, a company established under the National Collaborative Research Infrastructure Strategy to provide nano and microfabrication facilities for Australia's researchers. This research was undertaken in part with the support of resources by the Institute for Advanced Engineering and Space Sciences at the University of Southern Queensland. The authors thank Dr. Fabian Zander for his assistance in measuring the applicator's impact velocity. This research received no specific grant from the public, commercial, or not-for-profit funding agencies.

Open access publishing facilitated by University of Southern Queensland, as part of the Wiley - University of Southern Queensland agreement via the Council of Australian University Librarians.

Conflict of Interest

The authors declare no conflict of interest.

Data Availability Statement

The data that support the findings of this study are available from the corresponding author upon reasonable request.

Keywords

drug delivery, microblade, micromolding, microneedle, two-photon polymerization

Received: May 19, 2022

Revised: June 19, 2022

Published online:

[1] R. S. J. Ingrole, E. Azizoglu, M. Dul, J. C. Birchall, H. S. Gill, M. R. Prausnitz, *Biomaterials* **2021**, 267, 120491.

[2] S. A. Ranamukhaarachchi, B. Stoeber, *Biomed. Microdevices* **2019**, 21, 100.

[3] R. V. Dixon, E. Skaria, W. M. Lau, P. Manning, M. A. Birch-Machin, S. M. Moghimi, K. W. Ng, *Acta Pharm. Sin. B* **2021**, 11, 2344.

[4] E. Larrañeta, R. E. M. Lutton, A. D. Woolfson, R. F. Donnelly, *Mater. Sci. Eng., R* **2016**, 104, 1.

[5] Z. Faraji Rad, P. D. Prewett, G. J. Davies, *Beilstein J. Nanotechnol.* **2021**, 12, 1034.

[6] T. M. Tuan-Mahmood, M. T. McCrudden, B. M. Torrisi, E. McAlister, M. J. Garland, T. R. Singh, R. F. Donnelly, *Eur. J. Pharm. Sci.* **2013**, 50, 623.

[7] S. Indermun, R. Luttge, Y. E. Choonara, P. Kumar, L. C. du Toit, G. Modi, V. Pillay, *J. Controlled Release* **2014**, 185, 130.

[8] Z. Faraji Rad, P. D. Prewett, G. J. Davies, *Microsyst. Nanoeng.* **2021**, 7, 71.

[9] Z. Faraji Rad, P. D. Prewett, G. J. Davies, *Manuf. Lett.* **2021**, 30, 39.

[10] F. K. Aldawood, A. Andar, S. Desai, *Polymers* **2021**, 13, 2815.

[11] J. H. Jung, S. G. Jin, *J. Pharm. Invest.* **2021**, 51, 503.

[12] A. Tucak, M. Sirbubalo, L. Hindija, O. Rahic, J. Hadziabdic, K. Muhamedagic, A. Cekic, E. Vranic, *Micromachines* **2020**, 11, 961.

[13] S. Khan, A. Hasan, F. Attar, M. M. N. Babadaei, H. A. Zeinabad, M. Salehi, M. Alizadeh, M. Hassan, H. Derakhshankhah, M. R. Hamblin, Q. Bai, M. Sharifi, M. Falahati, T. L. M. Ten Hagen, *J. Controlled Release* **2021**, 338, 341.

[14] A. R. Johnson, A. T. Procopio, *3D Print. Med.* **2019**, 5, 2.

[15] V. Ebrahimnejad, P. D. Prewett, G. J. Davies, Z. Faraji Rad, *Adv. Mater. Interfaces* **2022**, 9, 2101856.

[16] J. H. Park, M. G. Allen, M. R. Prausnitz, *J. Controlled Release* **2005**, 104, 51.

[17] J. Zhu, X. Zhou, H. J. Kim, M. Qu, X. Jiang, K. Lee, L. Ren, Q. Wu, C. Wang, X. Zhu, P. Tebon, S. Zhang, J. Lee, N. Ashammakhi, S. Ahadian, M. R. Dokmeci, Z. Gu, W. Sun, A. Khademhosseini, *Small* **2020**, 16, 1905910.

[18] S. Lin, G. Quan, A. Hou, P. Yang, T. Peng, Y. Gu, W. Qin, R. Liu, X. Ma, X. Pan, H. Liu, L. Wang, C. Wu, *J. Controlled Release* **2019**, 306, 69.

[19] S. Dottermusch, D. Busko, M. Langenhorst, U. W. Paetzold, B. S. Richards, *Opt. Lett.* **2019**, 44, 29.

[20] M. J. Uddin, N. Scoutaris, S. N. Economidou, C. Giraud, B. Z. Chowdhry, R. F. Donnelly, D. Douroumis, *Mater. Sci. Eng., C* **2020**, 107, 110248.

[21] S. D. Gittard, B. Chen, H. Xu, A. Ovsianikov, B. N. Chichkov, N. A. Monteiro-Riviere, R. J. Narayan, *J. Adhes. Sci. Technol.* **2013**, 27, 227.

[22] M. L. Crichton, C. Archer-Jones, S. Meliga, G. Edwards, D. Martin, H. Huang, M. A. F. Kendall, *Acta Biomater.* **2016**, 36, 186.

[23] E. Z. Loizidou, N. T. Inoue, J. Ashton-Barnett, D. A. Barrow, C. J. Allender, *Eur. J. Pharm. Biopharm.* **2016**, 107, 1.

[24] S. P. Davis, B. J. Landis, Z. H. Adams, M. G. Allen, M. R. Prausnitz, *J. Biomech.* **2004**, 37, 1155.

[25] H. S. Gill, M. R. Prausnitz, *J. Controlled Release* **2007**, 117, 227.

[26] G. Ma, C. Wu, *J. Controlled Release* **2017**, 251, 11.

[27] P. P. Samant, M. R. Prausnitz, *Proc. Natl. Acad. Sci. USA* **2018**, 115, 4583.

[28] M. Sausse Lhernould, C. Gobillon, P. Lambert, *ONdrugDelivery* **2013**, 40, 29.

[29] P. Khanna, K. Luongo, J. A. Strom, S. Bhansali, *J. Micromech. Microeng.* **2010**, 20, 045011.

[30] M. Leone, B. H. van Oorschot, M. R. Nejadnik, A. Bocchino, M. Rosato, G. Kersten, C. O'Mahony, J. Bouwstra, K. van der Maaden, *Pharmaceutics* **2018**, 10, 211.

[31] H. B. Song, K. J. Lee, I. H. Seo, J. Y. Lee, S. M. Lee, J. H. Kim, J. H. Kim, W. Ryu, *J. Controlled Release* **2015**, 209, 272.

[32] O. Olatunji, D. B. Das, M. J. Garland, L. Belaid, R. F. Donnelly, *J. Pharm. Sci.* **2013**, 102, 1209.

[33] Z. Faraji Rad, R. E. Nordon, G. J. Davies, C. J. Anthony, P. Prewett, (NewSouth Innovations Pty Ltd, University of Birmingham), *US Patent 10850082*, **2020**.

[34] S. A. Ranamukhaarachchi, S. Lehnert, S. L. Ranamukhaarachchi, L. Sprenger, T. Schneider, I. Mansoor, K. Rai, U. O. Hafeli, B. Stoeber, *Sci. Rep.* **2016**, 6, 32074.

- [35] H. V. Tran, F. Charleux, M. Rachik, A. Ehrlicher, M. C. Ho Ba Tho, *Comput. Methods Biomech. Biomed. Eng.* **2007**, *10*, 401.
- [36] R. F. Donnelly, T. R. Singh, M. M. Tunney, D. I. Morrow, P. A. McCarron, C. O'Mahony, A. D. Woolfson, *Pharm. Res.* **2009**, *26*, 2513.
- [37] P. Anantaworasakul, W. Chaiyana, B. B. Michniak-Kohn, W. Rungseewijitprapa, C. Ampasavate, *Pharmaceutics* **2020**, *12*, 463.
- [38] Z. Faraji Rad, R. E. Nordon, C. J. Anthony, L. Bilston, P. D. Prewett, J. Y. Arns, C. H. Arns, L. Zhang, G. J. Davies, *Microsyst. Nanoeng.* **2017**, *3*, 17034.
- [39] K. Levi, R. J. Weber, J. Q. Do, R. H. Dauskardt, *Int. J. Cosmet. Sci.* **2010**, *32*, 276.
- [40] W. Shu, H. Heimark, N. Bertollo, D. J. Tobin, E. D. O'Cearbhaill, A. N. Annaidh, *Acta Biomater.* **2021**, *135*, 403.
- [41] F. H. Silver, G. P. Seehra, J. W. Freeman, D. DeVore, *J. Appl. Polym. Sci.* **2002**, *86*, 1978.
- [42] P. Shewmon, *Diffusion in Solids*, 2 ed., Springer, Cham, Switzerland **2016**.
- [43] A. Göpferich, G. Lee, *Int. J. Pharm.* **1991**, *71*, 245.
- [44] M. P. di Cagno, F. Clarelli, J. Våbenø, C. Lesley, S. D. Rahman, J. Cauzzo, E. Franceschinis, N. Realdon, P. C. Stein, *Mol. Pharmaceutics* **2018**, *15*, 1488.
- [45] M. C. Chen, M. H. Ling, K. Y. Lai, E. Pramudityo, *Biomacromolecules* **2012**, *13*, 4022.
- [46] A. S. Cordeiro, I. A. Tekko, M. H. Jomaa, L. Vora, E. McAlister, F. Volpe-Zanutto, M. Nethery, P. T. Baine, N. Mitchell, D. W. McNeill, R. F. Donnelly, *Pharm. Res.* **2020**, *37*, 174.
- [47] J. W. Lee, J. H. Park, M. R. Prausnitz, *Biomaterials* **2008**, *29*, 2113.
- [48] M. L. Crichton, A. Ansaldo, X. Chen, T. W. Prow, G. J. Fernando, M. A. Kendall, *Biomaterials* **2010**, *31*, 4562.
- [49] T. M. Blicharz, P. Gong, B. M. Bunner, L. L. Chu, K. M. Leonard, J. A. Wakefield, R. E. Williams, M. Dadgar, C. A. Tagliabue, R. El Khaja, S. L. Marlin, R. Haghgoeie, S. P. Davis, D. E. Chickering, H. Bernstein, *Nat. Biomed. Eng.* **2018**, *2*, 151.
- [50] S. C. Meliga, J. W. Coffey, M. L. Crichton, C. Flaim, M. Veidt, M. A. F. Kendall, *Acta Biomater.* **2017**, *48*, 341.
- [51] F. J. Verbaan, S. M. Bal, D. J. van den Berg, W. H. Groenink, H. Verpoorten, R. Luttmge, J. A. Bouwstra, *J. Controlled Release* **2007**, *117*, 238.
- [52] F. J. Verbaan, S. M. Bal, D. J. van den Berg, J. A. Dijkstra, M. van Hecke, H. Verpoorten, A. van den Berg, R. Luttmge, J. A. Bouwstra, *J. Controlled Release* **2008**, *128*, 80.
- [53] K. van der Maaden, E. Sekerdag, W. Jiskoot, J. Bouwstra, *AAPS J.* **2014**, *16*, 681.
- [54] B. Al-Qallaf, D. B. Das, A. Davidson, *Asia-Pac. J. Chem. Eng.* **2009**, *4*, 845.
- [55] D. S. Wishart, Y. D. Feunang, A. C. Guo, E. J. Lo, A. Marcu, J. R. Grant, T. Sajed, D. Johnson, C. Li, Z. Sayeeda, N. Assempour, I. Iynkkaran, Y. Liu, A. Maciejewski, N. Gale, A. Wilson, L. Chin, R. Cummings, D. Le, A. Pon, C. Knox, M. Wilson, *Nucleic Acids Res.* **2018**, *46*, D1074.
- [56] Z. Faraji Rad, P. D. Prewett, G. J. Davies, *Addit. Manuf.* **2022**, *56*, 102953.
- [57] V. Ebrahiminejad, Z. Faraji Rad, P. D. Prewett, G. J. Davies, *Beilstein J. Nanotechnol.* **2022**, *13*, 629.

4.2 Chapter Summary

This chapter introduced the novel integrated MB devices with open channels and reservoirs with potential drug delivery and diagnostics applications. Due to the singular integrated design, these microdevices can be an alternative to MN arrays, which are costly, time-consuming, and have limited penetration capability due to highly dense projections. Five different MBs were replicated on a single substrate using modified printing codes of the TPP process. The master MBs were used to make the PDMS moulds and further used for soft embossing Zeonor 1060R thermoplastic replicas. SEM imaging from the replicated samples indicated ~ 5.63 % overall shrinkage. Mechanical compression tests and theoretical investigation showed a direct relationship between increasing initial stiffness and failure points with the geometrical aspects such as increasing MB blade angle and reducing eccentricity. A computer simulation was used to study the mechanics of MB insertion and penetration and the diffusion kinetics and concentrations of drug-coated MBs with different geometries. The FEA results from the 3D planner symmetrical analysis of MB insertions into the multilayered hyperelastic skin model were coupled with the results from the mechanical compression test. The ratios of failure forces to MB peak insertion forces were then determined to evaluate the SM values for different MB types.

The FEA results and confocal imaging from the skin insertion tests confirmed that reducing blade angle was critical in reducing the insertion force and improving the penetration. Similarly, increasing eccentricity resulted in a non-uniform drug distribution. This indicated the need for an optimisation method to specify the range of MB angles, ensuring low insertion force and maximum penetration while maintaining sufficient mechanical integrity. The outcome indicated that low cost and time-effective MB replication combined with the sufficient

mechanical strength of thermoplastic MBs ($SM > 1$) make MB designs a potential mass scalable alternative for conventional MN arrays.

CHAPTER 5: PAPER 4 - Effects of Low-Frequency Vibration and Skin Strains on Insertion Mechanics and Drug Diffusion of PVA/PVP Dissolving MNs

5.1 Introduction

Despite the promising applications of MNs for drug delivery and diagnostics, maintaining insertion safety, controlled drug release, and effective penetration remain a challenge. This study evaluated the effects of external stimulants, such as skin straining and vibrations, on MN insertion and extraction. A multifeatured impact applicator capable of adjustable impact speed, MN vibrations, and skin strain was designed and manufactured for the skin insertion experiments. The PVA/PVP DMNP replicas were fabricated using PDMS moulds from two consecutive masters manufactured through TPP and soft embossing techniques. The replicated DMNPs were mechanically tested using compression and lateral bending tests to evaluate the SM value. The final skin insertion tests were conducted on porcine abdominal skin using the PVA/PVP DMNPs encapsulated with FSS as the model drug. The study aimed to investigate the kinetics of drug diffusion and concentration of FSS using two modes of vibrations, including ERM and LRA, at low-frequency ranges. The study also developed a novel FEA procedure to model the MN insertion mechanics into the multi-layered hyperelastic skin model under external effects of vibrations and skin strains.

Influence of Low-Frequency Vibration and Skin Strain on Insertion Mechanics and Drug Diffusion of PVA/PVP Dissolving Microneedles

Vahid Ebrahimejad¹, Atefeh Malek-khatabi², Zahra Faraji Rad*¹

¹ School of Engineering
University of Southern Queensland
Springfield, QLD 4300, Australia

² Department of Pharmaceutical Biomaterials and Medical Biomaterials Research Centre
Faculty of Pharmacy
Tehran University of Medical Sciences
Tehran 1417614411, Iran
Email: zahra.farajirad@usq.edu.au

Keywords: Dissolving microneedles, Drug delivery, Low-frequency vibration, Skin strain, the Insertion force

Abstract

Microneedles (MNs) offer a promising solution for increasing the effectiveness of transdermal drug delivery (TDD) and diagnostics. However, challenges such as large-scale manufacturing, partial MN penetration, and uncontrolled drug delivery limit the effectiveness of the technology. To overcome these challenges, the current research examines the effects of skin strain and vibration on MN insertion and drug delivery. A novel multifeatured impact applicator has been developed for improving skin insertion that features a combination of skin stretching, eccentric rotating mass (ERM), and linear resonant actuator (LRA) micro-vibration capabilities. In addition, a scalable replication method for dissolving microneedle patches (DMNPs) has been developed using two-photon polymerisation (TPP) and soft embossing processes. The DMNPs are used to evaluate the diffusion and concentration of a model drug, fluorescein sodium salt (FSS), when applied using ERM and LRA micro-vibration at different frequencies. A new computer simulation method is also presented to model the MN insertion into the multi-layered

hyperelastic skin model, incorporating skin strain and vibrational effects. The results from the experiments and simulations indicate that applying skin strain and vibration decreases the force required for MN insertion and extraction from the skin. Similarly, increasing the ERM and LRA vibrational frequency enhances the dissolution and diffusion depth of the model drug in the skin. This suggests that applying vibration and stretching to the skin are effective and promising methods of TDD via DMNPs, which can enhance the drug permeability and effectiveness of MN devices.

1. Introduction

TDD through skin layers is among the safest routes of drug administration. Compared to the oral route of administration, TDDs eliminate the first-pass metabolism and harsh environment of the gastrointestinal tract. It can protect the vital body organs, especially the liver, against drug side effects and conserves drug dosage forms from the acidic environment of the stomach.^[1] Despite these advantages, drug administration through the skin is challenging due to the skin *stratum corneum* (SC) barrier.^[2] Researchers have tried to overcome this barrier by improving pharmaceutical formulations. Among the third generation of TDDs, MN development is being progressed by clinical trials for the administration of small and macromolecule drug agents with great efficiency.^[3] TDD via non-invasive MN devices is a promising technique that offers several advantages, such as simplicity, reducing sharp and bio-hazardous wastes, and the potential for self-administration.^[4] Micro-pores created by MNs in the skin facilitate drug and vaccine delivery.^[5] In response to pandemics such as Covid 19, MN patches can enable vaccination through the sustainable release of highly concentrated vaccines to a localized skin area.^[6-8] MNs also have applications in point-of-care diagnostics, such as sampling ISF for biomarker detection.

MNs are manufactured using various techniques, including laser cutting, laser ablation, lithography, dry/wet etching, reactive ion etching, deep reactive ion etching, micro moulding, injection moulding, hot and soft embossing, additive manufacturing via 3D printing, and TPP.^[9] Each technique is suitable for fabricating specific materials and has different fabrication times, production costs, accuracy, precision, robustness, and limitations.^[10] Laser cutting and ablation methods are generally used to manufacture solid metallic MNs. These methods are time-effective; however, they are associated with high manufacturing costs, the risk of forming cracks, and fatigue due to the thermal effects, and thus are unsuitable for mass production.^[10,11] Lithography requires subsequent dry/wet etching processes to form the final MN shape. Despite the high popularity of the method, it is a multi-step process, which results in an extended manufacturing time.^[12] Additive manufacturing (AM) by conventional 3D printing of MN prototypes is a cost-effective method with high throughput.^[2] Conventional 3D printing offers low accuracy and resolution of the printed parts.^[10] AM via the TPP technique is an alternative method for manufacturing complex 3D geometries with high precision and sub-micron resolution; however, TPP is still a slow process, thus mainly used for prototyping.^[13] Micromoulding is used to replicate MNs from a master and a polydimethylsiloxane (PDMS) negative mould. Micromoulding is a cost-effective approach for replicating polymer MNs such as poly (vinyl alcohol) (PVA), poly(vinylpyrrolidone) (PVP),^[14] or thermoplastics.^[13,15] Techniques such as injection moulding and hot and soft embossing are also promising low-cost methods for MN mass-scale productions.^[10]

MNs are categorized into solid, coated, hollow, hydrogels, and dissolving types designed to serve specific therapeutic purposes. These microdevices are fabricated using various materials, including metal, silicon, polymers, silica glass, and ceramics.^[16] Solid MN patches are generally manufactured with metals, silicon, and recently thermoplastic cyclic olefin polymer (COP) polymers,^[17] which possess high mechanical strength. Uncoated solid MNs create micro

pathways to enhance skin permeability before the topical application of a drug.^[18,19] Drug-coated solid MNs can deliver a small amount of the target drug with a rapid decay in drug concentration over time.^[20] The amount of drug dissolution using coated MN patches depends on coating thickness and MN size.^[21] Solid and coated MNs are frequently studied for drug delivery; however, they have limited drug transport through the skin due to their structure and the amount of drug that can be loaded.^[22] Hollow MNs are made from silicon, metal, glass, and polymers, which allow for the transfer of a more significant amount of fluid formulation by diffusion using pressure, capillary, or electrical-driven forces.^[19,23] The MN bore size and release pressure define the kinetics of drug transport through hollow MNs.^[18,24] Hollow MNs are capable of enhanced and precise drug delivery but still require costly and complicated manufacturing setups.^[25]

Hydrogel-forming MNs are used for both drug delivery and biofluid sampling. The MNs will swell upon insertion into the skin due to the hydrophilic nature of the hydrogels.^[13] Hydrogel-forming MNs are used for TDD of drugs by loading drugs into their polymeric structure during manufacturing or into a separate reservoir that is connected to the MNs for delivery.^[26,27] Polymers such as polysaccharides are biocompatible due to similarities with extracellular matrix components and can be easily removed in the kidney based on its size and molecular weight. Derivatives of cellulose, chitosan, and hyaluronic acids are both biocompatible and biodegradable, making them a good candidate (Markovsky et al. 2012; Shelke et al. 2014). Dissolving MNs are made from biodegradable polymer matrix or sugar-containing active substances, which enable sustained dissolution of drug cargo over time without leaving residues.^[2] This delivery method encapsulates drugs inside the polymeric matrix of DMNPs to facilitate sustained delivery of a higher dose of pharmaceuticals.^[28] The kinetic and dissolution rates of therapeutic payloads depend on the polymeric composition and fabrication process. Drug release can be through water-soluble polymers such as PVP, PVA,

carboxymethyl cellulose (CMC), dextran, or via biodegradable compositions including poly(lactide-co-glycolide) (PLGA), poly (lactic acid), chitosan, or poly (glycolic acid).^[19] However, partial penetration of MNs due to skin elasticity results in low efficacy of drug delivery.^[29]

To achieve efficient TDD, MNs must penetrate through the SC barrier, the outermost layer of skin.^[30] SC consists of elongated dead corneocytes joint by interstitial lipid matrix.^[31] SC is the most compact skin layer in dry conditions.^[32] MN partial penetration is mainly associated with skin nonlinear viscoelastic properties, irregular surfaces, and the tendency to fold around MN projections.^[33-35] These conditions may cause early failures, such as MN buckling and bending.^[16] To overcome these challenges, several studies evaluated the parameters that enhance the penetration efficiency and safety margin (SM) of MNs. SM is defined as the ratio of MN failure force to MN insertion force (F_{ins}) (the maximum force reached before SC rupture).^[17] To reduce the F_{ins} and improve the SM,^[36,37] the geometrical parameters of the MNs are important. By optimizing the geometrical parameters, the F_{ins} can be reduced, which in turn increases the SM. For example, increasing MN interspacing,^[38] reducing tip diameter,^[37,39] optimizing MN width and tip angle affects the F_{ins} .^[39] In addition, using auxiliary tools such as applicators, applying vibration, and increasing insertion velocity with an applicator have been shown to reduce the insertion force and facilitate penetration.^[37,38] Yang and Zahn studied MN insertion on excised animal skin to evaluate the effects of vibration on the MNs insertion using an unspecified frequency. The results demonstrated a > 70 % reduction in F_{ins} from ~ 0.28 to 0.08 N.^[40] The study did not indicate the value of frequencies applied nor the amount in which the vibration influenced various stages of MN insertion, such as the moment of insertion and the extraction phase.

In another study, Al Qallaf et al. indicated that specific MN shapes, such as cylindrical/rectangular cuboids, along with the number of projections within a patch, can

influence the insulin concentration within the blood samples (ng mL^{-1}). This study showed that MN interspacing, MN thickness, and penetration depth had less significance on insulin delivery.^[41] To improve drug transport through the skin, external factors such as iontophoresis can be used, which involves generating an electric potential gradient across the skin.^[18] Niamlang and Sirivat reported that using electric fields from 0 to 0.1 V improved the drug diffusion coefficient ($\text{cm}^2 \text{s}^{-1}$), which peaked at 0.1 V, demonstrating an increase of 357.8%.^[42] However, iontophoresis alone cannot transport the macromolecules through the SC barrier, indicating the need for combining the technique with MN devices to improve the permeability.^[25] Enhancing permeability can be achieved via sonophoresis, which involves ultrasonic vibration ($> 20 \text{ kHz}$). This method induces thermal effects on the skin subjects and requires sophisticated instrumentation.^[43] Vibration and agitation speeds are also reported to enhance drug dissolution and delivery.^[44-46] Seeger et al. analysed and tested the early studies conducted by Beyer and Smith on the dissolution rate of tolbutamide (used for the treatment of non-insulin-dependent diabetes mellitus) [47] and the Embil and Torosian studies on enteric-coated aspirin^[48] and confirmed the strong effects of increasing vibration on the drug dissolution time at a low agitation speed of 50 rpm.^[46] The release profiles indicated a strong relationship between an agitation speed of 50 rpm and dissolution, which enhanced the drug dissolution rate upon increasing vibration levels.^[46] Liu et al. studied the effect of vibration at 3200, 4800, and 6400 rpm on drug dissolution. They concluded that an increase of low-frequency vibrations from 3200 to 6400 rpm indicated a \sim fivefold increase in tetramethylpyrazine hydrochloride (TMPH) permeation over time, a drug used for the treatment of cardiovascular and cerebrovascular diseases.^[45] Drug dissolution strongly depends on drug properties, formulation, dissolution method,^[46] and application technique. Thus, to better understand drug dissolution mechanics, studies need to investigate the drugs with different MWs and various methods of excitations, such as low-frequency LRA and ERM.

The current study investigates the effects of external factors, such as variable skin strain and vibration excitations, on MN insertion mechanics using skin models. The experiments on the skin model provide insight into the effects of strain and vibrations on MN insertion and extraction mechanics. Moreover, the dissolution kinetics and concentration levels of the model drug are determined and compared for low-frequency vibrations using both ERM and LRA modes. The study also presents a cost-effective, fast, and mass-scalable method for manufacturing highly accurate DMNPs replicated using a PVA/PVP polymeric formulation. The proposed replication process involves using TPP to print primary masters, followed by using a soft embossing technique to create the secondary masters. The new approach overcomes the challenge associated with the slow TPP process and enables simultaneous replication of highly accurate DMNP replicas in a rapid and cleanroom-free process. In addition, a finite element analysis (FEA) for studying MN insertion mechanics into the multi-layered hyperelastic skin model is introduced under the external effects of vibrations and skin strain. Despite recent developments in the computer simulation of MN insertion into multi-layered hyperelastic skin models, the impact of external simulants, such as vibration and skin strains during the MN insertion, are not investigated.

2. Experimental Section

2.1. Master MN Array Design and Fabrication

Consistent with our previous studies, 3D laser lithography using the Nanoscribe Photonic Professional GT 3D printer (Nanoscribe GmbH, Karlsruhe, Germany) was employed to fabricate the master mould.^[15,20,49] In summary, the 3D designs of a 9×9 master MN array and a single master MN (single MNs were fabricated to be used for mechanical compression and bending tests only) were created using SolidWorks (Dassault Systems SolidWorks Corporation, Concord, NH, USA) with an overall height of 1100 μm, 75 μm base fillets, and 500 μm interspacing for the MN array. The STL codes from SolidWorks were imported into

the DeScribe (Nanoscribe GmbH, Karlsruhe, Germany) software to specify print settings tailored to the design. The models were printed separately with 100 mW laser power, a scanning speed of 100 mm s⁻¹, and shell and triangular scaffolds with 20 µm wall spacing. Parameters such as 2 µm slicing distance, 4 base slice counts, null shear angle (0°), and 0.6 interface position were used to reduce print time and sample delamination from the substrate. The output GWL file, which stored the printing specifications, was further imported into NanoWrite software (NanoScribe GmbH, Karlsruhe, Germany) linked to the NanoScribe system for printing.

The TPP system incorporates a pulsed erbium-doped femtosecond fibre laser source with a Centre wavelength of 780 nm for exposing the photoresist. Based on the two-photon absorption theory, when the combined energy of two photons surpasses the absorption energy threshold of the photoresist, the nonlinear response occurs at the focused point, which enables the polymerisation of high-resolution structures.^[50] Initially, a drop of negative-tone IP-S photoresist (Nanoscribe GmbH, Karlsruhe, Germany) drop cast onto the indium tin oxide (ITO) conductive side of a glass substrate and inserted into the NanoScribe system. The objective lens with × 25 magnification and NA of 0.8 focused the laser beam into the photoresist. MN structures were then written in galvo scan mode in *X* and *Y* directions and piezo offsetting mode in the *Z* direction. Following the print, the samples were further developed for 10 minutes in propylene glycol monomethyl ether acetate (PGMEA) solution, then rinsed for 2 minutes in isopropyl alcohol (IPA), and finally air-dried.

2.2. Casting Negative PDMS Mould for Replication of Thermoplastic MN Arrays

Polydimethylsiloxane (PDMS) (SYLGARD 184 Silicone Elastomer Kit, Dow Corning, Midland, MI, USA) was used for creating a negative mould of the master MN array. A 1:10 solution of curing agent/base was initially mixed and then degassed in a planetary mixer for air bubble removal. PDMS solution was then poured on the MN array printed via TPP in a petri

dish and cured for 2 hr inside the oven at 80 °C. Finally, the soft negative PDMS mould was peeled off from the MN master for replication. A similar process was conducted to create a negative PDMD mould of the single MN.

2.3. Fabrication of Secondary Master MN Arrays using Thermoplastics

The PDMS negative mould of the master MN array was placed between 40 mm diameter rheometer plates (TA Instruments, New Castle, USA). A total of four pellets (cyclo-olefin polymer, Zeonor 1060R) were placed on the PDMS cavities, and the chamber temperature was increased to 163 °C, which is 63 °C above the thermoplastic glass transition temperature ($T_g=100$ °C). Keeping the lower plate fixed, the upper plate was lowered as a function of time to press the melted thermoplastic pellets into the PDMS cavities while limiting the axial force to 21 ± 3 N. To control the axial force and prevent damage to the PDMS moulds, upper plate downward displacement was reduced over time based on a nonlinear model from 100 μm per interval to 25 μm for 1 hr until the upper plate reached 200 μm above the PDMS surface.^[49] The chamber temperature was then reduced to 10 °C for 15 minutes to allow for thermoplastic solidification. Upon solidification, replicas were peeled off the soft PDMS mould (**Figure 1a**). The process was repeated eight times to create eight thermoplastic MN arrays to be used as the secondary master MN arrays.

2.4. Replication of PVA/PVP DMNPs

The eight thermoplastic MN masters were used as secondary masters for fabricating eight negative PDMS moulds for PVA/PVP DMNPs replication. Thus, the thermoplastic MNs underwent a similar process described in section 2.2 to make the PDMS negative moulds. A PDMS ring was attached to each mould using PDMS-to-PDMS bonding by oxygen plasma (Pie Scientific, California, USA). The PDMS moulds were then cured at 80 °C for 15 minutes before cutting them to fit into the 50 mL centrifuge tube (Figure 1b). The rings surrounding the PDMS cavities acted as liquid solution containers for the centrifugation process.

The PVA, PVP, and FSS were purchased from Sigma-Aldrich (Sigma-Aldrich Corp., St. Louis, MO, USA) to prepare the model drug solution. PVA 30 kDa (15 % w/v) was slowly added to 20 mL of D.I water, stirred at 750 rpm for 1 hr at 60 °C, and placed inside an ultrasonic bath for 2 hr for further dissolution. PVP 40 kDa (50 % w/v) was then gently added to the solution and stirred until dissolved. A separate solution of FSS (0.4 % w/v) in 2 mL ethanol 70 % was then added to the PVA/PVP solution and stirred for 30 minutes at 60 °C until dissolved.

To create DMNPs, 50 µL of PVA/PVP/FSS solution was placed on each PDMS mould. The moulds were then carefully placed inside 50 mL centrifuge tubes. During each replication process, eight sample tubes were centrifuged simultaneously using Allegra X-30 swinging bucket centrifuge (Beckman Coulter, Brea, USA) at 4000 rpm for 30 minutes. The moulds containing the solutions were then kept inside a laboratory oven for 2 hr to initiate solidification. In the next step, 100 µL of PVA/PVP solution without the model drug was poured on each partially dried mould and centrifuged at 4000 rpm for 20 minutes. The excess solutions were then removed, and the PDMS moulds were kept inside an incubator at 37 °C for another 72 hr. Once MN patches were peeled off from the moulds, they were refrigerated until further use (Figure 1c). Similar procedures were performed to replicate the single PVA/PVP MNs for compression and bending tests.

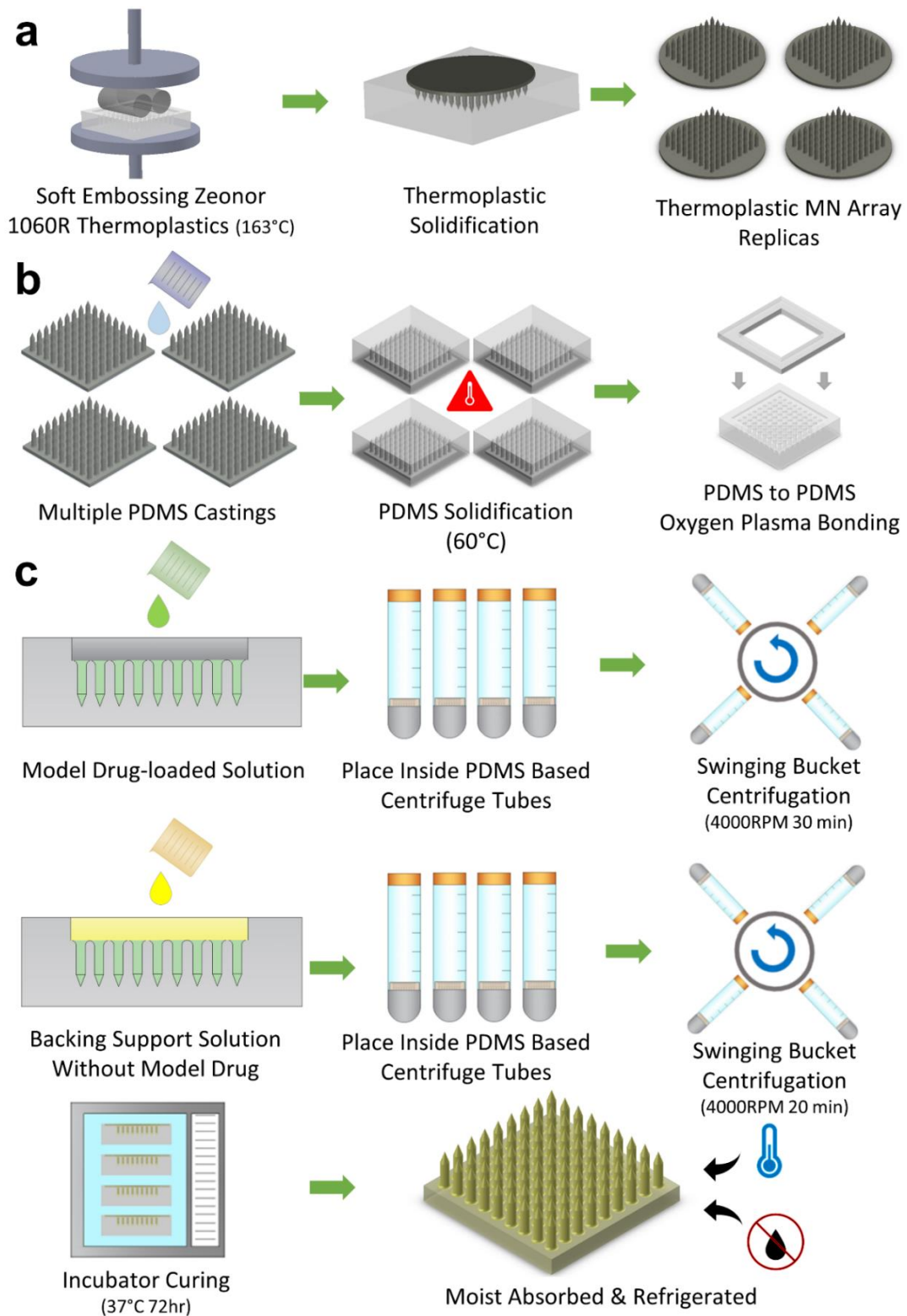


Figure 1: Replication process of PVA/PVP DMNPs (a) multiple replications of thermoplastic MN patches using the soft embossing technique, (b) creating multiple PDMS negative moulds from the replicated thermoplastic MNs, (c) replication of PVA/PVP DMNPs via PDMS negative moulds and centrifugation.

2.5. Mechanical Strength Testing of MNs

The mechanical strength of PVA/PVP DMNPs was investigated on single PVA/PVP MNs using axial compression and lateral bending tests. Both tests were conducted using the TRIOS package linked with the TA hybrid rheometer previously used for soft embossing (section 2.3). During the axial compression test, the PVA/PVP MN was attached to the lower disk with double-sided tape while the upper disk of the rheometer was lowered to measure the force of fracture. The bending test was performed by attaching the PVA/PVP MN to a 90° custom-made metal stub using double-sided tape. A premade metallic block was attached to the upper disk of the rheometer and lowered during the test. The metal block provided uniform contact with the PVA/PVP MN tip to apply the lateral force. During the two tests, force and displacement data were recorded to determine the mechanical behaviour and failure points. Data were then plotted by MATLAB (Natick, MA, USA) software to be compared against the theoretical models.

2.6. Scanning Electron Microscopy

The morphology and dimensions of PVA/PVP DMNPs and mechanically tested MNs were measured using a scanning electron microscope (SEM, JOEL JSM-7001F). Samples were coated with a 10 nm layer of platinum using JOEL Desktop Sputterer. To measure the length and base diameter of DMNPs, a 90° angled metal stub was used to hold the samples. The secondary electron detector with an accelerating voltage of 2 kV in high vacuum mode was used for mechanically tested MNs. However, the accelerating voltage was increased to 10 kV to enhance the field depth for imaging the PVA/PVP DMNPs.

2.7. Manufacturing Featured Impact Applicator

The novel spring-loaded applicator was designed in SolidWorks software (Dassault Systems SolidWorks Corporation, Concord, NH, USA). The model was then printed using a Teirtime X5 3D printer (Teirtime Corporation, Milpitas, CA, USA) from polylactic acid (PLA) filament.

This applicator is the advanced version of the impact applicator used in our previous studies.^[20,49] The new design can adjust impact velocity, enabling two regulatable ERM/LRA modes of vibration, and is equipped with a skin stretching mechanism.

The impact velocity control mechanism has a grooved plunger and a top screw for velocity regulations, enabling velocities of 1.5, 3, and 4.5 m s⁻¹. The plunger is fixed by the locking mechanism and released by pressing the push button (**Figure 2a**). While the grooved plunger enables exact impact velocities of 1.5, 3, and 4.5 m s⁻¹, minute adjustments using the top screw can give a broader range of impact velocities ranging from 1.5 to 5.5 m s⁻¹. A high-speed camera and theoretical models were used to measure the impact velocity of the current prototype, as described in our previous study.^[20]

The applicator's skin stretching mechanism is incorporated with stretching arms equipped with torsion springs for direct skin extension and compression springs for the applicator settlement on the skin surface through height adjustments (Figure 2b). To apply two modes of vibration, LRA and ERM micro-vibration devices with ~ 50 - 250 Hz frequency range were purchased from Precision Microdrives (London, UK) and inserted into the slots in the plunger plate where the DMNPs attach. A custom-made electronic circuit was built to switch and regulate the micro driver frequencies. The circuit contained a 5 k Ω potentiometer, a 510 Ω resistor, and an NPN 2N2222a transistor with an ON/OFF switch to regulate the LRA/ERM vibrations. This circuit is powered by a 3.7 V polymer lithium-ion battery (Ecocell, Castle Hill, New South Wales, Australia) equipped with MicroUSB Lilon/LiPoly charger jack (Adafruit Industries, New York City, New York, USA). The range of LRA and ERM frequencies was measured and recorded using digital multimeters in a series of current and voltage tests against the manufacturer performance graphs (Figure 2c).

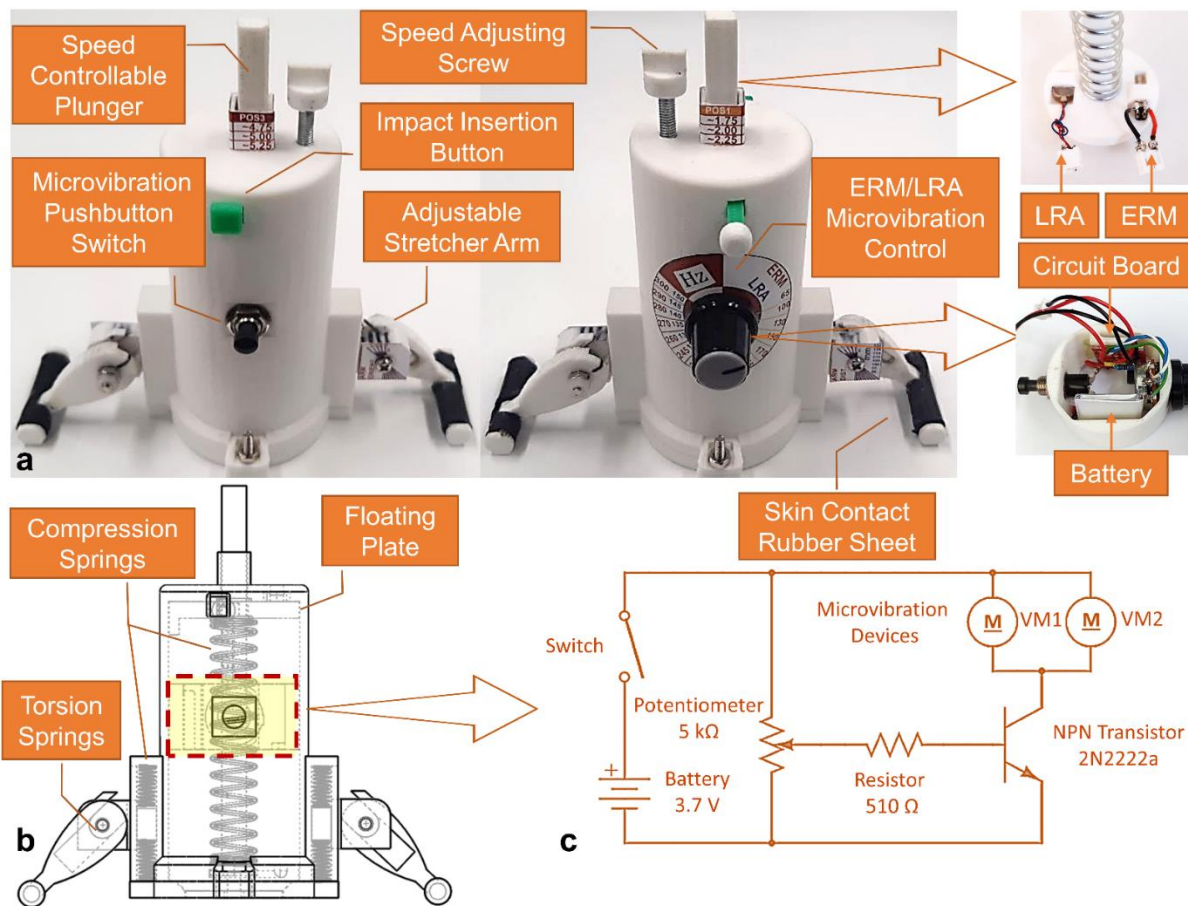


Figure 2: The impact applicator for insertion of MNs into the skin. The 3D printed prototype features regulatable impact velocity, stretching arm mechanism, and ERM/LRA vibration systems. (a) The spring-loaded impact velocity can be regulated via pre-set velocities (1.5, 3, 4.5 m s^{-1}) on the grooved plunger or minute adjustments to the floating plate using the top screw. The skin insertion is triggered using the locking mechanism by pressing the push button. Skin stretching can be performed using the extendable side arms. Two pairs of compression springs enable the applicator settlement on the skin surface through height adjustment before the torsion springs can directly initiate the skin extension. (b) A cross-sectional view of the applicator showing compression and torsion springs and floating plate. (c) To regulate the ERM/LRA vibrations, an electronic circuit containing a 3.7 V polymer lithium-ion battery, 5 k Ω potentiometer, 510 Ω resistor, 2N2222a NPN transistor, and MicroUSB charger port with ON/OFF switch was built to control the vibration frequency.

2.8. Evaluation of Strain and Vibration on Mechanics of MN Insertion and Extraction

MN insertion and extraction mechanics were studied to determine the effects of strain and vibration on the SM. As a skin model, a PDMS sample with 4 ± 0.1 mm thickness was placed on the 3D printed PLA platform and then fixed by the skin stretching mechanism. To prevent the early contact of the PVA/PVP DMNP base with the skin model, an alternative 4 mm BD Ultra-Fine™ PEN Needles (Franklin Lakes, New Jersey, USA) for insulin injection was used. In the previous study by Park et al., the interface area of polymeric MNs inserted into the human cadaver skin showed the most influence on the insertion mechanics compared to other geometrical features.^[51] Thus, PEN needles with a similar base diameter (230 μm) and tip size (1.6 μm) were assumed to be the suitable replacement for this particular study for the PVA/PVP DMNPs.^[49] The PEN needles were attached to the rheometer upper plate using double-sided tapes. While force-displacement data were recorded, the needle was inserted and extracted by 4 mm into the skin model. As shown in **Figure 3a**, insertion tests were conducted with various strains of 0 to 0.2 and vibration ranges of 0, 50, 150, and 250 Hz.

2.9. Skin Insertion and Diffusion Study of DMNPs

The penetration efficiency, drug diffusion, and concentration of the model drug encapsulated in DMNPs were studied using porcine abdominal skin. These studies were performed with experimental procedures approval obtained from the University of Southern Queensland (USQ) and the University of Queensland (UQ) animal ethics (Ethics Number: 20EXE005) and biosafety committees (Biosafety Number: 21BIOS003). Porcine cadaver skin was shaved and sliced into 3 ± 0.1 mm sizes using scalpel blades, and the fat layer was removed from underneath the skin. The skin tissue was kept at -20 °C and naturally thawed before insertion tests. During the tests, a previously reported stretching mechanism capable of accurately adjusting skin strain was used.^[20,49] The porcine skins were stretched by ~ 5 % from the undeformed state to mimic the skin *in vivo* condition.^[52] A total of 32 DMNPs were tested on

the porcine skin. For each test, a DMNP was attached to the applicator's plunger using double-sided tape and then inserted into the skin at 3 m s^{-1} using 0, 50, 100, 150, and 200 Hz ($n = 4$) for LRA and 0, 50, 150, and 250 Hz ($n = 4$) for ERM-induced vibrations for four minutes (Figure 3b). The current frequency range aligns with a previous study conducted by Liu et al. at 3200, 4800, and 6400 rpm (~ 53.3 to ~ 106.7 Hz).^[45] Through a series of potentiometer orientations, the input voltage and current electronic circuit were measured using high-precision multi-meters to estimate the frequency based on the micromotor's performance curves. Due to various achievable speeds on Precision Microdrives performance curves and limitations in settings for lower frequencies, not all frequencies were aligned. Duration of insertion is based on observation of the time taken for the FSS model drug to thoroughly dissolve inside the skin when 9×9 DMNPs are applied at 250 Hz frequency and 3 m s^{-1} impact speed. Penetration and diffusion of the FSS drug model were then examined after 20 minutes with a confocal microscope (CLSM, Zeiss LSM710, Germany) using Z-stack and tile scan techniques with run times of ~ 20 minutes.

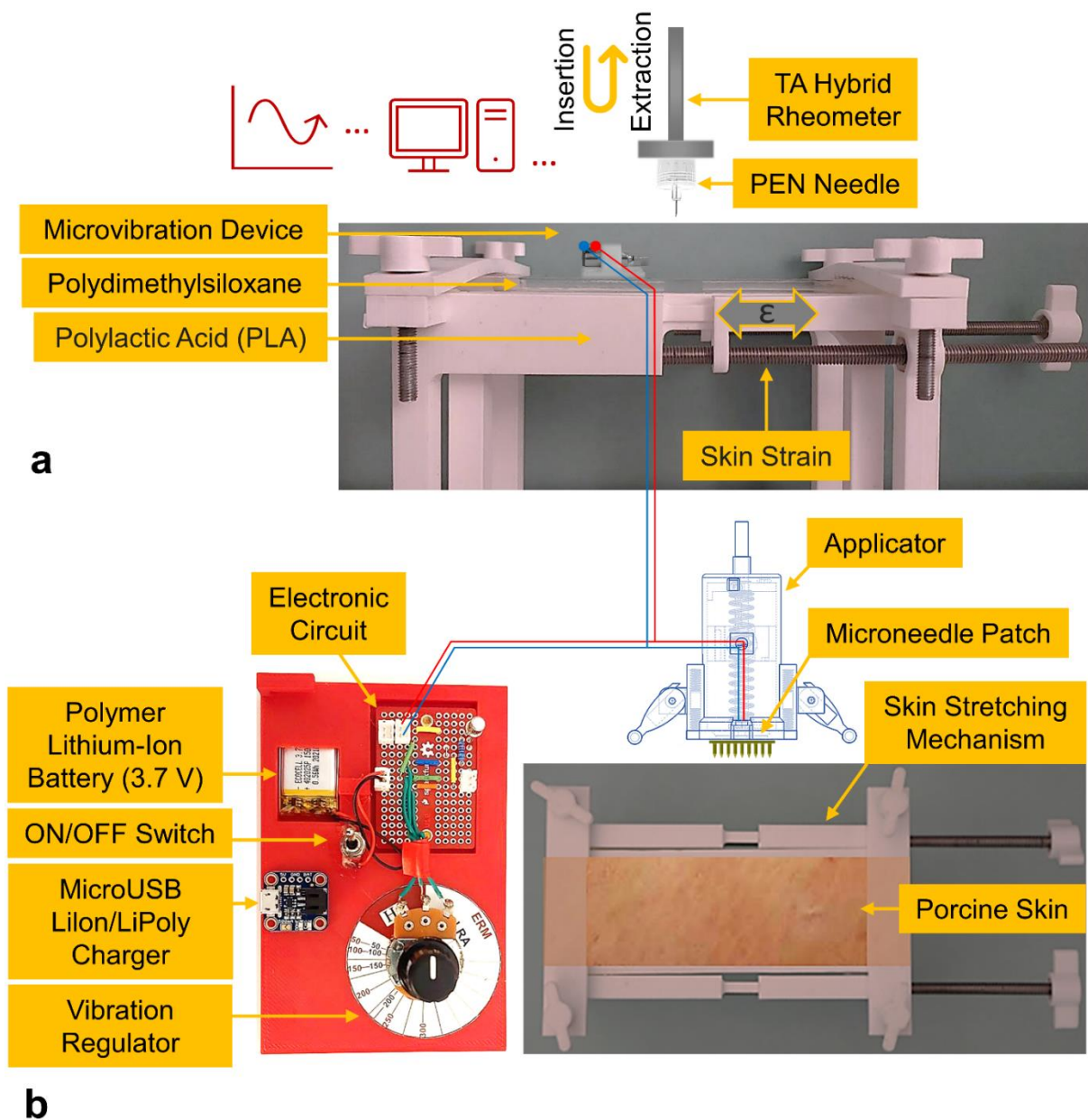


Figure 3: The experimental setup for (a) insertion tests on porcine skin using the applicator incorporating vibration for quantification of model drug diffusion and (b) PEN needle insertion tests using a rheometer, including the effects of skin strain and vibration on insertion and extraction mechanisms.

2.10. Liquid Chromatography Mass Spectrometry (LC-MS) Analysis

To determine the concentration of the model drug, LC-MS analysis was conducted using a Thermo U3000 HPLC liquid chromatography (LC) system coupled to a Bruker Micro TOF Q II mass spectrometer (MS) (Bruker Corporation, Massachusetts, USA). LC-MS is a technique

for separating compounds from the sample using mobile and stationary phases. This is followed by dissolving the compound into a gas phase and ionisation inside a column before conducting the mass analysis. Current analysis was performed using a C18 HPLC column (Phenomenex Kinetex 100 A, $50 \times 2.1 \text{ mm} \times 2.6 \text{ }\mu\text{m}$) at $200 \text{ }\mu\text{L min}^{-1}$. Buffer A was 18.2 Mohm purified water with 0.2 % formic acid, and buffer B was 80 % Acetonitrile (aq) with 0.2 % formic acid. A gradient was established at $40 \text{ }^\circ\text{C}$ starting at 10 % buffer B for 2 minutes, followed by a linear ramping to 65 % B over 7 minutes. This was followed by a linear ramping to 100 % B over 12 seconds and held at 100 % for 1 minute. It was then returned to 10 % B over 12 seconds and held at 10 % for 2.6 minutes. The first 2 minutes of each analysis were diverted to waste. The microTOF Q II was operated in positive mode with nebulizer gas at 0.4 bar, dry gas at 4 L min^{-1} , the dry temperature at $200 \text{ }^\circ\text{C}$, the transfer time of $70 \text{ }\mu\text{s}$, pre-pulse storage of $5 \text{ }\mu\text{s m z}^{-1} 50$ -1000, and spectra time of 2 seconds. During the test, the collisional sweeping varied from 150 to 600 Vpp. The acquisition was controlled using Hystar3.2 SR2, MicroTOF Control 1.3, and Chromeleon 6.8. The data was visualised using Data Analysis 4.0 and Quant Analysis 2.0. The MicroTOF Q was calibrated before testing each sample batch using ESI-L tuning mix – p/n 1969-85000. During the LC-MS analysis, the FSS calibration curve was created using different FSS/Milli-Q water solutions standards (1:1000, 2:1000, 1:10000, 2:10000 v/v), which yielded an accuracy of $R^2 = 0.99$.

2.11. FEA of MN Insertion into Skin with Strain and Vibration Effects

A specific simulation paradigm using ANSYS (2020 R1, ANSYS, Canonsburg, Pennsylvania, USA) was created to evaluate the mechanics of MN insertion into the skin when applying strain and vibration. For skin strain models, the stretching of the skin was modelled in the Static Structural module, which is linked to the Explicit Dynamics module used for modelling the MN insertions. The vibration simulation was initiated by introducing the results from the Modal and Harmonic Response modules into the Static Structural module, which is further

linked to the Explicit Dynamics for the MN insertion model. Based on Equation 1, a sinusoidal forced vibration was assumed for the insertion of MN into the skin model incorporating vibration,

$$M\ddot{x} + c\dot{x} + kx = me\omega^2 \sin(\omega t) \quad (1)$$

Where m is the weight of the rotating mass, e is the eccentricity, and ω is the vibration frequency. The XYZ displacements from the vibration excitation were imported to the Static Structural module using the External Data module. The MN insertion model is then performed using the Explicit Dynamics module. The skin model was assumed to comprise three layers (1) SC, (2) dermis, and (3) hypodermis, with thicknesses of 26 μm , 2 mm, and 1.1 mm, respectively. Ogden model (first order) material properties were specified for the dermis layer.^[53] However, the SC and hypodermis layers were assumed to possess linear elastic responses. Quadrilateral meshing with a bias factor of 10 was used to generate smaller elements in the vicinity of MN-skin interfaces. The friction coefficient of 0.42 was applied between the contact surfaces.^[54] MNs were inserted into the skin layers with a velocity of 3 m s^{-1} while recording the force-displacement data. The erosion algorithm setup enabled the piercing of MNs into the skin by eliminating elements reaching the failure stress while maintaining their inertia effect. Moreover, automatic mass scaling with minimum Courant-Friedrichs–Lewy (CFL) time step of 1 picosecond was used to reduce the simulation run time.^[55] The mass scale algorithm was used to artificially increase the elemental density by increasing the time required for a sound wave to traverse the smallest elements. **Table 1** shows the material properties that were allocated to MN and individual skin layers.

Table 1: Material properties applied for MN and multi-layered human skin model in ANSYS explicit dynamics.

Parameter	MN	SC	Dermis	Hypodermis
Mathematical model	Linear elastic	Linear elastic	Hyperelastic: Ogden 1 st order	Linear elastic
Thickness [mm]	-	0.026	2	1.1
Young Modulus [MPa]	1400	139	-	0.1
Poisson ratio	0.48	0.49	0.49	0.48
Density [kg mm ⁻³]	1.3 E-6	1.3 E-6	1.2 E-6	9.71 E-7
Hyperelastic Coefficients MU1, A1 [MPa]	-	-	0.0977, 16.09	-
Incompressibility factor [MPa ⁻¹]	-	-	0.0745	-
Failure criteria [MPa]	-	20	7	-
Refs.	[56]	[54,57]	[54,58]	[54]

2.12. Governing Equations for Drug Diffusion and Vibrations in Fluid-Structure Interaction Systems

Mass transport of the model drug can be presented in the general form of the convection-diffusion formula. However, as the velocity of fluid around the dissolving MNs is negligible, for a cylindrical shape, mass transport is dominated by diffusion, which can be expressed in Equation (1) as follows:

$$\frac{\partial C}{\partial t} = \frac{D_d}{r} \frac{\partial}{\partial r} \left(r \frac{\partial C}{\partial r} \right) \quad (1)$$

Where r is the cylinder radius, D_d is the drug coefficient, and C is the drug concentration. During the delivery process for cylindrical dissolving MNs, the dissolution of the model drug can be assumed to be uniform from the surfaces. Therefore, the base angle (θ), which is the

ratio of the dissolving MN diameter (D) to height (h) remains constant. The time rate of volume reduction can be calculated using Equation (2) as follows:

$$\frac{dV_c}{dt} = \frac{3\pi}{4} \tan^2 \theta h^2 \frac{dh}{dt} \quad (2)$$

According to free convective mass transfer explained in Equation (3), the polymeric matrix is dissolved based on the concentration difference between dissolving MNs and surrounding:^[65]

$$J = K_D \left(C_S - \left(\frac{1-\beta}{\beta} \right) C \right) \quad (3)$$

Where C_S is the solubility of matrix material in water (kg m^{-3}), C is drug concentration in the skin layer (kg m^{-3}), and β is the drug mass fraction in dissolving MN. K_D is the mass transfer coefficient (m s^{-1}) which depends on dissolving MN design, fluid properties, and diffusivity.^[66]

Thus, the volume change of cylindrical dissolving MN can be represented in Equation (4) as:

$$\frac{dV_c}{dt} = \frac{3\pi}{4\rho} \tan^2 \theta h^2 K_D \left(C_S - \left(\frac{1-\beta}{\beta} \right) C \right) \quad (4)$$

Effects of dissolving MN vibration can be mathematically explained using fluid-structure interaction systems by modelling the acceleration of a cylindrical body immersed in a fluid. This is due to the dissolution and shrinkage of dissolving MN projections after the insertion inside the microchannels filled with bodily fluids. By neglecting the cross-coupling effects of fluid inertia, the one-directional equation of motion can be represented in Equation (5) as shown below:^[67]

$$(m_s + m_d)\ddot{x} + \left(C_s + \frac{4}{3\pi} \rho d C_D x_0 \omega \right) \dot{x} + k_s x = F_0 \sin(\omega t) \quad (5)$$

Where m_s is the dissolving MN weight, C_s is the dissolving MN damping coefficient, K_s is the dissolving MN stiffness, ρ is the bodily fluid density, d is the dissolving MN diameter, C_D is the drag coefficient, x_0 is the small amplitude, ω is the angular frequency F_0 is the forced vibration for different frequencies that was explained in section 2.1. During the vibration, the

effects of fluid on the dissolving MNs can be represented as an additional reactive force on the body, which is expressed using added/virtual mass (m_a). For the case of a cylinder confined in a concentric tubular space filled with compressible and viscous fluid, the added mass (m_a) can be found using:^[68]

$$m_a = \rho\pi a^2 \left(\frac{b^2+a^2}{b^2-a^2} + \frac{2}{a} \sqrt{\frac{2\nu}{\omega}} \right) \quad (6)$$

Where a is the dissolving MN radius, b is the microchannel radius, ρ is the bodily fluid density, ν is the fluid viscosity, and ω is the angular frequency (**Figure 4**). During the dissolution process, as the dissolving MN continues to shrink, the diameter ratio (b/a) increases, reducing the added mass value. This shows that the vibrational effect during the dissolution is strongly related to the dissolving MN diameter at any point in time, thus exponentially reducing over time. In Equation (5), C_D depends on cross-section shape, fluid viscosity (ν), vibration frequency (f), and amplitude (x_0). This is approximated by Wang in Equation (7) for circular cylindrical shapes as follows:^[69]

$$C_D = \frac{3d\pi^2}{4x_0} \left[\left(\frac{\pi f d^2}{\nu} \right)^{-\frac{1}{2}} + \left(\frac{\pi f d^2}{\nu} \right)^{-1} + \left(\frac{\pi f d^2}{\nu} \right)^{-\frac{3}{2}} + \dots \right] \quad (7)$$

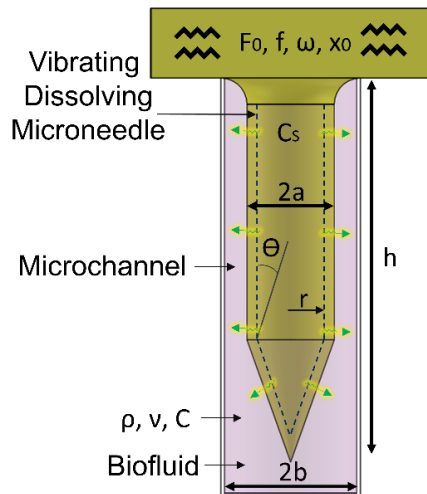


Figure 4: Schematic representation of the vibration-induced dissolving MN dissolution inside a microchannel after insertion into a skin subject.

2.13. Statistical Analysis

Morphological measurements, mechanical failure points, diffusion, and model drug concentrations were presented as the mean \pm standard deviation ($n = 4$). Standard deviations from the mean were expressed by error bars. Statistical analysis was also performed using one-way ANOVA for the comparisons between model drug diffusion and concentrations. For this study, the p-value was set at $p < 0.05$ for the statistical significance. Microsoft Excel and Office 365 (Microsoft Corporation, Redmond, WA, USA) were used for statistical calculations.

3. Results

3.1. Fabrication of DMNPs

The 9×9 master MN array was printed from IP-S photoresist using the TPP technique in ~ 20 hr with submicron resolution. The master MN array was used to create a PDMS negative mould for the replication of thermoplastic MNs. Thermoplastic (Zeonor 1060R) MN arrays were replicated using a hybrid rheometer in ~ 1 hr using the PDMS negative mould and soft embossing process. Due to the long printing time of the TPP process, the manufacturing process is only suitable for prototyping; therefore, the replicated thermoplastic MNs were used to produce multiple secondary negative moulds of the master. Eight negative PDMS moulds

were created from the thermoplastic MN masters in a relatively short process. Subsequently, a total of 35 PVA/PVP DMNPs were made using micro moulding with swinging centrifugation and heat treatment in a standard laboratory incubator. While three samples were used to observe the geometrical shrinkages, the remaining 32 samples were used to perform skin insertion tests using LRA (n=4) and ERM (n=4) modes for four different vibrations. SEM measurements of the replicated DMNPs showed an average of $951.95 \pm 3.38 \mu\text{m}$ (n=3) overall height, $218.81 \pm 5.18 \mu\text{m}$ (n=3) base diameter, and $6.45 \pm 0.42 \mu\text{m}$ (n=3) tip diameter. These data indicated $8.91 \pm 0.32 \%$ longitudinal (height) and $14.32 \pm 2.03 \%$ lateral (base diameter) shrinkages compared to the thermoplastic secondary masters. This also shows a longitudinal shrinkage of $13.46 \pm 0.31 \%$ and lateral shrinkages of $12.48 \pm 2.07 \%$ from the original geometrical parameters ($250 \mu\text{m}$ base diameter, $1100 \mu\text{m}$ height). During the soft embossing and micro moulding processes, no defects were observed on the PDMS moulds. **Figure 5** shows the SEM images of the arrays made from the TPP process using IP-S photoresist, Zeonor 1060R thermoplastic MNs, and PVA/PVP DMNPs.

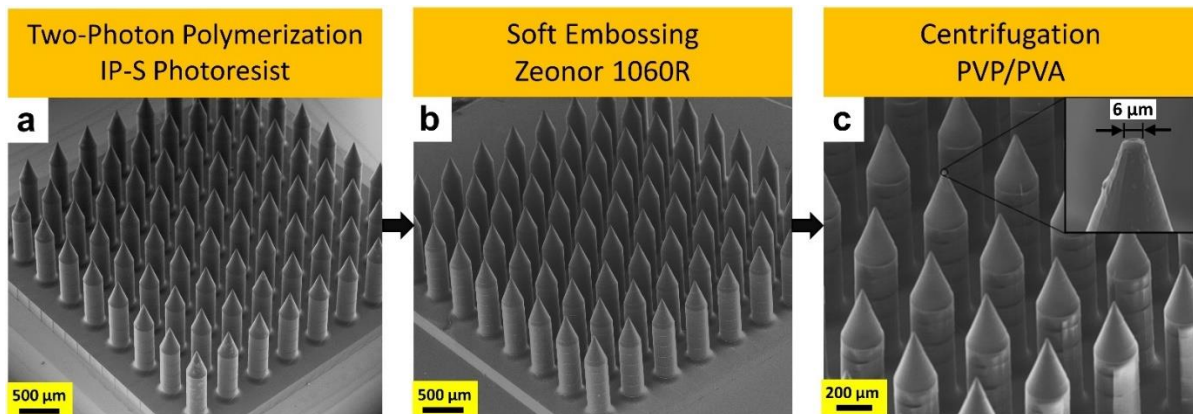


Figure 5: SEM images of (a) 9×9 MN array fabricated using TPP as the primary master, (b) secondary master replicated via soft embossing of thermoplastics (Zeonor 1060R), (c) PVA/PVP DMNPs replicated from the secondary masters using PDMS moulds and micromoulding technique with $\sim 6 \mu\text{m}$ tip diameter.

3.2. MN Mechanical Strength

To evaluate the mechanical behaviour and failure points, quasi-static compression and bending tests were conducted using rheometer parallel plates on single PVA/PVP MNs. The force-displacement graphs of the data indicated a rise that peaked at the failure point before a sharp drop in the data. The compression test results show that the buckling failure force is 0.65 ± 0.04 N (**Figure 6a**), and the bending failure is 0.33 ± 0.02 N (**Figure 6b**). Based on theoretical models, critical buckling load can also be estimated using the following formula:

$$F_{buckling} = \frac{\pi^3 a^4 E}{16L^2} \quad (8)$$

Where a is the MN radius (0.125 mm), L is the MN effective length (1 mm), and E is the elastic modulus (1400 MPa).^[56] For the case of bending, the maximum bending load can also be found using:^[59]

$$F_{bending} = \frac{K_t \sigma_y \pi a^3}{4L} \quad (9)$$

Where K_t is the stress correction factor for shafts with base fillets (1.75), σ_y is yield stress (77.4 MPa), a is the MN radius (0.125 mm), and L is the MN effective length (0.675 mm).^[60] Based on theoretical analysis, Equations (8) and (9) predicted that the buckling and bending failures occur at 0.63 N and 0.31 N, respectively, which are in accordance with the experimental results. SEM images of the DMNPs following the mechanical tests are shown in **Figure 6c**. The compression test indicated a near-tip failure due to direct contact with the metal plate and buckling failure at a distance (x) from the MN base. However, bending failure occurred directly at the MN base, coinciding with the base fillet.

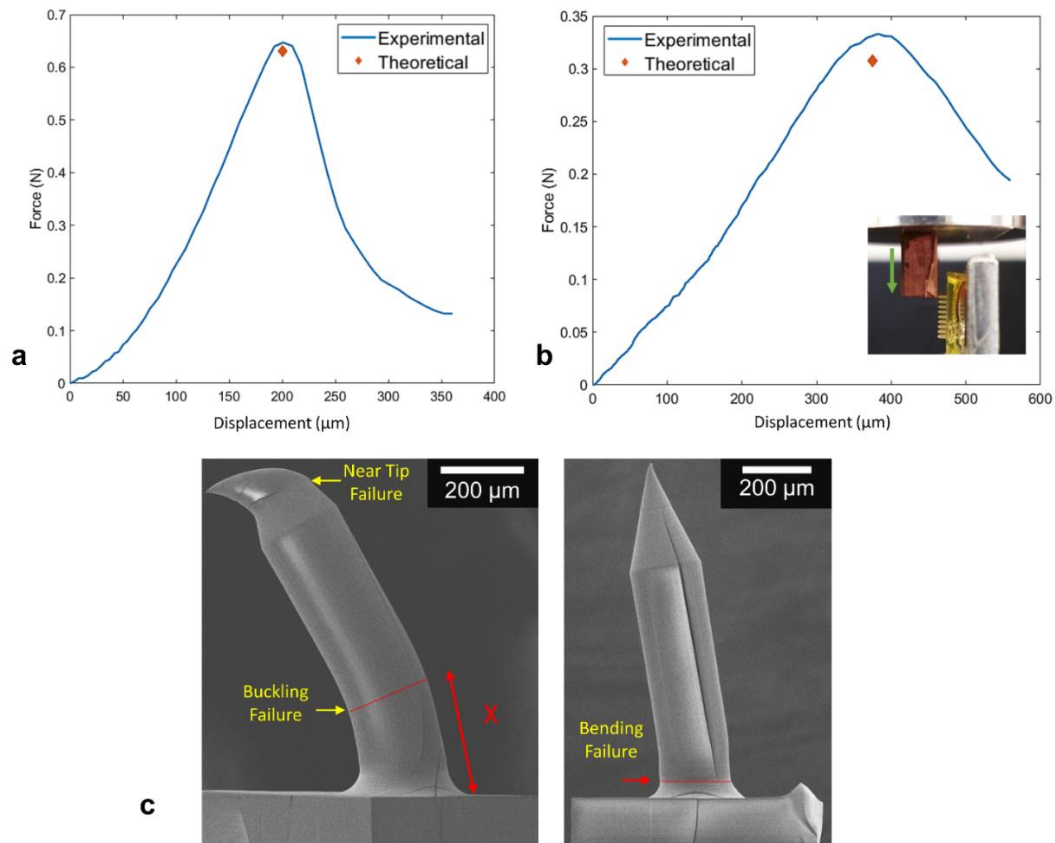


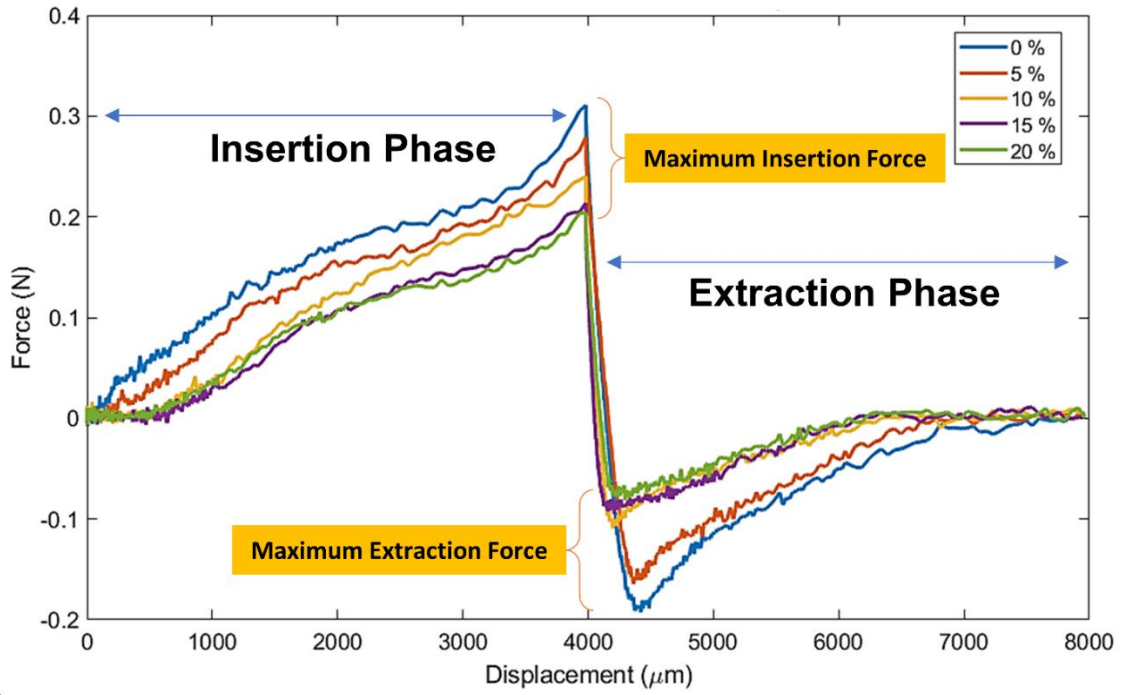
Figure 6: The mechanical testing results, including (a) axial compression and (b) bending tests on an MN, compared against theoretical models. (c) SEM images of a single MN after compression test indicate near tip and buckling failures at a distance (x) from the base, followed by SEM image of bending failure which occurred at the MN base.

3.3. Effects of Vibration and Strain on Insertion Force of MNs

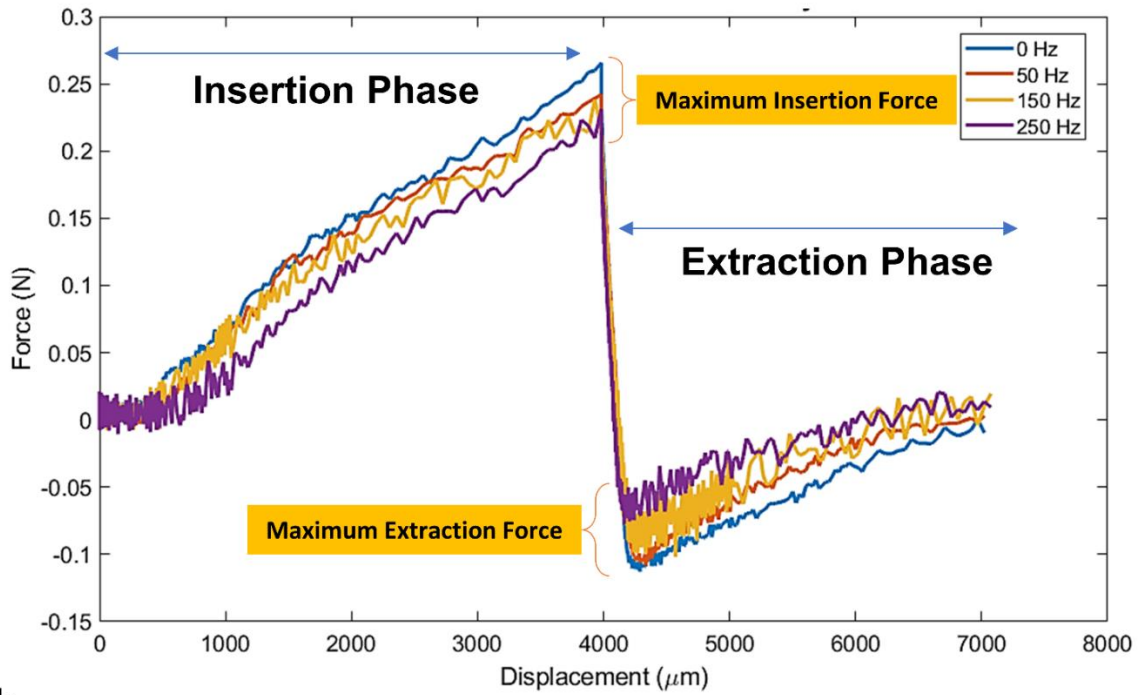
3.3.1. Experimental Results using PEN Needle

The effects of vibration excitation and strain were evaluated using a rheometer to measure the insertion and extraction mechanics of PEN needles. The force-displacement data were recorded during the PEN needle insertions and extractions phases. A PDMS sample, as a skin model, was subjected to strain using a custom-made stretching tool at 0 %, 5 %, 10 %, 15 %, and 20 % relative to its unstretched condition.^[49] In each case, the PEN needle was inserted into the sample until it reached a depth of 4 mm and then withdrawn back to the original position. Throughout the experiments, force increased gradually and peaked at F_{ins} before a sudden drop.

The extraction phase lay in the negative region with a peak at F_{ext} , steadily moving back to the starting point. During the PEN needle insertion phase, an evident reduction in F_{ins} was observed from 0.311, 0.279, 0.24, 0.214, to 0.204 N for strain rates of 0 %, 5 %, 10 %, 15 %, and 20 %, respectively. A similar trend occurred during the extraction phase, indicating a reduction in the magnitude of extraction force. The results showed that F_{ext} reduced from 0.192, 0.164, 0.109, 0.095, to 0.081 N for strains of 0 %, 5 %, 10 %, 15 %, and 20 % (no vibrations), respectively (**Figure 7a**). A similar insertion procedure was applied to test vibration excitations. At 0, 50, 150, and 250 Hz vibrations (constant 5 % strain), F_{ins} were recorded as 0.286, 0.262, 0.258, and 0.251 N, respectively. Similarly, the extraction phase showed reductions in the F_{ext} from 0.093, 0.088, and 0.082 to 0.057 N for vibrations applied at 0, 50, 150, and 250 Hz, respectively (**Figure 7b**).



a



b

Figure 7: Force-displacement diagrams during PEN needle insertion and extraction phases for varying (a) strain rates of 0 - 20 %, and (b) vibrations excitation ranges of 0 - 250 Hz.

3.3.2. FEA Results

FEA analysis of the MN insertion mechanism was conducted using the interconnection of different modules in ANSYS software. Modal, Harmonic Response, External Data, Static Structural, and Explicit Dynamics modules were used to model skin insertion incorporating strain and vibration excitation. The multi-layered skin was modelled by planar symmetry, and boundary conditions shown in **Figure 8a** were activated at the level of Explicit Dynamics to maintain the results from the Static Structural module. During the analysis, the insertion force was plotted against the MN displacement penetrating the skin model. The results indicated a rise in the recorded force that peaked at the F_{ins} before a sudden drop at the skin puncture point. Figure 8b shows the effects of increasing vibration excitations from 0 to 50, 150, and 250 Hz on the F_{ins} , showing the F_{ins} have reduced to 0.098, 0.097, 0.096, and 0.078 N, respectively. The drop in F_{ins} became profound upon a further increase in the applied frequency from 150 Hz to 250 Hz. The application of skin strains at 0 %, 2.5 %, 5 %, 7.5 %, and 10 % also resulted in a reduction of F_{ins} which were 0.13, 0.123, 0.114, 0.101, and 0.088 N, respectively. Figure 8c shows these force-displacement diagrams for MN-skin insertions with different skin strain rates ranging from 0 - 10 %.

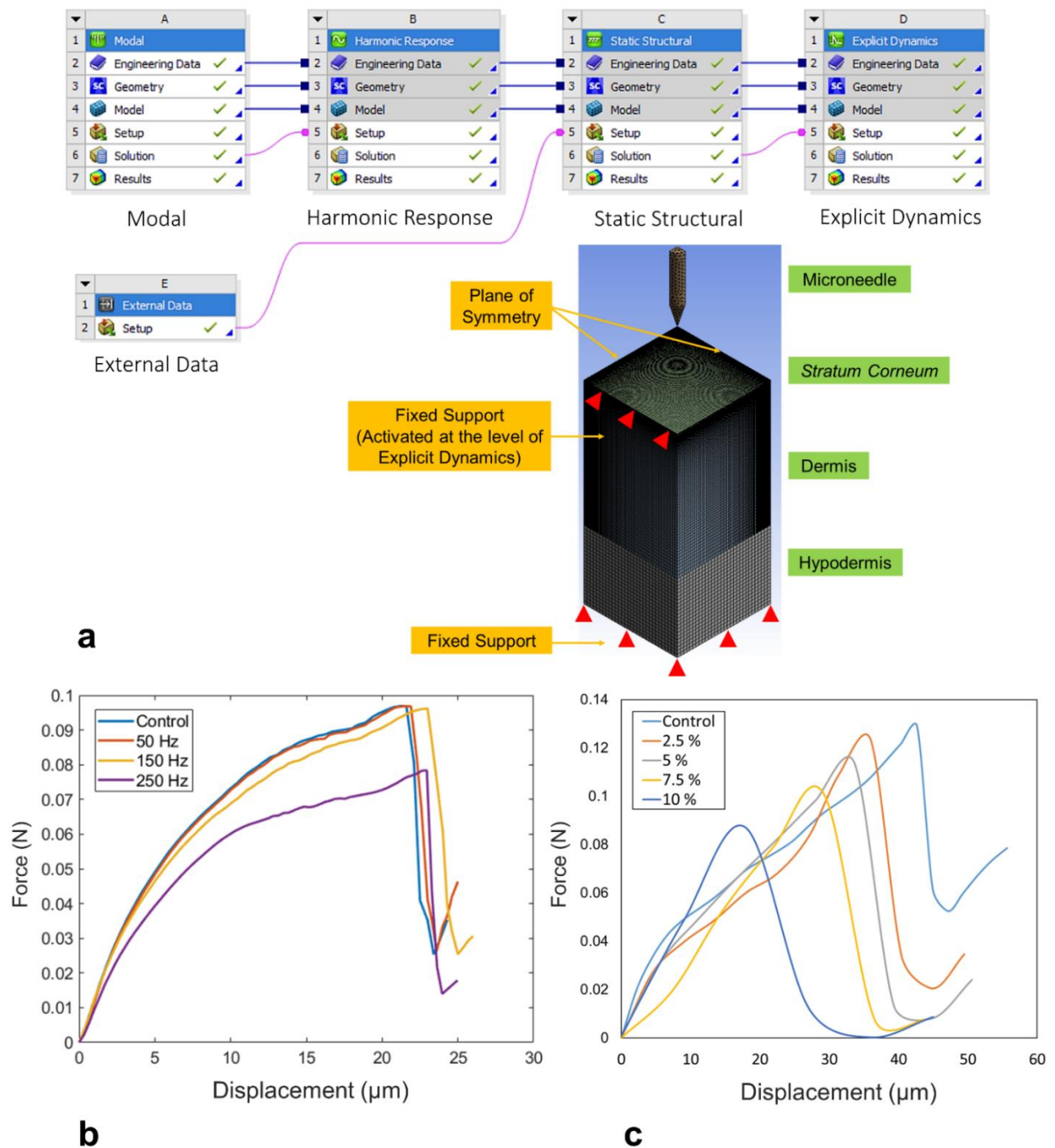


Figure 8: (a) Simulation setup paradigm of MN insertion into the multi-layered skin model incorporating vibration excitation. The FEA force-displacement results for (b) vibrations between 0 - 250 Hz and (c) strain rates between 0 - 10 %.

3.4. Effects of Low-Frequency Vibration on Penetration and Diffusion of Model Drug

3.4.1. Diffusion of FSS Model Drug

Confocal imaging was performed to evaluate the penetration depth and diffusion pattern of the DMNPs inside the cadaver porcine skin tissues. Thirty-two tests were conducted to assess the effects of LRA and ERM vibrations on DMNPs when applied to the tissues at 3 m s^{-1} for four minutes. **Figure 9a** shows the depth-coded and confocal image of FSS diffusion after ~ 30 minutes post-experiment, which is captured using the Z-stacking technique. The confocal image was used to examine the model drug diffusion of DMNPs influenced by LRA and ERM vibrations at various frequencies ($n=4$) ranging from 0 Hz to 250 Hz. During the non-vibrated (0 Hz) insertion test, the mean diffusion after ~ 30 minutes ($n=4$) was to a depth of $246.85 \pm 40.96 \mu\text{m}$ under the skin surface. However, when the ERM vibration excitation of 50, 150, and 250 Hz was introduced, the maximum diffusion of the FSS drug model improved to $273.05 \pm 34.98 \mu\text{m}$, $324.51 \pm 42.40 \mu\text{m}$, and $387.68 \pm 49.63 \mu\text{m}$ under the skin surface, respectively. A similar set of experiments were performed using LRA vibrations at 50, 100, 150, and 200 Hz, which resulted in the diffusion of the model drug to a depth of $379.01 \pm 25.44 \mu\text{m}$, $428.87 \pm 14.25 \mu\text{m}$, $491.14 \pm 21.45 \mu\text{m}$, and $532.63 \pm 23.69 \mu\text{m}$, respectively. All the data were recorded 30 minutes after insertion. The results showed that increasing the vibration enhanced the PVA/PVP dissolution over a constant holding time of four minutes. Figure 8a shows the optical images of a DMNP after applications on the porcine skin at different vibration frequencies. In all tests, the DMNPs were dissolved during the skin insertion tests, and the drug was delivered into the underlying skin layers.

Another method of evaluating the diffusion of DMNPs was to plot the average FSS intensity for the entire patch versus the base length of the MN patch containing a row of nine projections. Therefore, Figure 9b represents the improvements in FSS intensity through nine consecutive peaks when the frequency was increased from 0 to 250 Hz. In the case of MNs positioned at

the Centre of the DMNPs, the average FSS intensity was lower than MNs located around the edge of the patch. This indicates the “bed of nails” effects where central MNs have only partially penetrated the skin. Based on the “bed of nails” definition, as the outer MNs have stretched the skin first, the inner MNs require higher pressure to reach a similar penetration depth.^[61,62] The outcomes from the diffusion analysis using the confocal images were then compared to the FEA simulation of 3 m s^{-1} MN impact insertion at 0, 50, 150, and 250 Hz skin vibration. The data from the impact simulation showed a linear increase in the penetration depth from $161.12 \text{ }\mu\text{m}$, $164.34 \text{ }\mu\text{m}$, and $176.52 \text{ }\mu\text{m}$ to $200.76 \text{ }\mu\text{m}$. Comparing the experimental and simulation results validated the effects of increasing vibration on the overall penetration depth. The higher penetration observed in experimental data is due to the additional diffusion of FSS into the deeper skin layers during the ~ 30 minutes post-insertion confocal imaging (Figure 9c).

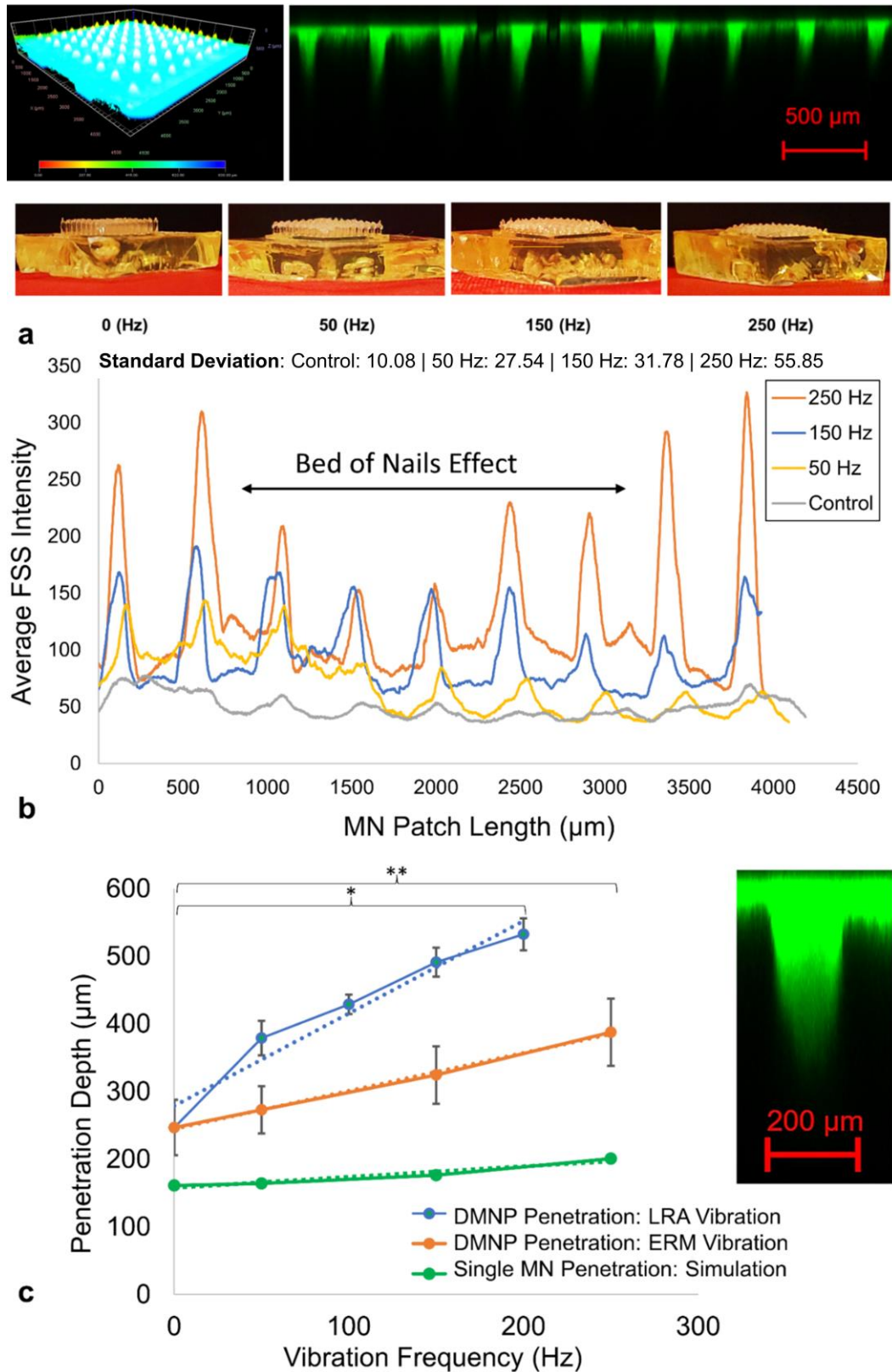


Figure 9: (a) Confocal microscope image of DMNPs applied into the porcine cadaver skin at 250 Hz frequency, and the optical images of a typical DMNP dissolution pattern for different ERM vibration frequencies (0 - 250 Hz) four minutes after application into the porcine skin.

(b) Average FSS diffusion intensity across the entire DMNPs (81 samples) versus MN patch length (~ 4500 μm across all nine MN projections). The graph shows the bed of nail effects at the central part of the MN patches. (c) Penetration depth (μm) of the FSS model drug versus vibration frequency (Hz). The graph compares the data obtained from confocal microscopy for the diffusion depth of the FSS model drug after ~ 30 minutes with the FEA data of MN penetration applied at different vibration frequencies. Data are represented as mean \pm SD (*) $p < 0.0001$, (**) $p < 0.05$ (One-way ANOVA).

3.4.2. Concentrations of FSS Model Drug

LC-MS analysis was used to determine the FSS concentration for different vibrational frequencies after each insertion test using the dissolution of DMNPs/Milli-Q water solutions. Calibration curves were developed for FSS solutions based on predetermined concentrations. The ERM-based frequency that ranged between 0, 50, 150, and 250 Hz resulted in concentrations of 2.64 ± 0.14 , 2.78 ± 0.1 , 2.94 ± 0.21 , and $2.93 \pm 0.05 \mu\text{g L}^{-1}$, respectively. Similarly, vibration based on the LRA excitations of 50, 100, 150, and 200 Hz resulted in concentrations of 2.8 ± 0.05 , 2.89 ± 0.07 , 2.96 ± 0.02 , $2.98 \pm 0.03 \mu\text{g L}^{-1}$, respectively. The results showed that inducing 250 Hz ERM frequency and 200 Hz LRA frequency vibrations resulted in a 10.98 % and 12.88 % increase in the FSS concentration compared to the control case (0 Hz). **Figure 10** shows the bar chart with mean and standard deviation error bars (n=4) of FSS concentrations for ERM and LRA-induced vibration experiments.

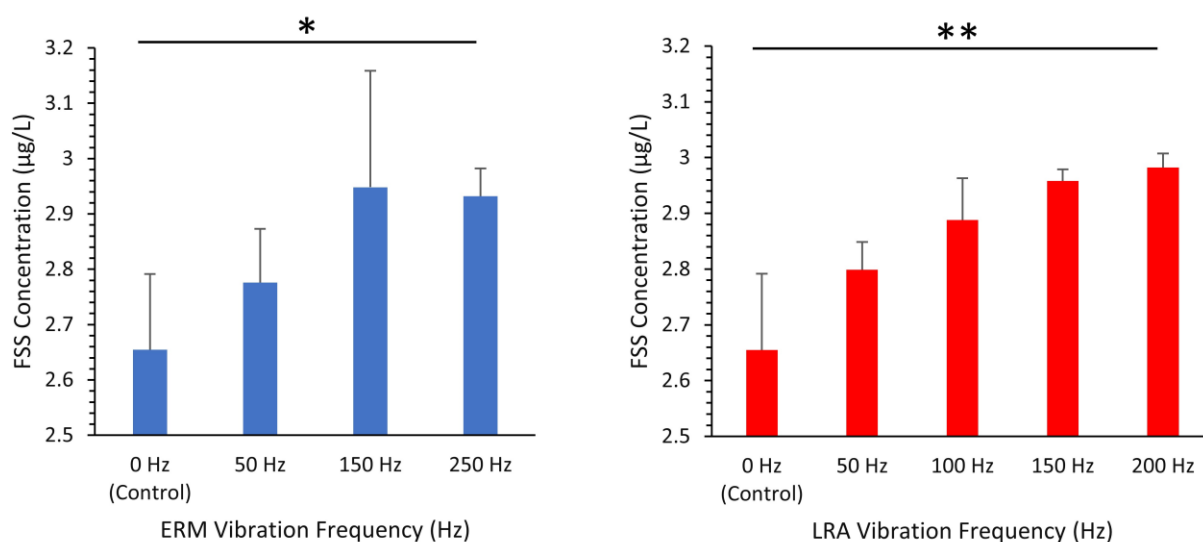


Figure 10: The FSS drug model concentration for ERM and LRA-induced tests at different vibration frequencies. Data are represented as mean + SD, (*) $p < 0.05$, (**) $p < 0.0001$ (One-way ANOVA).

4. Discussion

4.1 Fabrication of DMNPs

The current study reported on a new multi-stage replication of PVA/PVP DMNPs to reduce the overall replication time. TPP technique was used to fabricate primary master MN arrays. The PDMS negative mould of the primary master MN array was produced for replications of multiple thermoplastic MN arrays through a well-established soft embossing process developed in our group.^[15,20,49] The replicated thermoplastics (Zeonor 1060R) previously fabricated by our group had high fidelity, and the PDMS negative moulds were intact after > 30 replication cycles.^[49] This study used the replicated thermoplastic MN arrays, for the first time, as the secondary masters to make several PDMS moulds for the replication of PVA/PVP DMNPs in a short time. This approach reduced the overall fabrication time from 746 hr to 98 hr per set of ten DMNPs, demonstrating a ~ 86.9 % decrease in the total fabrication time. To estimate the total time, combination of the times required for TPP, post TPP curing, PDMS micro moulding, soft embossing, centrifugation, and incubation curing for single and double

master methods are 11 hr, 1 hr, 3 hr, 1 hr, 10 hr, and 720 hr compared to 11 hr, 1 hr, 3 hr, 10 hr, 1 hr, and 72 hr, respectively. The PVA/PVP DMNPs exhibited 13.46 ± 0.31 % longitudinal shrinkage compared to the original design parameters and 8.9 ± 0.32 % shrinkage compared to the thermoplastic secondary master MN arrays.^[49] The shrinkage in the size of the final MN replicas from the master MN array signifies the need for design adjustments or slowing the replication process to achieve the required sizing; however, this could significantly increase the production time.

4.2 MN Mechanical Strength

To perform the mechanical tests, DMNPs were fabricated in the form of single PVA/PVP MNs through a similar process as MN patches. The experimental and theoretical studies on compression and bending experiments showed that DMNPs possess sufficient structural integrity for skin insertion and penetration. Due to the skin's irregular structure and the presence of wrinkles, the evaluation of the bending strength of the MNs was equally important to the compression.^[17] The compression results for our PVA/PVP MNs showed a buckling failure of 0.65 ± 0.04 N at the quasi-static condition. However, a bending failure of 0.33 ± 0.02 N was recorded, which is in accordance with Demir et al. bending experiments on (Polyglycolide) PGA MNs with similar geometry and a bending failure of 0.24 ± 0.05 N.^[63] Considering the effects of shrinkages in height and base diameter using Equations 2 and 3, the predicted drop in the bending and buckling failures compared to actual design parameters is 29.57 % and 35.25 %, respectively. Despite the lower mechanical strength of the PVA/PVP MNs compared to our previously studied thermoplastics MNs,^[49] the SM for PVA/PVP DMNPs, which is the ratio of buckling failure to F_{ins} , was estimated to be ~ 2.5 , which is well greater than unity ($SM > 1$) that is required for insertion of MNs into the skin without failure. **Figure 11** indicates the effects of different strains and vibration frequencies on the estimated SM values of DMNP replicas.

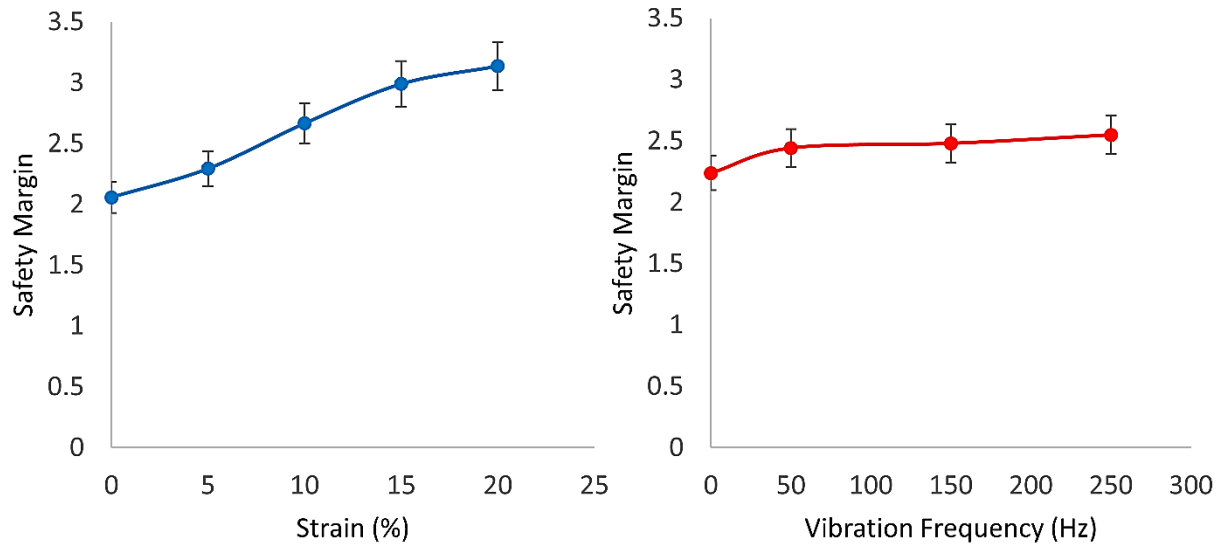


Figure 11: Effects of strains and vibration frequencies on the safety margin of DMNPs.

4.3. MN Insertion Mechanism using Skin Strain and Vibration

In this study, we used a skin stretching tool^[49] to investigate the mechanism of MN insertion and extraction on the PDMS skin model with different strains (0 %, 5 %, 10 %, 15 %, and 20 %). The results showed 34.4 % and 57.8 % reductions in the maximum insertion (F_{ins}) and extraction (F_{ext}) forces when the strain value increased from 0 % to 20 %. Additionally, FEA simulations of MN insertions were conducted on a multi-layered hyperelastic skin model with strains of 0 %, 2.5 %, 5 %, 7.5 %, and 10 %. The data showed that increasing the skin strain from 0 % to 10 % resulted in a 32.31 % reduction in F_{ins} . In a similar study, Shu et al. conducted a 3D hyperelastic, anisotropic pre-stressed MN insertion simulation model. The results demonstrated that by increasing skin pretension from 0 % to 10 %, the penetration force was reduced by 13 %. The disparity between the results is due to different material characterisations and thicknesses for skin models. During FEA simulations, Shu et al. used the Neo-Hookean, Gasser-Ogden-Holzapfel, and linear elastic mechanical models with the thicknesses of 0.02, 2.5, and 1 mm for SC, dermis, and hypodermis skin layers.^[54] The current simulation was limited to Ogden 1st order for 2 mm dermis layer, and linear elastic models for a 0.026 mm SC and 1.1 mm hypodermic layers.

Yang and Zahn previously reported the effect of the vibratory actuator in reducing the F_{ins} from ~ 0.28 to 0.08 N at an unspecified kHz range.^[40] Here, we applied a low-frequency spectrum ranging from 0 Hz to 250 Hz to measure the insertion and extraction forces of PEN needles on the PDMS artificial skin model. By increasing the frequency to 250 Hz, the F_{ins} reduced by 12.24 % from 0.286 N to 0.251 N, while F_{ext} remarkably reduced by 43.01 % from 0.093 N to 0.057 N. When experimental results were compared to FEA results, the magnitude of recorded data was different for various excitations. For instance, when the frequency was increased from 0 to 250 Hz, F_{ins} was reduced from 0.098 to 0.078 N, which indicated a 20.4 % reduction in F_{ins} . Despite the direct effects of vibratory microdevices on the reduction of insertion and extraction loads, the degree to which force can be reduced depends on different factors, such as the nature of the skin model, relative humidity, skin location, and orientation.^[64] For instance, in this study, the experiments incorporated the PDMS substrates, while the FEA simulation used a multilayered hyperelastic model for different skin layers.

The strain and vibration in both experiments and simulations initiated a sharp increase in the force data when the needle and skin were in direct contact prior to the rapture. This is followed by a moderate rise in the force during which the needle tip partially penetrates the top layer of the skin. The final exponential rise in the force records indicated the final tip-SC interaction phase before a sudden drop when the entire tip has passed through the SC layer of skin. Despite the efforts to maintain identical test conditions for the actual experiment and FEA analysis, the differences in the F_{ins} results are mainly due to variations in the thickness of skin layers, relative humidity of actual porcine skin compared to the associated hyperelastic model, and difference in the strain rates.

4.4. Effects of Low-Frequency Vibration on Model Drug Diffusion and Concentration

The diffusion of the FSS model drug was evaluated for a series of LRA and ERM vibrations using maximum FSS diffusion depth and concentration. The results showed increasing the ERM frequency from 50 Hz to 250 Hz improved the diffusion depth by 41.98 %, from $273.05 \pm 34.98 \mu\text{m}$ to $387.68 \pm 49.63 \mu\text{m}$ in 30 minutes. Application of LRA frequency from 50 Hz to 200 Hz showed a 40.54 % increase in FSS diffusion depth from $379.01 \pm 25.44 \mu\text{m}$ to $532.63 \pm 23.69 \mu\text{m}$. Due to the nature of excitations, at a constant frequency of 150 Hz, vibration using LRA indicated a 51.35 % higher diffusion rate than that of the ERM. To validate the diffusion depth, the results were compared to the FEA analysis of MN penetration depth at 3 m s^{-1} . For instance, for 50 Hz and 150 Hz, the penetration was $161.12 \mu\text{m}$ and $176.52 \mu\text{m}$, respectively. Despite similar trends for diffusion depth using both experimental and FEA results upon increasing frequencies, the magnitudes of penetration depth are deemed incomparable. Since FEA results indicated the maximum penetration reached by the MN model, higher penetration depth from confocal experiments represents the average depth of diffused FSS at a certain detection setting. When compared to FSS diffusion depth after ~ 30 minutes, LRA and ERM diffusions reached $273.05 \pm 34.98 \mu\text{m}$ and $324.51 \pm 42.40 \mu\text{m}$ in 50 Hz and $379.01 \pm 25.44 \mu\text{m}$ and $491.14 \pm 21.45 \mu\text{m}$ in 150 Hz, indicating a two-fold average increase in the FSS diffusion depth. In general, the central DMNPs indicated lower diffusion depth due to the “bed of nails” effect, which mainly depends on MN interspacing. The “bed of nails” in a dense MN array is defined as when the skin is locally stretched by the outermost MNs, resulting in the central MNs exerting the applied force on the stretched skin.^[61] Therefore, a higher applied force is required as the pressure exerted by the individual MN tips is insufficient to penetrate the skin.^[62]

Measurements for the concentration of the FSS model drug showed a direct relationship between the vibrational frequency and dissolution rate. For the case of ERM vibration,

increasing vibration from 0 Hz to 250 Hz increased the FSS concentration by 10.98 % from $2.64 \pm 0.14 \mu\text{g L}^{-1}$ to $2.93 \pm 0.05 \mu\text{g L}^{-1}$. The LRA showed a greater improvement of 12.88 %, with $2.98 \pm 0.03 \mu\text{g L}^{-1}$ at 200 Hz. Based on Equation (10), increasing the vibration frequency reduces the coefficient of drag (C_D), which, as a result, improves the PVA/PVP dissolution rate (Equation (8)). In addition, higher penetration achieved upon increasing vibrational frequencies can expose more MN volume in the confined biofluidic space, which, according to Equation (7), reduces the total time required to dissolve the entire MN projection. According to the previous results from MB drug simulation of coated MBs,^[20] during the insertion time, the FSS drug concentration (C) in the skin increases, which, based on Equation (4), reduces the DMNP's dissolution rate. This signifies the importance of external stimulants, such as vibrations, to further enhance the dissolution rate. The findings also indicated that parts of the DMNP bases which were in contact with porcine skin were dissolved both on the skin surface and into the microchannels created after penetration. Similarly, Liu et al. measured tetramethylpyrazine (TMPH) delivery using vertical vibration ranges of 3200, 4800, and 6400 rpm on solid MNs. The results indicated that increasing vibration from 3200 rpm to 6400 rpm resulted in a five-fold increase in TMPH permeation.^[45]

Our study tested a relatively higher molecular weight (MW) model drug of $376.27 \text{ g mol}^{-1}$, which is more challenging than the study by Liu et al. FSS drug model can also represent FDA-approved drugs for transdermal delivery, such as Fentanyl (MW $\approx 336.5 \text{ g mol}^{-1}$) for acute postoperative pain, Oxybutynin (MW $\approx 357.49 \text{ g mol}^{-1}$) for overactive bladder, and Norelgestromin (MW $\approx 327.47 \text{ g mol}^{-1}$) for hormonal contraceptives.^[70] (Singh et al. 2010). Seeger et al. also previously reported on the effects of vibration on the dissolution of oral drug formulation. The dissolution degree generally depends on the dissolution method, drug properties, and formulation.^[46]

5. Conclusion

The application of MN technology is becoming a promising method for TDD. This study introduced a procedure for replicating PVA/PVP DMNPs using TPP, soft embossing, and PDMS micromoulding techniques. The proposed manufacturing method used MNs made of IP-S and Zeonor 1060R thermoplastic as primary and secondary master structures to create PVA/PVP DMNPs. The overall replication time was reduced by ~ 86.9 % for each set of ten PVA/PVP DMNPs while maintaining high accuracy and fidelity. The replicated PVA/PVP DMNPs successfully penetrated the skin models without buckling or bending failure.

MN insertion and extraction mechanisms were tested for varying vibration frequencies and strains using a rheometer. Effects of vibration and strains were verified by reducing peak insertion and extraction force during the skin insertions. A simulation paradigm was also introduced for MN penetration into the multi-layered skin model with hyperelastic mechanical behaviour incorporating skin vibrations and strains. FEA and experimental results confirmed 32.31 % and 22.83 % reductions in insertion force at 10 % skin model strains, respectively. For the case of vibrations, these reductions were 2.1 % and 9.8 % for insertion force at 150 Hz.

Skin insertion tests were conducted on porcine skin using a novel prototype impact applicator capable of ERM/LRA micro-vibration. To mimic the skin *in vivo* condition, a skin stretching mechanism was used to regulate the skin stretch.^[49] The study evaluated the penetration depth, diffusion pattern, and concentrations of a model drug. The results showed LRA and ERM vibrations facilitated the penetration and diffusion of the model drug and enhanced the FSS concentrations. The FSS concentration increased by 11.36 % ERM and 12.12 % LRA at 150 Hz vibration; an average twofold increase in diffusion depth was recorded for ERM/LRA-induced vibration.

This paper provided the potential solutions for two of the main MN challenges with regard to mass producibility, improvements in MN penetration and drug diffusion. The MN insertion was based on a novel impact applicator capable of adjustment for impact velocity, skin tautness, and vibrations, which can be tailored to different skin ages and locations. The results also showed a ten-fold reduction in DMNP production time when two master MN arrays were used. This proposed manufacturing method can be adopted for applications where maintaining precision and timely replication is essential. Moreover, applying low-frequency vibration and skin strain considerably improved the insertion safety and drug diffusion of PVA/PVP DMNPs. Hence, implementing multifeatured impact applicators with external stimulants can improve the overall MN penetration and drug diffusion.

Acknowledgements

This work used the Queensland node of the NCRIS-enabled Australian National Fabrication Facility (ANFF). This research was undertaken in part with the support of resources from the Institute for Advanced Engineering and Space Sciences at the University of Southern Queensland. The current study also used the resources available at the Australian Institute for Bioengineering and Nanotechnology (AIBN) at the University of Queensland. This research received no specific grants from public, commercial, or not-for-profit funding agencies.

Conflicts of Interest

The authors declare no competing interests.

Data Availability Statement

The data that support the findings of this study are available from the corresponding author upon reasonable request.

References

- [1] W. Y. Jeong, M. Kwon, H. E. Choi, K. S. Kim, *Biomater. Res.* **2021**, 25, 24.
- [2] J. H. Jung, S. G. Jin, *J. Pharm. Investig.* **2021**, 1.

- [3] M. R. Prausnitz, *Adv. Drug Deliv. Rev.* **2004**, *56*, 581.
- [4] G. Ma, C. Wu, *J. Control Release* **2017**, *251*, 11.
- [5] J. Yang, X. Liu, Y. Fu, Y. Song, *Acta Pharm. Sin. B.* **2019**, *9*, 469.
- [6] M. S. Lee, C. X. Pan, V. E. Nambudiri, *Ther. Adv. Vaccines Immunother.* **2021**, *9*, 25151355211039073.
- [7] G. M. Glenn, R. T. Kenney, *Curr. Top. Microbiol. Immunol.* **2006**, *304*, 247.
- [8] X. Chen, G. J. Fernando, M. L. Crichton, C. Flaim, S. R. Yukiko, E. J. Fairmaid, H. J. Corbett, C. A. Primiero, A. B. Ansaldo, I. H. Frazer, L. E. Brown, M. A. Kendall, *J. Control Release* **2011**, *152*, 349.
- [9] R. Nagarkar, M. Singh, H. X. Nguyen, S. Jonnalagadda, *J. Drug. Deliv. Sci. Technol.* **2020**, *59*, 101923.
- [10] F. K. Aldawood, A. Andar, S. Desai, *Polymers (Basel)* **2021**, *13*, 2815.
- [11] R. E. Lutton, E. Larraneta, M. C. Kearney, P. Boyd, A. D. Woolfson, R. F. Donnelly, *Int. J. Pharm.* **2015**, *494*, 417.
- [12] H. R. Nejad, A. Sadeqi, G. Kiaee, S. Sonkusale, *Microsyst. Nanoeng.* **2018**, *4*, 17073.
- [13] S. Dharadhar, A. Majumdar, S. Dhoble, V. Patravale, *Drug Dev. Ind. Pharm.* **2019**, *45*, 188.
- [14] A. Malek-Khatabi, Z. Faraji Rad, M. Rad-Malekshahi, H. Akbarijavar, *Mater. Lett.* **2023**, *330*, 133328.
- [15] Z. Faraji Rad, R. E. Nordon, C. J. Anthony, L. Bilston, P. D. Prewett, J. Y. Arns, C. H. Arns, L. Zhang, G. J. Davies, *Microsyst. Nanoeng.* **2017**, *3*, 17034.
- [16] R. F. Donnelly, T. R. Raj Singh, E. Larrañeta, M. McCrudden, *Microneedles for Drug and Vaccine Delivery and Patient Monitoring*, John Wiley & Sons Ltd, Queen's University Belfast, UK, **2018**.
- [17] V. Ebrahiminejad, P. D. Prewett, G. J. Davies, Z. Faraji Rad, *Adv. Mater. Interfaces* **2022**, *9*, 2101856.
- [18] T. Waghule, G. Singhvi, S. K. Dubey, M. M. Pandey, G. Gupta, M. Singh, K. Dua, *Biomed. Pharmacother.* **2019**, *109*, 1249.

- [19] E. Larrañeta, R. E. M. Lutton, A. D. Woolfson, R. F. Donnelly, *Mater. Sci. Eng.: R: Rep.* **2016**, *104*, 1.
- [20] V. Ebrahimejad, Z. Faraji Rad, *Adv. Mater. Interfaces* **2022**, *9*, 2201115.
- [21] J. Li, M. Zeng, H. Shan, C. Tong, *Curr. Med. Chem.* **2017**, *24*, 2413.
- [22] Y. C. Kim, J. H. Park, M. R. Prausnitz, *Adv. Drug Deliv. Rev.* **2012**, *64*, 1547.
- [23] N. Roxhed, P. Griss, G. Stemme, *Biomed. Microdevices* **2008**, *10*, 271.
- [24] M. R. Prausnitz, *Annu. Rev. Chem. Biomol. Eng.* **2017**, *8*, 177.
- [25] X. Jiang, H. Zhao, W. Li, *Front Bioeng. Biotechnol.* **2022**, *10*, 840395.
- [26] R. F. Donnelly, T. R. Singh, M. J. Garland, K. Migalska, R. Majithiya, C. M. McCrudden, P. L. Kole, T. M. Mahmood, H. O. McCarthy, A. D. Woolfson, *Adv. Funct. Mater.* **2012**, *22*, 4879.
- [27] J. G. Turner, L. R. White, P. Estrela, H. S. Leese, *Macromol. Biosci.* **2021**, *21*, e2000307.
- [28] I. A. Tekko, A. D. Permana, L. Vora, T. Hatahet, H. O. McCarthy, R. F. Donnelly, *Eur. J. Pharmacol.* **2020**, *152*, 105469.
- [29] S. F. Lahiji, M. Dangol, H. Jung, *Sci. Rep.* **2015**, *5*, 7914.
- [30] M. Shikida, S. Kitamura, C. Miyake, K. Bessho, *Microsyst. Technol.* **2013**, *20*, 2239.
- [31] X. Liu, J. Cleary, G. K. German, *Acta Biomater.* **2016**, *43*, 78.
- [32] P. F. Humbert, F. , H. Maibach, P. Agache, *Agache's Measuring the Skin*, Springer, Switzerland, **2017**.
- [33] M. M. Badran, J. Kuntsche, A. Fahr, *Eur. J. Pharm. Sci.* **2009**, *36*, 511.
- [34] M. L. Crichton, A. Ansaldo, X. Chen, T. W. Prow, G. J. Fernando, M. A. Kendall, *Biomaterials* **2010**, *31*, 4562.
- [35] R. F. Donnelly, M. J. Garland, D. I. J. Morrow, K. Migalska, T. R. R. Singh, R. Majithiya, A. D. Woolfson, *J. Controlled Release* **2010**, *147*, 333.
- [36] P. Khanna, K. Luongo, J. Strom, S. Bhansali, *J. Micromech. Microeng. J. Micromech. Microeng.* **2010**, *20*, 045011.
- [37] S. A. Ranamukhaarachchi, B. Stoeber, *Biomed. Microdevices* **2019**, *21*, 100.

- [38] O. Olatunji, D. B. Das, M. J. Garland, L. Belaid, R. F. Donnelly, *J. Pharm. Sci.* **2013**, *102*, 1209.
- [39] B. Ahn, *Int. J. Control. Autom. Syst.* **2019**, *18*, 143.
- [40] M. Yang, J. D. Zahn, *Biomed. Microdevices* **2004**, *6*, 177.
- [41] B. Al-Qallaf, D. B. Das, A. Davidson, *Asia-Pac. J. Chem. Eng.* **2009**, *4*, 845.
- [42] S. Niamlang, A. Sirivat, *J. Drug Deliv.* **2009**, *16*, 378.
- [43] M. R. Prausnitz, S. Mitragotri, R. Langer, *Nat. Rev. Drug Discov.* **2004**, *3*, 115.
- [44] S. M. Flaherty, I. J. Russell, A. N. Lukashkin, *J. Drug Deliv.* **2021**, *28*, 1312.
- [45] T.-T. Liu, K. Chen, Q. Wang, *Drug Deliv. Transl. Res.* **2018**, *8*, 1025.
- [46] N. Seeger, S. Lange, S. Klein, *AAPS J.* **2015**, *16*, 759.
- [47] W. F. Beyer, D. L. Smith, *J. Pharm. Sci.* **1971**, *60*, 496.
- [48] K. Embil, G. Torosian, *J. Pharm. Sci.* **1979**, *68*, 1336.
- [49] V. Ebrahiminejad, Z. Faraji Rad, P. D. Prewett, G. J. Davies, *Beilstein J. Nanotechnol.* **2022**, *13*, 629.
- [50] Z. Faraji Rad, P. D. Prewett, G. J. Davies, *Addit. Manuf.* **2022**, *56*, 102953.
- [51] J. H. Park, M. G. Allen, M. R. Prausnitz, *J. Control Release* **2005**, *104*, 51.
- [52] H. V. Tran, F. Charleux, M. Rachik, A. Ehrlacher, M. C. Ho Ba Tho, *Comput. Methods Biomech. Biomed. Engin.* **2007**, *10*, 401.
- [53] O. A. Shergold, N. A. Fleck, D. Radford, *Int. J. Impact Eng.* **2006**, *32*, 1384.
- [54] W. Shu, H. Heimark, N. Bertollo, D. J. Tobin, E. D. O'Cearbhaill, A. N. Annaidh, *Acta Biomater.* **2021**, *135*, 403.
- [55] S. C. Meliga, J. W. Coffey, M. L. Crichton, C. Flaim, M. Veidt, M. A. F. Kendall, *Acta Biomater.* **2017**, *48*, 341.
- [56] N. Jain, V. K. Singh, S. Chauhan, *J. Mech. Behav. Biomed. Mater.* **2017**, *26*, 213.
- [57] S. A. Ranamukhaarachchi, S. Lehnert, S. L. Ranamukhaarachchi, L. Sprenger, T. Schneider, I. Mansoor, K. Rai, U. O. Hafeli, B. Stoeber, *Sci. Rep.* **2016**, *6*, 32074.

- [58] F. H. Silver, G. P. Seehra, J. W. Freeman, D. DeVore, *J. Appl. Polym. Sci.* **2002**, 86, 1978.
- [59] F. P. Beer, E. R. Johnston Jr., J. T. DeWolf, D. F. Mazurek, *Mechanics of Materials*, McGraw-Hill Education, New York, NY, USA, **2015**.
- [60] S. K. Sharma, J. Prakash, P. K. Pujari, *Phys. Chem. Chem. Phys.* **2015**, 17, 29201.
- [61] M. Sausse Lhernould, C. Gobillon, P. Lambert, *On Drug Delivery Magazine* **2013**, 29.
- [62] M. Gülçür, J.-M. Romano, P. Penchev, T. Gough, E. Brown, S. Dimov, B. Whiteside, *CIRP J. Manuf. Sci. Technol.* **2021**, 32, 311.
- [63] Y. K. Demir, Z. Akan, O. Kerimoglu, *PLoS One* **2013**, 8, e77289.
- [64] H. Joodaki, M. B. Panzer, *Proc. Inst. Mech. Eng. H.* **2018**, 232, 323.
- [65] K. S. Kim, K. Ita, L. Simon, *Eur. J. Pharm. Sci.* **2015**, 68, 137.
- [66] E. L. Zoudani, M. Soltani, *Eur. J. Pharm. Sci.* **2020**, 150, 105339.
- [67] T. Nakamura, S. Kaneko, F. Inada, M. Kato, K. Ishihara, T. Nishihara, M. A. Langthjem, in *Flow-induced Vibrations*, Academic Press, Oxford, UK 2014, Ch. 8.
- [68] S. S. Chen, M. W. Wambsganss, J. A. Jendrzejczyk, *J. Appl. Mech.* **1976**, 43, 325.
- [69] C. Y. Wang, *J. Fluid Mech.* **1968**, 32, 55.
- [70] T. Singh, R. Majithiya, R. Shaikh, Y. K. Demir, R. Donnelly, *Pharmaceutical Manufacturing and Packing Sourcer* **2010**, 15, 27-29.

5.2 Chapter Summary

In this study, a potential mass-scalable process for replication of PVA/PVP DMNPs using both primary TPP and secondary soft embossed master MN arrays was introduced. The new method showed an 86 % reduction in fabrication time for each set of ten DMNPs while maintaining high accuracy and fidelity. A series of compression and bending tests on the PVA/PVP replicas measured the failure points of 0.65 ± 0.04 N and 0.33 ± 0.02 N, respectively. Compared to insertion outcomes from the BD Ultra-Fine™ 4 mm PEN needles as the model representative, the SM value of ~ 2.5 was predicted for the current geometry ($SM > 1$). The second section of the study investigated experiments and FEA simulations on the effects of skin strains and vibrations on the mechanics of MN insertion. For instance, the FEA and experimental results indicated 32.31 % and 22.83 % reductions in the insertion force applied at 10 % skin model strains, respectively. For the vibration study, these reductions were 2.1 % and 9.8 % for insertion force for the case of 150 Hz induced vibration.

The final part of the research investigated the effects of LRA/ERM modes of low-frequency vibrations on the dissolution kinetics and concentrations of the FSS model drug. The results from confocal imaging and LC-MS analysis showed that both LRA and ERM vibrations facilitated the dissolution of the model drug and enhanced the FSS concentrations. For instance, the model drug concentration increased by 11.36 % for ERM and 12.12 % for LRA-induced vibrations when conducted at 150 Hz. The results also indicated an average twofold increase in the diffusion depth for LRA compared to the ERM-induced vibrations.

CHAPTER 6: DISCUSSION AND CONCLUSION

6.1 General

MNs have been extensively researched for TDD and diagnostics. These microdevices can facilitate a non-invasive and painless insertion with the potential for self-administration. Despite the advances in MN technology, this technique is associated with concerns such as cost-effective manufacturing, mechanical strength, and effective insertion. The partial penetration of MNs results in ineffective drug delivery or sampling. Moreover, the research outcomes may lack reliability and repeatability due to the skin's inherent elasticity, folds, and wrinkles.

To address the abovementioned issues, the literature has focused on improving the MN design, fabrication, replication, and skin insertion methods. For instance, several studies investigated geometrical features such as MN interspacing, length, base diameter, tip area, and projection density. Parts of the research also evaluated the effects of material selection, fabrication techniques, and insertion methods, such as pressing force and impact velocity for application. Therefore, current research started with a comprehensive review of the status quo to broaden the knowledge. This includes the all-inclusive skin mechanical behaviour, the effects of geometry, materials, insertion methods, and external stimulants on the MN mechanical strength, skin insertion, penetration depth, and drug diffusion. A part of the literature search was then dedicated to recent applications of AMSMs and computer simulation approaches to model MN insertion and drug diffusion. According to the promising outcomes from the literature, existing gaps were found and investigated in this research.

The thesis is divided into three main sections: MN and MB microdevices, impact applicators, and external skin stimulants. To address the aims and objectives of the study defined in sections 1.2.1 to 1.2.4, four phases of this research were conducted as follows:

1. Evaluation of the effects of different skin strains and vibrations on MN insertion and extraction mechanics, along with the investigation of model drug diffusion and concentration for vibration-induced skin subjects (sections 1.2.2 and 1.2.4).
2. Development and manufacturing of multifeatured impact applicator capable of regulatable impact speed, adjustable skin stretching, and two ERM/LRA vibration modes (sections 1.2.2 and 1.2.4).
3. Investigation of the potential biomedical application of integrated MB devices with five different geometries as an alternative for MN arrays. The study focused on the mechanical strength, insertion safety, penetration depth, and concentration gradient of a model drug (sections 1.2.1, 1.2.2 and 1.2.3).
4. Development of a novel FEA simulation paradigm using HPC to model the mechanics of MN and MB insertions into the multi-layered hyperelastic skin model incorporating skin strains and vibrations. The computer simulation also included modelling the drug diffusion and concentration gradients of different MB designs inside a multi-layered skin model (section 1.2.3).

6.2 Effects of skin strain, modes of low-frequency vibration, and impact speed on MN penetration and model drug diffusion mechanism.

The first part of this study conducted experiments to evaluate the effects of different skin strains and vibrations on the MN insertion and extraction mechanism. Thus, the force-displacement data were recorded for insertion and extraction of BD Ultra-Fine PEN needle used for insulin delivery into the PDMS artificial skin model with PLA substrate. The other part of the research investigated the effects of ERM/LRA-induced vibrations on the kinetics of FSS diffusion and concentration. This is followed by comparing the penetration efficiency of MN insertions using regulatable impact speeds and a commercial applicator. The key findings from these studies were as follows:

- The application of a custom-made skin stretching mechanism enabled skin stretching in a controlled manner, which can help mimic skin *in vivo* conditions.
- Skin strain directly correlates with the reduction of MN insertion and extraction force. 34.4 % and 57.8 % reductions were recorded for the peak insertion (F_{ins}) and extraction (F_{ext}) forces when the strain value increased from 0 % to 20 %.
- Vibration excitations on the skin facilitated the insertion and extraction process by reducing the insertion and extraction force. By increasing the frequency from 0 Hz to 250 Hz, the F_{ins} reduced by 12.24 %, while F_{ext} remarkably reduced by 43.01 %.
- DMNPs can provide a controlled release of the model drug in a certain insertion time. Hence, the application of PVA/PVP DMNPs facilitated the study of the effects of vibrations on the model drug diffusion depth and concentration. By increasing the ERM-induced vibration from 0 Hz to 250 Hz, the diffusion depth and concentration of the FSS model drug increased by 41.98 ± 18.35 % and 10.98 ± 3.6 %, respectively.
- LRA-induced vibrations of DMNPs also enhanced the diffusion depth and concentration of the model drug inside the skin. Increasing the LRA-induced vibration from 0 Hz to 200 Hz improved the diffusion depth and concentration of the FSS drug model by 40.54 ± 13.1 % and 12.88 ± 3.22 %, respectively.
- Impact speed significantly increased APE and FPL by increasing the impact velocity from 1.5 m/s to 4.5 m/s, an average increase of 69.89 ± 7.62 % observed for APE values.
- Commercial applicators with fixed impact speed and without the capability for controlled skin stretching can only be used for specific MN patch designs. However, our prototype impact applicator indicated the potential to be used for various MN patch and MB designs (see [section 6.3](#)).

6.3 Design, fabrication, and assembly of multifeatured impact applicator prototypes for drug delivery and diagnostics applications.

Considerable parts of the research required the application of solid and dissolving MNs on the skin subjects while incorporating different impact speeds, ERM/LRA modes of vibrations, and skin surface stretching. Thus, a novel multifeatured impact applicator that could combine MN impact velocity, vibration excitation, and skin strain was prototyped and provisionally patented (Provisional Patent Application No. 2022903335). Different experimental tests, such as high-speed camera, circuit electric charge flow, voltage, and spring mechanism, were conducted to measure and specify the impact velocity, vibration frequency, and strain ranges based on different configurations. The current design introduced three novel arrangements, which are as follows:

- Regulatable impact velocity via two mechanisms of the grooved plunger and floating plate. This arrangement enables both pre-set and miniature speed-adjusting capabilities tailorable to different MN patch attributes. High-speed camera tests showed that the impact speeds varied between ~ 1.5 m/s and ~ 5.5 m/s at different positions, with the potential for broader velocity ranges based on the spring stiffness.
- A combined ERM/LRA vibration excitations were induced on the MN patches using a simple electronic circuit designed for frequency adjustments and powered by a rechargeable lithium polymer battery. In this study, based on the current/voltage measurements in the circuit, the estimated range of frequencies was between 50 Hz to 250 Hz for ERM and 50 Hz to 200 Hz for LRA modes. Broader ranges of optimum frequency can also be achieved based on the selection of micro-vibration devices and circuit components.
- Simple arm mechanism design for skin stretching before insertion of MN patch. The mechanism holds pairs of torsion and compression springs for stretching and height

alignments. The stretching mechanism enables mimicking of the skin *in vivo* condition and applies to different age brackets and skin locations. The experiments measured up to ~22 N skin strains for different arm orientations. Similarly, the stretch intensity can be changed based on the selection of torsion and compression springs.

6.4 Evaluating the potential application of MB devices for biomedical applications.

MN array fabrication remains a costly, inefficient, and time-consuming method of delivering target drugs or sampling. The MN arrays with ten to thousands of projections result in partial penetration and can lead to a “bed of nails” effect. Therefore, single integrated MB devices with side channels were proposed as a potential alternative for MN arrays. Different blade angles and eccentricity levels were included in five nominated geometrical designs. To estimate the SM value, the thermoplastic Zeonor 1060R MBs replicas were experimentally tested and combined with FEA simulation of MB insertion into the multi-layered hyperelastic skin model. This study also aimed to evaluate the diffusion kinetics for various MB geometrical designs using a combination of experimental tests on porcine abdominal skin and simulation of model drug diffusion inside a multi-layered skin model. The key findings of this study are as follows:

- Due to the integrated and compact nature of the proposed MB microdevices, through modification to Data File codes, five different MBs with various geometrical parameters were fabricated simultaneously on a 25 × 25 mm ITO slide. The overall TPP print time was reduced by ~ 63.3 % compared to a 9 × 9 MN array on a similar substrate, making MBs microdevices remarkably time-effective for mass-scale manufacturing.
- FSS-coated MBs enabled the platform for comparison between the effects of geometry on the diffusion depth and concentration of model drug using both *in vitro* experiments and simulations ([section 6.5](#)).

- Increasing MB blade angles from 60°, 90°, 120° to 180° increased the initial modulus and failure points from 2.71 to 17.03 N/mm while it reduced the FPL values and penetration depth from 28.58 ± 7.28 % to 16.25 ± 4.3 %. Moreover, including the eccentricity factor enhanced the FPL values and reduced the initial stiffness. Eccentricity also introduced uneven distribution of the model drug. During the tests, the square type (180°) MB possessed the highest mechanical strength. However, the outcomes from drug diffusion and penetration depth showed significantly different results to other MBs and hence concluded to be the least effective design.
- Despite relatively low FPL results on the full-thickness porcine abdominal skin, all replicated MBs successfully penetrated the SC layer and indicated SMs greater than unity ($SM > 1$).
- MBs with 900 μm overall height yielded ~ 849.29 μm , which indicates ~ 5.64 % shrinkage over all geometries. Compared to the case of the 9×9 MN array, which possesses an average height of ~ 1.05 mm and is based on a 1.1 mm design with ~ 4.55 %, MBs have a similar shrinkage rate. However, during the skin insertion tests at 4.5 m/s impact speed, FSS diffusion depth for MBs was almost three times more than MN arrays (Figure 4).

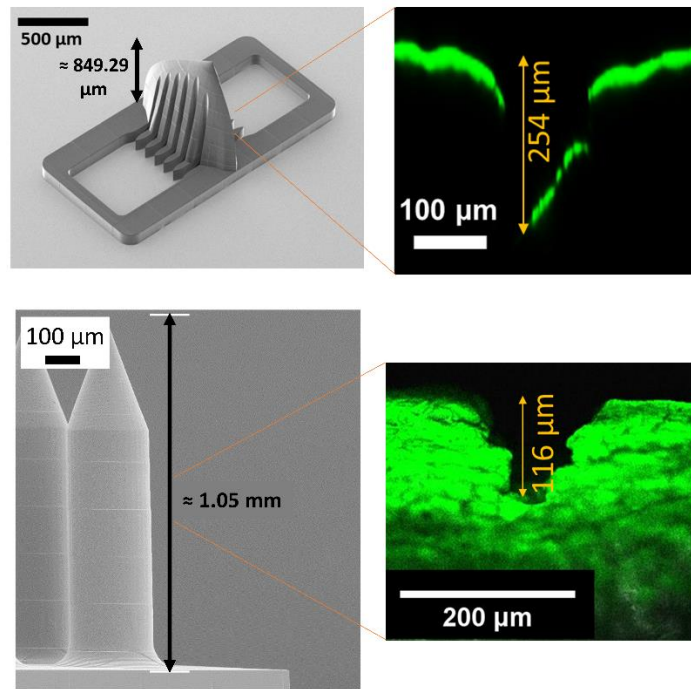


Figure 4: Side-by-side comparison of a sample thermoplastic MB with corresponding MN array, with respective diffusion depths at 4.5 m/s impact insertion.

6.5 Investigations on simulation of drug diffusion and novel FEA paradigm for MN and MB skin insertions incorporating skin strains and vibration.

Despite the significance of experimental investigations, the reliability and reproducibility of research outcomes remain challenging. To address this issue, AMSM and computer simulations can enable significantly less different test results. During this research, computer simulations of MN skin insertion and drug diffusion into the multi-layered skin model were performed using ANSYS (2020 R1, ANSYS, Canonsburg, Pennsylvania, USA) and COMSOL (COMSOL Multiphysics, COMSOL AB, Sweden) software packages, respectively. The main considerations for these simulations were as follows:

- Axisymmetric and planer symmetrical analysis for MN and MB insertion into the multi-layered skin hyperelastic model, with interconnected modules to incorporate the effects of skin strain and vibration.

- Drug-coated MB delivery using mathematical decay function to estimate the drug concentration and diffusion flux for different MB designs over time.
- The simulation results on MBs (Types 1-5) showed a 27.3 % higher drug concentration near the MB Type 3 tip, which was the highest concentration among concentric MBs. At the subcutaneous junction, this increase in the concentration was less noticeable (17.7 %).
- FEA simulations of MN insertions on a multi-layered hyperelastic skin model indicated that increasing the skin strain from 0 % to 10 % resulted in a 32.31 % reduction in F_{ins} .
- A similar FEA setup to evaluate the effects of 0 to 250 Hz vibration frequencies indicated a 20.41 % reduction in F_{ins} .

6.6 Outcome and significance of the Study

This research investigated the MN technology for coated and dissolving TDD using MN patches and various patented MB microdevices. While Zeonor 1060R thermoplastics were used for coated drug delivery of MN arrays and MBs, process optimisations were carried out to optimise the PVP: PVA ratio based on the composition and MW for dissolving MNs. An in-depth investigation was also conducted on reducing TPP print time through parameter optimisation and modifying the general writing language (GWL) writing codes (see [Appendix C](#)).

To address the MN application method, a novel impact applicator with multiple features was designed, manufactured, and provisionally patented (Application No. 2022903335). The prototype applicator can regulate impact velocity and skin surface stretching and induce two ERM/LRA vibrations modes during the MN insertions. This is followed by an insight into the effects of external stimulants, such as different skin strains and vibration, on the mechanics of MN insertion and extraction (see [Appendix B](#)).

During the research, skin insertion tests incorporated a new proposed skin stretching mechanism to control stretching intensity, mimic the skin in vivo condition, and achieve reproducible and reliable results. The concentration of the model drug was determined in the presence of two modes of ERM and LRA vibrations during the skin insertion of encapsulated DMNPs and compared with no-vibration scenarios. The experimental outcome was then coupled with theoretical analysis and finite element method to validate the results. The current research also proposed a new FEA paradigm to simulate the penetration of MN models into the multi-layered skin model considering the effects of different skin strains and vibration excitations, which are solved by the HPC (see [Appendix A](#)).

6.7 Recommendations for future research

6.7.1 *General*

Undertaking safe, time-effective, cost-beneficial design and manufacturing techniques can pave the way for applying TDD and diagnostics using MN technology. To achieve these goals, the following sections focus on three avenues for future research. The initial recommendation discusses the need for mechanical strength and solubility of PVA/PVP MN patches with different compositions ([Section 6.7.2](#)). The following section explains a particular design and its related replication method ([Section 6.7.3](#)) for potential application in sampling biofluids for monitoring and diagnostics. Further advancement to impact applicator is also explained ([Section 6.7.4](#)) to enable for transfer and collection of the biofluids.

6.7.2 *Material composition optimisation for PVA/PVP MN patches for Sampling*

The water solubility of PVA/PVP MN patches depends mainly on the composition ratio and MW. One study can investigate the effects of different PVA/PVP ratios and varying MWs to evaluate the mechanical strength, drug dissolution kinetics, and potential for sampling biofluids. During the current study, a range of 5 % to 20 % (w/v) PVA (30 kDa) with constant 50 % (w/v) PVP (40 kDa) in D.I water was prepared and optimised for replication of DMNPs

for drug delivery purposes. Increasing the PVA proportion and MW can improve the mechanical strength and reduce the dissolution rate, which can be suitable for sampling biofluids such as ISF.

6.7.3 *MNs for monitoring and diagnostics*

Adjustments to the MN patch material selection and geometrical parameters can facilitate sampling biofluids such as ISF. Here, a proposal for future research is made to investigate the MN patches replicated using PVA (87 kDa) 15 % (w/v) / PVP (40 kDa) 50 % (w/v) in Milli-Q water as a potential candidate for sampling ISF. The proposed design includes MN projections with side channels, a parabolic concave base, and a central channel for transferring these biofluids. PVA/PVP is a decent candidate as the natural dehydration process creates an inward curve on the opposite side of the patch which is suitable for the accumulation of biofluids.

A solution of PVA (87 kDa) 15 % (w/v) and PVP (40 kDa) 50 % (w/v) was made in 20 mL Milli-Q water according to the process explained in journal article 4 ([Chapter 5](#)). 100 μ L of the PVA/PVP solution is poured on the PDMS mould cavity, placed inside the PDMS-based centrifuge tube and centrifuged using the swinging bucket (90° angle) at 4000 rpm for 30 minutes (Figure 5A). Another 50 μ L (or similar) of PVA/PVP solution was gently poured on the rest of the solution to ensure that the circular opening was almost filled.

The sample is then placed inside a custom-made 3D-printed holder. A 1 mm thick steel microrod is inserted into the centre of the mould to displace the PVA/PVP solution. The entire setup is placed inside the laboratory incubator at 37° for 72 hr. Subsequently, the PVA/PVP MN patch replica is peeled off from the PDMS mould; and the microrod is carefully removed from the centre. This approach resulted in a central microchannel for transferring the biofluids from the MN patch side to the opposite natural microwell. This natural microwell is created

through capillary effects at the interface between PVA/PVP solution with outer circular edges and Centred microrod during dehydration (Figure 5B).

Figure 5C shows the SEM images from the final PVA/PVP MN patch replica. A total of 90 MN projections with side channels faced the main central channel. The projections are located on a parabolic concave base with a vertex-focal point distance of 5 mm, possessing 400 μm and 100 μm outer and inner base thicknesses, respectively. The integration of open channel projections and the non-linear base is linked to a 1 mm microchannel connecting both sides of the replicated MN patch.

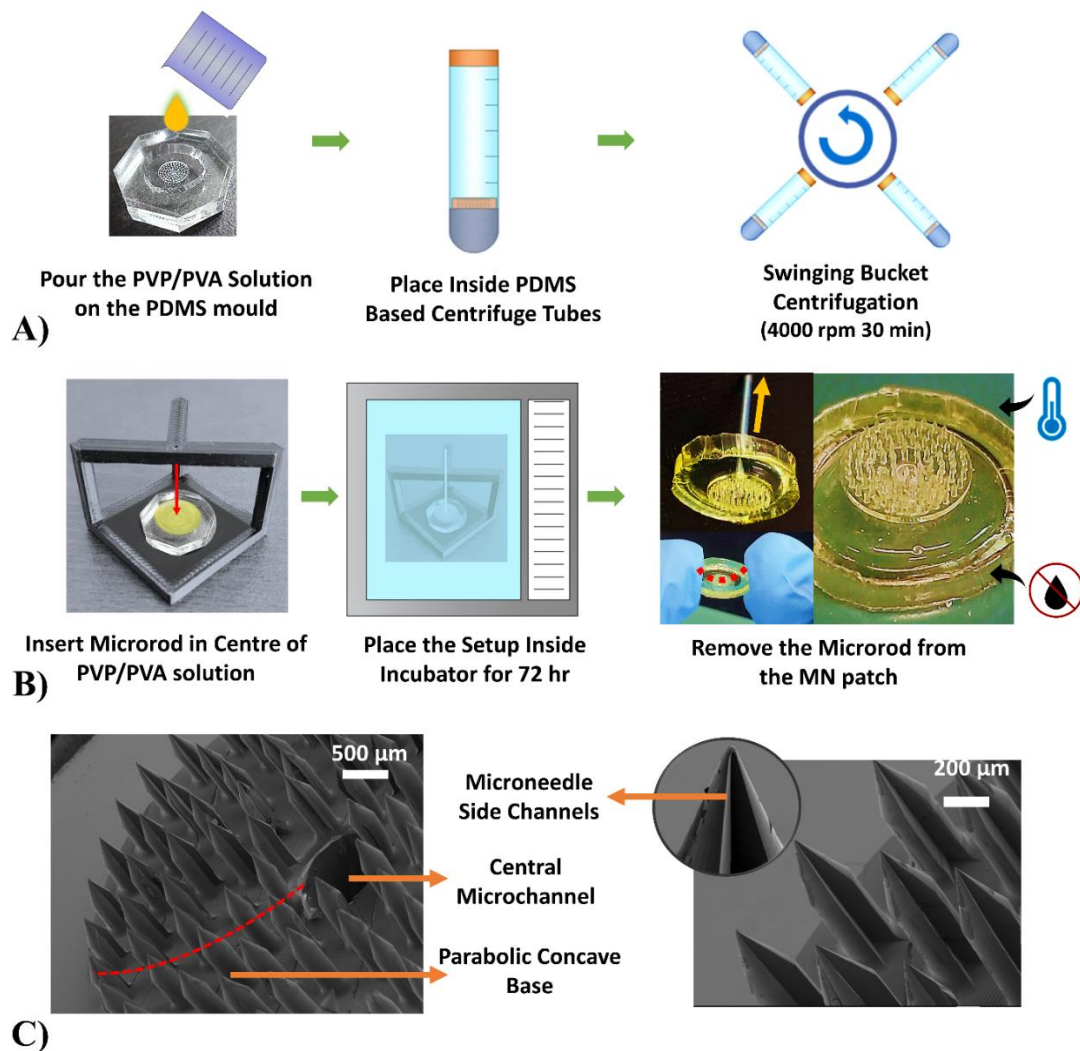


Figure 5: The PVA/PVP MN patch replication for the sampling process. The procedure involves (A) swinging bucket centrifugation, followed by (B) microrod insertion and curing

inside the incubator. (C) The SEM images show the geometrical features, such as the parabolic concave base, projection side channel, and central microchannel for biofluid transfer.

6.7.4 Advancement for impact applicator

The provisionally patented impact applicator can be further advanced to contain features such as micropumps for sampling biofluids. When combined with the stretching part, the volume of ISF sampling is expected to improve remarkably. The following section details a proposal to test the PVA/PVP MN patch design explained above for sampling purposes. The general aim is to create negative pressure at the insertion area to facilitate the transfer and collection of the biofluid.

Replicated MN patches can be integrated into the multifeatured impact applicators to enhance the penetration and extraction volume. This can influence the reliability and accuracy of POC monitoring and diagnostics. The future recommendation focuses on the geometrical and administrative development of MN patches with a side/central channel to generate negative pressure at the insertion area when integrated with a micropump system. As suggested in Figure 6A, the MN patch's geometrical parameters, such as MN side channels, central microchannel, and natural inward curves, can play an important role in transferring and collecting samples. As part of the applicator's development, a micropump system capable of adjusting the negative pressure can also be connected to the MN patches through the internal pathway inside the applicator plunger (see Figure 6A). To avoid vacuum leakage, the MN can be attached to the plunger using a soft rubber/foam layer with double-sided tape. This proposed assembly can create negative pressure at the skin insertion area, facilitating biofluid extraction. Moreover, as shown in Figure 6B, the recommended impact applicator can be integrated with sampling test kits or POC diagnostics and monitoring systems to maximise the sampling volume and improve the accuracy and reliability of the test results.

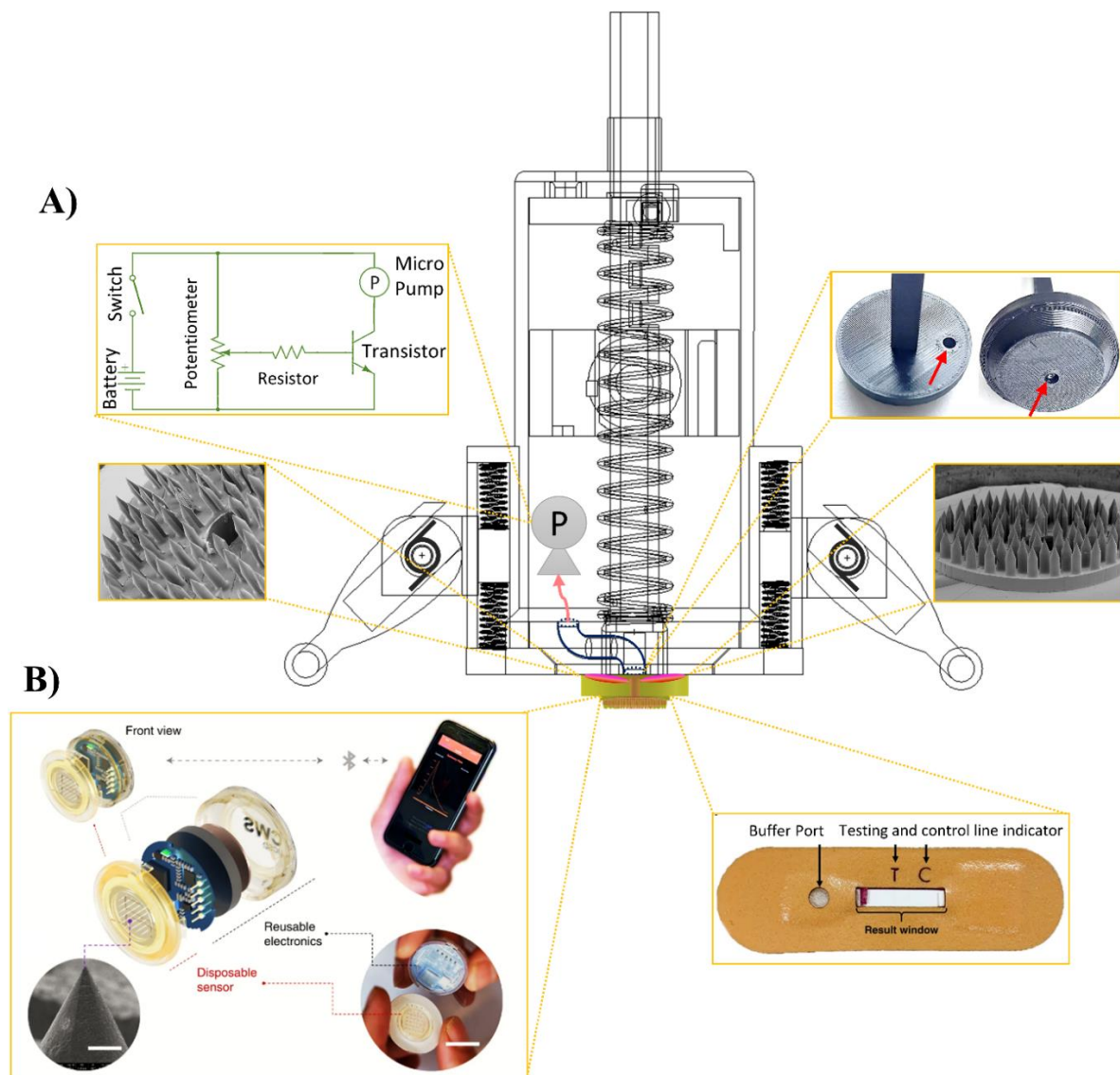


Figure 6: Proposed impact applicator advancements and possible integration with existing technology. A) MNs for sampling attached to the rubber-sealed plunger. The centre of the plunger is connected to the regulated micropump placed inside the applicator. The interconnected channels enable the negative pressure to reach the insertion area. B) The applicator with the capability for regulating impact skin, skin surface stretching, micro pump negative pressure, and ERM/LRA modes of vibration can be integrated with existing diagnostic test kits (Figure reproduced with permission, Nature 2020) or POC monitoring systems (Figure reproduced with permission, Nature 2022) to maximise the sampling and improves the reliability and accuracy of the results.

REFERENCES

- Aldawood, FK, Andar, A & Desai, S 2021, 'A Comprehensive Review of Microneedles: Types, Materials, Processes, Characterizations and Applications', *Polymers (Basel)*, vol. 13, no. 16.
- Bhatnagar, S, Dave, K & Venuganti, VVK 2017, 'Microneedles in the clinic', *J Control Release*, vol. 260, pp. 164-82.
- Cantor, A 2005, *Non-Skin-Contacting Microneedle Array Applicator*, 3M Innovative Properties Co, US20080009811A1.
- Cantor, A, Frederickson, FL, Johnson, PR & Ringsred, TK 2008, *Low-Profile Microneedle Array Applicator*, Kindeva Drug Delivery LP, US20080114298A1.
- Cheung, K & Das, DB 2016, 'Microneedles for drug delivery: trends and progress', *Drug Deliv*, vol. 23, no. 7, pp. 2338-54.
- Cheung, K, Han, T & Das, DB 2014, 'Effect of force of microneedle insertion on the permeability of insulin in skin', *J Diabetes Sci Technol*, vol. 8, no. 3, pp. 444-52.
- Clarke, GM, Delmore, MD, Domroese, MK, Ferber, RH, Jacobs, JD, Keister, JC & Frederickson, FL 2003, *Microneedle devices and microneedle delivery apparatus*, US8900194B2.
- Cordeiro, AS, Tekko, IA, Jomaa, MH, Vora, L, McAlister, E, Volpe-Zanutto, F, Nethery, M, Baine, PT, Mitchell, N, McNeill, DW & Donnelly, RF 2020, 'Two-Photon Polymerisation 3D Printing of Microneedle Array Templates with Versatile Designs: Application in the Development of Polymeric Drug Delivery Systems', *Pharm Res*, vol. 37, no. 9, p. 174.
- Cormier, MJN, Young, WA, Johnson, JA, Daddona, PE & Ameri, M 2003, *Transdermal drug delivery devices having coated microprotrusions*, WO2004002566A1.

Date, AA & Nagarsenker, MS 2008, 'Parenteral microemulsions: an overview', *Int J Pharm*, vol. 355, no. 1-2, pp. 19-30.

Desai, S, Craps, M & Esho, T 2013, 'Direct writing of nanomaterials for flexible thin-film transistors (fTFTs)', *The International Journal of Advanced Manufacturing Technology*, vol. 64, no. 1, pp. 537-43.

Dharadhar, S, Majumdar, A, Dhoble, S & Patravale, V 2019, 'Microneedles for transdermal drug delivery: a systematic review', *Drug Dev Ind Pharm*, vol. 45, no. 2, pp. 188-201.

Dixon, RV, Skaria, E, Lau, WM, Manning, P, Birch-Machin, MA, Moghimi, SM & Ng, KW 2021, 'Microneedle-based devices for point-of-care infectious disease diagnostics', *Acta Pharm Sin B*, vol. 11, no. 8, pp. 2344-61.

Donnelly, RF, Raj Singh, TR & Woolfson, AD 2010, 'Microneedle-based drug delivery systems: microfabrication, drug delivery, and safety', *Drug Deliv*, vol. 17, no. 4, pp. 187-207.

Donnelly, RF, Singh, TR, Morrow, DI & Woolfson, AD 2012, *Microneedle-Mediated Transdermal and Intradermal Drug Delivery*, John Wiley & Sons, Hoboken, NJ, USA.

Donnelly, RF, Raj Singh, TR, Larrañeta, E & McCrudden, M 2018, *Microneedles for Drug and Vaccine Delivery and Patient Monitoring*, 1st edn, John Wiley & Sons Ltd, Queen's University Belfast, UK.

Donnelly, RF, Garland, MJ, Morrow, DIJ, Migalska, K, Singh, TRR, Majithiya, R & Woolfson, AD 2010, 'Optical coherence tomography is a valuable tool in the study of the effects of microneedle geometry on skin penetration characteristics and in-skin dissolution', *Journal of controlled release : official journal of the Controlled Release Society*, vol. 147, no. 3, pp. 333-41.

Donnelly, RF, Garland Mj Fau - Morrow, DIJ, Morrow Di Fau - Migalska, K, Migalska K Fau - Singh, TRR, Singh Tr Fau - Majithiya, R, Majithiya R Fau - Woolfson, AD & Woolfson, AD 2010, 'Optical coherence tomography is a valuable tool in the study of the effects of microneedle geometry on skin penetration characteristics and in-skin dissolution', *Journal of Controlled Release*, vol. 147, no. 1873-4995 (Electronic), pp. 333-41.

Ebrahiminejad, V, Faraji Rad, Z, Prewett, PD & Davies, GJ 2022, 'Fabrication and testing of polymer microneedles for transdermal drug delivery', *Beilstein J Nanotechnol*, vol. 13, pp. 629-40.

Ebrahiminejad, V, Prewett, PD, Davies, GJ & Faraji Rad, Z 2022, 'Microneedle Arrays for Drug Delivery and Diagnostics: Toward an Optimized Design, Reliable Insertion, and Penetration', *Advanced Materials Interfaces*, vol. 9.

Faraji Rad, Z, Prewett, PD & Davies, GJ 2022, 'Parametric optimization of two-photon direct laser writing process for manufacturing polymeric microneedles', *Additive Manufacturing*, vol. 56, p. 102953.

Faraji Rad, Z, Nordon, RE, Davies, GJ, Anthony, CJ & Prewett, PD 2020, *Microfluidic devices and fabrication*, NewSouth Innovations Pty Ltd, University of Birmingham, US. 10850082B2.

Faraji Rad, Z, Nordon, RE, Anthony, CJ, Bilston, L, Prewett, PD, Arns, JY, Arns, CH, Zhang, L & Davies, GJ 2017, 'High-fidelity replication of thermoplastic microneedles with open microfluidic channels', *Microsystem Nanoengineering*, vol. 3, p. 17034.

Griffiths, CA 2008, 'Micro Injection Moulding: Tooling and Process Factors', University of Wales, Cardiff

Gülçür, M, Romano, J-M, Penchev, P, Gough, T, Brown, E, Dimov, S & Whiteside, B 2021, 'A cost-effective process chain for thermoplastic microneedle manufacture combining laser micro-machining and micro-injection moulding', *CIRP Journal of Manufacturing Science and Technology*, vol. 32, pp. 311-21.

Hong, X, Wei, L, Wu, F, Wu, Z, Chen, L, Liu, Z & Yuan, W 2013, 'Dissolving and biodegradable microneedle technologies for transdermal sustained delivery of drug and vaccine', *Drug Des Devel Ther*, vol. 7, pp. 945-52.

Hopcroft, MA, Nix, WD & Kenny, TW 2010, 'What is the Young's Modulus of Silicon?', *Journal of Microelectromechanical Systems*, vol. 19, no. 2, pp. 229-38.

Indermun, S, Luttge, R, Choonara, YE, Kumar, P, du Toit, LC, Modi, G & Pillay, V 2014, 'Current advances in the fabrication of microneedles for transdermal delivery', *J Control Release*, vol. 185, pp. 130-8.

Inou, A, Takigawa, M, Sekiguchi, T, Nakahara, K & Watanabe, T 2010, *Transdermal administration device*, WO2010010974.

Ita, K 2015, 'Transdermal Delivery of Drugs with Microneedles-Potential and Challenges', *Pharmaceutics*, vol. 7, no. 3, pp. 90-105.

Jacoby, E, Jarrahan, C, Hull, HF & Zehring, D 2015, 'Opportunities and challenges in delivering influenza vaccine by microneedle patch', *Vaccine*, vol. 33, no. 37, pp. 4699-704.

Jung, JH & Jin, SG 2021, 'Microneedle for transdermal drug delivery: current trends and fabrication', *J Pharm Investig*, pp. 1-15.

Keum, DH, Jung, HS, Wang, T, Shin, MH, Kim, YE, Kim, KH, Ahn, GO & Hahn, SK 2015, 'Microneedle biosensor for real-time electrical detection of nitric oxide for in situ cancer diagnosis during endomicroscopy', *Adv Healthc Mater*, vol. 4, no. 8, pp. 1153-8.

Khan, S, Hasan, A, Attar, F, Babadaei, MMN, Zeinabad, HA, Salehi, M, Alizadeh, M, Hassan, M, Derakhshankhah, H, Hamblin, MR, Bai, Q, Sharifi, M, Falahati, M & Ten Hagen, TLM 2021, 'Diagnostic and drug release systems based on microneedle arrays in breast cancer therapy', *J Control Release*, vol. 338, pp. 341-57.

Khanna, P, Luongo, K, Strom, JA & Bhansali, S 2010, 'Sharpening of hollow silicon microneedles to reduce skin penetration force', *Journal of Micromechanics and Microengineering*, vol. 20, no. 4, p. 045011.

Kim, YC, Park, JH & Prausnitz, MR 2012, 'Microneedles for drug and vaccine delivery', *Adv Drug Deliv Rev*, vol. 64, no. 14, pp. 1547-68.

Larrañeta, E, Lutton, REM, Woolfson, AD & Donnelly, RF 2016, 'Microneedle arrays as transdermal and intradermal drug delivery systems: Materials science, manufacture and

commercial development', *Materials Science and Engineering: R: Reports*, vol. 104, pp. 1-32.

Lastovich, AG, Evans, JD & Pettis, RJ 2002, *Microdevice and Method of Manufacturing a Microdevice*, Becton Dickinson and Co, WO2002005890.

Leboulanger, B, Guy, RH & Delgado-Charro, MB 2004, 'Reverse iontophoresis for non-invasive transdermal monitoring', *Physiol Meas*, vol. 25, no. 3, pp. R35-50.

Lee, D-S, Li, CG, Ihm, C & Jung, H 2018, 'A three-dimensional and bevel-angled ultrahigh aspect ratio microneedle for minimally invasive and painless blood sampling', *Sensors and Actuators B: Chemical*, vol. 255, pp. 384-90.

Lee, G, Ma, Y, Lee, Y-h & Jung, H 2018, 'Clinical Evaluation of a Low-pain Long Microneedle for Subcutaneous Insulin Injection', *BioChip Journal*, vol. 12, no. 4, pp. 309-16.

Lee, J & Hong, S 2006, *Microneedle roller*, KR100874254B1.

Lee, JW, Han, MR & Park, JH 2013, 'Polymer microneedles for transdermal drug delivery', *J Drug Target*, vol. 21, no. 3, pp. 211-23.

Leone, M, van Oorschot, BH, Nejadnik, MR, Bocchino, A, Rosato, M, Kersten, G, O'Mahony, C, Bouwstra, J & van der Maaden, K 2018, 'Universal Applicator for Digitally-Controlled Pressing Force and Impact Velocity Insertion of Microneedles into Skin', *Pharmaceutics*, vol. 10, no. 4.

Lin, C, Clark, R, Tu, P, Bosworth, HB & Zullig, LL 2017, 'Breast cancer oral anti-cancer medication adherence: a systematic review of psychosocial motivators and barriers', *Breast Cancer Res Treat*, vol. 165, no. 2, pp. 247-60.

Madden, J, O'Mahony, C, Thompson, M, O'Riordan, A & Galvin, P 2020, 'Biosensing in dermal interstitial fluid using microneedle based electrochemical devices', *Sensing and Bio-Sensing Research*, vol. 29, p. 100348.

Markovsky, E, Baabur-Cohen, H, Eldar-Boock, A, Omer, L, Tiram, G, Ferber, S, Ofek, P, Polyak, D, Scomparin, A & Satchi-Fainaro, R 2012, 'Administration, distribution, metabolism and elimination of polymer therapeutics', *J Control Release*, vol. 161, no. 2, pp. 446-60.

Mi-young, K & Tae-gyu, C 2018, *Skin ultrasonics injector*, KR102085434B1.

Miller, P, Moorman, M, Manginell, R, Ashlee, C, Brener, I, Wheeler, D, Narayan, R & Polsky, R 2016, 'Towards an Integrated Microneedle Total Analysis Chip for Protein Detection', *Electroanalysis*, vol. 28, no. 6, pp. 1305-10.

Miyano, T, Tobinaga, Y, Kanno, T, Matsuzaki, Y, Takeda, H, Wakui, M & Hanada, K 2005, 'Sugar Micro Needles as Transdermic Drug Delivery System', *Biomedical Microdevices*, vol. 7, no. 3, pp. 185-8.

Niinomi, M & Nakai, M 2011, 'Titanium-Based Biomaterials for Preventing Stress Shielding between Implant Devices and Bone', *Int J Biomater*, vol. 2011, p. 836587.

Olatunji, O, Das, DB, Garland, MJ, Belaid, L & Donnelly, RF 2013, 'Influence of array interspacing on the force required for successful microneedle skin penetration: theoretical and practical approaches', *J Pharm Sci*, vol. 102, no. 4, pp. 1209-21.

Palmer, P, J. 2001, *Method and apparatus for enhancing penetration of a member for the intradermal sampling or administration of a substance*, Becton Dickinson and Co, US6537242B1.

Park, JH, Allen, MG & Prausnitz, MR 2005, 'Biodegradable polymer microneedles: fabrication, mechanics and transdermal drug delivery', *J Control Release*, vol. 104, no. 1, pp. 51-66.

Park, S 2008, *Manufacturing method of microneedle adhesion of ultrasonic vibration skin stimulator*, KR101055698B1.

Pettis, RJ, Martin, FE & Kaestner, SA 2009, *Microneedle-based pen device for drug delivery and method for using same*, Becton Dickinson and Co, US8900186B2.

Prausnitz, MR, Allen, MG & Gujral, IJ 1999, *Microneedle drug delivery device*, Georgia Tech Research Corp Valeritas Inc, US6611707B1.

Prausnitz, MR, Allen, MG, Henry, S, McAllister, DV, Ackley, DE & Jackson, T 2004, *Devices and methods for enhanced microneedle penetration of biological barriers*, Georgia Tech Research Corp Valeritas Inc, US6743211B1.

Ranamukhaarachchi, SA & Stoeber, B 2019, 'Determining the factors affecting dynamic insertion of microneedles into skin', *Biomed Microdevices*, vol. 21, no. 4, p. 100.

Rau, JL 2005, 'The inhalation of drugs: advantages and problems', *Respir Care*, vol. 50, no. 3, pp. 367-82.

Ringsred, TK & Frederickson, FL 2015, *Microneedle array applicator and retainer*, US9174035B2.

Romanyuk, AV, Zvezdin, VN, Samant, P, Grenader, MI, Zemlyanova, M & Prausnitz, MR 2014, 'Collection of analytes from microneedle patches', *Anal Chem*, vol. 86, no. 21, pp. 10520-3.

Samant, PP & Prausnitz, MR 2018, 'Mechanisms of sampling interstitial fluid from skin using a microneedle patch', *Proc Natl Acad Sci U S A*, vol. 115, no. 18, pp. 4583-8.

Sammoura, F, Kang, J, Heo, Y-M, Jung, T & Lin, L 2006, 'Polymeric microneedle fabrication using a microinjection molding technique', *Microsystem Technologies*, vol. 13, no. 5-6, pp. 517-22.

Sausse, M, Deleers, M, Vandormael, D & Lenders, C 2012, *Devices for puncturing a human or animal body's membrane*, WO2012126784A1.

Seung-goo, J & Geun-sik, K 2015, *Device for injecting drug into skin*, KR101608179B1.

Shelke, NB, James, R, Laurencin, CT & Kumbar, SG 2014, 'Polysaccharide biomaterials for drug delivery and regenerative engineering', *Polymers for Advanced Technologies*, vol. 25, no. 5, pp. 448-60.

Shu, W, Heimark, H, Bertollo, N, Tobin, DJ, O'Cearbhaill, ED & Annaidh, AN 2021, 'Insights into the mechanics of solid conical microneedle array insertion into skin using the finite element method', *Acta Biomaterialia*, vol. 135, pp. 403-13.

Singh, T, Majithiya, R, Shaikh, R, Demir, YK & Donnelly, R 2010, 'Microneedle Magic', *Pharmaceutical Manufacturing and Packing Sourcer*, vol. 15, pp. 27-9.

Tehrani, F, Teymourian, H, Wuerstle, B, Kavner, J, Patel, R, Furnidge, A, Aghavali, R, Hosseini-Toudeshki, H, Brown, C, Zhang, F, Mahato, K, Li, Z, Barfidokht, A, Yin, L, Warren, P, Huang, N, Patel, Z, Mercier, PP & Wang, J 2022, 'An integrated wearable microneedle array for the continuous monitoring of multiple biomarkers in interstitial fluid', *Nat Biomed Eng*, vol. 6, no. 11, pp. 1214-24.

Tokumoto, S, Matsudo, T & Kuwahara, T 2007, *rasdemal drug administration appartus having microneedles*, WO2007091608

Trautman, JC & Olson, L 2006, *Self-actuating applicator for microprojection array*.

van der Maaden, K, Sekerdag, E, Jiskoot, W & Bouwstra, J 2014, 'Impact-insertion applicator improves reliability of skin penetration by solid microneedle arrays', *AAPS J*, vol. 16, no. 4, pp. 681-4.

Vaxxas 2023, *Technology Platform*, viewed 21 May 2023, <<https://www.vaxxas.com/technology-platform/>>.

Verbaan, FJ, Bal, SM, van den Berg, DJ, Dijksman, JA, van Hecke, M, Verpoorten, H, van den Berg, A, Luttge, R & Bouwstra, JA 2008, 'Improved piercing of microneedle arrays in dermatomed human skin by an impact insertion method', *J Control Release*, vol. 128, no. 1, pp. 80-8.

Vicente-Perez, EM, Quinn, HL, McAlister, E, O'Neill, S, Hanna, LA, Barry, JG & Donnelly, RF 2016, 'The Use of a Pressure-Indicating Sensor Film to Provide Feedback upon Hydrogel-Forming Microneedle Array Self-Application In Vivo', *Pharm Res*, vol. 33, no. 12, pp. 3072-80.

Waghule, T, Singhvi, G, Dubey, SK, Pandey, MM, Gupta, G, Singh, M & Dua, K 2019, 'Microneedles: A smart approach and increasing potential for transdermal drug delivery system', *Biomed Pharmacother*, vol. 109, pp. 1249-58.

Wilkinson, BJ & Newby, M 2003, *Method and device for intradermally delivering a substance*, Becton Dickinson, WO2003084598.

Yang, J, Liu, X, Fu, Y & Song, Y 2019, 'Recent advances of microneedles for biomedical applications: drug delivery and beyond', *Acta Pharm Sin B*, vol. 9, no. 3, pp. 469-83.

Yang, M & Zahn, JD 2004, 'Microneedle insertion force reduction using vibratory actuation', *Biomed Microdevices*, vol. 6, no. 3, pp. 177-82.

APPENDIX A: High-Performance Computing

MN-skin insertion mechanics in Chapters 4 and 5 were simulated using ANSYS workbench (2021 R2 version). The simulation was initiated with MN insertion into the multi-layered hyperelastic skin model. This was followed by the MN insertion incorporating external effects such as skin strain and vibration excitation. During the simulation, ANSYS modules of Modal, Harmonic Response, External Data, Static Structural, and Explicit Dynamics were interconnected to perform the analyses. For vibration excitation, the results from Modal, Harmonic Response, and External Data were imported into the solution level of the Static Structural module to load the vibration displacements. These results further became the initial conditions, where the actual penetration was modelled using Explicit Dynamics. This module incorporates an erosion algorithm that removes the elements that reach the point of material failure. The run time for Explicit Dynamics analysis depends on the smallest element in the overall mesh. Large deformations reduce the minimum distance between these elements, which results in the reduction of time steps. Penetration and impact modelling using explicit methods are associated with crushing the contact elements, which run the risk of increasing the overall run time. Equation A.1 shows the effects of minimum elemental size (h) and speed of sound propagating through certain materials (c) on the overall time step (Δt).

$$\Delta t \leq f * \left(\frac{h}{c}\right)_{min} \quad (\text{A.1})$$

Methods such as mass scaling with Courant-Friedrichs–Lewy (CFL) time step of 1 picosecond and meshing techniques such as hexahedron significantly prevented extensive run time. Moreover, HPC systems were used to distribute the simulation jobs between multiple CPU cores. Following the completion of HPC tutorials, the UniSQ HPC facility was made accessible to run large simulations with several nodes simultaneously.

A.1 High-performance computing paradigm

Figure A.1 indicates the link between the user's database, the HPC directory, and the mechanism for transferring job files across the systems. Initially, a journal file was generated to record the execution process of the ANSYS model. The ANSYS Journal file includes opening, unblocking, and updating the existing model. Then, the journal file, ANSYS.wbpj, and project files were transferred via File Zilla software to the HPC directory. A Shell Code (section A.2) was further created containing the information for loading ANSYS software and allocating nodes, CPUs, and memory, then transferred to the HPC directory for execution. Upon calling this shell file the Windows command line, the ANSYS is launched and updated in the background, and the results are saved in the HPC directory. Strudel software was also used for the visualisation of the ANSYS workbench environment. Strudel launches a remote desktop instance through a visualisation node on the server by creating an SSH tunnel and launching TurboVNC. ANSYS results files are then transferred to the user's database via File Zilla for post-processing analysis.

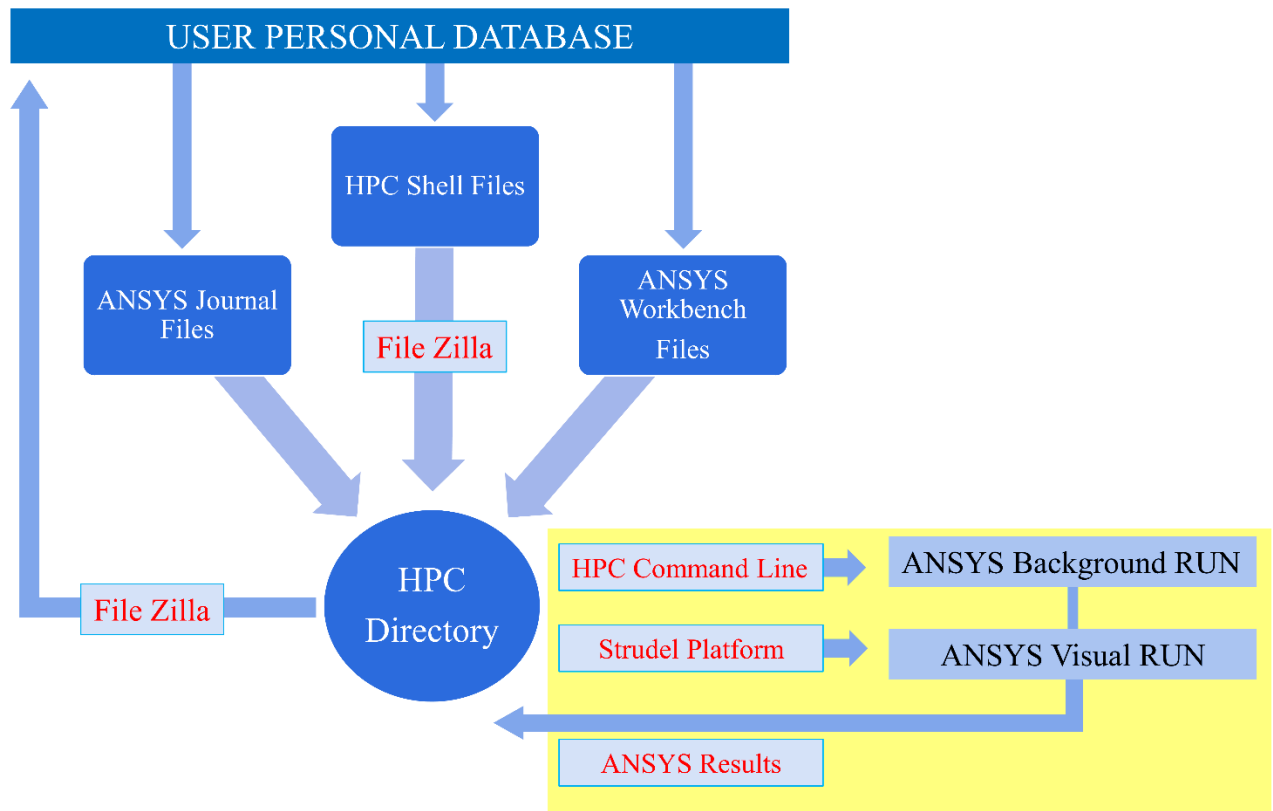


Figure A.1: The schematic paradigm representation of the HPC process indicates the link between the user's database, HPC directory, and ANSYS workbench.

A.2 PBS Code and ANSYS journal file

As described in section A.1, two sets of program codes were prepared for the HPC process, including the Shell file and the ANSYS journal file. The ANSYS journal file is designed to open the project file from the directory, update the project modules, initiate the solving process, and save the result files into the HPC directory. In addition, a PBS code was prepared for individual project files to allocate the number of nodes, CPUs, wall time, and memory. The ANSYS Workbench is launched following the configuration settings, and journal code is called for the project execution. Table A.1 shows the typical sample journal and PBS codes with their brief applications for this project.

Table A.1: PBS and journal codes developed for the HPC process.

Sample Code	Application
<pre># encoding: utf-8 # 2020 R1 SetScriptVersion(Version="20.1.164") Open(FilePath="/home/u1102079/AxisymmetricalStretch.wbpj") Extensions.UnloadExtension(Id="5e7e01a6-8601-11e8-9f8c-28f10e13ffe6", Version="2020.1", Format="Binary") Update() Save(Overwrite=True)</pre>	<ul style="list-style-type: none"> - Open the ANSYS Workbench project file. - Update all the modules within the project. - Save the result files into the HPC directory.
<pre>#!/bin/bash #### Set shell #PBS -S /bin/bash #### Job Name #PBS -N Explicit #### Set default resources requirements for the job #### - these can be overridden on the qsub command line #PBS -l select=2:ncpus=20:mem=252Gb #PBS -l walltime=72:00:00 #### Request that regular output (stdout) and #### terminal output (stderr) goes to the same file #PBS -j oe #### Mail Options #PBS -m abe #PBS -M vahid.ebrahiminejad@usq.edu.au #PBS -P u1102079-FoR 0913 #### Set the queue to run the job on #PBS -q default module load ansys/20.1 #### Goto the directory from which you submitted the job cd \$PBS_O_WORKDIR #### Set the number of processors to run on nprocs=`cat \$PBS_NODEFILE wc -l` #### Start calculation runwb2 -B -R ExplicitNewSkin.wbjn</pre>	<ul style="list-style-type: none"> - Allocations for the number of nodes, CPUs, wall time, and memory. - Launching the ANSYS Workbench Software in the background. - Call the ANSYS journal file to initiate the calculation.

APPENDIX B: Impact applicator test results

To perform MN and MB insertion tests into the skin subjects, prototype impact applicators were designed, manufactured, and assembled. The applicator with an overall size of 45 mm × 95 mm was modelled in SolidWorks. Using PLA filaments, the STL design files were printed by the 3D printer (Teirtime Corporation, Milpitas, CA, USA). The prototype applicator can adjust impact speed, skin strain, and vibration excitations. The following sections explain different components of the applicator and test results for the mechanisms. Figure B.1 shows the final prototype assembly and the explanations of various components.

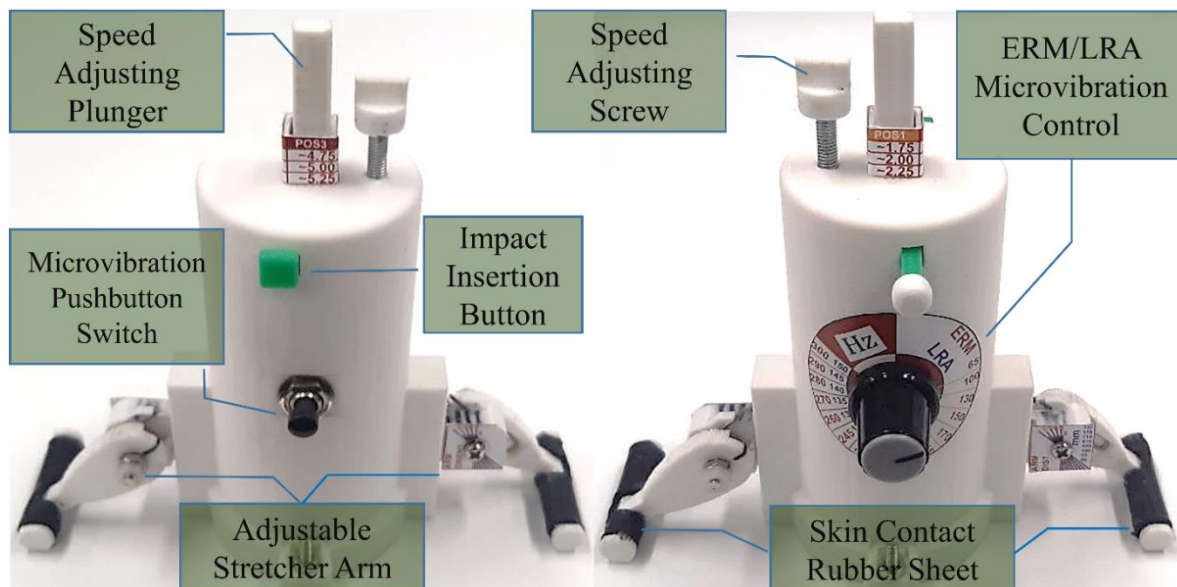


Figure B.1: Impact applicator assembly featuring regulatable impact speed, skin strain, and vibration.

B.1 Impact speed and locking mechanism

The impact speed system comprises fixed and floating speed adjusters, which can be triggered using a locking mechanism. The fixed speed mechanism uses a 1.1 N/mm C-766 compression spring (Century Spring, California, USA) attached to a grooved plunger with three release positions. A locking mechanism is designed to push a spring-loaded button to release the

plunger. To further adjust the impact speed, the compression spring is attached to the floating plate, which can be moved by the top screw. These minute displacements can regulate the impact velocity beyond the pre-set values.

To determine the actual impact speeds, high-speed camera experiments were performed. Figure B.2 shows the arrangement to conduct the test using a high-speed camera (Photron Fastcam SA3) equipped with Nikon Nikkor 50 mm f 1.4 lenses. The applicator is fixed to a 3D-printed base using double-sided tape and then placed at a fixed distance from the camera. The measurements were initially performed on the three fixed positions during the experiment, followed by three further small adjustments using the top screw. Then, the locking mechanism was triggered by pressing the push button while the camera captured the moving images at 4000 fps. Images were then imported into ImageJ (U. S. National Institutes of Health, Bethesda, MD, USA) to stack at equally time-spaced frames to estimate the impact speed.

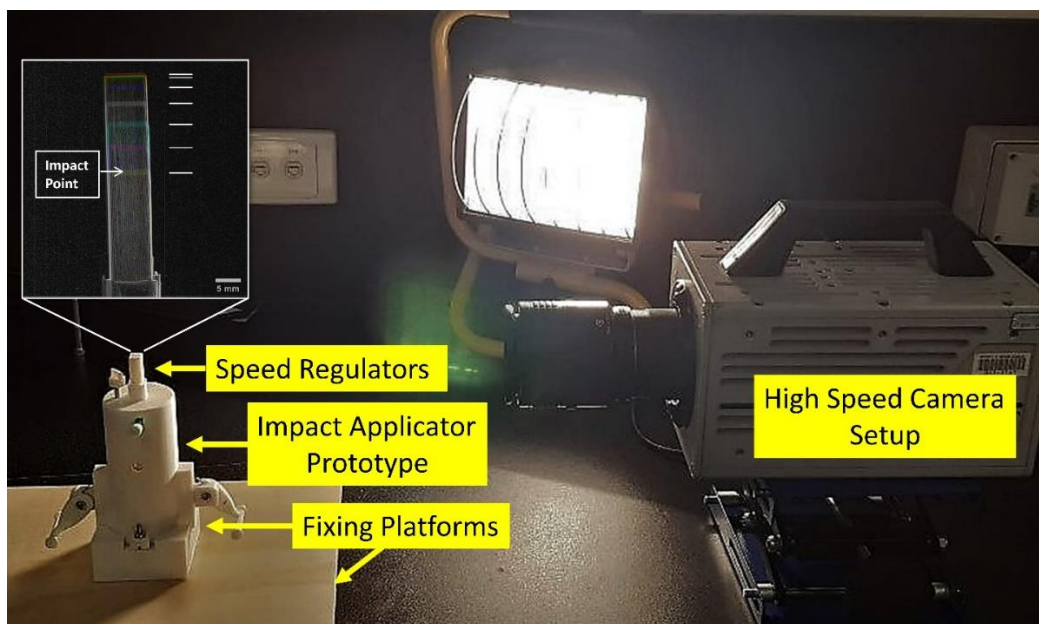


Figure B.2: High-speed camera setup for measurements of the prototype impact velocity at different positions.

The results from the impact applicator speeds are shown in Figure B.3. These data from high-speed camera tests comprise impact velocities from three main slots where the top screw is

positioned at zero, along with three additional data with the top screw adjusted at different positions. According to the overall results, impact speeds varied between ~ 1.5 and ~ 5.5 m/s for the plunger positions. Linear polynomial curve fit applied to these data showed the accuracy of $R^2 = 0.95$. The experimental outcomes were also validated by energy theory and plotted against the piston positions. Equation B.1 estimates the impact velocity at different positions (x), where M is the combined masses of the plunger and MN, x_0 is the initial position, and k is the spring constant. Although the experimental and theoretical energy models showed similar patterns, factors such as sliding friction and air resistance resulted in lower experimental records.

$$V_{impact} = \sqrt{\frac{2(Mg(x-x_0)+0.5k(x^2-x_0^2))}{M}} \quad (B.1)$$

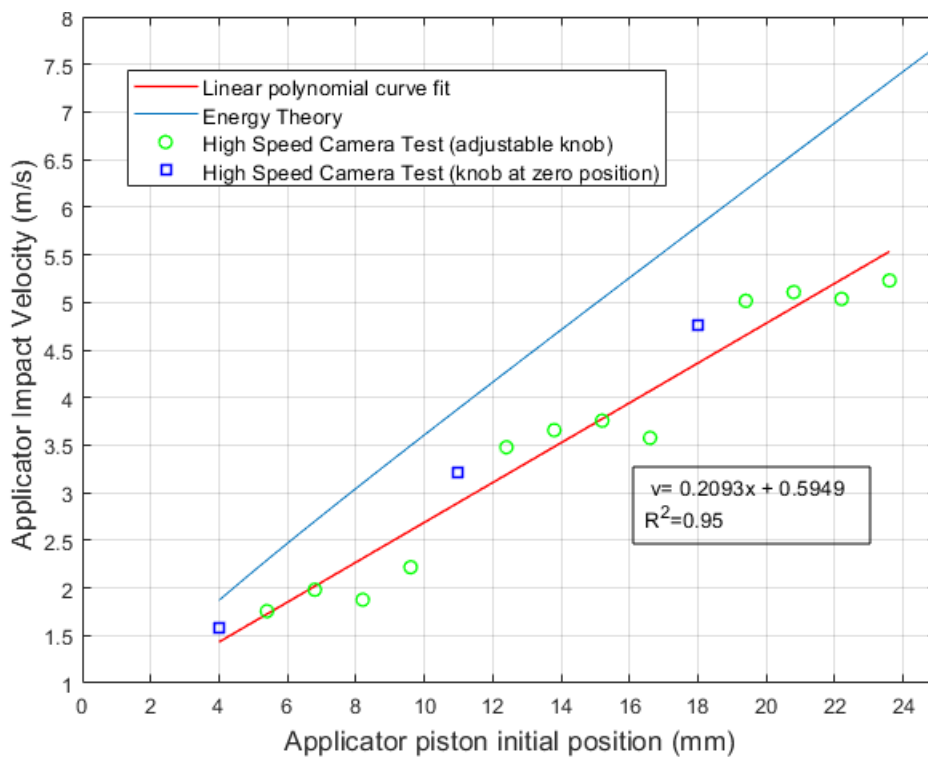


Figure B.3: Graph representation of high-speed camera experimental results for applicator impact velocity compared with energy method.

B.2 Stretching arm mechanism

The skin stretching mechanism consists of arms at both sides of the impact applicator. Each arm is attached to three springs, including two compression springs ($k_c = 0.19$ N/mm) for height adjustments and one torsion spring ($k_t = 0.29$ N.mm/deg) to enable the skin surface tension. The intensity of tensions is directly proportional to the arm orientations; therefore, various arm orientations were marked on each arm to reference different tensions. To measure the overall tension at various arm orientations, a mechanism with sliding plates supported by compression springs was custom-built and assembled (Figure B.4). The mechanism was then connected and locked to the applicator arms at different orientations of 15° to 40° to estimate the compression in the springs ($n = 3$). These spring compressions were converted to tension forces and plotted against the arm orientation. The tensions found from the experiments were then compared against the analytical model consisting of arm orientation (θ), compression spring stiffness (k_c), torsion spring stiffness (k_t) and spring compression (y) parameters (Equation B.2). Test results indicated that reducing arm angle (θ) was associated with a higher applicable tension (T) on the skin. Although the mathematical model was in close alignment with experimental findings, the theoretical model formed a nonlinear behaviour (Figure B.5).

$$T = \frac{2k_c y \cos(\theta) + k_t \theta}{L \sin(\theta)} \quad (\text{B.2})$$

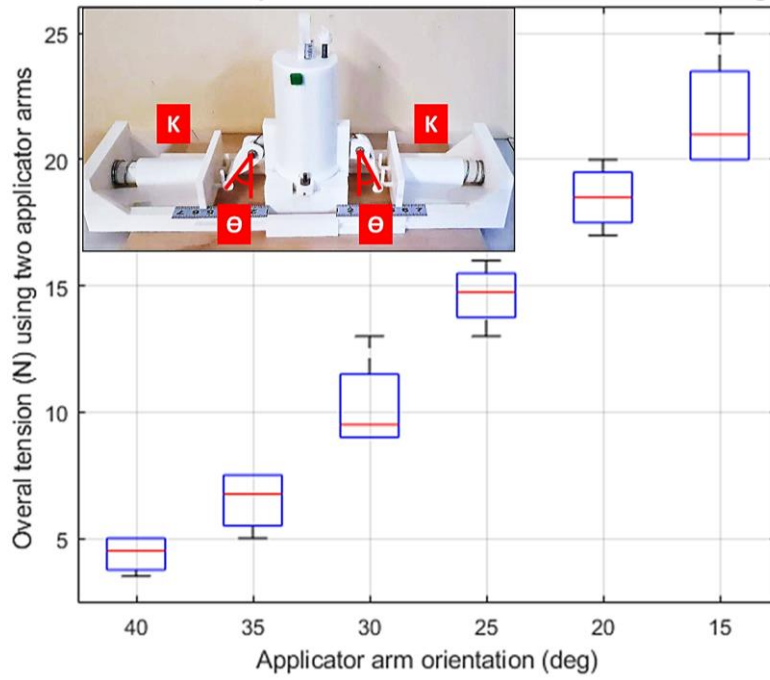


Figure B.4: Test setup for estimating actual tension at different arm orientations, with overall tension plotted in Box and Whisker format for different arm orientations (15° - 40°).

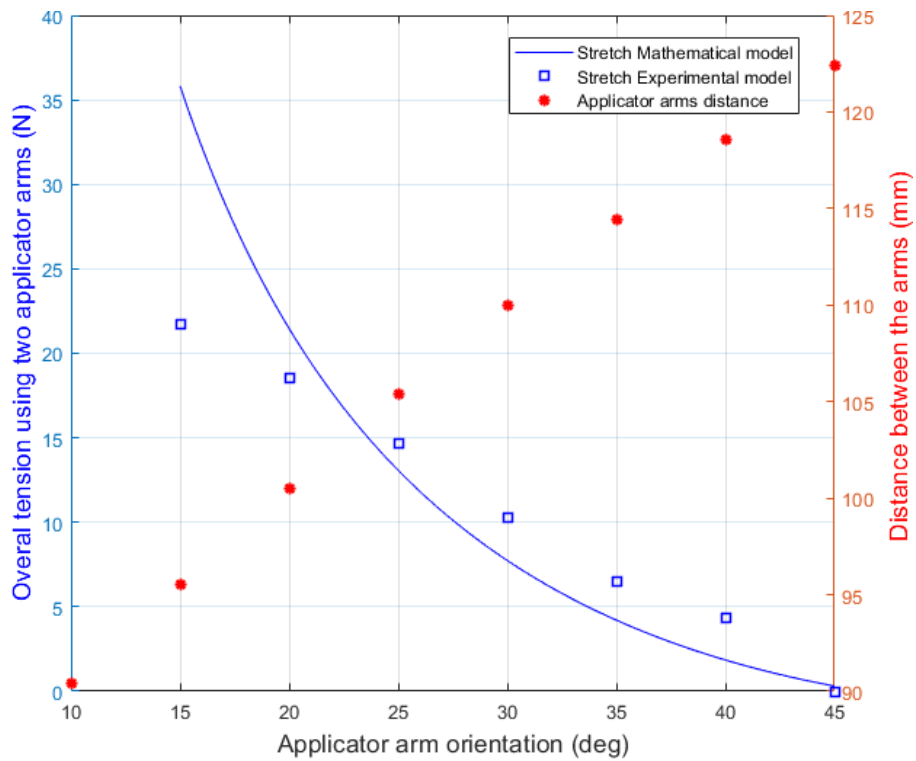


Figure B.5: Graph representation of potentially applicable tension of applicator prototype at different arm orientations. Experimental results were compared with a theoretical model.

B.3 ERM/LRA vibration excitation system

The impact applicator featured two vibration excitations modes, ERM and LRA. LRA and ERM micro-vibration devices were purchased from Precision Microdrives (London, UK) with a $\sim 50 - 250$ Hz low-frequency range capability. These micro-vibration devices were inserted and fixed into the predesigned slots on the internal plunger plate. An electronic circuit was also designed to regulate the frequencies. This simple circuit consisted of a 3.7 V USB chargeable polymer lithium-ion battery (Ecocell, NSW, Australia), 5 k Ω potentiometer, 510 Ω resistor, and NPN 2N2222A transistor with an ON/OFF switch (Figure B.6). The circuit was then tested using technical multimeters against the manufacturer performance graphs.

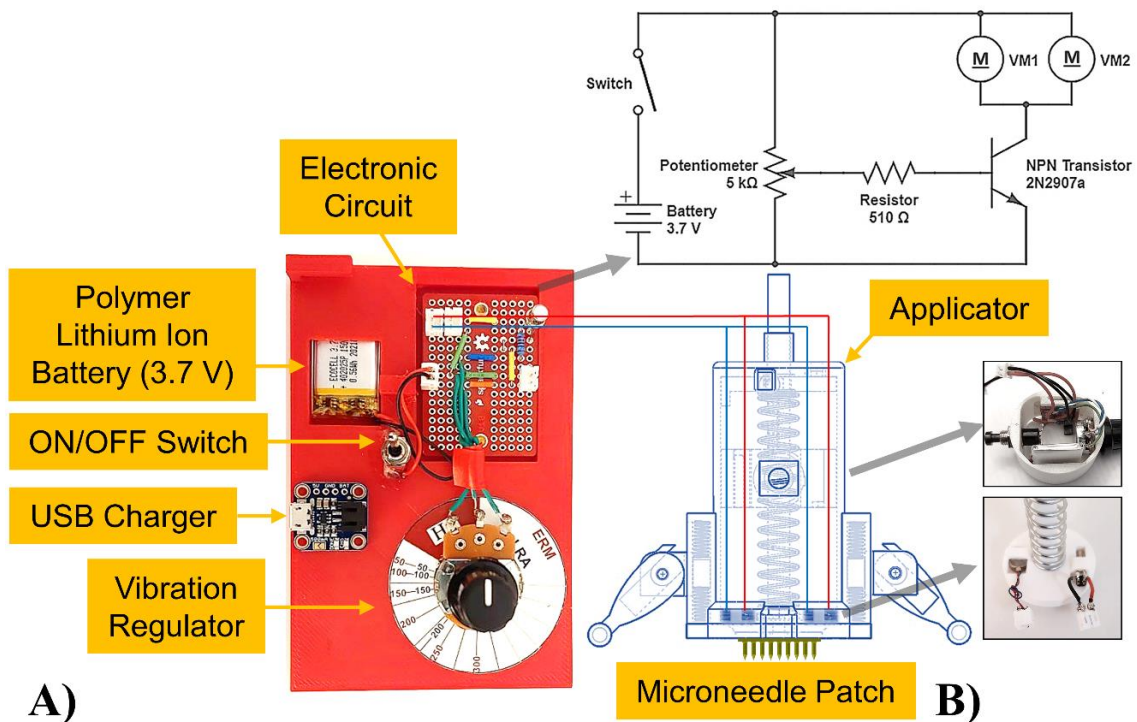


Figure B.6: Schematic representation of impact applicator vibration system and circuit board.

A) The extended version of the circuit board was used for more straightforward control during skin insertion tests. B) The current circuit was then compacted and inserted inside the applicator.

The circuit was passed through a technical multimeter device to measure the voltage and current at different potentiometer orientations, and then the voltage and current readings were recorded. Figure B.7 shows that for the 5 kΩ potentiometer, the device activated at 90° - 300°, increasing the angle of the current and voltage increased from 40 to 170 mA, and 0.5 to 3.5 V, respectively. The activation for the ERM type was initiated at 90° orientation while the position for the LRA type was delayed to the position of 165°. These Voltage (V) and current measurements (mA) were also plotted and compared against the performance graphs provided by the vendor. The maximum frequencies recorded for ERM and LRA microdevices were approximately 300 and 200 Hz, respectively. Figure B.8 shows the potentiometer knob position versus the average generated frequencies for ERM and LRA microdevices.

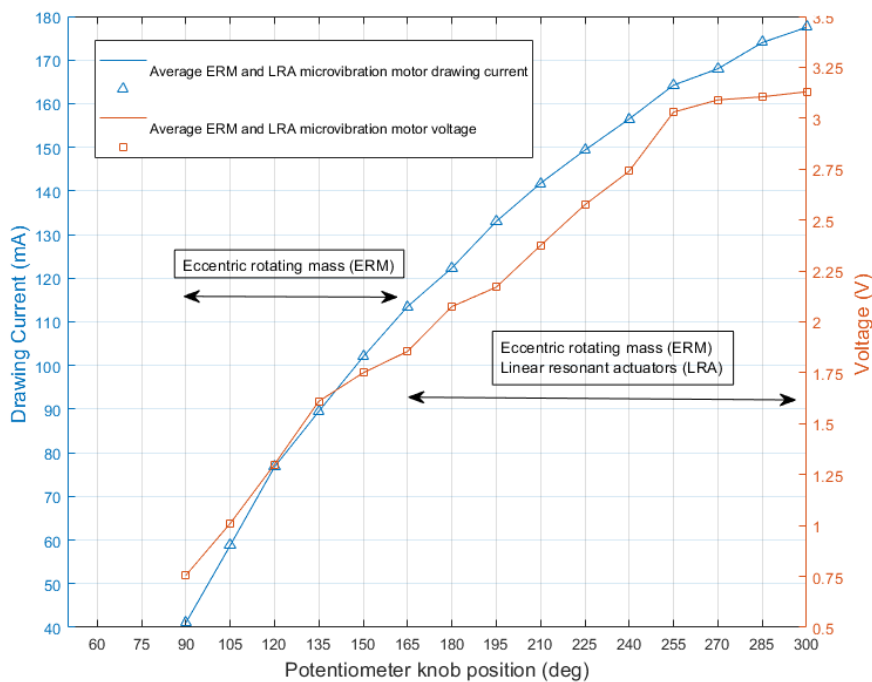


Figure B.7: Graph representation of average voltage and current records for ERM and LRA micro-vibration devices for 5 kΩ potentiometer at different orientations. These readings were compared against the performance graphs to estimate the actual frequency.

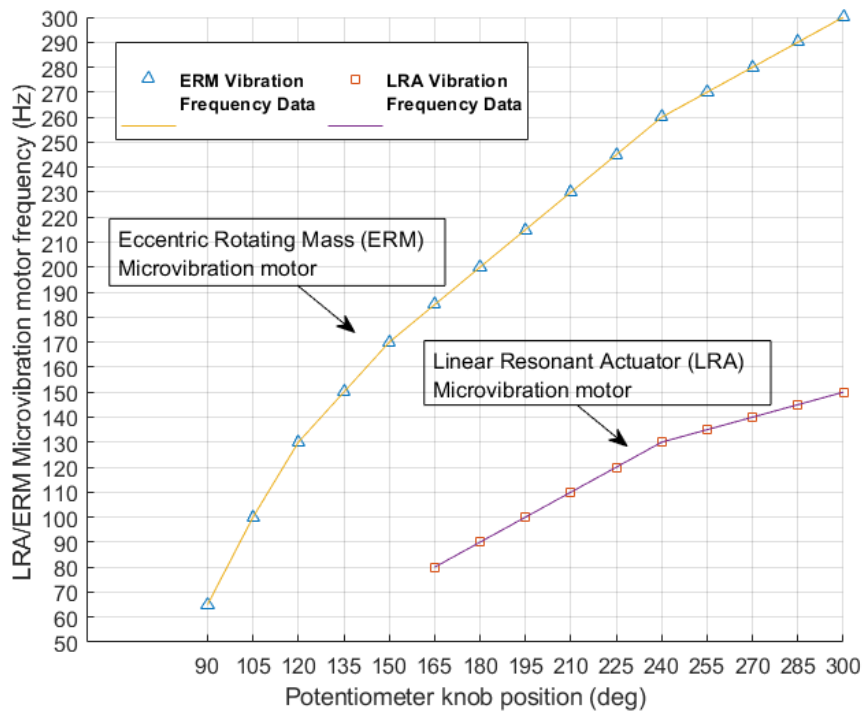


Figure B.8: Potentiometer knob position versus frequency for LRA and ERM micro-vibration devices. While ERM type activation range was recorded from $\sim 90^\circ$ to 300° , the LRA type indicated delayed activation from $\sim 165^\circ$ to 300° .

APPENDIX C: Development of GWL codes for printing multiple samples on a single substrate

Part of this research was to investigate methods of reducing MN fabrication time. The TPP method is a highly accurate and cost-effective technique with timely print time. This section modifies the GWL data files to print six different MB geometries on a 25 × 25 mm ITO substrate. The method used a GWL data file as the basis, and the remaining codes were then written and copied to the same code. Thus, once an MB sample is printed on the substrate, using a series of GWL manual codes, the stage is moved to the following location to print the new MB sample (Figure C.1).

Using the series of GWL codes shown in Figure C.1, the stage is initially moved in 2D (*XY*) space to the location of the subsequent MB sample. As the vertical position of the stage is on the MB tip, the piezo level is then pulled back to zero. Finally, before initiating the polymerisation process, the lens-substrate interface was set to 0.5 μm into the interface position. The following outlines briefly describe the codes applied during the MB prints using the TPP technique:

- **FindInterfaceAt \$interfacePos** (Find the interface between lens-substrate)
- **MoveStageY #** (Moves the stage by # μm relative to latest Y position)
- **MoveStageX #** (Moves the stage by # μm relative to latest X position)
- **PiezoGotoZ 0** (Bring the stage to zero vertical position)
- **var \$interfacePos = #** (Sets the initial print position relative to the interface)

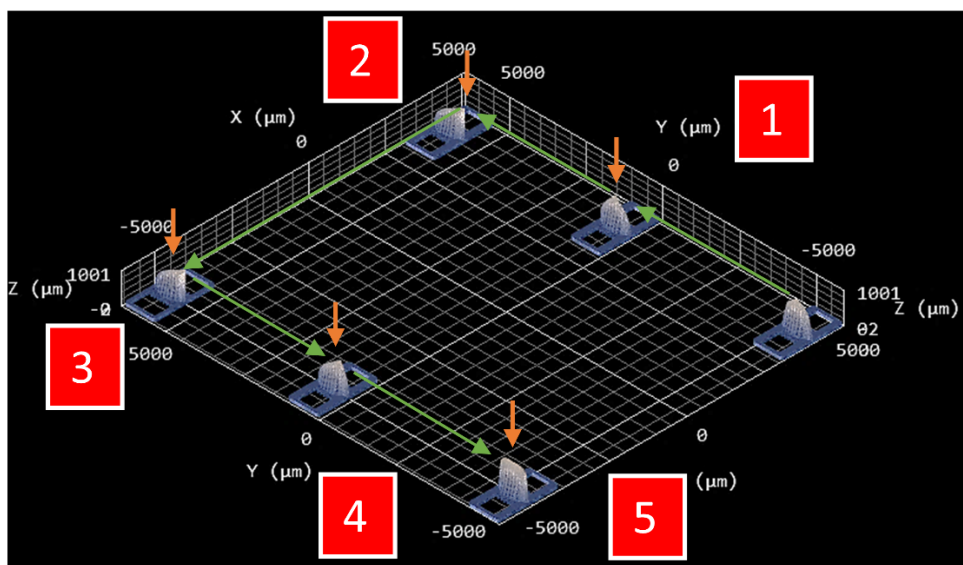
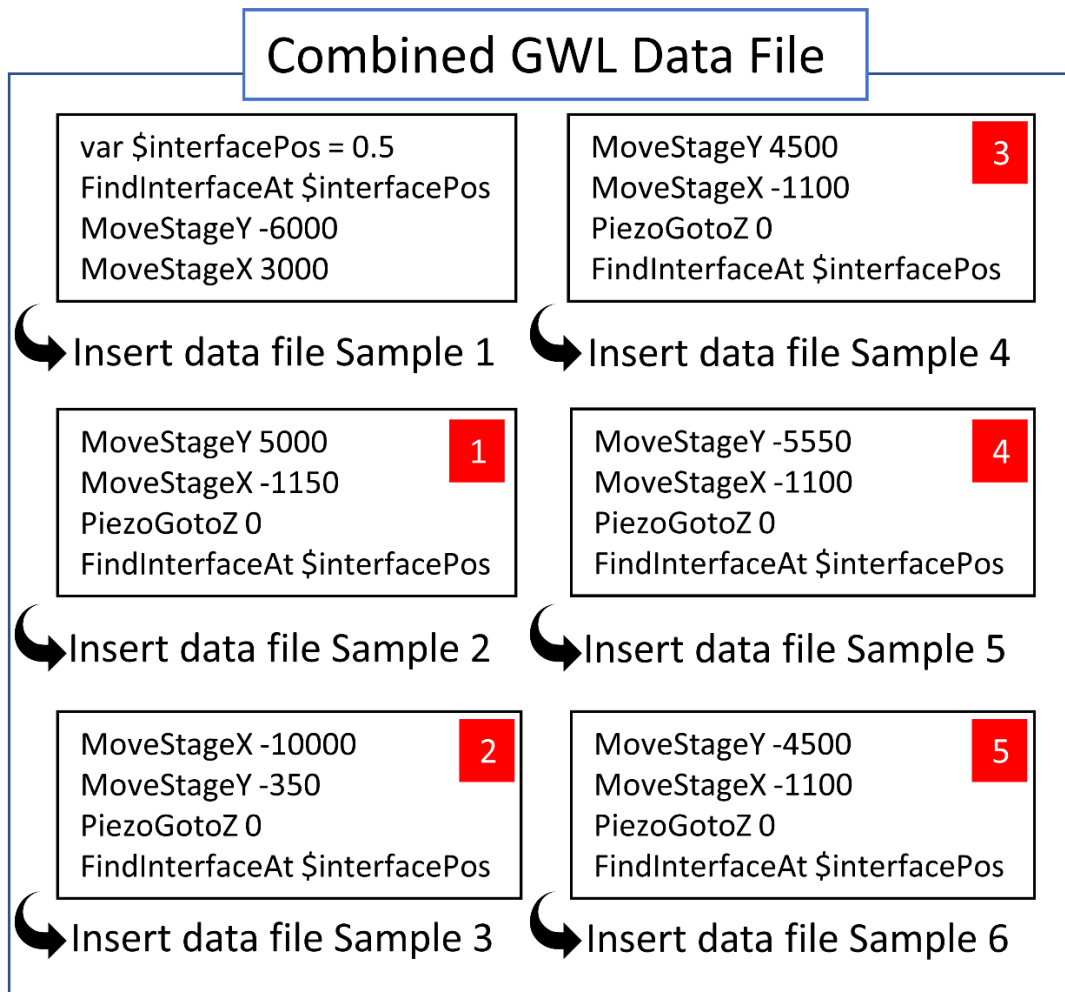


Figure C.1: TPP prints of different MB samples on a single ITO substrate. The codes for stage movements are written between subsequent MB data files. Numbers and arrows on the photo indicate the stage repositioning before running each sample data file.

APPENDIX D: Micro & Nano Engineering Conference (Turin, Italy 2021)

Polymer Microneedles for Transdermal Theranostics and Vaccination



Vahid.ebrahimejad@usq.edu.au

Supervisors: Dr. Zahra Faraji Rad, Prof. Peter Schubel

Vahid Ebrahimejad^a, Zahra Faraji Rad^a, Philip D Prewett^{b,c}, Graham J Davies^{b,d}

^a University of Southern Queensland, Australia

^b University of Birmingham, UK

^c Oxacus Ltd, UK

^d University of New South Wales, Australia



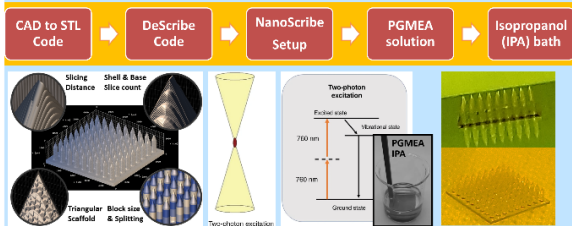
Introduction

The COVID-19 pandemic highlights the need for mass vaccination and inexpensive, rapid, point of care (POC) testing which could extend beyond viruses to bacterial infections and medical emergencies like heart attack. Patch diagnostics could replace current vaccinations and laboratory tests using cheap, mass manufacturable polymer microneedles instead of hypodermics. The commercial potential is considerable, with the POC rapid diagnosis market alone predicted to grow to \$38bn by 2022. Microneedle (MN) patches must have low risk of damage and must penetrate the skin painlessly, with low force, without using expensive applicators. Our microneedle patches are made from a cyclo-olefine polymer (COP) using a hot embossing process with a master mould made by two-photon 3D printing.

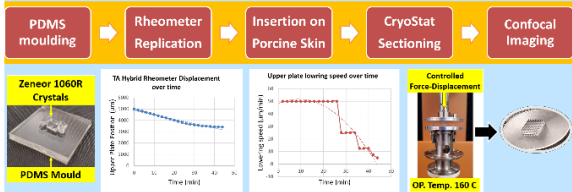
The current research investigates the effects of geometrical design, fabrication process, mechanical strength, and application methods on the insertion process, including mechanisms for damage to the microneedles.

Methodology

Microneedle Design and Fabrication: STL codes for 9x9 MN arrays are generated from the CAD design, then converted to GWL code using DeScribe software. GWL files are imported to the NanoScribe Two Photon Printing (TPP) System. IP-S resin is coated onto Indium Tin Oxide (ITO) glass wafers before TPP exposure. The patterned wafers are cured and washed by PGMEA and Isopropanol (IPA) for 10 and 3 min, respectively. The master moulds are used to make PDMS secondary moulds for hot embossing of the MN patch arrays.



PDMS Moulding and Replication: PDMS solution is poured onto the resin MN array master mould and heated at 80°C for 1 hour. A TA hybrid rheometer is used to melt the Zeonor 1060R COP crystals (Zeon GmbH) while pressing forcing the sample against the PDMS mould. After cooling, polymer replica MNs are released.



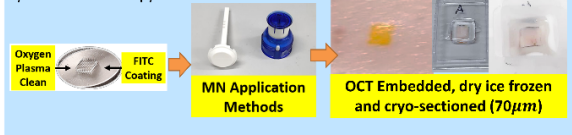
MN Array Mechanical Tests: Single COP polymer MNs, designed with base flanges for additional strength, were subjected to quasi-static compression tests conducted at 1 $\mu\text{m} \cdot \text{s}^{-1}$ speed to evaluate the MN tip and buckling failure load and its location. Failure load is an essential figure of merit, used to determine the MN array safety margin (SM). For shaft radius a , MN length L , and Elastic modulus E the vertical buckling force is:

$$F_b = \frac{\pi^3 a^4 E}{16 L^2}$$

The distance from the tip of bending fracture by a lateral force F_l for Yield Stress σ_y is:

$$x = \pi \frac{a^3 \sigma_y}{4 F_l}$$

Porcine Skin Insertion Tests: After Animal Ethics and Biosafety approvals from USQ and UQ, porcine skin samples were prepared, frozen and sectioned. MN arrays were cleaned using oxygen plasma for 1 min before coating with FITC fluorescein dye. The MN arrays were then inserted into the skin using pressing force from a commercial applicator. Further tests used a prototype "impact" applicator providing dynamic insertion in the speed range 1.5 - 4.5 $\text{m} \cdot \text{s}^{-1}$. Test samples were then embedded in optical cutting temperature (OCT) compound and sectioned using a cryostat in preparation for imaging by confocal microscopy.



Results

Figure 1 shows the results of mechanical and skin insertion tests for an array of polymer MNs, revealing both near-tip and buckling failure scenarios due to 1.3 N quasi-static force increasing with speed to 1.8 N at 50 $\text{m} \cdot \text{s}^{-1}$. There was a remarkable increase in array penetration efficiency (APE) of 22% with increasing impact speed from 3 to 4.5 $\text{m} \cdot \text{s}^{-1}$ (Figure 2). There was no piercing through the porcine stratum corneum using a commercial MN applicator, but our novel prototype applicator produced successful penetration of stiff porcine back skin (Figure 3).

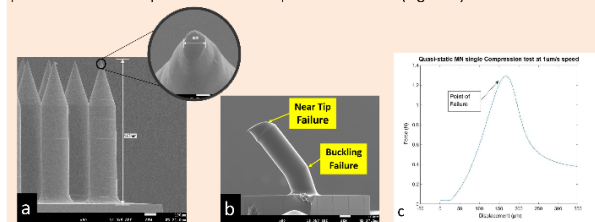


Figure 1: a) Scanning electron Microscopy (SEM) of moulded microneedles with 4.5% and 2% height and width shrinkage, respectively, relative to the resin mould. b) SEM of single MN after compression test, showing effects due to buckling and tip failure. Note the base flange. c) Force-Displacement data for single MN indicating failure point at 1.3 N.

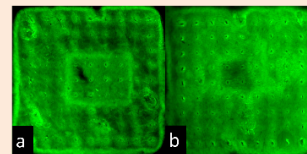


Figure 2: a) Stereo Microscopy images of FITC on tape-stripped skin surface indicates improved array penetration efficiency (penetrating fraction of the array) of 22% (from 70.3% to 92.5%), when impact speed is increased from 3 $\text{m} \cdot \text{s}^{-1}$ to 4.5 $\text{m} \cdot \text{s}^{-1}$ using the prototype applicator.

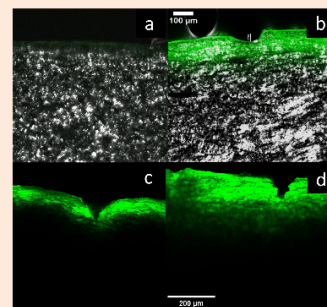


Figure 3: Confocal images of cryo-sectioned porcine back skin showing a) control skin without FITC solution. b) MN array patch on the skin showing penetration failure using the commercial applicator. c) enhanced MN penetration and FITC diffusion into the skin, using the prototype impact applicator at 3 $\text{m} \cdot \text{s}^{-1}$ speed. d) As for c) at 4.5 $\text{m} \cdot \text{s}^{-1}$ speed.

Conclusions and Future Work

- Microneedle patch arrays have the potential to meet the need for mass vaccination and cheap, rapid, point-of-care theranostics, with self-administration a possibility. Two-Photon Polymerization (TPP) is an emerging technique for use with hot embossing to make batches of polymer microneedles (MNs).
- High fidelity Zeonor 1060R polymer MN arrays were made from PDMS secondary moulds using controlled force-distance (F-D) programmes adjusted experimentally according to MN design. The maximum shrinkage was 4.5%.
- Porcine skin insertion tests reveal experimental details of the tip damage and buckling which can occur in uncontrolled use, even when the design incorporates a base flange for extra strength. Experiments showed that a commercial applicator was less effective than thumb pressure insertion. But initial promising results were achieved using our own prototype dynamic impact insertion applicator.
- Future work will include further skin insertion tests and final design optimisation of MN arrays and the new applicator, leading to ethical trials involving human skin.

APPENDIX E: COPYRIGHT PERMISSIONS

30/12/2022, 18:28

RightsLink Printable License

SPRINGER NATURE LICENSE TERMS AND CONDITIONS

Dec 30, 2022

This Agreement between University of Southern Queensland -- Vahid Ebrahimejad ("You") and Springer Nature ("Springer Nature") consists of your license details and the terms and conditions provided by Springer Nature and Copyright Clearance Center.

License Number	5458650323027
License date	Dec 30, 2022
Licensed Content Publisher	Springer Nature
Licensed Content Publication	Nature Biomedical Engineering
Licensed Content Title	An integrated wearable microneedle array for the continuous monitoring of multiple biomarkers in interstitial fluid
Licensed Content Author	Farshad Tehrani et al
Licensed Content Date	May 9, 2022
Type of Use	Thesis/Dissertation
Requestor type	academic/university or research institute
Format	print and electronic
Portion	figures/tables/illustrations
Number of figures/tables/illustrations	1
High-res required	no

Will you be translating? no

Circulation/distribution 50000 or greater

Author of this Springer Nature content no

Title DESIGN AND FABRICATION OF MICRONEEDLE PATCHES, MICROBLADES AND FEATURED INSERTION APPLICATOR FOR OPTIMISING TRANSDERMAL DRUG DELIVERY

Institution name University of Southern Queensland

Expected presentation date Mar 2023

Portions Figure 1 part d

Requestor Location University of Southern Queensland
37 Sinnathamby Blvd, Springfield Central

Springfield Central, QLD 4300
Australia
Attn: University of Southern Queensland

Total 0.00 AUD

Terms and Conditions

Springer Nature Customer Service Centre GmbH Terms and Conditions

The following terms and conditions ("Terms and Conditions") together with the terms specified in your [RightsLink] constitute the License ("License") between you as Licensee and Springer Nature Customer Service Centre GmbH as Licensor. By clicking 'accept' and completing the transaction for your use of the material ("Licensed Material"), you confirm your acceptance of and obligation to be bound by these Terms and Conditions.

1. Grant and Scope of License

1. 1. The Licensor grants you a personal, non-exclusive, non-transferable, non-sublicensable, revocable, world-wide License to reproduce, distribute, communicate to the public, make available, broadcast, electronically transmit or create derivative works using the Licensed Material for the purpose(s) specified in your RightsLink Licence Details only. Licenses are granted for the specific use requested in the order and for no other use, subject to these Terms and Conditions. You acknowledge and

agree that the rights granted to you under this License do not include the right to modify, edit, translate, include in collective works, or create derivative works of the Licensed Material in whole or in part unless expressly stated in your RightsLink Licence Details. You may use the Licensed Material only as permitted under this Agreement and will not reproduce, distribute, display, perform, or otherwise use or exploit any Licensed Material in any way, in whole or in part, except as expressly permitted by this License.

1. 2. You may only use the Licensed Content in the manner and to the extent permitted by these Terms and Conditions, by your RightsLink Licence Details and by any applicable laws.

1. 3. A separate license may be required for any additional use of the Licensed Material, e.g. where a license has been purchased for print use only, separate permission must be obtained for electronic re-use. Similarly, a License is only valid in the language selected and does not apply for editions in other languages unless additional translation rights have been granted separately in the License.

1. 4. Any content within the Licensed Material that is owned by third parties is expressly excluded from the License.

1. 5. Rights for additional reuses such as custom editions, computer/mobile applications, film or TV reuses and/or any other derivative rights requests require additional permission and may be subject to an additional fee. Please apply to journalpermissions@springernature.com or bookpermissions@springernature.com for these rights.

2. Reservation of Rights

Licensor reserves all rights not expressly granted to you under this License. You acknowledge and agree that nothing in this License limits or restricts Licensor's rights in or use of the Licensed Material in any way. Neither this License, nor any act, omission, or statement by Licensor or you, conveys any ownership right to you in any Licensed Material, or to any element or portion thereof. As between Licensor and you, Licensor owns and retains all right, title, and interest in and to the Licensed Material subject to the license granted in Section 1.1. Your permission to use the Licensed Material is expressly conditioned on you not impairing Licensor's or the applicable copyright owner's rights in the Licensed Material in any way.

3. Restrictions on use

3. 1. Minor editing privileges are allowed for adaptations for stylistic purposes or formatting purposes provided such alterations do not alter the original meaning or intention of the Licensed Material and the new figure(s) are still accurate and representative of the Licensed Material. Any other changes including but not limited to, cropping, adapting, and/or omitting material that affect the meaning, intention or moral rights of the author(s) are strictly prohibited.

3. 2. You must not use any Licensed Material as part of any design or trademark.

3. 3. Licensed Material may be used in Open Access Publications (OAP), but any such reuse must include a clear acknowledgment of this permission visible at the same time as the figures/tables/illustration or abstract and which must indicate that the Licensed Material is not part of the governing OA license but has been reproduced with permission. This may be indicated according to any standard referencing system but must include at a minimum 'Book/Journal title, Author, Journal Name (if applicable), Volume (if applicable), Publisher, Year, reproduced with permission from SNCSC'.

4. STM Permission Guidelines

4. 1. An alternative scope of license may apply to signatories of the STM Permissions Guidelines ("STM PG") as amended from time to time and made available at <https://www.stm-assoc.org/intellectual-property/permissions/permissions-guidelines/>.
4. 2. For content reuse requests that qualify for permission under the STM PG, and which may be updated from time to time, the STM PG supersede the terms and conditions contained in this License.
4. 3. If a License has been granted under the STM PG, but the STM PG no longer apply at the time of publication, further permission must be sought from the Rightsholder. Contact journalpermissions@springernature.com or bookpermissions@springernature.com for these rights.

5. Duration of License

5. 1. Unless otherwise indicated on your License, a License is valid from the date of purchase ("License Date") until the end of the relevant period in the below table:

Reuse in a medical communications project	Reuse up to distribution or time period indicated in License
Reuse in a dissertation/thesis	Lifetime of thesis
Reuse in a journal/magazine	Lifetime of journal/magazine
Reuse in a book/textbook	Lifetime of edition
Reuse on a website	1 year unless otherwise specified in the License
Reuse in a presentation/slide kit/poster	Lifetime of presentation/slide kit/poster. Note: publication whether electronic or in print of presentation/slide kit/poster may require further permission.
Reuse in conference proceedings	Lifetime of conference proceedings
Reuse in an annual report	Lifetime of annual report
Reuse in training/CME materials	Reuse up to distribution or time period indicated in License
Reuse in newsmedia	Lifetime of newsmedia
Reuse in coursepack/classroom materials	Reuse up to distribution and/or time period indicated in license

6. Acknowledgement

6. 1. The Licensor's permission must be acknowledged next to the Licensed Material in print. In electronic form, this acknowledgement must be visible at the same time as the figures/tables/illustrations or abstract and must be hyperlinked to the journal/book's homepage.
6. 2. Acknowledgement may be provided according to any standard referencing system and at a minimum should include "Author, Article/Book Title, Journal name/Book imprint, volume, page number, year, Springer Nature".

7. Reuse in a dissertation or thesis

7. 1. Where 'reuse in a dissertation/thesis' has been selected, the following terms apply: Print rights of the Version of Record are provided for; electronic rights for use only on institutional repository as defined by the Sherpa guideline (www.sherpa.ac.uk/romeo/) and only up to what is required by the awarding institution.

7. 2. For theses published under an ISBN or ISSN, separate permission is required. Please contact journalpermissions@springernature.com or bookpermissions@springernature.com for these rights.

7. 3. Authors must properly cite the published manuscript in their thesis according to current citation standards and include the following acknowledgement: *'Reproduced with permission from Springer Nature'*.

8. License Fee

You must pay the fee set forth in the License Agreement (the "License Fees"). All amounts payable by you under this License are exclusive of any sales, use, withholding, value added or similar taxes, government fees or levies or other assessments. Collection and/or remittance of such taxes to the relevant tax authority shall be the responsibility of the party who has the legal obligation to do so.

9. Warranty

9. 1. The Licensor warrants that it has, to the best of its knowledge, the rights to license reuse of the Licensed Material. **You are solely responsible for ensuring that the material you wish to license is original to the Licensor and does not carry the copyright of another entity or third party (as credited in the published version).** If the credit line on any part of the Licensed Material indicates that it was reprinted or adapted with permission from another source, then you should seek additional permission from that source to reuse the material.

9. 2. EXCEPT FOR THE EXPRESS WARRANTY STATED HEREIN AND TO THE EXTENT PERMITTED BY APPLICABLE LAW, LICENSOR PROVIDES THE LICENSED MATERIAL "AS IS" AND MAKES NO OTHER REPRESENTATION OR WARRANTY. LICENSOR EXPRESSLY DISCLAIMS ANY LIABILITY FOR ANY CLAIM ARISING FROM OR OUT OF THE CONTENT, INCLUDING BUT NOT LIMITED TO ANY ERRORS, INACCURACIES, OMISSIONS, OR DEFECTS CONTAINED THEREIN, AND ANY IMPLIED OR EXPRESS WARRANTY AS TO MERCHANTABILITY OR FITNESS FOR A PARTICULAR PURPOSE. IN NO EVENT SHALL LICENSOR BE LIABLE TO YOU OR ANY OTHER PARTY OR ANY OTHER PERSON OR FOR ANY SPECIAL, CONSEQUENTIAL, INCIDENTAL, INDIRECT, PUNITIVE, OR EXEMPLARY DAMAGES, HOWEVER CAUSED, ARISING OUT OF OR IN CONNECTION WITH THE DOWNLOADING, VIEWING OR USE OF THE LICENSED MATERIAL REGARDLESS OF THE FORM OF ACTION, WHETHER FOR BREACH OF CONTRACT, BREACH OF WARRANTY, TORT, NEGLIGENCE, INFRINGEMENT OR OTHERWISE (INCLUDING, WITHOUT LIMITATION, DAMAGES BASED ON LOSS OF PROFITS, DATA, FILES, USE, BUSINESS OPPORTUNITY OR CLAIMS OF THIRD PARTIES), AND WHETHER OR NOT THE PARTY HAS BEEN ADVISED OF THE POSSIBILITY OF SUCH DAMAGES. THIS LIMITATION APPLIES NOTWITHSTANDING ANY FAILURE OF ESSENTIAL PURPOSE OF ANY LIMITED REMEDY PROVIDED HEREIN.

10. Termination and Cancellation

10. 1. The License and all rights granted hereunder will continue until the end of the applicable period shown in Clause 5.1 above. Thereafter, this license will be

terminated and all rights granted hereunder will cease.

10. 2. Licensor reserves the right to terminate the License in the event that payment is not received in full or if you breach the terms of this License.

11. General

11. 1. The License and the rights and obligations of the parties hereto shall be construed, interpreted and determined in accordance with the laws of the Federal Republic of Germany without reference to the stipulations of the CISG (United Nations Convention on Contracts for the International Sale of Goods) or to Germany's choice-of-law principle.

11. 2. The parties acknowledge and agree that any controversies and disputes arising out of this License shall be decided exclusively by the courts of or having jurisdiction for Heidelberg, Germany, as far as legally permissible.

11. 3. This License is solely for Licensor's and Licensee's benefit. It is not for the benefit of any other person or entity.

Questions? For questions on Copyright Clearance Center accounts or website issues please contact springernaturesupport@copyright.com or +1-855-239-3415 (toll free in the US) or +1-978-646-2777. For questions on Springer Nature licensing please visit <https://www.springernature.com/gp/partners/rights-permissions-third-party-distribution>

Other Conditions:

Version 1.4 - Dec 2022

Questions? customercare@copyright.com or +1-855-239-3415 (toll free in the US) or +1-978-646-2777.



?
Help ▾

Live Chat

Microneedle-based skin patch for blood-free rapid diagnostic testing

SPRINGER NATURE

Author: Xue Jiang et al

Publication: Microsystems & Nanoengineering

Publisher: Springer Nature

Date: Nov 2, 2020

Copyright © 2020, The Author(s)

Creative Commons

This is an open access article distributed under the terms of the [Creative Commons CC BY](#) license, which permits unrestricted use, distribution, and reproduction in any medium, provided the original work is properly cited.

You are not required to obtain permission to reuse this article.

To request permission for a type of use not listed, please contact [Springer Nature](#)

**JOHN WILEY AND SONS LICENSE
TERMS AND CONDITIONS**

May 06, 2023

This Agreement between University of Southern Queensland -- Vahid Ebrahimejad ("You") and John Wiley and Sons ("John Wiley and Sons") consists of your license details and the terms and conditions provided by John Wiley and Sons and Copyright Clearance Center.

License Number 5542890721926

License date May 06, 2023

Licensed Content
Publisher John Wiley and SonsLicensed Content
Publication Advanced Materials InterfacesLicensed Content
Title Microneedle Arrays for Drug Delivery and Diagnostics: Toward an
Optimized Design, Reliable Insertion, and PenetrationLicensed Content
Author Zahra Faraji Rad, Graham J. Davies, Philip D. Prewett, et alLicensed Content
Date Jan 21, 2022Licensed Content
Volume 9Licensed Content
Issue 6Licensed Content
Pages 26

Type of use Dissertation/Thesis

Requestor type	Author of this Wiley article
Format	Print and electronic
Portion	Full article
Will you be translating?	No
Title	DESIGN AND FABRICATION OF MICRONEEDLE PATCHES, MICROBLADES AND FEATURED INSERTION APPLICATOR FOR OPTIMISING TRANSDERMAL DRUG DELIVERY
Institution name	University of Southern Queensland
Expected presentation date	May 2023
Requestor Location	University of Southern Queensland 37 Sinnathamby Blvd, Springfield Central Springfield Central, QLD 4300 Australia Attn: University of Southern Queensland
Publisher Tax ID	EU826007151
Total	0.00 USD

Terms and Conditions

TERMS AND CONDITIONS

This copyrighted material is owned by or exclusively licensed to John Wiley & Sons, Inc. or one of its group companies (each a "Wiley Company") or handled on behalf of a society with which a Wiley Company has exclusive publishing rights in relation to a particular work (collectively "WILEY"). By clicking "accept" in connection with completing this licensing transaction, you agree that the following terms and conditions apply to this transaction (along with the billing and payment terms and conditions established by the Copyright Clearance Center Inc., ("CCC's Billing and Payment terms and conditions"), at the time that you opened your RightsLink account (these are available at any time at <http://myaccount.copyright.com>).

Terms and Conditions

- The materials you have requested permission to reproduce or reuse (the "Wiley Materials") are protected by copyright.
- You are hereby granted a personal, non-exclusive, non-sub licensable (on a stand-alone basis), non-transferable, worldwide, limited license to reproduce the Wiley Materials for the purpose specified in the licensing process. This license, **and any CONTENT (PDF or image file) purchased as part of your order**, is for a one-time use only and limited to any maximum distribution number specified in the license. The first instance of republication or reuse granted by this license must be completed within two years of the date of the grant of this license (although copies prepared before the end date may be distributed thereafter). The Wiley Materials shall not be used in any other manner or for any other purpose, beyond what is granted in the license. Permission is granted subject to an appropriate acknowledgement given to the author, title of the material/book/journal and the publisher. You shall also duplicate the copyright notice that appears in the Wiley publication in your use of the Wiley Material. Permission is also granted on the understanding that nowhere in the text is a previously published source acknowledged for all or part of this Wiley Material. Any third party content is expressly excluded from this permission.
- With respect to the Wiley Materials, all rights are reserved. Except as expressly granted by the terms of the license, no part of the Wiley Materials may be copied, modified, adapted (except for minor reformatting required by the new Publication), translated, reproduced, transferred or distributed, in any form or by any means, and no derivative works may be made based on the Wiley Materials without the prior permission of the respective copyright owner. **For STM Signatory Publishers clearing permission under the terms of the [STM Permissions Guidelines](#) only, the terms of the license are extended to include subsequent editions and for editions in other languages, provided such editions are for the work as a whole in situ and does not involve the separate exploitation of the permitted figures or extracts**, You may not alter, remove or suppress in any manner any copyright, trademark or other notices displayed by the Wiley Materials. You may not license, rent, sell, loan, lease, pledge, offer as security, transfer or assign the Wiley Materials on a stand-alone basis, or any of the rights granted to you hereunder to any other person.
- The Wiley Materials and all of the intellectual property rights therein shall at all times remain the exclusive property of John Wiley & Sons Inc, the Wiley Companies, or their respective licensors, and your interest therein is only that of having possession of and the right to reproduce the Wiley Materials pursuant to Section 2 herein during the continuance of this Agreement. You agree that you own no right, title or interest in or to the Wiley Materials or any of the intellectual property rights therein. You shall have no rights hereunder other than the license as provided for above in Section 2. No right, license or interest to any trademark, trade name, service mark or other branding ("Marks") of WILEY or its licensors is granted hereunder, and you agree that you shall not assert any such right, license or interest with respect thereto
- NEITHER WILEY NOR ITS LICENSORS MAKES ANY WARRANTY OR REPRESENTATION OF ANY KIND TO YOU OR ANY THIRD PARTY, EXPRESS, IMPLIED OR STATUTORY, WITH RESPECT TO THE MATERIALS OR THE ACCURACY OF ANY INFORMATION CONTAINED IN THE MATERIALS, INCLUDING, WITHOUT LIMITATION, ANY IMPLIED WARRANTY OF MERCHANTABILITY, ACCURACY, SATISFACTORY QUALITY, FITNESS FOR A PARTICULAR PURPOSE, USABILITY, INTEGRATION OR NON-INFRINGEMENT AND ALL SUCH WARRANTIES ARE HEREBY EXCLUDED BY WILEY AND ITS LICENSORS AND WAIVED BY YOU.
- WILEY shall have the right to terminate this Agreement immediately upon breach of this Agreement by you.

- You shall indemnify, defend and hold harmless WILEY, its Licensors and their respective directors, officers, agents and employees, from and against any actual or threatened claims, demands, causes of action or proceedings arising from any breach of this Agreement by you.
- IN NO EVENT SHALL WILEY OR ITS LICENSORS BE LIABLE TO YOU OR ANY OTHER PARTY OR ANY OTHER PERSON OR ENTITY FOR ANY SPECIAL, CONSEQUENTIAL, INCIDENTAL, INDIRECT, EXEMPLARY OR PUNITIVE DAMAGES, HOWEVER CAUSED, ARISING OUT OF OR IN CONNECTION WITH THE DOWNLOADING, PROVISIONING, VIEWING OR USE OF THE MATERIALS REGARDLESS OF THE FORM OF ACTION, WHETHER FOR BREACH OF CONTRACT, BREACH OF WARRANTY, TORT, NEGLIGENCE, INFRINGEMENT OR OTHERWISE (INCLUDING, WITHOUT LIMITATION, DAMAGES BASED ON LOSS OF PROFITS, DATA, FILES, USE, BUSINESS OPPORTUNITY OR CLAIMS OF THIRD PARTIES), AND WHETHER OR NOT THE PARTY HAS BEEN ADVISED OF THE POSSIBILITY OF SUCH DAMAGES. THIS LIMITATION SHALL APPLY NOTWITHSTANDING ANY FAILURE OF ESSENTIAL PURPOSE OF ANY LIMITED REMEDY PROVIDED HEREIN.
- Should any provision of this Agreement be held by a court of competent jurisdiction to be illegal, invalid, or unenforceable, that provision shall be deemed amended to achieve as nearly as possible the same economic effect as the original provision, and the legality, validity and enforceability of the remaining provisions of this Agreement shall not be affected or impaired thereby.
- The failure of either party to enforce any term or condition of this Agreement shall not constitute a waiver of either party's right to enforce each and every term and condition of this Agreement. No breach under this agreement shall be deemed waived or excused by either party unless such waiver or consent is in writing signed by the party granting such waiver or consent. The waiver by or consent of a party to a breach of any provision of this Agreement shall not operate or be construed as a waiver of or consent to any other or subsequent breach by such other party.
- This Agreement may not be assigned (including by operation of law or otherwise) by you without WILEY's prior written consent.
- Any fee required for this permission shall be non-refundable after thirty (30) days from receipt by the CCC.
- These terms and conditions together with CCC's Billing and Payment terms and conditions (which are incorporated herein) form the entire agreement between you and WILEY concerning this licensing transaction and (in the absence of fraud) supersedes all prior agreements and representations of the parties, oral or written. This Agreement may not be amended except in writing signed by both parties. This Agreement shall be binding upon and inure to the benefit of the parties' successors, legal representatives, and authorized assigns.
- In the event of any conflict between your obligations established by these terms and conditions and those established by CCC's Billing and Payment terms and conditions, these terms and conditions shall prevail.
- WILEY expressly reserves all rights not specifically granted in the combination of (i) the license details provided by you and accepted in the course of this licensing transaction, (ii) these terms and conditions and (iii) CCC's Billing and Payment terms and conditions.

- This Agreement will be void if the Type of Use, Format, Circulation, or Requestor Type was misrepresented during the licensing process.
- This Agreement shall be governed by and construed in accordance with the laws of the State of New York, USA, without regards to such state's conflict of law rules. Any legal action, suit or proceeding arising out of or relating to these Terms and Conditions or the breach thereof shall be instituted in a court of competent jurisdiction in New York County in the State of New York in the United States of America and each party hereby consents and submits to the personal jurisdiction of such court, waives any objection to venue in such court and consents to service of process by registered or certified mail, return receipt requested, at the last known address of such party.

WILEY OPEN ACCESS TERMS AND CONDITIONS

Wiley Publishes Open Access Articles in fully Open Access Journals and in Subscription journals offering Online Open. Although most of the fully Open Access journals publish open access articles under the terms of the Creative Commons Attribution (CC BY) License only, the subscription journals and a few of the Open Access Journals offer a choice of Creative Commons Licenses. The license type is clearly identified on the article.

The Creative Commons Attribution License

The [Creative Commons Attribution License \(CC-BY\)](#) allows users to copy, distribute and transmit an article, adapt the article and make commercial use of the article. The CC-BY license permits commercial and non-

Creative Commons Attribution Non-Commercial License

The [Creative Commons Attribution Non-Commercial \(CC-BY-NC\) License](#) permits use, distribution and reproduction in any medium, provided the original work is properly cited and is not used for commercial purposes.(see below)

Creative Commons Attribution-Non-Commercial-NoDerivs License

The [Creative Commons Attribution Non-Commercial-NoDerivs License \(CC-BY-NC-ND\)](#) permits use, distribution and reproduction in any medium, provided the original work is properly cited, is not used for commercial purposes and no modifications or adaptations are made. (see below)

Use by commercial "for-profit" organizations

Use of Wiley Open Access articles for commercial, promotional, or marketing purposes requires further explicit permission from Wiley and will be subject to a fee.

Further details can be found on Wiley Online Library
<http://olabout.wiley.com/WileyCDA/Section/id-410895.html>

Other Terms and Conditions:

v1.10 Last updated September 2015

Questions? customercare@copyright.com.